High-order spectral element methods for the simulation of compressible turbulent flows

Niccolo Tonicello

▶ **To cite this version:**

Niccolo Tonicello. High-order spectral element methods for the simulation of compressible turbulent flows. Fluid mechanics [physics.class-ph]. Normandie Université, 2021. English. NNT : 2021NORMR046 . tel-03405449v1

HAL Id: tel-03405449

https://theses.hal.science/tel-03405449v1

Submitted on 27 Oct 2021 (v1), last revised 27 Oct 2021 (v2)

HAL is a multi-disciplinary open access archive for the deposit and dissemination of scientific research documents, whether they are published or not. The documents may come from teaching and research institutions in France or abroad, or from public or private research centers.

L'archive ouverte pluridisciplinaire **HAL**, est destinée au dépôt et à la diffusion de documents scientifiques de niveau recherche, publiés ou non, émanant des établissements d'enseignement et de recherche français ou étrangers, des laboratoires publics ou privés.

Normandie Université

THÈSE

Pour obtenir le diplôme de doctorat

Spécialité MECANIQUE DES FLUIDES, ENERGETIQUE, THERMIQUE, COMBUSTION, ACOUSTIQUE

Préparée au sein de l'Université de Rouen Normandie

High-order spectral element methods for the simulation of compressible turbulent flows

Présentée et soutenue par
Niccolo TONICELLO

Thèse soutenue le 28/09/2021 devant le jury composé de		
M. ERIC LAMBALLAIS	PROFESSEUR DES UNIVERSITES, UNIVERSITE POITIERS	Rapporteur du jury
M. FRANCK NICOUD	PROFESSEUR DES UNIVERSITES, UNIVERSITE MONTPELLIER 2 SCIENCES ET TEC	Rapporteur du jury
M. ABDELLAH HADJADJ	PROFESSEUR DES UNIVERSITES, INSA DE ROUEN NORMANDIE	Membre du jury
M. GUIDO LODATO	MAITRE DE CONFERENCES, INSA DE ROUEN NORMANDIE	Membre du jury
M. GIANMARCO MENGALDO	PROFESSEUR DES UNIVERSITES, Université Nationale de Singapour (NUS)	Membre du jury
M. STEPHANE MOREAU	PROFESSEUR DES UNIVERSITES, Université de Sherbrooke (Canada)	Membre du jury
M. LUC VERVISCH	PROFESSEUR DES UNIVERSITES, INSA DE ROUEN NORMANDIE	Directeur de thèse

Thèse dirigée par LUC VERVISCH, COMPLEXE DE RECHERCHE INTERPROFESSIONEL EN AEROTHERMOCHIMIE

UNIVERSITÉ DE ROUEN NORMANDIE

ED 591 PSIME

CORIA UMR 6614

High-order spectral element methods for the simulation of compressible turbulent flows

Thesis submitted for the degree of Doctor of Philosophy of the University of Rouen Normandie

Niccolò Tonicello

niccolo.tonicello@coria.fr

Jury:

Eric Lamballais	Université de Poitiers	Rapporteur
Franck Nicoud	Université de Montpellier	Rapporteur
Abdellah Hadjadj	INSA de Rouen Normandie	Examinateur
Gianmarco Mengaldo	Université Nationale de Singapour	Examinateur
Stephane Moreau	Université de Sherbrooke	Examinateur
Guido Lodato	INSA de Rouen Normandie	Co-Directeur de thèse
Luc Vervisch	INSA de Rouen Normandie	Directeur de thèse

CORIA UMR 6614 - University of Rouen Normandie

Technopole du Madrillet, B.P. 8

76801 Saint-Etienne du Rouvray - France

Acknowledgements

When I was about to finish my Master degree in Italy I had only one clear idea for the future: apply for a PhD in a foreign country. Everyone who did it knows how many applications are generally sent in the deep ocean, hoping for a chance to play in the top league. It is now funny to remember that when I received the first interview request by Dr. Lodato, I almost forgot I applied for that position in the first place. As it often happens in life, I didn't realise that mine was about to change radically. I had the best three years of my life in France, diving into a similar, but at the same time different, colourful culture, made by wonderful people and awful weather.

I wish to thank my Advisors, Prof. Luc Vervisch and Dr. Guido Lodato, for giving me the opportunity to pursue my professional goals and for their valuable guidance. I thank them for the independence and trust they gave me since the very first day. I thank them for treating me as a professional and not as a student, as a man and not as a child, for trusting me along these years, for leading me to the best possible version of myself. At the same time, of course, I thank them for the fundamental role they had in my work, for their advices and guidance, both scientifically and personally. I particularly thank Dr. Lodato for helping me in the many panic attacks I had during these three years. He once told me: "At a certain point, it doesn't really matter how many papers you published or your h-index, but the hours you spend playing with your son". I will keep these words with me forever, as bedrock of my future professional life.

Secondly, I want to thank my family, for being a solid pylon in my life. I thank my mom and dad, Cristina and Amedeo, for always believing in me and for always supporting me to pursue my dreams (even outside our beloved country). I also thank my sister and brother in law, Carlotta and Nicolò, for giving me critical advices both professionally but most importantly personally.

Finally I thank all the people working at CORIA and INSA. I felt welcomed since the very first day in such an amazing environment of inclusion and vibrating diversity. In these years, I met great people (mostly foreigners) that helped me so much in my everyday struggles. I want to thank, in particular, Diego and Sabina, for giving me shelter in many different occasions from the many psychological (and physical) storms during my PhD. Along

them, I thank Cléante for bearing my persistently annoying and depressing petulance. I thank Alberto and Lorenzo for giving me the priceless opportunity to hear my mother-tongue language and to nostalgically remember those wonderful rain-free summers in Italy. I thank Victor for trying, in his last few months in Normandy, to help me with my hopeless social awkwardness. I finally thank, from the bottom of my heart, Louise, for showing me how to be brave and gentle in these challenging times.

I also thank everyone who was not physically here in Normandy but still close to me from different corners of the world: Gabriele from Paris, Riccardo from Barcelona and Dario from Trieste. Our long-distance discussions about the scientific community and, in general, about the research environment helped me a lot in my growth over the years. I finally thank my friends from Italy, in particular Riccardo, Martino and Gianmarco. You made all the many trips to Italy always enjoyable and each one of them special in a unique way.

I do believe we all sit on the shoulders of giants and I can only hope I gave my small contribution in the limitless field of Computational Fluid Dynamics. Adding that little pinnacle, apparently useless, on top of a magnificent cathedral.

Enjoy the reading.

Abstract

This thesis is focused on the application of high-order methods to compressible turbulent flows. Aspects such as numerical dissipation/dispersion, dynamic Sub-Grid Scale modelling, shock-capturing techniques and compressibility effects on turbulence modelling are thoroughly discussed. The thesis manuscript is organised for increasing levels of complexity, leading ultimately to the simulation of fully compressible turbulent flows where all the up-mentioned difficulties are simultaneously involved. The results presented in this work fit into development of reliable and robust high-order solvers for computational fluid dynamics applications.

An innovative generalisation of standard spectral analyses techniques applied to high-order methods is first presented. Special attention is dedicated to the Spectral Difference scheme used for the numerical simulations performed for this thesis. Spectral analyses of high-order methods are normally based on the numerical discretisation of the one-dimensional linear advection equation. In the present work, such approach has been generalised for non-constant advection velocities to gain more meaningful insights about high-order numerical discretisations of non-linear equations, such as Navier-Stokes or Euler equations. The Spectral Difference method has shown some significant differences with respect to the correspondent Flux Reconstruction recovering scheme when non-constant advection velocities are considered. The general behaviour of dissipative curves has shown remarkable deviations between SD, FR-SD and the Flux Reconstruction Discontinuous Galerkin recovering scheme. Numerical experiments have been conducted to highlight the role played by numerical fluxes and order of approximation for Spectral Difference and FR-DG methods.

The informations gathered from spectral analyses are then used to present the Spectral Element Dynamic Model. The SEDM has been developed by Chapelier & Lodato [1] to link numerical dissipation, which represents a typical build-in feature of spectral element methods, and classical explicit SGS dissipation within the framework of Large-Eddy Simulations of turbulent flows. A series of relevant transitional turbulent flows are then considered to better evaluate the performance of the SEDM in more complex conditions. Namely, a zero-pressure-gradient flow over a flat plate and a low-Reynolds SD7003 airfoil simulation. Both computations are meant to study in deep

the dynamic nature of the SEDM for complex geometries and transitional flows.

Within the framework of compressible flows, an innovative low dissipative bulk-based artificial viscosity shock-capturing technique is presented and analysed in detail. Numerical simulations in one to three dimensions, inviscid and viscous, laminar and turbulent flows are considered to provide a sufficiently wide range of flow configurations where the proposed model performs well. In particular, in comparison with another widely diffused artificial viscosity model based on a laplacian regularisation. The bulk-based artificial viscosity provides, in fact, considerably reduced levels of artificial dissipation of vortical structures, keeping, at the same time, the simulation stable.

Finally, in the last part of the manuscript, the coexistence of all the up-mentioned investigations and models presented throughout the thesis is studied for more complex compressible turbulent flows. Among these, the transonic flow around an RAE2822 airfoil and the interaction between a turbulent boundary layer with a 24° compression ramp have been simulated using an LES approach, where the SEDM has been coupled with the proposed bulk-based AV technique. Both simulations provided results in good agreement with other simulations and experiments, certifying the robustness and reliability of the combined effect of the two models.

In the end, in order to generalise even more the SEDM to more compressible applications, a Direct Numerical Simulation study for a compression/expansion ramp configuration has been performed. The highly-resolved data have been used to reveal insightful informations regarding the SGS kinetic energy dissipation expected to take place in the presence of non-negligible compressibility effects for wall bounded flows. The impact of the spherical part of the SGS tensor (*i.e.*, the turbulent kinetic energy), often not explicitly modelled for weakly compressible flows, appeared to have a relevant role in kinetic energy transfer. The SGS dissipation term has shown to be directly connected to the local levels of compressibility, identified by the velocity dilatation field. Compressions motions are more likely to experience classical direct kinetic energy cascade, whereas expansions promote back-scatter phenomena. Such informations can be particularly useful in the development of more compressible formulations of classical LES models, including, for example, a model for the spherical part of the SGS tensor.

All the contributions, ideas and investigations presented in this thesis represent the first step toward a unified LES model able to handle, at the same time, both turbulence under-resolution and shock-waves with techniques and strategies specifically tailored for high-order numerical schemes.

Resumé

Cette thèse se concentre sur l'application des méthodes d'ordre élevé aux écoulements turbulents compressibles. Des aspects tels que la dissipation/dispersion numérique, la modélisation dynamique à l'échelle de sous-maille (SGS), les techniques de capture des chocs et les effets de la compressibilité sur la modélisation de la turbulence sont discutés. Le manuscrit de thèse est organisé selon des niveaux de complexité croissants, menant à la simulation d'écoulements turbulents entièrement compressibles où toutes les difficultés mentionnées ci-dessus sont simultanément impliquées. Les résultats présentés dans ce travail s'inscrivent dans le développement de solveurs d'ordre élevé fiables et robustes pour les applications de mécanique des fluides numérique.

Une généralisation innovante des techniques d'analyses spectrales standard appliquées aux méthodes d'ordre élevé est d'abord présentée. Une attention particulière est consacrée au schéma de différence spectrale utilisé pour les simulations numériques réalisées dans le cadre de cette thèse. Les analyses spectrales des méthodes d'ordre élevé sont généralement basées sur la discrétisation numérique de l'équation d'advection linéaire unidimensionnelle. Dans ce travail de thèse, cette approche a été généralisée pour des vitesses d'advection non constantes afin d'obtenir des informations plus significatives sur les discrétisations numériques d'ordre élevé des équations non linéaires, telles que les équations de Navier-Stokes ou d'Euler. La méthode de différence spectrale a montré quelques différences significatives par rapport au schéma correspondant de récupération par reconstruction de flux lorsque des vitesses d'advection non constantes sont considérées. Le comportement général des courbes dissipatives a montré des écarts remarquables entre la méthode SD, la méthode FR-SD et le schéma de récupération par reconstruction de flux de Galerkin discontinu. Des expériences numériques ont été menées pour mettre en évidence le rôle joué par les flux numériques et l'ordre d'approximation pour les méthodes SD et FR-DG.

Les informations recueillies à partir des analyses spectrales sont ensuite utilisées pour présenter le modèle dynamique des éléments spectraux. Le modèle SEDM a été développé par Chapelier & Lodato [1] pour relier la dissipation numérique, qui représente une caractéristique intégrale typique des méthodes par éléments spectraux, et la dissipation de sous-maille ex-

plicite classique dans le cadre des simulations à grande échelle d'écoulements turbulents. Une série d'écoulements turbulents transitoires pertinents sont ensuite considérés pour mieux évaluer la performance du modèle SEDM dans des conditions plus complexes. Il s'agit d'un écoulement à gradient de pression nul sur une plaque plane et d'une simulation d'un profil aérodynamique SD7003 à faible nombre de Reynolds. Les deux calculs sont destinés à étudier en profondeur la nature dynamique du modèle SEDM pour des géométries complexes et des écoulements transitoires.

Dans le cadre des écoulements compressibles, une technique innovante de capture des chocs par viscosité artificielle à faible dissipation est présentée et analysée en détail. Des simulations numériques unidimensionnel et tridimensionnel, inviscides et visqueuses, laminaires et turbulentes, sont considérées comme fournissant une gamme suffisamment large de configurations d'écoulement où le modèle proposé donne de bons résultats. En particulier, en comparaison avec un autre modèle de viscosité artificielle largement répandu basé sur une régularisation laplacienne. La viscosité artificielle basée sur le volume fournit des niveaux considérablement réduits de dissipation artificielle des structures tourbillonnaires, en gardant, en même temps, la simulation stable.

Enfin, dans la dernière partie du manuscrit, la coexistence de toutes les recherches et modèles présentés tout au long de la thèse est étudiée pour des écoulements turbulents compressibles plus complexes. Parmi ceux-ci, l'écoulement transsonique autour d'un profilé RAE2822 et l'interaction entre une couche limite turbulente et une rampe de compression de 24° ont été simulés à l'aide d'une approche LES, où le modèle SEDM a été couplé avec la technique AV basée sur le volume proposée. Les deux simulations ont fourni des résultats en accord avec d'autres simulations et expériences, certifiant la robustesse et la fiabilité de l'effet combiné des deux modèles.

Enfin, afin de généraliser encore plus le modèle SEDM à des applications plus compressibles, une étude en simulation numérique directe pour une configuration de rampe de compression/détente a été réalisée. Les données hautement résolues ont été utilisées pour révéler des informations instructives sur la dissipation de l'énergie cinétique de sous-maille qui devrait avoir lieu en présence d'effets de compressibilité non négligeables pour des écoulements limités par des parois. L'impact de la partie sphérique du tenseur SGS (*i.e.*, l'énergie cinétique turbulente), souvent non modélisée explicitement pour les écoulements faiblement compressibles, est apparu comme ayant un rôle pertinent dans le transfert d'énergie cinétique. Le terme de dissipation SGS s'est avéré être directement lié aux niveaux locaux de compressibilité, identifiés par le champ de dilatation de la vitesse. Les mouvements de compression sont plus susceptibles de connaître une cascade d'énergie cinétique directe classique, tandis que les expansions favorisent les phénomènes de rétrodiffusion. Ces informations peuvent être particulièrement utiles dans le développement de formulations plus compressibles des modèles LES classiques, y compris,

par exemple, un modèle pour la partie sphérique du tenseur SGS.

Toutes les contributions, idées et recherches présentées dans cette thèse représentent le premier pas vers un modèle LES unifié capable de traiter, en même temps, la sous-résolution de la turbulence et les ondes de choc avec des techniques et stratégies spécifiquement adaptées aux schémas numériques d'ordre élevé.

Contents

List of Figures

List of Tables

Chapter 1

Introduction

Contents

1.1 Background and motivations

High-order methods for fluid dynamics represent a trending topic in the Computational Fluid Dynamics (CFD) community, gaining more and more popularity in both academia and industry. Their computational efficiency and geometric flexibility make them promising candidates as building blocks for the next generation of commercial solvers. In particular, high-order methods have shown encouraging results in the simulations of vortical flows due to their intrinsic numerical properties, leading to a widespread use of them in both Direct Numerical Simulations (DNS) and Large-Eddy Simulations (LES). Nonetheless, the level of robustness and reliability provided by low-order methods such as classical finite volumes approaches, is still currently out of reach, at least for under-resolved flows as it happens in LES. The general structure and the dynamics of numerical errors in under-resolved flows still represents a major issue in high-order simulations, both in terms of stability and turbulent modelling. The interplay between the errors associated to the spatial discretisation and turbulence dynamics plays a central role in the development of high-order schemes. The community of high-order methods is consequently constantly looking for innovative and insightful numerical analyses tools to gain a deep understanding of the intrinsic numerical properties of the scheme. Based on such knowledge, classical turbulence modelling needs to be specifically tailored to the numerical scheme in order to work harmoniously in a wide range of different turbulent flows.

As a secondary note, the CFD community, driven by more and more demanding industrial queries, is rapidly shifting toward more and more com-

plex flows, involving, among many others, compressibility, multiple phases and chemical reactions. Considering more complex applications, using the same numerical scheme developed for simpler sets of equations, clearly brings additional complications in terms of numerics and modelling. The present work will consider the relevant difficulties in the simulation of compressible flows using high-order methods. In particular, as it is well-known, compressible gas-dynamics is intrinsically characterised by the natural development of discontinuities in the flow field, also known as shock-waves. The numerical description of very sharp feature such as shock-waves represent another major research branch in the high-order methods community.

Finally, considering compressible turbulent flows, not every numerical treatment of shock-waves will be allowed, since numerics, turbulence modelling and shock-capturing need to coexist at the same time. Each of them cannot be developed individually as the whole ensemble needs to work as a unity.

The present work aims at a first step toward the development of a unified LES model, able to deal with turbulence under-resolution and shock-waves at the same time within the high-order framework of the Spectral Difference scheme.

1.2 Outline

The present thesis will be organised in agreement with the previous discussion, gradually increasing the level of complexity, leading only at the end to high-order simulations of fully compressible turbulent flows. The first three chapter will be introductory: chapter 2 will be focused on the set of continuous equations used throughout the thesis, chapter 3 will introduce the main turbulence modelling concepts within the framework of Large-Eddy Simulations, and chapter 4 will introduce the specific numerical scheme employed in the present work, the Spectral Difference (SD) scheme.

Once the numerical and modelling set-up has been properly introduced, the concepts of numerical dispersion and dissipation, along with classical and innovative techniques to quantify them, will be discussed in chapter 5. Chapter 5 will be focused on the numerical scheme only, on its properties and general dynamics in the simulation of under-resolved turbulent flows. Chapter 5 is based on the published work "*A Comparative Study from Spectral Analyses of High-Order Methods with Non-Constant Advection Velocities*" [15].

Chapter 6 will treat how numerical dissipation, introduced in the previous chapter, needs to be taken into account in the development of LES models for high-order numerical schemes. The Spectral Element Dynamics Model (SEDM), which is based on a well-balanced interaction between numerical dissipation and classical explicit Sub-Grid Scales (SGS) modelling will be introduced. A series of numerical experiments involving the SEDM

will be presented and discussed. Chapter 6 is based on two different publications on "Flow, Turbulence and Combustion". Namely, "*Large-Eddy Simulation of Bypass Transition on a Zero-Pressure-Gradient Flat Plate Using the Spectral-Element Dynamic Model*" [16] and "*Analysis of High-order Explicit LES Dynamic Modeling Applied to Airfoil Flows*" [17].

Chapters 7 and 8 will be focused on the role played by compressibility in the simulation of turbulent flows. In particular, in chapter 7, a low dissipative, bulk-based artificial viscosity model will be introduced as suitable shock-capturing technique for the simulation of compressible turbulent flows. Chapter 7 is based on the "Computer & Fluids" paper "*Entropy preserving low dissipative shock capturing with wave-characteristic based sensor for high-order methods*" [18].

The final chapter 8 will include all the previously presented topics at the same time. Both LES and DNS of compressible turbulent flows will be considered. The LES computations will be mainly focused on the mutual interaction between shock-capturing and turbulence model. On the other hand, the DNS aims at a better understanding on the role played by compressibility in terms of mathematical modelling.

Finally, the second part of the thesis collects the first page of the archival journal publications relevant to this Ph.D. Thesis.

Chapter 2

Fundamentals

Contents

2.1 Fluid mechanics fundamentals

The motion of a compressible viscous fluid is completely described by the imposition of local conservation of mass, momentum and energy. Each of them, in a cartesian framework, can be expressed as a Partial Differential equation (PDE). In the following Einstein summation convention for repeated indices has been employed.

1. Conservation of mass,

$$\frac{\partial \rho}{\partial t} + \frac{\partial (\rho u_j)}{\partial x_j} = 0 \tag{2.1}$$

   where ρ is the fluid's density and u_j is the velocity component along the direction x_j.

2. Conservation of momentum

$$\frac{\partial \rho u_i}{\partial t} + \frac{\partial (\rho u_i u_j)}{\partial x_j} = \frac{\partial \sigma_{ij}}{\partial x_j} + \rho f_i, \qquad (i = 1, 2, 3) \tag{2.2}$$

   where $\sigma_{ij} = A_{ij} - p\delta_{ij}$ is the tensor of surface stresses accounting for viscous actions A_{ij} and thermodynamic pressure p, and f_i denotes the i-th component of body forces per unit of mass acting on the fluid element

3. Conservation of total energy

$$\frac{\partial \rho E}{\partial t} + \frac{\partial (\rho E u_j)}{\partial x_j} = \frac{\partial (\sigma_{ij} u_i)}{\partial x_j} + \rho u_i f_i - \frac{\partial Q_j}{\partial x_j} \tag{2.3}$$

where $E = e + u_k u_k/2$ is the total energy (with e the internal energy), and Q_k is the k-th component of the heat flux vector.

The above five equations, which constitute the Navier-Stokes (NS) system of equations, are used to obtain the five unknowns, represented by the conserved variables $\mathbf{U} = (\rho, \rho u_1, \rho u_2, \rho u_3, \rho E)^T$. All the other terms appearing in the equations (σ_{ij}, Q and f) are either analytical functions or they can be expressed as functions of $\mathbf{U}$.

In particular, the following assumptions are usually made:

1. The fluid is Newtonian and follows the Stokes Law for mono-atomic gases:

$$A_{ij} = 2\mu S_{ij} \tag{2.4}$$

where μ is the dynamic viscosity and S_{ij} is the deviatoric part of the velocity gradient tensor

$$S_{ij} = \frac{1}{2}\left(\frac{\partial u_i}{\partial x_j} + \frac{\partial u_j}{\partial x_i}\right) - \frac{1}{3}\delta_{ij}\frac{\partial u_k}{\partial x_k}. \tag{2.5}$$

2. The fluid evolves following the equation of state of calorically perfect gas:

$$p = \rho R T, \tag{2.6}$$

$$e = c_v T, \tag{2.7}$$

$$c_p = c_v + R, \tag{2.8}$$

$$\gamma = c_p / c_v, \tag{2.9}$$

where T is the temperature, c_p and c_v are the the specific heat, respectively, at constant pressure and volume, $R = \mathcal{R}/M_w$ is the gas constant computed form the universal gas constant $\mathcal{R} = 8.31451\text{J}/(\text{mol K})$ and the gas molar weigth M_w, and $\gamma = 1.4$. The total energy density, in particular, may be expressed as

$$\rho E = \frac{1}{2}\rho u_k u_k + \frac{p}{\gamma - 1}. \tag{2.10}$$

3. The heat flux Q_k follows the Fourier's law

$$Q_k = -\lambda \frac{\partial T}{\partial x_k} = -\frac{\mu c_p}{\mathrm{Pr}} \frac{\partial T}{\partial x_k}, \tag{2.11}$$

where λ is the thermal conductivity, and Pr is the Prandtl number.

4. The dynamic viscosity of the fluid μ may be computed from the temperature T using the Sutherland's law:

$$\mu(T) = \mu_{\mathrm{ref}} \left(\frac{T}{T_{\mathrm{ref}}} \right)^{3/2} \frac{T_{\mathrm{ref}} + T_S}{T + T_S} \tag{2.12}$$

5. Body forces can be neglected, *i.e.* $f_i = 0$.

In this way the problem can be written in a more compact vectorial form as:

$$\frac{\partial \mathbf{U}}{\partial t} + \frac{\partial \mathbf{F}^k}{\partial x_k} + \frac{\partial \mathbf{D}^k}{\partial x_k} = \mathbf{0}, \tag{2.13}$$

where $\mathbf{F}$ and $\mathbf{D}$ denote, respectively, inviscid and viscous fluxes, defined as

$$\mathbf{F}^k = \begin{pmatrix} \rho u_k \\ \rho u_1 u_k + \delta_{1k} p \\ \rho u_2 u_k + \delta_{2k} p \\ \rho u_3 u_k + \delta_{3k} p \\ (\rho E + p) u_k \end{pmatrix}, \qquad \mathbf{D}^k = \begin{pmatrix} 0 \\ -2\mu S_{1k} \\ -2\mu S_{2k} \\ -2\mu S_{3k} \\ -2\mu u_j S_{kj} - \frac{\mu c_p}{\mathrm{Pr}} \frac{\partial T}{\partial x_k} \end{pmatrix}. \tag{2.14}$$

2.2 The dimensionless formulation

In order to better understand the problem of turbulence, the non-dimensional set of Navier-Stokes equations are introduced. The relevant normalisation procedure is summarised below. To simplify the formulation, viscosity is considered constant.

Let ρ_R, u_R, l_R and T_R be the reference density, velocity, length and temperature respectively. The relevant dimensionless quantities are

$$\rho^* = \rho/\rho_R, \quad u_i^* = u_i/u_R, \quad x_i^* = x_i/l_R, \quad T^* = T/T_R, \tag{2.15}$$

where the subscript $(\cdot)^*$ is now used to address normalised non-dimensional quantities. The reference time and pressure may be derived by dimensional analysis as:

$$t_R = l_R/u_R, \quad p_R = \rho_R u_R^2. \tag{2.16}$$

Moreover, the dimensionless equation of state is obtained as:

$$p^* = \rho^* R^* T^*, \tag{2.17}$$

with

$$R^* = \frac{1}{\gamma \mathrm{Ma}^2} \quad \text{and} \quad \mathrm{Ma} = \frac{u_R}{\sqrt{\gamma R T_R}} = \frac{u_R}{a_R}, \tag{2.18}$$

where a_R is the reference speed of sound.
Dividing the internal energy by u_R^2 and the total energy by $\rho_R u_R^2$ and using the identity $R^* = RT_R/u_R^2$, the following relations descend immediately:

$$e^* = \frac{R^* T^*}{\gamma - 1} = c_v^* T^*, \quad \text{and} \quad \rho^* E^* = \frac{1}{2}\rho^* u_k^* u_k^* + \frac{p^*}{\gamma - 1}, \tag{2.19}$$

where $c_v^* = R^*/(\gamma - 1) = c_v T_R/u_R^2$ is related to γ and Ma. Evidently, the dimensionless specific heat at constant volume and pressure are related to their dimensional counterparts by the following identities:

$$c_v^* = c_v T_R/u_R^2 \quad \text{and} \quad c_p^* = \gamma c_v^* = c_p T_R/u_R^2. \tag{2.20}$$

Using Eqs. (2.15), (2.16), (2.18), (2.19), (2.20) and related identities, the dimensionless Navier-Stokes equations become:

$$\begin{aligned}
\frac{\partial \rho^*}{\partial t^*} + \frac{\partial (\rho^* u_j^*)}{\partial x_j^*} &= 0, \\
\frac{\partial (\rho^* u_i^*)}{\partial t^*} + \frac{\partial}{\partial x_j^*}(\rho^* u_i^* u_j^* + p^* \delta_{ij}) &= \frac{1}{\mathrm{Re}} \frac{\partial}{\partial x_j^*}(2 S_{ij}^*), \\
\frac{\partial (\rho^* E^*)}{\partial t^*} + \frac{\partial}{\partial x_j^*}[(\rho^* E^* + p^*) u_j^*] &= \frac{1}{\mathrm{Re}} \frac{\partial}{\partial x_j^*}\left(2 S_{ij}^* u_i^* + \frac{c_p^*}{\mathrm{Pr}} \frac{\partial T^*}{\partial x_j^*}\right),
\end{aligned} \tag{2.21}$$

where $\mathrm{Re} = \rho_R u_R l_R/\mu$.

The dimensionless equations are formally identical to the dimensional counterparts, with all the quantities replaced by *starred* ones. Based on this consideration, in all the next sections, no distinction will be made anymore between dimensional and dimensionless formulations.

2.3 A brief introduction to turbulence

Looking closer to Eq. (2.21), the first thing that can be noticed is that for high values of the parameter Re, the viscous effects become less and less important, hence the flow tends to be almost inviscid. On the other hand, when Re is small, viscous effects become more and more important with respect to convective forces.

The importance of this parameter was first pointed out by Reynolds while making experimental observations of the flow along straight smooth pipes, He notice that, for some certain values of the ratio

$$\frac{\rho U l}{\mu}, \tag{2.22}$$

with U the average fluid velocity in the pipe and l its radius, the flow was changing radically from "direct" motion into "sinuous" motions, indicating what nowadays is commonly referred to ad "laminar" and "turbulent" flow regimes.

If U is the typical velocity of the flow, l_u is the typical length of the streamline pattern and l_v is the typical length of the cross-stream velocity gradients, it is easily shown, by simple dimensional considerations, that the inertial and viscous forces for unit of volume of fluid scale as $\rho U^2/l_u$ and $\mu U/l_v^2$ respectively. Hence, provided that l is properly chosen,

$$\mathrm{Re} = \frac{\rho U l}{\mu}, \tag{2.23}$$

namely the Reynolds number, represents the relative intensity of inertial forces compared to the viscous ones. When inertial forces are predominant over viscous forces, the fluid motion is more prone to instabilities. And, since the non-linear nature of Navier-Stokes equations – expressed by the convective term $\rho u_i u_j$– makes them extremely sensitive to small differences in the initial conditions, chaotic, or turbulent, motion is generally the outcome of those instabilities. In other words, fluid flows are always naturally unstable, and these instabilities can be properly controlled tuning the level of viscosity. The Reynolds number quantifies the ratio between the convective (non-linear) term in Navier-Stokes equations and the viscous forces, providing a qualitative recipe to distinguish between laminar and turbulent flows. Nonetheless, the specific transition between the two phases is not always easily determined as it strongly depends on the particular flow characteristics. In fact, an intermediate state is usually identified as "transition" where the flow is not laminar nor fully turbulent. It is then evident that a formal definition of turbulence is not trivial and possibly not even useful.

Sometimes, a practical example can reveal much more insight that any mathematical formalism. Consider the flow around a cylinder for low enough viscosity values and suppose that the velocity field in a certain location of the wake behind is available at any instant for a certain time. From an experimental point of view, repeating the measure for the same amount of time and in the same conditions will provide always different results. Of course, experimental uncertainties can be many and not necessarily related to turbulence. Nevertheless, these differences are commonly amplified by turbulence. If instead, a time-averaging operation is applied to all the measurements, the output will be the same. This is a fundamental point of turbulence understanding: every turbulence theory needs to be statistical. At each location and each time instant, the flow field will look random and chaotic, while its statistical properties are smooth functions. It exists a fascinating coexistence of randomness and determinism hidden inside Navier-Stokes equations. With this in mind a general flow field can be decomposed as:

$$\mathbf{u}(\mathbf{x}, t) = \langle \mathbf{u}(\mathbf{x}, t) \rangle + \mathbf{u}'(\mathbf{x}, t), \tag{2.24}$$

where the average operator ($\langle\cdot\rangle$) has been introduced. The averaged velocity $\langle\mathbf{u}(\mathbf{x},t)\rangle$ needs to be interpreted as a statistical mean flow while $\mathbf{u}'(\mathbf{x},t)$ represents velocity fluctuations around the mean value. The mean flow is smooth and it obeys to deterministic equations while velocities fluctuations are random variables varying at any instant of time and any spatial location. In a physical sense, fluctuations are intrinsically linked to vortical structures. Geometrical properties of the flows, nevertheless, impose some bounds on the amplitude and behaviour of such fluctuations. Largest vortices will have dimensions comparable to the characteristic length scales of the problem, while the smallest are more universal and representative of turbulence. Largest vortices are advected in the flow by the mean flow. Due to non-linear instabilities smaller and smaller eddies are generated by a break-up mechanism. The kinetic energy contained in the large scales is then progressively transferred to smaller and smaller scales, until it is finally dissipated by viscous forces. This process is commonly known as *energy cascade* and it represents probably one of the most popular phenomenological descriptions of turbulence as it was first proposed by Richardson in 1922 [19]. It also highlights the dualism between convective and viscous forces. Convective forces provide the large scale kinetic energy coming from the mean flow; viscous forces, instead, are responsible of the dissipation at the smallest scales. There exist then a set of characteristic lengths and velocities scales such that the correspondent Reynolds number is close to 1, *i.e.*, convective and viscous forces are comparable:

$$\frac{u_\eta \eta}{\nu} \sim 1, \tag{2.25}$$

where η is this small-scale characteristic length and u_η the correspondent characteristic velocity. It is then necessary to relate such quantities to the mean flow to have a quantitative measure of turbulence and its scales.

An important quantity, as already stated, is represented by the kinetic energy and its viscous dissipation, which can be formally written, for incompressible flows, as:

$$\overline{\varepsilon} = 2\nu S_{ij} S_{ij}. \tag{2.26}$$

Since viscous dissipation is supposed to be strictly related to the smallest scales, using simple dimensional analysis, it is possible to obtain:

$$\overline{\varepsilon} \sim \nu \frac{u_\eta^2}{\eta^2}. \tag{2.27}$$

At this point Kolmogorov's theory [20] can be introduced. According to Kolmogorov's first similarity hypothesis, at smallest scales, the only relevant quantities influencing the flow are the kinetic energy dissipation $\overline{\varepsilon}$ and the viscosity ν. From dimensional analysis is then possible to write explicitly η and u_η as

$$\eta = \overline{\varepsilon}^{-1/4} \nu^{3/4} \quad \text{and} \quad u_\eta = (\nu\overline{\varepsilon})^{1/4}. \tag{2.28}$$

This range of scales much smaller than the characteristic length scale l_R is normally called *universal equilibrium range*. At the same time, under the equilibrium hypothesis, the rate at which energy is passed down the cascade, must be equal to the rate of energy dissipation:

$$\nu \frac{u_\eta^2}{\eta^2} \sim \bar{\varepsilon} \sim \frac{\partial(\frac{1}{2}u_k u_k)}{\partial t} \sim u_R^3/l_R \tag{2.29}$$

This expression gives the necessary link between large and small scales. In particular, after some algebra, it is possible to write:

$$\eta \sim l_R \mathrm{Re}^{-3/4} \quad \text{and} \quad u_\eta \sim \quad u_R \mathrm{Re}^{-1/4}. \tag{2.30}$$

It is then interesting to notice that high values of the Reynolds number provide larger and larger separation between large and small scales of the flow. For this reason, turbulence is often described as a strongly "multiscale" problem: a wide range of scales are indeed involved in the dynamics of the flow, varying from the large scales imposed by the geometry of the specific flow, to the smallest viscous scales.

Kolmogorov's second similarity hypothesis assumes the existence of two sub-ranges within the universal equilibrium range: *inertial* and *viscous* sub-ranges. The latter involves the smallest scales and it satisfies all the previously stated properties, while the latter involves intermediate scales $\eta \ll l \ll l_R$. Within this sub-range, the flow depends only on the scale l and the dissipation rate $\bar{\varepsilon}$. This is commonly called *inertial subrange* and it is characterised by the energy cascade from large to small scales.

Another useful statistical tool in turbulence is the spatial cross correlation

$$R_{ij}(\mathbf{x}, t) = \langle \mathbf{u}_i(\mathbf{x}_0, t) \mathbf{u}_j(\mathbf{x}_0 + \mathbf{x}, t) \rangle, \tag{2.31}$$

as it quantifies the correlation, *i.e.*, the mutual influence, between velocities at different locations. In order to express the different scales, it is sometimes useful to work in Fourier space. The energy spectrum tensor $\mathbb{E}_{ij}(\boldsymbol{\kappa})$ with the wavenumber $\boldsymbol{\kappa}$ can be expressed as:

$$\mathbb{E}_{ij}(\boldsymbol{\kappa}) = \frac{1}{(2\pi)^3} \int \int \int_{-\infty}^{\infty} e^{-i\boldsymbol{\kappa}\cdot\mathbf{x}} R_{ij}(\mathbf{x}) d\mathbf{x}. \tag{2.32}$$

Then, the scalar kinetic energy spectrum can be written as:

$$\mathbb{E}(\kappa) = \oint \frac{1}{2} \mathbb{E}_{ii}(\boldsymbol{\kappa}) dS(\kappa), \tag{2.33}$$

where $\kappa = ||\boldsymbol{\kappa}||$. The kinetic energy spectrum quantifies the distribution of energy along wavenumbers/frequencies instead of scales. The dimensional analysis used in the previous calculations can be applied in the Fourier space too. The energy spectrum within the universal equilibrium range, according

to Kolmogorov's first similarity hypothesis, may be written as a function of $\overline{\varepsilon}$ and ν only. Using dimensional analysis, it is possible to obtain the following expression for the inertial subrange:

$$\mathbb{E} = \mathbb{E}(\kappa, \overline{\varepsilon}) = C_\kappa \overline{\varepsilon}^{2/3} \kappa^{-5/3}, \tag{2.34}$$

where C_κ is commonly indicated as the Kolmogorov constant. Eq. (2.34) is commonly known as the Kolmogorov's $\kappa^{-5/3}$ law. For the viscous subrange, dimensional analysis does not provide a solution and the kinetic energy spectrum takes the more general form:

$$\mathbb{E} = C_\kappa \overline{\varepsilon}^{2/3} \kappa^{-5/3} f(\kappa\eta). \tag{2.35}$$

A schematic representation of a typical kinetic energy spectrum of a turbulent flow is reported in Fig. 2.1. In such figure it is possible to observe

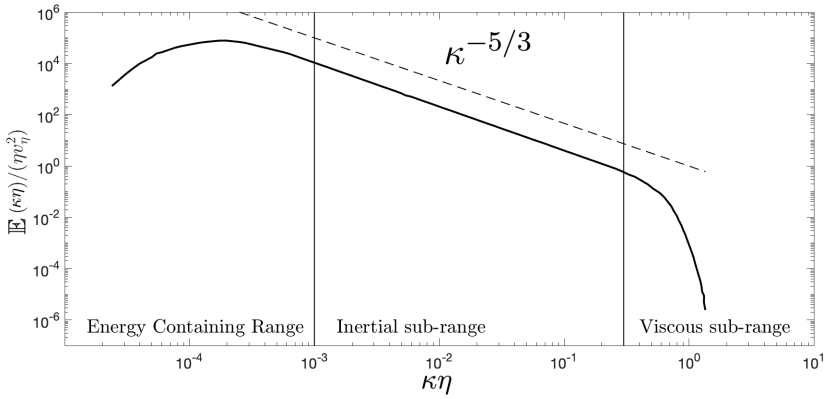

Figure 2.1: Schematic example of kinetic energy spectrum.

the consequences of the kinetic energy cascade. Most of the kinetic energy is contained in the largest scales, where the spectrum reaches its maximum values. Subsequently, an inertial range with constant slope, denoted as the inertial sub-range, represents the kinetic energy transfer from the largest scales to the viscous scales. At the beginning of the viscous sub-range, the kinetic energy dissipation rate increases, and the modes associated to large wavenumbers drop abruptly. The sudden decrease of such modes is representative of the viscous dissipation acting on the kinetic energy transferred from the large scales motion.

Chapter 3

Large Eddy Simulations

Contents

3.1 Introduction

Turbulent flows are characterised by a wide range of time and spatial scales which non-linearly interact with each other. Either the simulation or the modelling of such interactions can be particularly complex. On one hand, the grid size can be chosen small enough to catch the dynamics of even the smallest scales involved in the physical problem. Such scales, however, can be particularly small and cause the simulation to be computationally very expensive, even for simple geometries. The numerical resolution of the whole spectrum of scales, varying from the large ones, linked to boundary conditions and geometry of the problem, to the smallest, viscous scales, is commonly called "Direct Numerical Simulation". Despite the rapidly growing computational power of modern architectures, DNS is still out of reach for many relatively simple flows.

On the other hand, for industrial applications, it is not always necessary to have very accurate temporal knowledge of the flow field. Statistical quantities are sometimes sufficient for the design of engineering prototypes, as, for example, the mean pressure load of a rigid boundary, or the mean heat flux at the wall. The numerical resolution of the "Reynolds-Averaged Navier-Stokes" (RANS) equations, aims at resolving only the statistical means of relevant variables such as the velocity field, pressure or temperature. Statistical means are much smoother than the instantaneous flow field and a much reduced resolution is needed to represent them. Nonetheless, the local interactions between scales, which would be directly solved in DNS, need to be properly modelled in the RANS framework, where only the first mode (*i.e.*, the mean) is available. The gain in computational efficiency, consequently, is worth only if coupled with accurate turbulence modelling.

A possible midway solution between DNS and RANS is represented by "Large-Eddy Simulations". Large scales are the most energetic scales involved in the problem. The large-scale motions are responsible for the production of kinetic energy and are strongly dependent on the general flow configuration (boundary conditions, geometry, etc.). The smallest scales, instead, are representative of viscous effects which are normally assumed to be much more universal and independent with respect to the specific turbulent flow. The idea of LES consists in resolving the large scales and model the small, universal scales. With respect to DNS, the computational cost is considerably reduced. At the same time, since most of the scales are numerically resolved, LES models are normally much less complex than RANS models. Due to their flexibility, LES are considered the natural evolution of RANS approaches in the next generation of commercial codes for industrial applications.

3.2 The filtered Navier-Stokes Equations

Length-scale separation, on a generic quantity $\phi(\boldsymbol{x}, t)$, is achieved in physical space by means of the convolution product

$$\overline{\phi}(\boldsymbol{x}, t) = \int_{-\infty}^{+\infty} \phi(\boldsymbol{\xi}, t) G_\Delta(\boldsymbol{x} - \boldsymbol{\xi}) d^3\boldsymbol{\xi} \tag{3.1}$$

where G_Δ is the convolution kernel associated to the filter operation at cutoff length Δ. Using the superscript $(\cdot)^\star$ to indicate Fourier transformed quantities, previous equation can be rewritten, using the Convolution Theorem, to the point-wise multiplication in Fourier space:

$$\overline{\phi}^\star(\boldsymbol{\kappa}, \omega) = \phi^\star(\boldsymbol{\kappa}, \omega) G^\star_{k_c}(\boldsymbol{\kappa}), \tag{3.2}$$

where $G^\star_{\kappa_c}(\boldsymbol{\kappa})$ is the transfer function, namely, the Fourier transform, associated to the convolution kernel $G_\Delta(\boldsymbol{x})$, $\boldsymbol{\kappa}$ and ω are the wavelength and the

phase respectively and $\kappa_c = 2\pi/\Delta$ is the cutoff wave-number. The spectral representation of ϕ may be then truncated at wave-number κ_c by an appropriately chosen low-pass filter $G^{\star}_{\kappa_c}$. For the filtered Navier-Stokes to be tractable, the filter has to:

1. conserve constant values; this is equivalent to the normalization condition:
$$\int_{-\infty}^{+\infty} G_{\Delta}(\boldsymbol{\xi}) d^3\boldsymbol{\xi} = 1 \tag{3.3}$$
2. be linear, *i.e.* $\overline{\phi + \psi} = \overline{\phi} + \overline{\psi}$
3. commute with derivation in space and time:
$$\overline{\frac{\partial \phi}{\partial t}} = \frac{\partial \overline{\phi}}{\partial t}, \quad \overline{\frac{\partial \phi}{\partial x_i}} = \frac{\partial \overline{\phi}}{\partial x_i}. \tag{3.4}$$

The first two requirements are generally met with a properly defined filter (the second condition, in particular, is ensured by the linearity of convolution operation). The third requirement is a bit more complex in nature. Commutation errors arise when the filter is anisotropic [21] (*e.g.*, when solid boundaries are present or when the computational grid is not uniform) or, for instance, when Favre-filtering (the relevant definition will be given later) is adopted. On this regard, additional approximations will be made case by case. In all the developments which follow, it is assumed that the filter operator commutes with spatial and temporal differentiation. Typical filters used to perform spatial scale separation are the top-hat, the Gaussian and the spectral cutoff filters.

Using the above definitions and applying the commutation property, the filtered Navier-Stokes equations are obtained:

$$\frac{\partial \overline{\boldsymbol{U}}}{\partial t} + \frac{\partial \overline{\boldsymbol{F}}^k}{\partial x_k} + \frac{\partial \overline{\boldsymbol{D}}^k}{\partial x_k} = \boldsymbol{0} \tag{3.5}$$

with

$$\overline{\boldsymbol{U}} = \begin{pmatrix} \overline{\rho} \\ \overline{\rho u_1} \\ \overline{\rho u_2} \\ \overline{\rho u_3} \\ \overline{\rho E} \end{pmatrix}, \quad \overline{\boldsymbol{F}}^k = \begin{pmatrix} \overline{\rho u_k} \\ \overline{\rho u_1 u_k} + \delta_{1k}\overline{p} \\ \overline{\rho u_2 u_k} + \delta_{2k}\overline{p} \\ \overline{\rho u_3 u_k} + \delta_{3k}\overline{p} \\ \overline{(\rho E + p) u_k} \end{pmatrix}, \quad \overline{\boldsymbol{D}}^k = \begin{pmatrix} 0 \\ -2\overline{\mu S_{1k}} \\ -2\overline{\mu S_{2k}} \\ -2\overline{\mu S_{3k}} \\ -2\overline{\mu u_j S_{kj}} - \frac{\overline{\mu c_p}}{\mathrm{Pr}} \overline{\frac{\partial T}{\partial x_k}} \end{pmatrix}, \tag{3.6}$$

the filtered energy and the filtered equation of state being given by the following relations

$$\overline{\rho E} = \overline{\rho c_v T} + \frac{1}{2}\overline{\rho u_k u_k} = \frac{\overline{p}}{\gamma - 1} + \frac{1}{2}\overline{\rho u_k u_k}, \quad \text{and} \quad \overline{p} = \overline{\rho R T}. \tag{3.7}$$

Following the same methodology generally applied when solving the compressible LES equations, in order to avoid unclosed SGS terms in the continuity equation, a density-weighted Favre filter operator *tilde* may be introduced; this operator, which represents density weighted filtering, is defined for a given quantity ϕ as:

$$\widetilde{\phi} = \frac{\overline{\rho\phi}}{\overline{\rho}}, \quad \rightarrow \quad \overline{\rho\phi} = \overline{\rho}\widetilde{\phi} \tag{3.8}$$

The advantage of using Favre-filtered equations is twofold:

1. The absence of SGS terms in the mass conservation equation where the theoretically unclosed term $\overline{\rho u_i}$ can be expressed as a function of the Favre filtered velocity as $\overline{\rho}\widetilde{u}_i$. A smaller number of unclosed SGS contributions, of course, gives a simplified theoretical modelling of turbulence.

2. The Favre-filtered equations are structurally similar to their correspondent incompressible formulations providing a natural generalization of theoretical and modelling results of incompressible turbulence.

The non-linear interaction terms in the flux vector $\overline{\boldsymbol{F}}^k$ are then decomposed in resolved and SGS parts, the former being accessible from the filtered solution and the latter, namely the SGS terms now included into the diffusive vector $\overline{\boldsymbol{D}}^k$, requiring modelling. The form of vectors $\overline{\boldsymbol{U}}$, $\overline{\boldsymbol{F}}^k$ and $\overline{\boldsymbol{D}}^k$ can then be re-expressed with the explicit application of Favre filtering:

$$\overline{\boldsymbol{U}} = \begin{pmatrix} \overline{\rho} \\ \overline{\rho}\widetilde{u}_1 \\ \overline{\rho}\widetilde{u}_2 \\ \overline{\rho}\widetilde{u}_3 \\ \overline{\rho}\widetilde{E} \end{pmatrix}, \overline{\boldsymbol{F}}^k = \begin{pmatrix} \overline{\rho}\widetilde{u}_k \\ \overline{\rho}\widetilde{u}_1\widetilde{u}_k + \delta_{1k}\overline{p} \\ \overline{\rho}\widetilde{u}_2\widetilde{u}_k + \delta_{1k}\overline{p} \\ \overline{\rho}\widetilde{u}_3\widetilde{u}_k + \delta_{1k}\overline{p} \\ (\overline{\rho}\widetilde{E} + \overline{p})\widetilde{u}_k \end{pmatrix}, \overline{\boldsymbol{D}}^k = \begin{pmatrix} 0 \\ -2\overline{\mu S_{1k}} - \tau_{1k} \\ -2\overline{\mu S_{2k}} - \tau_{2k} \\ -2\overline{\mu S_{3k}} - \tau_{3k} \\ -2\overline{\mu u_j S_{kj}} - \frac{\mu c_p}{\mathrm{Pr}}\overline{\frac{\partial T}{\partial x_k}} - q_k \end{pmatrix} \tag{3.9}$$

where τ_{ij} and q_k are the unclosed SGS terms:

$$\tau_{ij} = \overline{\rho}(\widetilde{u}_i\widetilde{u}_j - \widetilde{u_i u_j}), \tag{3.10}$$

$$\begin{aligned} q_k = (\overline{\rho}\widetilde{E} + \overline{p})\widetilde{u}_k - \overline{(\rho E + p)u_k} &= c_v\overline{\rho}(\widetilde{T}\widetilde{u}_k - \widetilde{Tu_k}) \\ &+ \overline{p}\widetilde{u}_k - \overline{pu_k} \\ &+ \frac{1}{2}(\overline{\rho}(\widetilde{u_j u_j}\widetilde{u}_k - \widetilde{u_j u_j u_k})), \end{aligned} \tag{3.11}$$

Using the above decomposition and the Favre-filtering operator, the total filtered energy becomes:

$$\overline{\rho}\widetilde{E} = \frac{\overline{p}}{\gamma - 1} + \frac{1}{2}\overline{\rho}\widetilde{u}_k\widetilde{u}_k - \frac{1}{2}\tau_{kk}, \quad \text{and} \quad \overline{p} = \overline{\rho}R\widetilde{T} \tag{3.12}$$

Considering different sets of filtered quantities as unknowns can lead to different formulations of the filtered Navier-Stokes Equations, resulting in different sets of SGS terms to be modelled. The equations expressed in this form naturally lead to the choice of $\overline{\rho}$, $\widetilde{u}_i$ and $\widetilde{E}$ as unknowns. Such option is equivalent to pick the filtered conservative variables $\overline{\mathbf{U}}$ since both $\widetilde{u}_i$ and $\widetilde{E}$ can be evaluated using the filtered density:

$$\begin{aligned} \widetilde{u}_i &= \overline{U}_{i+1}/\overline{U}_1, \quad (i = 1, 2, 3) \\ \widetilde{E} &= \overline{U}_5/\overline{U}_1. \end{aligned} \tag{3.13}$$

For this choice of variables, all terms included in the diffusive fluxes are unclosed and proper modelling is needed to express them as functions of the Favre-filtered quantities.

Sub-grid terms involving viscous or heat fluxes are usually considered relatively small for high Reynolds number flows. It is, in fact, assumed that viscous scales, which are considerably smaller than the cutoff length, will be only mildly affected by the filtering operation. Mathematically, it is normally assumed that

$$2\overline{\mu S_{ij}} \approx 2\overline{\mu}\widetilde{S}_{ij}, \tag{3.14}$$

$$2\overline{\mu S_{kj} u_j} \approx 2\overline{\mu}\widetilde{S}_{kj}\widetilde{u}_j, \tag{3.15}$$

and

$$\overline{\frac{\mu c_p}{\mathrm{Pr}}\frac{\partial T}{\partial x_k}} \approx \frac{\overline{\mu} c_p}{\mathrm{Pr}}\frac{\partial \widetilde{T}}{\partial x_k}. \tag{3.16}$$

On the contrary, for similar reasons, inviscid sub-grid terms cannot be neglected and proper modelling is needed. In particular, the unclosed SGS terms are represented in Eq. 3.9 by τ_{ij} and q_k.

At this point a choice regarding the spherical part of the SGS tensor τ_{ij} is in order. Notice that the spherical part of τ_{ij} appears not only in the momentum conservation law but also in the energy equation. The choice regarding the spherical part of the SGS tensor can lead to different forms of filtered energy equation. In the present work, the solution proposed by Ducros [22] and Lesieur [23] has been employed. The spherical part of the SGS tensor is incorporated in a *macropressure*. Hence, the spherical part of the SGS tensor is not modelled. Nevertheless, such choice implies consequences on the energy equation which will be briefly summarized.

The resolved macropressure is then defined as

$$\overline{\omega} = \bar{p} - \frac{1}{3}\tau_{kk}. \tag{3.17}$$

In this way the convective and diffusive fluxes can be re-written as

$$\overline{\boldsymbol{F}}^k = \begin{pmatrix} \overline{\rho}\widetilde{u}_k \\ \overline{\rho}\widetilde{u}_1\widetilde{u}_k + \delta_{1k}\overline{\omega} \\ \overline{\rho}\widetilde{u}_2\widetilde{u}_k + \delta_{1k}\overline{\omega} \\ \overline{\rho}\widetilde{u}_3\widetilde{u}_k + \delta_{1k}\overline{\omega} \\ (\overline{\rho}\widetilde{E} + \overline{\omega})\widetilde{u}_k \end{pmatrix}, \qquad \overline{\mathbf{D}^k} = \begin{pmatrix} 0 \\ -2\overline{\mu S_{1k}} - \tau^d_{1k} \\ -2\overline{\mu S_{2k}} - \tau^d_{2k} \\ -2\overline{\mu S_{3k}} - \tau^d_{3k} \\ -2\overline{\mu u_j A_{kj}} - \overline{\frac{\mu c_p}{\mathrm{Pr}}\frac{\partial T}{\partial x_k}} - q_k \end{pmatrix}. \quad (3.18)$$

Where the subscript $(\cdot)^d$ denotes the deviatoric part of the SGS tensor $\tau^d_{ij} = \tau_{ij} - \frac{1}{3}\tau_{kk}\delta_{ij}$. Since filtered pressure is no more accessible from filtered variables, the SGS energy flux q_k has been redefined in terms of resolved macropressure:

$$q_k = (\overline{\rho}\widetilde{E} + \overline{\omega})\widetilde{u}_k - \overline{(\rho E + p)u_k}. \quad (3.19)$$

Moreover, observing that the filtered total energy contains the trace of the SGS tensor, a resolved macrotemperature needs to be defined as well, such that the total energy is computable from resolved quantities:

$$\overline{\rho}\widetilde{E} = \overline{\rho}c_v\widetilde{\theta} + \frac{1}{2}\overline{\rho}\widetilde{u}_k\widetilde{u}_k, \quad \text{with} \quad \widetilde{\theta} = \widetilde{T} - \frac{1}{2\overline{\rho}c_v}\tau_{kk}. \quad (3.20)$$

The filtered state equation in terms of macropressure and macrotemperature reads:

$$\overline{\omega} = \overline{\rho}R\widetilde{T} - \frac{1}{3}\tau_{kk} = \overline{\rho}R\widetilde{\theta} + \overline{\rho}R\frac{1}{2\overline{\rho}c_v}\tau_{kk} = \overline{\rho}R\widetilde{\theta} + \frac{3\gamma - 5}{6}\tau_{kk}, \quad (3.21)$$

suggesting that, for τ_{kk} sufficiently small, macropressure and macrotemperature may be related by the usual equation of state, *i.e.*,

$$\overline{\omega} = \overline{\rho}R\widetilde{\theta} \quad (3.22)$$

defining the sub-grid Mach number as

$$M^2_{\mathrm{sgs}} = \frac{\tau_{kk}}{\overline{\rho}a^2} = \frac{\tau_{kk}}{\gamma\overline{p}}, \quad (3.23)$$

this condition becomes:

$$\frac{|3\gamma - 5|}{6}\gamma M^2_{\mathrm{sgs}} \ll 1. \quad (3.24)$$

For $\gamma = 1.4$ for instance, this condition is ≈ 1.6 times less restrictive on M_{sgs} than just neglecting the effects of the SGS stress' trace compared to the filtered thermodynamic pressure:

$$\frac{1}{3}\tau_{kk} \ll \overline{p}, \quad \rightarrow \quad \frac{1}{3}\gamma M_{\mathrm{sgs}} \ll 1. \quad (3.25)$$

A final remark needs to be done regarding the definition of the SGS energy flux, which is now defined using macropressure and macrotemperature:

$$\begin{aligned} q_k = (\overline{\rho}\widetilde{E} + \overline{\omega})\widetilde{u}_k - \overline{(\rho E + p)u_k} = c_v\overline{\rho}(\widetilde{\theta}\widetilde{u}_k - \widetilde{Tu_k}) \\ + \overline{\omega}\widetilde{u}_k - \overline{pu_k} \\ + \frac{1}{2}(\overline{\rho}(\widetilde{u_j u_j}\widetilde{u}_k - \widetilde{u_j u_j u_k})), \end{aligned} \tag{3.26}$$

Finally, the assumption on heat sub-grid flux applies to the macrotemperature as well, namely,

$$\overline{\frac{\mu c_p}{\mathrm{Pr}}\frac{\partial T}{\partial x_k}} \approx \frac{\overline{\mu} c_p}{\mathrm{Pr}}\frac{\partial \widetilde{\theta}}{\partial x_k}. \tag{3.27}$$

A possible alternative which includes the spherical part of the SGS tensor can be also obtained. In this work, it has been followed the guideline proposed by Vreman et al. [24]. The mathematical modelling is almost identical with the previous discussion except for the energy equation, which needs a specific treatment. In particular, a conservation law for a large-scale total energy can be written as:

$$\begin{aligned} \frac{\partial(\overline{\rho}\widehat{E})}{\partial t} + \frac{\partial}{\partial x_j}((\overline{\rho}\widehat{E} + \overline{p})\widetilde{u}_j) = \frac{\partial}{\partial x_j}(2\overline{\mu}\widetilde{S}_{ij}\widetilde{u}_i) - \frac{\partial}{\partial x_j}\left(\frac{\overline{\mu}c_p}{\mathrm{Pr}}\frac{\partial \widetilde{T}_j}{\partial x_j}\right) \\ -B_1 - B_2 + B_3 - B_4 + B_5 + B_6 - B_7, \end{aligned} \tag{3.28}$$

where $\widehat{E} = \frac{\overline{p}}{\gamma-1} + \frac{1}{2}\overline{\rho}\widetilde{u}_k\widetilde{u}_k$ and additional unclosed terms are defined as:

$$\begin{aligned} B_1 =& \frac{1}{\gamma-1}\frac{\partial}{\partial x_j}(\overline{pu_j} - \overline{p}\widetilde{u}_j), \\ B_2 =& \overline{p\frac{\partial u_k}{\partial x_k}} - \overline{p}\frac{\partial \widetilde{u}_k}{\partial x_k}, \\ B_3 =& \frac{\partial}{\partial x_j}(\tau_{ij}\widetilde{u}_i), \\ B_4 =& \tau_{ij}\frac{\partial \widetilde{u}_i}{\partial x_j}, \\ B_5 =& \overline{2\mu S_{ij}\frac{\partial u_i}{\partial x_j}} - \overline{2\mu S_{ij}}\frac{\partial \widetilde{u}_i}{\partial x_j}, \\ B_6 =& \frac{\partial}{\partial x_j}(\overline{2\mu S_{ij}}\widetilde{u}_i - 2\overline{\mu}\widetilde{S}_{ij}\widetilde{u}_i), \\ B_7 =& \frac{\partial}{\partial x_j}\left(\overline{\frac{\mu c_p}{\mathrm{Pr}}\frac{\partial T}{\partial x_j}} - \frac{\partial}{\partial x_j}\left(\frac{\overline{\mu}c_p}{\mathrm{Pr}}\frac{\partial \widetilde{T}_j}{\partial x_j}\right)\right). \end{aligned} \tag{3.29}$$

This equation is obtained by the subtraction of the transport equation for the turbulent kinetic energy (*i.e.*, the spherical part of τ_{ij}) from the filtered energy equation. In this way, the pressure herein considered is the actual

filtered pressure without the addition of the trace of τ_{ij}. Consequently, the main advantage of such formulation consists in an easier interpretation of the pressure field. In the weakly compressible formulation, in fact, the specific importance of the spherical part of the SGS tensor in the macropressure is generally unknown. On the other hand, as it can be clearly noticed, a significantly larger number of unclosed terms appear in the equation. Still, most of them are usually considered negligible and only B_1 and B_3 are commonly modelled.

Notice that in this case no assumption on the spherical part of the SGS tensor has been made. Consequently, each term involving τ_{ij} englobes automatically both deviatoric and spherical contributions. This is of course true also for the SGS tensor in the filtered momentum balance equation. Notice that the form of the equation is almost identical to the first formulation, where it has been chosen a different type of large-scale total energy. In the weakly compressible formulation the unknown is

$$\overline{\rho}\widetilde{E} = \frac{\overline{p}}{\gamma - 1} + \frac{1}{2}\overline{\rho}\widetilde{u_k u_k}, \tag{3.30}$$

whereas in this latter approach it is

$$\overline{\rho}\widehat{E} = \frac{\overline{p}}{\gamma - 1} + \frac{1}{2}\overline{\rho}\widetilde{u}_k\widetilde{u}_k. \tag{3.31}$$

A clear connection between the choice of resolved energy and the modelling of the spherical part of SGS tensor can be easily identified. Finally, it is worthwhile noticing that the relevance of the spherical part of the SGS tensor is intimately linked to the SGS Mach number and the level of compressibility will implicitly dictate which formulation is more suitable for a specific flow field. The role of compressibility, and in particular of the spherical part of the SGS tensor, will be thoroughly discussed in chapter 8.

3.3 Mathematical modelling

The unclosed terms which need to be modelled are the SGS tensor τ_{ij} and the SGS energy flux q_k, namely,

$$\tau_{ij} = \overline{\rho}(\widetilde{u}_i\widetilde{u}_j - \widetilde{u_i u_j}), \quad \text{and} \quad q_k = (\overline{\rho}\widetilde{E} + \overline{p})\widetilde{u}_k - \overline{(\rho E + p)u_k}. \tag{3.32}$$

Only the deviatoric part of τ_{ij} needs to be modelled if the first weakly compressible approach is considered. Only this specific case will be considered in the present section. The modelling of the spherical part, although widely diffused [25, 26], has been only mildly treated in the present work (see chapter 8).

Sub-Grid Scale modelling of turbulence consists in identifying the general algorithm that expresses the unclosed SGS terms as functions of the filtered

variables which are directly available from the simulation. This process can be represented by a simple analytical functional form of each term or by a more complex algorithm taking the resolved variables as general inputs. In simpler terms, turbulence modelling consists in an input-output relation where the input are the resolved variables and the output are the unclosed SGS terms. It is finally interesting to notice that also the choice of the resolved variables is arbitrary and it can lead to different modelling choices. If the conserved variables are the prescribed unknowns, then the available quantities for a turbulence model are entirely contained in the vector $\overline{\mathbf{U}}$. In particular the set of unknowns that can be used is:

$$\left\{\overline{\rho}, \overline{\rho u_1}, \overline{\rho u_2}, \overline{\rho u_3}, \overline{\rho E}\right\}. \tag{3.33}$$

On the other hand, if the fully-compressible formulation is considered, also the spherical part of the SGS tensor needs to be modelled and the choices on the resolved variables could differ. In fact, the resolved energy will be different as shown in Eqs. (3.30) and (3.31).

Then, the formal way to write the turbulence closure modelling problem is simply:

$$\begin{aligned} \tau_{ij}^d &= f_{ij}(\overline{\mathbf{U}}, \mathbf{x}, t), \\ q_k &= g_k(\overline{\mathbf{U}}, \mathbf{x}, t). \end{aligned} \tag{3.34}$$

Once this dependence is explicitly stated, the filtered equations can be numerically discretised, causing an ulterior non-trivial influence on turbulence modelling as it will be deeply analysed in the next chapters. Under-resolved flows, such as the ones normally modelled using the LES approach, are significantly influenced by the numerical discretisation and any specific turbulence model should be tailored based on the underlying numerical scheme used to solve the filtered equations. This concept will be fundamental throughout the whole thesis work and it will be deeply discussed in chapter 6.

Another fundamental difference in SGS modelling relies on the tensor or vector level of approximation of the unclosed terms. In fact, in order to obtain satisfying LES results, it is not always necessary to model unclosed terms on a tensor level (each component individually). Sometimes, SGS models base on their divergence (vector level), which is the actual term appearing in the filtered equations, can suffice to predict the correct dynamics of the resolved field. In other words, a tensor level model such as

$$\tau_{ij}^d = f_{ij}(\overline{\mathbf{U}}, \mathbf{x}, t) \quad \text{for} \quad i, j = 1, ..., 3$$

can be substituted by a vector-level model of the form

$$\frac{\partial \tau_{ij}^d}{\partial x_j} = f_i^*(\overline{\mathbf{U}}, \mathbf{x}, t) \quad \text{for} \quad i = 1, ..., 3$$

Since the SGS heat flux q_k is a vector, it can be modelled on a vector level as

$$q_k = g_k(\overline{\mathbf{U}}, \mathbf{x}, t) \quad \text{for} \quad k = 1, ..., 3$$

or, on a *scalar* level, as

$$\frac{\partial q_k}{\partial x_k} = g^*(\overline{\mathbf{U}}, \mathbf{x}, t).$$

Vectorial and tensor level approximations define the difference between *functional* and *stuctural* models. More specifically, the former aim to reproduce the effects of sub-grid terms on the resolved flow field, while the latter seek a good correlation on a tensor level too.

One of the most popular class of functional models is the Eddy-Viscosity or Sub-Grid Viscosity approximation. Eddy-viscosity models are based on the assumption of similarity between molecular diffusion mechanics and sub-grid scales energy transfers. The influence of unresolved scales on the large scale flow field is assumed to be essentially dissipative. Such an assumption was first proposed by Richardson's theory [27] on *energy cascade* and lately formalised by Kolmogorov [20]. The kinetic energy is produced by the large scale motions, characterised by the problem/s geometry and boundary conditions. Subsequently, the kinetic energy contained in the largest vortices is transferred to smaller and smaller scales through the vortex-stretching mechanism. For small enough scales, the viscous effects become comparable with convective stresses and the accumulated kinetic energy is finally dissipated. If these scales are excessively small, the computational cost of the numerical simulation required to resolve them can become extremely high. Using the assumption of energy cascade, instead, the influence of viscous scales on the resolved field can be easily modelled as a dissipative process. The simplest approach consists in the addition of turbulent dissipation:

$$\tau_{ij}^d = 2\nu_t(\widetilde{S}_{ij} - 2/3\delta_{ij}\widetilde{S}_{kk}). \tag{3.35}$$

Furthermore, employing the hypothesis of Eidson [28], the SGS energy flux can be directly related to the eddy-viscosity as

$$q_k = \gamma \frac{\overline{\rho}\nu_t}{\mathrm{Pr}_t} \frac{\partial \widetilde{e}}{\partial x_k}. \tag{3.36}$$

The closure problem is then solved when $\nu_t(\mathbf{x}, t)$ and $\mathrm{Pr}_t(\mathbf{x}, t)$ are defined. Notice that both can be spatially and time dependent. In fact, the eddy-viscosity is a property of the turbulence itself and it needs to be differently active depending on the different nature of the turbulent structures within the domain. The Prandtl number, instead, is generally taken as a constant value varying between 0.5 and 0.9 [29]. Among the advantages of eddy-viscosity models, simplicity and robustness are certainly the most important. The theoretical concept behind is intuitive and reliable. Nevertheless, in certain conditions, such assumptions can be dramatically simplistic, leading to

excessive dissipation, in particular in combination with high-order methods. Along the years, more and more complex models have been developed since the rise of LES. Most of them, leading to superior improvements with respect to classical models such Smagorinsky model. Nevertheless, more accurate predictions usually come along with more expensive algorithms and more delicate stability which could fail for certain complex simulations. It is in fact important to highlight how LES cannot be categorised neither as a merely numerical problem nor as a turbulence physics one. A deep understanding of the dynamics of turbulent flows is crucial. A strong theoretical background could potentially lead to very accurate models, but, if such models are extremely complex and expensive, the whole purpose of LES would be pointless. A good equilibrium between complexity and computational cost is pivotal for a successful SGS model.

3.4 A-priori and a-posteriori analyses

In order to evaluate the validity of particular SGS model, two main approaches are commonly practised in the literature: *a-priori* and *a-posteriori* testing [30, 31]. In the first approach, fully-resolved fields are available from DNS of specific turbulent flows. Explicit filtering is then applied to the DNS data in order to evaluate the unclosed SGS terms in the filtered equations. Such quantities can then be used as reference for the development of a specific SGS model built using the filtered variables. In this way it is possible to estimate the reliability and robustness of a certain SGS model without actually perform any Large-Eddy Simulation (*i.e.*, in a *offline* fashion). Following an a-posteriori approach, the problem is tackled in the opposite way, the theoretical filtered equations are simply discretised and the SGS model is directly employed in a LES computations. Secondly, quantities extracted from the LES can then be compared with measured mean velocity profiles for which an extensive set of experimental and DNS data are available in the literature. Of course, both approaches are needed in the development of innovative SGS models.

A-priori testing based on DNS data has shown some discouraging results: classical SGS models have shown poor correlation with respect to the SGS unclosed terms obtained from explicit filtering of DNS data. Nevertheless, it has also been noticed in multiple works ([32, 31, 33]) that poor a-priori correlations do not necessarily translate in poor results when the model is actually employed in a LES. In the same way, models which correlates very well with explicitly filtered quantities are not always suitable for LES and additional dissipative eddy-viscosity terms are usually needed (for example, the gradient/tensor diffusivity model [34] or Bardina's model [35]).

In ideal conditions the perfect equivalence between the two approaches would be likely to take place. For a given set filtered DNS fields, it is

reasonable to think that it would exists a certain SGS model capable of giving the same exact outcomes when actually applied to a real LES. Finding the exact model capable of such results, nevertheless has be theoretically proved to be impossible ([36, 37]) due to inevitable commutation errors.

In fact, the comparison between the two approaches relies in a fundamental assumption: the explicit filtering operation applied to the DNS data is representative of the numerical resolution of the filtered equations. In a sense, the filter kernel, implicitly defined through the discretisation of the filtered equations, is assumed to have an a-priori known expression (such as box-hat/gaussian/sharp spectral filter). The role played by the numerics, instead, is extremely complex and, in large part, characterised by unknown outcomes in terms of dissipation and regularity of the solution. The connection between the numerical scheme employed to solve the equations and the physical-based SGS model is a crucial aspect in the success or failure of the LES. Secondly, but not less importantly, the a-priori approach completely neglects the dynamics of the system, since the analysis is only based on snapshots of DNS filtered data. It is then commonly assumed that such deficiency would affect the reliability of a-posteriori approaches.

In the present work, both a-priori and a-posteriori approaches will be used to study the recently developed Spectral Element Dynamic Model (SEDM) [1] which will be briefly introduced in the next sections and thoroughly discussed in chapter 6.

3.5 Eddy-viscosity models

The Eddy-viscosity models belong to the class of functional SGS models. In fact, their goal is not reproducing exactly all the individual entries of the SGS tensor, but to reproduce the effect of such terms on the resolved fields. If the energy transfer within the inertial range of the kinetic energy spectrum is assumed to replicate classical molecular diffusion, then it is possible to model such transfer introducing a properly defined eddy-viscosity term. In other words, as already mentioned in the previous sections, the following approximations are commonly invoked:

$$\tau_{ij}^{d} = 2\nu_t(\widetilde{S}_{ij} - 2/3\delta_{ij}\widetilde{S}_{kk}), \tag{3.37}$$

and

$$q_k = \gamma\frac{\overline{\rho}\nu_t}{\mathrm{Pr}_t}\frac{\partial\widetilde{e}}{\partial x_k}. \tag{3.38}$$

Of course, many different eddy-viscosity models have been proposed over the years, each with specific desirable properties. In the present section, a brief overview on the most popular ones will be given.

3.5.1 Smagorinsky Model

Among the most used sub-grid eddy-viscosity models, the Smagorinsky model [38] computes the sub-grid viscosity ν_t as :

$$\nu_t = C_s^2 \Delta^2 |\widetilde{S}^d|, \tag{3.39}$$

where the tensor norm term is computed from the resolved strain rate tensor with the following relation

$$|\widetilde{S}^d| = (2\widetilde{S}_{ij}\widetilde{S}_{ij})^{1/2}, \tag{3.40}$$

and Δ is the grid level filter width. The model constant C_s can be theoretically determined from *Local Equilibrium Hypothesis* considerations or adapted for the specific problem. Typical values range from 0.1 to 0.2.

3.5.2 The wall-adapting local eddy-viscosity (WALE) model

The WALE model [39] was designed primarily to achieve the correct near-wall scaling behaviour, $\mathcal{O}(y^3)$, for the sub-grid eddy-viscosity by using a new operator $\mathcal{S}_{ij}^d$ defined as:

$$\mathcal{S}_{ij}^d = \frac{1}{2}(\overline{g}_{ij}^2 + \overline{g}_{ji}^2) - \frac{1}{3}\delta_{ij}\overline{g}_{kk}^2, \tag{3.41}$$

where $\mathcal{S}_{ij}^d$ is the traceless-symmetric part of the square of the velocity-gradient tensor $\overline{g}_{ij} = \partial\widetilde{u}_i/\partial x_j$. Since the term $\mathcal{S}_{ij}^d\mathcal{S}_{ij}^d$ scales as $\mathcal{O}(y^2)$, it is possible to construct an eddy-viscosity:

$$\nu_t = (C_\mathrm{w}\Delta)^2 \frac{(\mathcal{S}_{ij}^d\mathcal{S}_{ij}^d)^{3/2}}{(\widetilde{S}_{ij}\widetilde{S}_{ij})^{5/2} + (\mathcal{S}_{ij}^d\mathcal{S}_{ij}^d)^{5/4}}, \tag{3.42}$$

such that $\mathcal{O}(y^3)$ scaling may be achieved near the wall. In the equation above, C_w is the coefficient of the WALE model and is a user specified parameter. This coefficient has been calibrated using isotropic turbulence to obtain the relation $C_\mathrm{w}^2 = 10.6C_\mathrm{s}^2$, where C_s is the constant-coefficient Smagorinsky coefficient. Based upon this expression and the value of $C_\mathrm{s} = 0.1$ (typical for wall-bounded flows), we set the coefficient of the WALE model to 0.3 [40].

3.5.3 The SIGMA model

The SIGMA model [41] improves upon the behaviour of the WALE model by using the singular-value-decomposition of the velocity-gradient tensor to build the eddy-viscosity. This manner of constructing the sub-grid eddy-viscosity provides the model with many useful properties. For example the

SIGMA model vanishes completely in the presence of solid rotation and pure shear. By comparison, the WALE model only vanishes in the presence of pure shear. Furthermore, similar to the WALE model, $\mathcal{O}(y^3)$ scaling of the eddy-viscosity is achieved near the wall. The eddy-viscosity of the SIGMA model may be defined as:

$$\nu_t = (C_\sigma \Delta)^2 D_\sigma, \tag{3.43}$$

where:

$$D_\sigma = \frac{\sigma_3(\sigma_1 - \sigma_2)(\sigma_2 - \sigma_3)}{\sigma_1^2}, \tag{3.44}$$

and where $\sigma_1 \geq \sigma_2 \geq \sigma_3 \geq 0$ are the three, singular-values of the velocity gradient tensor $\overline{g}_{ij}$ (as defined in Sec. 3.5.2) and C_σ is the SIGMA model coefficient which is a user specified parameter. The value of C_σ has been evaluated to be 1.35 in Ref. [41].

3.5.4 Spectral Element Dynamic Model

The Spectral Element Dynamic Model [1] defines a constant kinematic eddy-viscosity within the element of the SD discretisation as:

$$\nu_t^n = C_{\text{SEDM}}^2 f(\sigma_n) \Delta_n \sqrt{k_n}\,, \tag{3.45}$$

where Δ_n is an estimate of the local cutoff length scale, $f(\sigma_n)$ is a spectral turbulence sensor, C_{SEDM} is a model constant and k_n is an estimate of the SGS turbulent kinetic energy within the element defined as:

$$k_n = \frac{1}{2}\left(\langle \widetilde{\mathbf{u}}_n \cdot \widetilde{\mathbf{u}}_n \rangle - \langle \widetilde{\mathbf{u}}_n \rangle \cdot \langle \widetilde{\mathbf{u}}_n \rangle \right), \tag{3.46}$$

where $\langle \cdot \rangle$ denotes spatial averaging within the element.

The expression for the turbulent sensor reads:

$$f(\sigma_n) = \begin{cases} 1 & \text{for } \sigma_n < \sigma_{\text{thr}}, \\ \dfrac{1}{2}\left\{ 1 + \sin\left[\dfrac{\pi(\sigma_{\text{t}} + \zeta - \sigma_n)}{2\zeta} \right] \right\} & \text{for } \sigma_{\text{thr}} \leq \sigma_n \leq \sigma_{\text{thr}} + 2\zeta\,, \\ 0 & \text{for } \sigma_n > \sigma_{\text{thr}} + 2\zeta\,, \end{cases} \tag{3.47}$$

where σ_n is a least square approximation of the decay exponent of the modes associated to Legendre polynomials within the n-th element.

Before the computation of the SGS terms, the eddy-viscosity is made linear across the elements to avoid discontinuities of ν_t within the domain.

Three parameters influence the level of dissipation introduced by the SGS model, namely, σ_{thr}, C_{SEDM} and ζ. Their values have been calibrated using low Mach number Taylor Green Vortex DNS data [1]. In all the simulations presented hereafter, the following set of values have been used:

$$C_{\text{SEDM}} = 0.23, \qquad \sigma_{\text{thr}} = 1.6, \qquad \zeta = 0.3\,. \tag{3.48}$$

Finally, the turbulent Prandlt number has been set to 0.5 [29]. A more detailed overview on the SEDM will be provided in chapter 6.

Chapter 4

Spectral Difference method

Contents

4.1 Introduction

The constant increase of computing power in modern hardware architectures made computational fluid dynamics a widely-used virtual prototyping tool [42]. Well established CFD softwares are now robust and reliable for many engineering design processes. Although, they still lack in accuracy for many delicate situations of high interest in engineering and applied sciences. Along these lines, innovative numerical high-order schemes gained a lot of interest in the last few decades, emerging as the building core of the next CFD generation [43]. Among them, the Spectral Difference method [44, 45, 46], which has been used in the present work. In the following sections the Spectral Difference method will be first introduced to discretise one-dimensional conservation laws and subsequently generalised for the three-dimensional Navier-Stokes equations. All the significant details about the numerical

scheme will be briefly mentioned to provide a satisfactory overall characterisation of the Spectral Difference scheme.

4.2 1D Spectral Difference method

The SD method solves the strong form of the differential equation using piecewise continuous functions as approximation space. Consequently, the solution is assumed to be discontinuous at elements interface. In order to have a consistent discretisation, the solution is interpolated using a polynomial of degree N while the flux, which is connected to the conservative variables via a divergence operator, is approximated with a polynomial of degree $N+1$. The most important ingredient of the SD discretisation is the definition of two different set of points: solution and flux points. The numerical solution is defined on the nodes x_i^s with i=0 to N. Fluxes, instead, are defined on a different set of nodes x_i^f, with i=0 to $N+1$, among which element boundary points are included. It shall be noted that, in the present study, the solution points are set as the Gauss-Legendre points of order $N+1$, a sensible choice to minimise aliasing errors in the nonlinear case while defining a well conditioned basis set for the solution interpolation [47], whereas the flux points are set as the Gauss-Legendre points of order N plus the two end points -1 and 1 to ensure linear stability [48]. An example of solution and flux points for a polynomial approximation of degree $N = 3$ is shown in Fig. 4.1.

Figure 4.1: Solution (red circles) and flux (blue squares) points of SD discretisation in the reference element ($N = 3$).

As in the FR scheme, the solution is approximated with a polynomial of degree N

$$\hat{u}(\hat{x}) = \sum_{i=0}^{N} u_i l_i^s(\hat{x}). \tag{4.1}$$

within the reference element $\Omega_n = \{\hat{x} | -1 \leq \hat{x} \leq 1\}$. In the one-dimensional case, the map linking the reference element to the physical element, and consequently $\hat{x}$ with x, is a simple linear transformation, acting on the length of the element.

At this point the FR scheme would use an interpolated flux (of degree N) on the same set of points and subsequently add a correction flux (of degree

$N+1$) defined on element extrema as well. In the SD scheme, instead, the values of the solution are extrapolated at the flux points

$$\hat{u}(\hat{x}_j^f) = \sum_{i=0}^{N} u_i l_i^s(\hat{x}_j^f), \qquad j = 0, ..., N+1, \tag{4.2}$$

and then used to compute fluxes on the same collocation basis:

$$f_j = \hat{f}(\hat{x}_j^f) = \hat{f}(\hat{u}(\hat{x}_j^f)). \tag{4.3}$$

Then, a continuous flux polynomial of degree $N+1$ is constructed, by Lagrange interpolation, using the fluxes evaluated from the interpolated solution at the interior flux points and the numerical fluxes at the element interfaces:

$$\hat{f}(\hat{x}) = \hat{f}_L^I l_0^f(\hat{x}) + \sum_{j=1}^{N} f_j l_j^f(\hat{x}) + \hat{f}_R^I l_{N+1}^f(\hat{x}). \tag{4.4}$$

In other words, the interpolated values of the flux at elements extrema are substituted by the interface numerical fluxes $\hat{f}_L^I$ and $\hat{f}_R^I$. Finally, the flux divergence is evaluated at the solution points,

$$\frac{\mathrm{d}\hat{f}}{\mathrm{d}\hat{x}}(\hat{x}_i^s) = \hat{f}_L^I \frac{\mathrm{d}l_0^f}{\mathrm{d}\hat{x}}(\hat{x}_i^s) + \sum_{j=1}^{N} f_j \frac{\mathrm{d}l_j^f}{\mathrm{d}\hat{x}}(\hat{x}_i^s) + \hat{f}_R^I \frac{\mathrm{d}l_{N+1}^f}{\mathrm{d}\hat{x}}(\hat{x}_i^s), \tag{4.5}$$

and the numerical solution can be advanced in time using a suitable time integration scheme discretising the following equation:

$$\frac{\mathrm{d}\hat{u}}{\mathrm{dt}} = -\frac{\mathrm{d}\hat{f}}{\mathrm{d}\hat{x}}(\hat{x}_i^s). \tag{4.6}$$

As example, in the case of linear advection equation, Eq. (4.6), for the n-th element, can be written in matrix form as

$$\frac{\mathrm{d}\hat{\mathbf{u}}_n}{\mathrm{dt}} = -2\mathbf{D}(\hat{f}_L \mathbb{1}^0 + \mathbf{M}\hat{\mathbf{u}}_n + \hat{f}_R \mathbb{1}^{N+1}), \tag{4.7}$$

where

$$\mathbf{D}_{ij} = \frac{\mathrm{d}l_j^f(\hat{x}_i^s)}{\mathrm{d}\hat{x}}, \qquad \mathbf{M}_{ij} = \begin{cases} 0 & \text{for} \quad i = 0, \\ 0 & \text{for} \quad i = N+1, \\ l_j^s(\hat{x}_i^f) & \text{otherwise}, \end{cases} \tag{4.8}$$

$\mathbb{1}_j^0 = \delta_{j0}$ and $\mathbb{1}_j^{N+1} = \delta_{j(N+1)}$ for $j = 0$ to $N+1$. In the above formalism, when the superscript s is used, the relevant index ranges from 0 to N, whereas, when the superscript f is adopted, the index goes from 0 to $N+1$. Hence, $\mathbf{D} \in \mathbb{R}^{(N+1)\times(N+2)}$ and $\mathbf{M} \in \mathbb{R}^{(N+2)\times(N+1)}$ resulting in a local linear system of dimensions $(N+1)\times(N+1)$. The subscript $(\cdot)_n$, instead, denotes

the element numbering. Notice how a clear distinction between the interior differential operator and the evaluation of the interface flux is evident in Eq. (4.7).

The core of the method is hidden inside the definition of the matrix $\mathbf{M}$, for which both nodal sets are needed, while the interface information is contained in the $\hat{f}_{L/R}$ terms. A specific SD method is completely defined by:

1. the location of both solution and flux points;

2. the expression of interface fluxes $\hat{f}_{L/R}$.

In chapter 5, the Flux Reconstruction (FR) scheme will be introduced. It will be shown that the different choice of correction functions in the FR method can be directly linked to the location of the solution points in the SD scheme. The interpolation operator between solution and flux points, in fact, implicitly defines the correction function of the corresponding FR recovering scheme. Nodes coordinates are somehow a useful degree of freedom that can be modified in order to increase accuracy and/or stability. In fact, some recent work has been done in optimised nodes location for SD methods [49].

4.3 Multi-dimensional formulation

Once the one-dimensional strategy is properly outlined, the three-dimensional SD discretisation of conservation laws can be easily generalised. The governing equations are once again transferred from the physical to the computational domain through the change of coordinates:

$$\mathbf{x} = \sum_{i=0}^{K} M_i(\hat{\mathbf{x}})\mathbf{x}_i \tag{4.9}$$

where K is the number of points defining the physical element, whereas $\mathbf{x}_i$ and M_i are the relevant position vectors (in physical space) and shape functions, respectively. The change of coordinates, in the one-dimensional case, consisted in a simple linear scaling of the element, whereas, in multiple dimensions, more complex deformations of the reference element are allowed. In this sense, using appropriate definition of coordinates transformation, it is possible to handle highly complex geometries with a reasonably small effort. Of course, the geometrical flexibility of spectral element methods represents a very powerful feature for realistic CFD configurations.

The general multi-dimensional conservation law can be expressed in the computational space as

$$\frac{\partial \mathbf{Q}}{\partial t} + \nabla_{\hat{x}} \cdot \mathbf{G} = \mathbf{0}, \tag{4.10}$$

with $\mathbf{Q} = \det(J)\mathbf{U}$, $\mathbf{G} = \mathrm{adj}(J) \cdot \mathbf{F}$, where $\det(J)$ and $\mathrm{adj}(J)$ respectively represent the determinant and the adjoint of the Jacobian of the transformation $J = \frac{\partial \hat{\mathbf{x}}}{\partial \mathbf{x}}$.

Within the element, solution and flux points are defined in a tensor product fashion, leading to the following expression of the interpolated representation of conserved variables:

$$\mathbf{U}(\hat{x}, \hat{y}, \hat{z}) = \sum_{i=0}^{N} \sum_{j=0}^{N} \sum_{k=0}^{N} \frac{\mathbf{Q}_{i,j,k}}{\det(J)_{i,j,k}} l_i^s(\hat{x}) l_j^s(\hat{y}) l_k^s(\hat{z}) \tag{4.11}$$

where $l_i(\hat{x})$, $l_j(\hat{y})$, $l_k(\hat{z})$ represent one dimensional Lagrange polynomials along the three dimensions of the reference element. Similarly to the one-dimensional case, along each direction, the polynomial approximation defines immediately a strategy to evaluate the conserved variables at the flux points. Namely,

$$\mathbf{U}_{f,j,k} = \sum_{i=0}^{N} \frac{\mathbf{Q}_{i,j,k}}{\det(J)_{i,j,k}} l_i^s(\hat{x}_f) \tag{4.12}$$

$$\mathbf{U}_{i,f,k} = \sum_{j=0}^{N} \frac{\mathbf{Q}_{i,j,k}}{\det(J)_{i,j,k}} l_j^s(\hat{y}_f) \tag{4.13}$$

$$\mathbf{U}_{i,j,f} = \sum_{k=0}^{N} \frac{\mathbf{Q}_{i,j,k}}{\det(J)_{i,j,k}} l_k^s(\hat{z}_f) \tag{4.14}$$

with $f = 0, ..., N+1$. An example of tensor product locations of solution

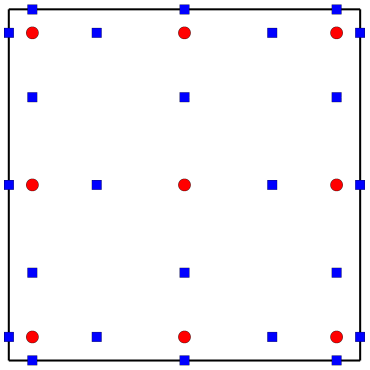

Figure 4.2: Distribution of solution (red circles) and flux points (blue squares) in the standard element for a 3-rd order spatial discretisation.

and flux points is shown in the reference element in Fig. 4.2.

Fluxes, considered along $\hat{x}$, $\hat{y}$ and $\hat{z}$, can be written as:

$$\mathbf{G}^1_{j,k}(\hat{x}) = \sum_{p=0}^{N+1} (\mathrm{adj}(J) \cdot \mathbf{F})^1_{p,j,k} l^f_p(\hat{x}), \tag{4.15}$$

$$\mathbf{G}^2_{i,k}(\hat{y}) = \sum_{p=0}^{N+1} (\mathrm{adj}(J) \cdot \mathbf{F})^2_{i,p,k} l^f_p(\hat{y}), \tag{4.16}$$

$$\mathbf{G}^3_{i,j}(\hat{z}) = \sum_{p=0}^{N+1} (\mathrm{adj}(J) \cdot \mathbf{F})^3_{i,j,p} l^f_p(\hat{z}), \tag{4.17}$$

where $(\mathrm{adj}(J) \cdot \mathbf{F})^d$ is the d-th component of $\mathrm{adj}(J) \cdot \mathbf{F}$ evaluated at the p-th flux point for fixed indices along the other two dimensions. Finally, l^f_p is the Lagrange polynomial defined on the p-th flux point, constructed on the flux points basis. Consequently, such polynomial is one order higher than the ones used to define conserved variables on the solution points. The point-wise values of the flux are computed using the reconstructed solution evaluated at the flux points, namely, $\mathbf{U}_{f,j,k}$, $\mathbf{U}_{i,f,k}$, $\mathbf{U}_{i,j,f}$ from Eqs. 4.12, 4.13 and 4.14 respectively. The reconstructed flux is only element-wise continuous and discontinuous across element interfaces. With regards to the interface contribution, a Riemann solver is employed to compute a common flux at the cell interface to ensure conservation and stability. Theory and common practices of Riemann solvers will be the focus of the next section. The flux is then made continuous replacing the element interface fluxes $\mathbf{F}_{0,j,k}$ and $\mathbf{F}_{N+1,j,k}$ (for fluxes along $\hat{x}$) with the one-valued numerical interface flux given by the approximate solution of the interface Riemann problem. The computation of the derivative along $\hat{x}$ is finally performed exactly in the same way as in the one-dimensional case. Namely, given the interpolation of the *corrected* fluxes $\widetilde{\mathbf{G}}(\hat{x})$, the derivative of $\widetilde{\mathbf{G}}(\hat{x})$ along $\hat{x}$, $\hat{y}$ and $\hat{z}$ is computed simply applying the derivative operator to Eqs. 4.15 4.16 and 4.17 respectively:

$$\frac{\partial}{\partial \hat{x}} \left(\widetilde{\mathbf{G}}^1_{j,k}(\hat{x}) \right) = \sum_{p=0}^{N+1} (\mathrm{adj}(J) \cdot \widetilde{\mathbf{F}})^1_{p,j,k} \frac{\mathrm{d}l^f_p(\hat{x})}{\mathrm{d}\hat{x}}, \tag{4.18}$$

$$\frac{\partial}{\partial \hat{y}} \left(\widetilde{\mathbf{G}}^2_{i,k}(\hat{y}) \right) = \sum_{p=0}^{N+1} (\mathrm{adj}(J) \cdot \widetilde{\mathbf{F}})^2_{p,i,k} \frac{\mathrm{d}l^f_p(\hat{y})}{\mathrm{d}\hat{y}}, \tag{4.19}$$

$$\frac{\partial}{\partial \hat{z}} \left(\widetilde{\mathbf{G}}^3_{i,j}(\hat{z}) \right) = \sum_{p=0}^{N+1} (\mathrm{adj}(J) \cdot \widetilde{\mathbf{F}})^3_{p,i,j} \frac{\mathrm{d}l^f_p(\hat{z})}{\mathrm{d}\hat{z}}. \tag{4.20}$$

All the previous expressions can be finally evaluated on the solutions points of each direction:

$$\frac{\partial}{\partial \hat{x}}\left(\widetilde{\mathbf{G}}^1_{i,j,k}\right) = \frac{\partial}{\partial \hat{x}}\left(\widetilde{\mathbf{G}}^1_{j,k}(\hat{x})\right)\Big|_{\hat{x}_i} \quad \text{with} \quad i = 0, ..., N \tag{4.21}$$

$$\frac{\partial}{\partial \hat{y}}\left(\widetilde{\mathbf{G}}^2_{i,j,k}\right) = \frac{\partial}{\partial \hat{y}}\left(\widetilde{\mathbf{G}}^2_{i,k}(\hat{y})\right)\Big|_{\hat{y}_j} \quad \text{with} \quad j = 0, ..., N \tag{4.22}$$

$$\frac{\partial}{\partial \hat{z}}\left(\widetilde{\mathbf{G}}^3_{i,j,k}\right) = \frac{\partial}{\partial \hat{z}}\left(\widetilde{\mathbf{G}}^3_{i,j}(\hat{z})\right)\Big|_{\hat{z}_k} \quad \text{with} \quad k = 0, ..., N \tag{4.23}$$

Finally, the semi-discrete SD discretisation of the conservation law 4.10 can be written as:

$$\frac{\partial \mathbf{Q}_{i,j,k}}{\partial t} + \frac{\partial}{\partial \hat{x}}\left(\widetilde{\mathbf{G}}^1_{i,j,k}\right) + \frac{\partial}{\partial \hat{y}}\left(\widetilde{\mathbf{G}}^2_{i,j,k}\right) + \frac{\partial}{\partial \hat{z}}\left(\widetilde{\mathbf{G}}^3_{i,j,k}\right) = \mathbf{0}. \tag{4.24}$$

In a similar manner, the same procedure can be repeated to compute viscous fluxes, where the extrapolation on the flux points is applied to fluxes involving first derivatives. In fact, after the computation of inviscid fluxes, the first derivatives of the conserved quantities are directly available within the element, and they can be used to evaluate viscous fluxes at the solution points. Given such information, the same strategy, briefly presented in this section, can be almost identically employed to compute the divergence of viscous fluxes. In analogy with respect to the computation of inviscid fluxes, an appropriate definition of interface fluxes will be needed. More details on Riemann solvers and viscous fluxes will be provided in the next sections.

4.4 Numerical fluxes

In the previous sections the general strategy to discretise a general conservation law using the SD scheme has been provided. It has been explained that fluxes are made continuous at the interface using numerical fluxes. In the three-dimensional discretisation of the Navier-Stokes equations, the numerical fluxes are obtained solving a Riemann problem.

Due to the intimate connection between upwinding fluxes and numerical dissipation, most of the present section will be focused on inviscid fluxes. In particular, Roe flux will be considered as one of the most representative examples of inviscid numerical flux for spectral element methods. Many other alternatives have been developed in the last decades giving a very vast choice of fluxes that can be used in solving compressible Navier-Stokes equations in an high-order discretisation framework (see [50] for an extensive review).

In a similar way, the literature on viscous numerical fluxes for high-order methods recently experienced a sensible grow [51, 52, 53]. Nevertheless,

in terms of numerical dissipation at high wavenumbers, numerical viscous fluxes play a less relevant role (see also [54]). The eventual dissipative term added to the numerical viscous flux is in fact usually proportional to the conserved variables' jumps across the element's interface, leading, ultimately, to a dissipative effect which is identical to the one associated to inviscid fluxes.

4.4.1 Inviscid fluxes

Characteristic Variables

Characteristic variables play a fundamental role in many different aspects of CFD, from characteristic-based boundary conditions [55, 56, 57, 58] to Godunov's methods for finite volume schemes [59]. In particular, as it will be explained in more details in the following sections, characteristic variables are very important in the theory and practice use of Riemann solvers as they give a fundamental understanding on how information propagates within the fluid domain.

As first building block, the eigenvalue formulation of the one-dimensional form of Euler equations will be considered as a simplified example of hyperbolic conservation law. In this particular setting, the governing equations can be written as:

$$\mathbf{U}_t + A\mathbf{U}_x = \mathbf{0}, \tag{4.25}$$

where

$$A = \begin{bmatrix} u & \rho & 0 \\ 0 & u & 1/\rho \\ 0 & \rho c^2 & u \end{bmatrix} \quad \text{with} \quad c = \sqrt{\mathrm{d}p/\mathrm{d}\rho}, \tag{4.26}$$

and $\mathbf{U} = (\rho, u, p)^T$.

One of the useful properties of the matrix A for hyperbolic conservation laws is that it can be diagonalised. Namely, the matrix A can be written as:

$$A = L^{-1}\Lambda L, \tag{4.27}$$

where L and L^{-1} can have different forms based on the normalisation coefficients. One of the most popular options leads to the following expressions:

$$L = \begin{bmatrix} 1 & \rho/2c & -\rho/2c \\ 0 & 1/2 & 1/2 \\ 0 & \rho c/2 & -\rho c/2 \end{bmatrix} \qquad \text{and} \qquad L^{-1} = \begin{bmatrix} 1 & 0 & -1/c^2 \\ 0 & 1 & 1/(\rho c) \\ 0 & 1 & -1/(\rho c) \end{bmatrix}, \tag{4.28}$$

whilst the corresponding eigenvalues are $\lambda_1 = u$, $\lambda_2 = u + c$ and $\lambda_3 = u - c$.

Multiplying both sides of 4.25 by L^{-1} Euler's equations read:

$$L^{-1}\mathbf{U}_t + L^{-1}A(LL^{-1})\mathbf{U}_x = \mathbf{0}. \tag{4.29}$$

In order to obtain an advantageous formulation, the matrix L is considered constant. Such approximation is essentially equivalent to assume that the equations can be locally linearised. Consequently, introducing the change of variables $\mathbf{W} = L^{-1}\mathbf{U}$, which from now on will be denoted as *characteristic variables*, Euler's equations take a very simple and powerful form:

$$\mathbf{W}_t + \Lambda \mathbf{W}_x = \mathbf{0}. \tag{4.30}$$

All the equations are now completely decoupled and a simple analytical solution is immediately available. Namely,

$$w_i(x,t) = w^0(x - \lambda_i t) \quad i = 1, ..., 3 \tag{4.31}$$

Consequently, it exists a local change of variables such that the new set of unknowns assume always a constant value along a certain space-time direction and the speed of propagation coincides with the magnitude of the eigenvalues.

Obviously, the matrix A (and so L, L^{-1} and Λ) is not constant, as it depends on the local values of $\mathbf{U}$. The present theory holds only locally. Nonetheless, the characteristic decomposition gives very important informations on the solution's structure. The local values of characteristic variables, as presented in the next sections, play a fundamental role in the framework of Riemann solvers.

Finally, notice that, once the characteristic equations are solved, the solution of conserved variables can be simply written as:

$$\mathbf{U}(x,t) = L\mathbf{W} = \sum_{i=1}^{3} w_i^0(x - \lambda_i t)\mathbf{L}^{(i)}. \tag{4.32}$$

Riemann Problem

The Riemann problem for the hyperbolic, constant coefficient system 4.25 can be defined as the following Initial Value Problem:

$$\mathbf{U}_t + A\mathbf{U}_x = \mathbf{0}, \tag{4.33}$$

with initial conditions

$$\mathbf{U}(x,0) = \begin{cases} \mathbf{U}_L & for \quad x < 0 \\ \mathbf{U}_R & for \quad x > 0 \end{cases} . \tag{4.34}$$

The general structure of the solution in the (x,t) plane is sketched in Fig. 4.3: a finite number of space-time waves characterised by different slopes (*i.e.*, propagation velocities) represent the full solution of the Riemann problem. Assuming that the matrix A is a constant, the Riemann problem can be

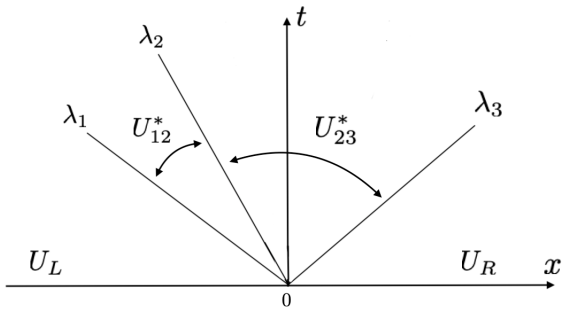

Figure 4.3: General solution structure.

easily solved using the characteristic change of variables introduced in the previous section.

As a first step, left and right states are defined using the vector space spanned by the eigenvectors of the matrix A. Namely,

$$\mathbf{U}_L = \sum_{i=1}^{3} \alpha_i \mathbf{L}^{(i)} \quad \text{and} \quad \mathbf{U}_R = \sum_{i=1}^{3} \beta_i \mathbf{L}^{(i)}. \tag{4.35}$$

The general solution is evaluated using the characteristic system which reads:

$$\mathbf{W}_t + \Lambda \mathbf{W}_x = 0, \tag{4.36}$$

with initial data

$$w_i^0(x) = \begin{cases} \alpha_i & x < 0 \\ \beta_i & x > 0 \end{cases} \qquad i = 1, ..., 3 \quad , \tag{4.37}$$

The solution of the characteristic system is then computed as:

$$w_i(x,t) = w_i^0(x - \lambda_i t) = \begin{cases} \alpha_i & x - \lambda_i t < 0 \\ \beta_i & x - \lambda_i t > 0 \end{cases} \quad , \tag{4.38}$$

and the solution in the primitive variables is simply defined by Eq. (4.32). In particular, whenever $x - \lambda_i t < 0$, the solution is just $\mathbf{U}_L$ and the linear combination of the eigenvectors defining the solution involves only α coefficients. Instead, if $x - \lambda_i t > 0$ only β coefficients will appear. In the middle, combinations of left and right states will emerge. In particular, in the case of three equations, the possible options are:

$$\begin{aligned} \mathbf{U}_{12}^* &= \beta_1 \mathbf{L}^{(1)} + \alpha_2 \mathbf{L}^{(2)} + \alpha_3 \mathbf{L}^{(3)}, \\ \mathbf{U}_{23}^* &= \beta_1 \mathbf{L}^{(1)} + \beta_2 \mathbf{L}^{(2)} + \alpha_3 \mathbf{L}^{(3)}. \end{aligned} \tag{4.39}$$

This idea is graphically pictured in Fig. 4.3.

The actual expression of the coefficients α and β can be easily found from Eqs. 4.35 which represent two linear systems to be solved.

Exact solvers

In the previous section a constant matrix A was considered to simplify the mathematical setting. Euler equations, instead, are strongly non-linear and the formulation becomes more complex. In other words, mathematically, the equations should be written as :

$$\mathbf{U}_t + A(\mathbf{U})\mathbf{U}_x = \mathbf{0}. \tag{4.40}$$

Moreover, in the previous case, everything was defined *a-priori*, meaning that the two waves were somehow intrinsically defined in the constant matrix A. In reality, the fully non-linear Riemann problem can lead to many different configurations. In the 1D case, three characteristics are present in the system and each of them can be a shock, a rarefaction wave or a contact discontinuity (so 10 alternative).

The basic idea of exact Riemann solvers relies on exact iterative methods, designed to find the intermediate state $(\rho^*, u^*, p^*)^T$, guessing a first general structure of the waves. Algebraic equations can be defined for shocks, expansions and contact discontinuities and the problem can ultimately be reduced to a systems of non-linear algebraic equations. This approach imposes the use of a Newton-type algorithm to solve them numerically.

Nevertheless, for the purposes of the present work, most of the attention will be focused on approximate solvers.

Godunov's Method

Godunov's method is one of the most famous numerical discretisation of non-linear systems. In order to deal with discontinuous solutions, an integral form of the equations is considered. The general conservation law

$$\mathbf{U}_t + \mathbf{F}(\mathbf{U})_x = \mathbf{0}, \tag{4.41}$$

can be integrated both in time and space, leading to the following expression:

$$\int_{x_1}^{x_2} \mathbf{U}(x, t_2)dx = \int_{x_1}^{x_2} \mathbf{U}(x, t_1)dx + \int_{t_1}^{t_2} (\mathbf{F}(\mathbf{U}(x_1, t)) - \mathbf{F}(\mathbf{U}(x_2, t)))dt. \tag{4.42}$$

The canonical paradigm considers then an element-wise constant solution as schematically shown in Fig. 4.4. After element-averaging, the Godunov method can be written as:

$$U_i^{n+1} = U_i^n + \frac{\Delta t}{\Delta x}[\mathbf{F}_{i-1/2} - \mathbf{F}_{i+1/2}], \tag{4.43}$$

with $\mathbf{F}_{i\pm1/2} = \mathbf{F}(\mathbf{U}_{i\pm1/2})$ and $\Delta t \leq \frac{\Delta x}{S_{max}^n}$ with S_{max}^n the maximum wave velocity in the whole domain.

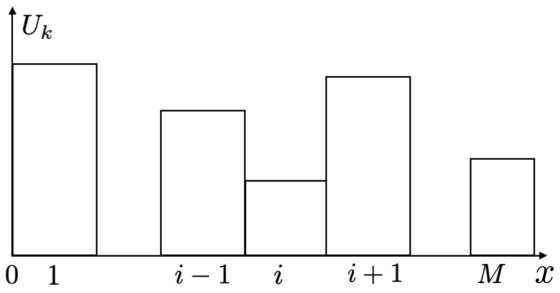

Figure 4.4: Graphical visualisation of Godunov's method.

A priori, the solution at interface is unknown, the only available informations are located at the cell center. Moreover, the solution is expected to be in the self-similar form $\mathbf{U}_{i+1/2}(x/t)$. Consequently, the evaluation of the Riemann problem $\mathrm{RP}(U_i^n, U_{i+1}^n)$ solution at $x/t = 0$ is needed to advance in time.

As already stated, it is possible to solve analytically the Riemann problem but most of the times this strategy can be very time-consuming and computationally inefficient. In fact, the errors associated to the spatial or temporal discretisation can be much larger than the errors arising from approximate Riemann solvers.

Approximate Riemann solvers

As previously state, the goal is to solve numerically the general initial boundary value problem:

$$\mathbf{U}_t + \mathbf{F}(\mathbf{U})_x = \mathbf{0}, \tag{4.44}$$

with initial data $\mathbf{U}(x,0) = \mathbf{U}^{(0)}(x)$, using the explicit conservative formula

$$\mathbf{U}_i^{n+1} = \mathbf{U}_i^n + \frac{\Delta t}{\Delta x}(\mathbf{F}_{i-1/2} - \mathbf{F}_{i+1/2}), \tag{4.45}$$

along with the Godunov intercell numerical flux

$$\mathbf{F}_{i\pm1/2} = \mathbf{F}(\mathbf{U}_{i\pm1/2}). \tag{4.46}$$

Considering now the equation

$$\mathbf{U}_t + A\mathbf{U}_x = \mathbf{0}, \tag{4.47}$$

the problem can be approximated imposing that $A \approx \tilde{A} = \tilde{A}(\mathbf{U}_L, \mathbf{U}_R)$. Once the matrix A is considered locally constant, the problem can be easily solved using the ideas presented in the first section for hyperbolic systems of equations with constant coefficients.

The choice of $\tilde{A}$ is only partially arbitrary. In fact, $\tilde{A}$ needs to fulfil some specific constraints associated to the equations.

It can be proven that for a general hyperbolic system, numerically resolved using Godunov method, the intercell fluxes can be generally defined as:

$$\mathbf{F}_{i+1/2} = \frac{1}{2}(\mathbf{F}_L + \mathbf{F}_R) - \frac{1}{2}\sum \tilde{\gamma}_i |\tilde{\lambda}_i| \tilde{\mathbf{L}}^{(i)}. \tag{4.48}$$

for some coefficients $\tilde{\gamma}_i$.

The different approximate Riemann solvers will differ from each other according to the specific definition of $\tilde{A}$. Once the approximated Jacobian is defined, the coefficients $\tilde{\gamma}_i$, eigenvalues $\tilde{\lambda}_i$ and eigenvectors $\tilde{L}^{(i)}$ can be evaluated and used to compute the interface flux $\mathbf{F}_{i+1/2}$ according to 4.48.

The coefficient $\tilde{\gamma}$'s are defined through the eigenvectors expansion of the primitive variables's jumps:

$$\Delta \mathbf{U} = \sum \tilde{\gamma}_i \tilde{\mathbf{L}}^{(i)}. \tag{4.49}$$

Explicit calculations for the original Roe's flux are reported in the Appendix C. Furthermore, the application of Roe's flux to the three-dimensional Euler equations is outlined in the Appendix D.

4.4.2 Viscous fluxes

In order to introduce the numerical discretisation of viscous numerical fluxes in Navier-Stokes equations, the general one-dimensional scalar conservation law will be used as guideline. How to generalise to three-dimensional systems of conservation laws has been already outlines in previous sections. The difference with respect to the previous formulations relies on the flux explicit dependence on the first derivatives of the solution. Namely,

$$\frac{\partial u}{\partial t} - \frac{\partial}{\partial x}\left(f\left(u, \frac{\partial u}{\partial x}\right)\right) = 0, \tag{4.50}$$

It can be useful to rewrite equation 4.50 as a system of first order equations as:

$$\begin{cases} \frac{\partial u}{\partial t} - \frac{\partial f(u,q)}{\partial x} = 0 \\ q - \frac{\partial u}{\partial x} = 0 \end{cases} \tag{4.51}$$

where q is commonly called auxiliary variable. Consequently, the first equation is referred to as the principal equation and the second as the auxiliary equation.

The classical procedure to compute viscous numerical fluxes starts with the resolution of the auxiliary equation in q which simply coincides with the first derivative of the conserved variable u. The first step is essentially an interpolation problem and it can be seen as the first full step of SD resolution

of a conservation law: the solution is extended to the edges of the element, is *corrected* using the interface fluxes and finally re-interpolated and derived on the solution points providing the derivative of u at each solution point. At this stage then, q and u are directly available on the solution points. This first step depends on the specific numerical flux for u used at interfaces. The common flux can be written in the generic form as:

$$\hat{u} = \frac{u_R + u_L}{2} + \beta \frac{u_R - u_L}{2}. \tag{4.52}$$

After the auxiliary equation is solved, both q and u are known. Consequently the flux function can be easily evaluated at the solution points. At this point, the procedure coincides with the standard SD strategy: the flux is interpolated at the edges, corrected and finally re-interpolated and differentiated on the solution points. In a similar way with respect to the first step, the only needed information relies on the interface flux, which will depend on left and right state of not only u but also q.

The interface value of u has been already defined in equation 4.52 but no definition has been given to the common value of q at the interface. The different choices on the interface value of q will lead to different well-known schemes used in the spectral element methods framework. Namely, in the case of Local Discontinuous Galerkin (LDG) [51],

$$\hat{q} = \frac{q_R + q_L}{2} - \beta \frac{q_R - q_L}{2} + \tau \frac{u_R - u_L}{2}, \tag{4.53}$$

where a penalty term proportional to the parameter τ can be added to control the jump at the interface. A similar definition is used in the internal penalty approach [52] where $\beta = 0$, giving

$$\hat{u} = \frac{u_R + u_L}{2} \quad \text{and} \quad \hat{q} = \frac{q_R + q_L}{2} + \tau \frac{u_R - u_L}{2}. \tag{4.54}$$

An even easier choice is to simply consider centered fluxes [60] of the form:

$$\hat{u} = \frac{u_R + u_L}{2} \quad \text{and} \quad \hat{q} = \frac{q_R + q_L}{2}. \tag{4.55}$$

It is then interesting to notice that the construction of the numerical viscous flux is based on two choices: the definition of an interface state for both u and q. Despite the similarities, the computation of the conserved variables at the interface and the definition of a common state is completely decoupled with respect to the inviscid flux computation. In other words, the definition of inviscid and viscous fluxes are independent one another.

4.5 Boundary conditions

A fundamental ingredient in any discretisation of compressible Navier-Stokes equations is represented by the implementation of appropriate boundary conditions. As commonly established in the research field, different approaches

can be followed in the imposition of boundary conditions in compressible flows. Each of such techniques can significantly influence the overall stability and accuracy of the numerical simulation. A deep discussion on the specific consequences of each approach is far beyond the purpose of the present work. The following considerations are meant to delineate a general guideline on the efficient implementation of boundary conditions in the SD high-order framework (see also [61] for an extensive summary).

As discussed in the previous sections, in the SD scheme, the solution is extrapolated from the solution points to the flux points which include the element's edge. The flux at the element's extrema is then *corrected* using a common interface flux. Within the general introduction of the numerical scheme, the computation of the interface flux was specified to be a function of the left and right states only, representing the combined information coming from the two elements sharing a common face. Of course, such scenario is not possible at the boundary elements, where boundary faces belong to only one element. A proper definition of the numerical flux at boundary faces is consequently needed. Two different approaches can be followed in this case. The interface flux can be defined either introducing a convenient *ghost state* and compute the interface flux as result of the Riemann solver applied to the interior and exterior (or ghost) states. Such approach is commonly denoted as *Weak-Riemann*. Alternatively, the common interface flux can be directly prescribed knowing the exact, expected values of the solution at the boundary. This latter approach is instead known as *Weak-Prescribed*. In the present work, both approaches will be discussed. A visual sketch of the Weak-Riemann approach using a ghost state is represented in Fig. 4.5. The definition of the ghost state will clearly depend on the specific type of

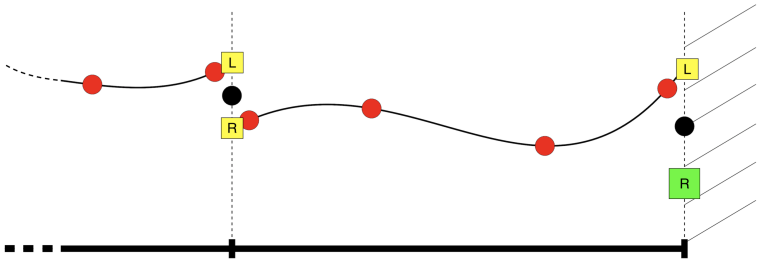

Figure 4.5: Visualisation of the *Weak-Riemann* approach applied to a right boundary edge. The green square represents the right (ghost) state which is chosen according to the specific boundary condition.

boundary condition. In the following subsections the most common choices of boundary conditions will be presented and an appropriate ghost state will be introduced for each of them. Without any loss of generality, in agreement with Fig. 4.5, the left state represents the interior of the domain and the

ghost state coincides with the right state. More precisely, if $\mathbf{F}^I$ denotes the flux at the interface, Weak-Riemann, and Weak-Prescribed can be written as

$$\begin{aligned} \text{Weak} - \text{Riemann}: &\quad \mathbf{F}^I = \text{RI}(\mathbf{U}_L, \mathbf{U}_R) \\ \text{Weak} - \text{Prescribed}: &\quad \mathbf{F}^I = \mathbf{F}^I(\mathbf{U}_{BC}) \end{aligned} \tag{4.56}$$

where $\text{RI}(\cdot,\cdot)$ represent a standard approximate/exact Riemann solver and $\mathbf{U}_{BC}$ the exact values of the conserved variables at the boundaries. In a similar way, for the diffusive fluxes, the following notation can be used:

$$\begin{aligned} \text{Weak} - \text{Riemann}: &\quad \mathbf{D}^I = \text{VF}(\mathbf{U}_L, \mathbf{U}_R, \nabla\mathbf{U}_L, \nabla\mathbf{U}_R) \\ \text{Weak} - \text{Prescribed}: &\quad \mathbf{D}^I = \mathbf{D}^I(\mathbf{U}_{BC}, \nabla\mathbf{U}_{BC}) \end{aligned} \tag{4.57}$$

where VF defines the full strategy already presented in previous chapters to compute viscous fluxes at the edges using left/right states and respective gradients.

4.5.1 Far field

The far-field boundary condition represent one of the most basic condition which is imposed in the numerical resolution of Euler equations. Consequently, in the case of the compressible Navier-Stokes equations, such conditions are imposed in regions of the flow where viscous effects are negligible. Normally, due to natural hyperbolic nature of Euler equations, a characteristic-based imposition of boundary conditions is needed. In this sense, the concept of Riemann invariant needs to be properly introduced. In a three-dimensional setup, considering a specific direction $\mathbf{n}$, the characteristic variables take the form:

$$\mathbf{W} = L^{-1}\mathbf{U} = \begin{pmatrix} \frac{p}{2a^2} - \frac{\rho u_n}{2a} \\ n_1\left(\rho - \frac{p}{a^2}\right) + \frac{\rho w_1}{a} \\ n_2\left(\rho - \frac{p}{a^2}\right) + \frac{\rho w_2}{a} \\ n_3\left(\rho - \frac{p}{a^2}\right) + \frac{\rho w_3}{a} \\ \frac{p}{2a^2} + \frac{\rho u_n}{2a} \end{pmatrix}. \tag{4.58}$$

where $u_n = \mathbf{u}\cdot\mathbf{n}$ and $\mathbf{w} = \mathbf{u}\times\mathbf{n}$ (for additional details, see Sec. D).
The case of an upper boundary is considered as a representative example. In fact, the far-field boundary condition is often applied to the top edge in boundary layer simulations. In other words, the case $\mathbf{n} = (0,1,0)^T$ is considered. In this conditions the characteristic variables reduce to:

$$\mathbf{W} = L^{-1}\mathbf{U} = \begin{pmatrix} \frac{p}{2a^2} - \frac{\rho u_2}{2a} \\ \frac{\rho w_1}{a} \\ \left(\rho - \frac{p}{a^2}\right) \\ \frac{\rho w_3}{a} \\ \frac{p}{2a^2} + \frac{\rho u_2}{2a} \end{pmatrix}. \tag{4.59}$$

Furthermore, using the isentropic assumption $p/\rho^{\gamma} = const$ it is possible to write

$$W_1 = u_2 + \frac{2a}{\gamma - 1} \quad \text{and} \quad W_5 = u_2 - \frac{2a}{\gamma - 1}, \tag{4.60}$$

which are commonly known as Riemann invariants associated to the incoming and outgoing acoustic waves. Based on the previous analysis, it is possible to consider all the possible combinations of supersonic/subsonic inflow/outflow and use the knowledge on the characteristic waves to compute explicitly the appropriate flux at the boundary. Namely, the correct values at the boundary will be written as

$$\mathbf{U}_{BC} = \begin{pmatrix} \rho_b \\ (\rho u_1)_b \\ (\rho u_2)_b \\ (\rho u_3)_b \\ E_b \end{pmatrix} \tag{4.61}$$

using appropriate values $(\cdot)_b$. The boundary flux can then be directly evaluated using a *Weak-Prescribed* approach. On the other hand, if a *Weak-Riemann* approach is preferred, a suitable ghost state can be defined as:

$$\mathbf{U}_{R} = \begin{pmatrix} \rho_\infty \\ (\rho u_1)_\infty \\ (\rho u_2)_\infty \\ (\rho u_3)_\infty \\ E_\infty \end{pmatrix}. \tag{4.62}$$

It can be proven, in fact, that any Riemann solver based on a characteristic decomposition (such as Roe, HLL or HLLC fluxes) automatically takes into account the sign of the normal velocity and the local Mach number.

4.5.2 Inflow/outflow

In regions of the flow where viscous effects are not negligible, different conditions with respect to the classical far-field boundary conditions need to be properly enforced. In particular, depending on the supersonic/subsonic regime and on the sign of the normal velocity, different combinations of imposed $(\cdot)_{BC}$ and extrapolated $(\cdot)_L$ values of the variables will be considered.

In particular, the following choices of ghost states are normally considered:

$$\text{Subsonic inflow} \quad : \quad \mathbf{U}_R = \begin{pmatrix} \rho_{BC} \\ (\rho u_1)_{BC} \\ (\rho u_2)_{BC} \\ (\rho u_3)_{BC} \\ E(p_L, \rho_{BC}, \mathbf{u}_{BC}) \end{pmatrix},$$

$$\text{Supersonic inflow} \quad : \quad \mathbf{U}_R = \begin{pmatrix} \rho_{BC} \\ (\rho u_1)_{BC} \\ (\rho u_2)_{BC} \\ (\rho u_3)_{BC} \\ E(p_{BC}, \rho_{BC}, \mathbf{u}_{BC}) \end{pmatrix},$$

$$\text{Subsonic outflow} \quad : \quad \mathbf{U}_R = \begin{pmatrix} \rho_L \\ (\rho u_1)_L \\ (\rho u_2)_L \\ (\rho u_3)_L \\ E(p_{BC}, \rho_L, \mathbf{u}_L) \end{pmatrix},$$

$$\text{Supersonic outflow} \quad : \quad \mathbf{U}_R = \begin{pmatrix} \rho_L \\ (\rho u_1)_L \\ (\rho u_2)_L \\ (\rho u_3)_L \\ E(p_L, \rho_L, \mathbf{u}_L) \end{pmatrix}.$$

Finally, since viscous effects are not negligible, also proper boundary viscous fluxes need to be defined. Recalling how viscous fluxes are evaluated in the Spectral Difference scheme, the first step consists in evaluating a common interface flux for the conserved variables. In the case of inflow/outflow boundary conditions, it is often imposed to have an intermediate auxiliary state

$$\mathbf{U}_{BC}^{aux} = \begin{pmatrix} \rho_L \\ (\rho u_1)_L \\ (\rho u_2)_L \\ (\rho u_3)_L \\ E(p_L, \rho_L, \mathbf{u}_L) \end{pmatrix}, \tag{4.63}$$

which is merely used to compute the gradients within the boundary element and evaluate the boundary viscous fluxes as $\mathbf{D}^I = \mathbf{D}^I(\mathbf{U}_{BC}^{aux}, (\nabla \mathbf{U})_L)$. Notice that only the gradients on the left state are considered, since at the boundary gradients are, in general, unknown.

4.5.3 Isothermal/Adiabatic no-slip wall

In addition to far-field and inflow/outflow boundary conditions, in the numerical discretisation of compressible Navier-Stokes equations, proper imposition of wall boundary conditions is needed. Among these, in the large majority of numerical simulations of engineering interest, isothermal and adiabatic no-slip wall conditions are the most commonly employed. In agreement with the previous subsection, proper inviscid and viscous numerical fluxes need to be defined at the wall using either Weak-Prescribed or Weak-Riemann approach.

In the computation of the inviscid fluxes, the following ghost state is used to imposed zero velocity at the wall:

$$\mathbf{U}_R = \begin{pmatrix} \rho_L \\ -(\rho u_1)_L \\ -(\rho u_2)_L \\ -(\rho u_3)_L \\ E_L \end{pmatrix}. \tag{4.64}$$

Imposing as ghost state the interior velocity with opposite sign clearly resembles the classical strategy commonly used in finite differences discretisations. The common interface inviscid flux is subsequently computed using a *Weak-Riemann* approach. The same ghost state is used for both isothermal and adiabatic conditions, which will differ in the treatment of the viscous numerical flux.

For the computation of the viscous fluxes, a first auxiliary inviscid step is needed and an interface inviscid flux is imposed. At this point, the procedure differs depending on whether isothermal or adiabatic condition is imposed. In particular, for the isothermal case the ghost state reads

$$\mathbf{U}_{BC}^{aux} = \begin{pmatrix} \rho_{BC} = \rho(p_L, T_{BC}) \\ 0 \\ 0 \\ 0 \\ E(p_L, \rho_{BC}, \mathbf{0}) \end{pmatrix}. \tag{4.65}$$

The prescribed wall temperature and the extrapolated pressure are used to evaluate the value of density at the wall. Subsequently, these values, combined with null velocity, are used to compute the total energy at the wall boundary.

Afterwards, similarly to the previous subsection, the viscous boundary flux is computed as $\mathbf{D}^I = \mathbf{D}^I(\mathbf{U}_{BC}^{aux}, (\nabla \mathbf{U})_L)$. Namely, only the extrapolated gradients from the inner part of the element (left state) are used for the computation of the viscous flux.

In the case of adiabatic wall, instead, the auxiliary intermediate state will read

$$\mathbf{U}_{BC}^{aux} = \begin{pmatrix} \rho_L \\ 0 \\ 0 \\ 0 \\ E(p_L, \rho_L, \mathbf{0}) \end{pmatrix}. \tag{4.66}$$

In this case, density and pressure are extrapolated and combined with null velocities to compute the right ghost state. Differently with respect to the previous case, instead of imposing a prescribed temperature at the wall, null values of temperature gradients are enforced. Consequently, the imposition of adiabatic boundary condition appears explicitly in the computation of the viscous numerical fluxes.

After imposing the auxiliary state $\mathbf{U}_{BC}^{aux}$, all the gradients are directly available at the solution points and, from direct extrapolation, on the wall boundary too. Similarly to the previous point, viscous fluxes are imposed using a *Weak-Prescribed* approach:

$$\mathbf{D}^I = \mathbf{D}^I(\mathbf{U}_{BC}, (\nabla \mathbf{U})^*), \tag{4.67}$$

where in the computation of $(\nabla \mathbf{U})^*$ all the gradients of the left state are used except the normal component of the heat flux, which is imposed to be zero:

$$(\kappa \nabla T \cdot \mathbf{n})_{BC} = 0. \tag{4.68}$$

4.6 Time-integration

In previous sections, a detailed strategy to approximate spatial derivatives using the high-order Spectral Difference scheme has been presented. In a more general sense, in the one-dimensional formulation, a specific approach to evaluate the term flux divergence $\frac{\partial f(\hat{\mathbf{u}})}{\partial \hat{x}}$ at the solution points has been introduced. The semi-discrete form of the SD discretisation of a general one-dimensional conservation law within the element n will take the following form:

$$\frac{\mathrm{d}\hat{\mathbf{u}}_n}{\mathrm{dt}} = -\frac{\partial \hat{f}_n(\hat{\mathbf{u}}_n)}{\partial \hat{x}} = \mathcal{L}(\hat{\mathbf{u}}_n), \tag{4.69}$$

where $\hat{\mathbf{u}}_n$ and $\hat{f}_n$ respectively represent the discrete representation of conserved variables and fluxes. Since the relationship $\hat{f}_n = \hat{f}_n(\hat{\mathbf{u}}_n)$ is often non-linear, explicit time-integration schemes have an immediate and straightforward implementation, whereas implicit time-integration is more complex. In the present work, only explicit time-integration schemes will be employed.

For the sake of simplicity, if a standard explicit Euler scheme is employed, the fully-discrete scheme will read:

$$\hat{\mathbf{u}}_n(t+\Delta t) = \hat{\mathbf{u}}_n(t) + \Delta t \mathcal{L}(\hat{\mathbf{u}}_n(t)) \tag{4.70}$$

Of course, more complex explicit time integration schemes can be considered. In particular, in many of the simulations considered in the following sections explicit Runge-Kutta (RK) schemes have been used.

For example, assuming the flux have no explicit dependence on time, the standard fourth-order four stage explicit RK method can be written as:

$$\begin{aligned}
\hat{\mathbf{u}}_1^\star &= \mathcal{L}(\hat{\mathbf{u}}_n(t)) \\
\hat{\mathbf{u}}_2^\star &= \mathcal{L}\left(\hat{\mathbf{u}}_n(t) + \frac{1}{2}\Delta t \hat{\mathbf{u}}_1^\star\right) \\
\hat{\mathbf{u}}_3^\star &= \mathcal{L}\left(\hat{\mathbf{u}}_n(t) + \frac{1}{2}\Delta t \hat{\mathbf{u}}_2^\star\right) \\
\hat{\mathbf{u}}_4^\star &= \mathcal{L}\left(\hat{\mathbf{u}}_n(t) + \Delta t \hat{\mathbf{u}}_3^\star\right) \\
\hat{\mathbf{u}}_n(t+\Delta t) &= \hat{\mathbf{u}}_n(t) + \frac{1}{6}\Delta t\left(\hat{\mathbf{u}}_1^\star + 2\hat{\mathbf{u}}_2^\star + 2\hat{\mathbf{u}}_3^\star + \hat{\mathbf{u}}_4^\star\right).
\end{aligned} \tag{4.71}$$

Once a strategy to compute the residual $\mathcal{L}(\cdot)$ is given, any RK scheme can be used to advance the solution over times.

As well known, explicit time-integration is limited by Courant-Friedrichs-Lewy (CFL) and Fourier (FOU) conditions which are respectively associate to the spatial discretisation of inviscid and viscous fluxes. In particular, the CFL and FOU time steps for the compressible Navier-Stokes equations are defined as:

$$\Delta t_{CFL} = \alpha_{CFL}\frac{h_s}{a} \quad \text{and} \quad \Delta t_{FOU} = \alpha_{FOU}\frac{h_f^2}{2D\mu/\rho} \tag{4.72}$$

where h_s and h_f quantify the spatial resolution of convective and diffusive fluxes, $a = \sqrt{u_k u_k} + \sqrt{\gamma p/\rho}$ is the spectral radius of the convective flux jacobian, and D is the dimension of the problem. More specifically, in the high-order, three-dimensional framework that will be often considered in the following sections, a measure of the local spatial resolution can be defined as:

$$h_s = \det(J)\cdot\xi_s \quad \text{and} \quad h_f = \det(J)\cdot\xi_f \tag{4.73}$$

where ξ_s and ξ_f represent the smallest distance of solution and flux points in the reference element.

The coefficients α_{CFL} and α_{FOU} set the maximum allowed time-step for each specific time-integration scheme. Once the two time steps are evaluated,

and the minimum value in the whole domain is computed, the prescribed time-step is selected as:

$$\Delta t_{max} = \frac{1}{\Delta t_{CFL}^{-1} + \Delta t_{FOU}^{-1}}. \tag{4.74}$$

Chapter 5

Spectral analysis for high-order methods

Contents

5.1 Introduction

The constant increase of computing power made computational fluid dynamics a widely-used virtual prototyping tool [42]. Well established CFD software are now robust, but they usually lack in accuracy for many delicate situations of high interest in engineering and applied sciences. Along these lines, innovative numerical high-order schemes gained a lot of interest

in the last few decades, appearing as the building core of the next CFD generation [43].

The theoretical analysis of such schemes is then of fundamental interest to understand the interaction between the numerics and the simulated flow physics, an interaction of paramount importance in the case of turbulent flows. A high-order discretisation of convective dominated flows is usually associated to two main numerical phenomena, respectively known as numerical diffusion (or dissipation) and dispersion. The former, as suggested by the name itself, consists in the introduction of numerical dissipation, usually at the smallest resolved scales, while the latter in the phase-shifting of propagating waves in the computational domain. Much interest has been focused on the numerical dissipation and multiple studies tried to use it as a built-in turbulence model for specific choices of numerical fluxes [62, 63, 64, 65, 66]. This approach is commonly known as Implicit Large Eddy Simulation (ILES). Despite the advantages in terms of computational efficiency and simplicity of implementation, it is not completely straightforward to match the level of numerical dissipation according to turbulence theory. This is particularly true for certain classes of high-order methods, such as the spectral element methods [67], for which the order of accuracy is a user-selectable parameter of the computation. In this challenging context, additional information on the response of the numerical discretisation becomes useful.

The present work is based on three main approaches to address accuracy and robustness of a numerical scheme: (a) temporal eigenanalysis, (b) spatial eigenanalysis and (c) non-modal analysis.

The first, temporal eigenanalysis, is the most popular technique to study the characteristic properties of a numerical discretisation and it has been employed to study a large variety of high-order methods [68, 69, 70, 71, 72, 73] varying from Compact Difference schemes to, more recently, spectral element methods, such as Discontinuous Galerkin (DG) [74, 75, 76], Flux Reconstruction [77, 78] and Spectral Difference [44, 45, 46] schemes.

The second approach, namely the spatial eigenanalysis, is less popular [79, 80, 81, 82] and represents a complementary analysis with respect to the classical approach of temporal eigenanalysis. In particular, the temporal eigenanalysis is used to characterise the temporal evolution of spatial oscillations, whereas the spatial eigenanalysis studies the spatial evolution of temporal perturbations. It is quite intuitive that both aspects are particularly important in under-resolved turbulent flows.

Finally, non-modal analysis has been considered as an ulterior approach based on hydrodynamic instability theory [83, 84, 85]. It constitutes an alternative strategy to study the diffusive behaviour of a numerical scheme without explicitly focussing on the spectral properties of the discretised equations. The short-term dynamics of the element-wise dynamical system is then examined, in a more intuitive and straightforward manner.

All the above mentioned techniques have been generalised to the non-

constant one-dimensional conservation law following the guideline presented in [86, 87] for the non-homogeneous linear advection equation.

The chapter is organised as follows: temporal, spatial and non-modal analyses are presented for the linear advection equation and later generalised to the standard one-dimensional conservation law. In this latter case, all the up-quoted techniques have been applied to a set of different advection velocities. Finally, theoretical findings are verified through a series of one-, two-, and three-dimensional simulations.

The first part of the chapter includes a detailed description of each technique, aimed to provide a sufficiently general introduction, even for readers who are not familiar with spectral analyses for high-order schemes.

It is worthwhile noting that the major focus of the present study is about the FR and SD discretisations, whose properties and formalism are summarised in Appendix A and chapter 4. Concerning the FR methodology, which can recover different types of schemes for linear advection (*cf.*Appendix B), recovered schemes through the FR formalism will be indicated hereafter by appending the label "-FR" to the relevant acronym (*e.g.*, SD-FR will refer to the FR scheme using the SD recovering correction functions). The theoretical framework and numerical results presented in this chapter have been published in "Journal of Scientific Computing" [15] (https://doi.org/10.1007/s10915-021-01484-1).

5.2 Standard temporal eigenanalysis

The temporal eigenanalysis is here presented for the FR method . The same procedure applied to the SD scheme would be almost identical.

In the standard temporal analysis, the linear advection equation is discretised looking for wave-like solutions in order to reduce the infinite dimensional problem to a simple element-wise local description. Then, dispersion and dissipation properties of any scheme follow directly from the corresponding eigensolutions.

Let us now suppose the case of a constant unitary advection velocity:

$$\frac{\partial u}{\partial t} + \frac{\partial u}{\partial x} = 0. \tag{5.1}$$

This equation admits plane wave solutions of the form

$$u = e^{\iota(\theta x - \omega t)}, \quad \text{with } \iota = \sqrt{-1}, \tag{5.2}$$

provided that the temporal frequency $\omega = \omega(\theta)$ is such that

$$\mathrm{Re}(\omega) = \theta \qquad \text{and} \qquad \mathrm{Im}(\omega) = 0, \tag{5.3}$$

where θ is a real prescribed wave number. Equation 5.3 provides what are respectively known as dispersion and diffusion relations for the exact plane

wave solution. Consider now a FR discretisation such that all elements Ω_h of the domain Ω have a fixed width $h_n = h = 1$. Under such assumptions, a FR semi-discretisation of Eq. (5.1) within the standard element Ω_n can be written as

$$\frac{\mathrm{d}\hat{u}_n}{\mathrm{dt}} = -2\sum_{j=0}^{N} \hat{u}_n \frac{\mathrm{d}l_j}{\mathrm{d}\hat{x}}(\hat{x}_i) - (2\hat{f}_L^I - 2\hat{u}_L)\frac{\mathrm{d}g_L}{\mathrm{d}\hat{x}}(\hat{x}_i) - (2\hat{f}_R^I - 2\hat{u}_R)\frac{\mathrm{d}g_R}{\mathrm{d}\hat{x}}(\hat{x}_i), \quad (5.4)$$

where $\hat{u}_L = \hat{u}_n(-1,t)$ and $\hat{u}_R = \hat{u}_n(+1,t)$.

To examine a sufficiently general framework, the following classes of numerical fluxes are now considered:

$$\hat{f}_L^I = (1-\alpha)\hat{u}_{n-1}(+1,t) + \alpha\hat{u}_n(-1,t) \quad (5.5)$$

and

$$\hat{f}_R^I = (1-\alpha)\hat{u}_n(+1,t) + \alpha\hat{u}_{n+1}(-1,t). \quad (5.6)$$

Notice that, for $\alpha = 0$, a full-upwind scheme is recovered whereas, for $\alpha = 0.5$, a centered flux is obtained. Strongly negative values of α (~ -50), instead, denote *hyper-upwind* numerical fluxes. The α parameter can be used to mimic different levels of interface upwinding that result from the use of different formulations of the actual numerical flux. Equation 5.4 can be rewritten, in matrix form, as:

$$\frac{\mathrm{d}\hat{\mathbf{u}}^n}{\mathrm{dt}} = -2\mathbf{D}\hat{\mathbf{u}}^n - (2\hat{f}_L^I - 2\mathbf{l}^T\hat{\mathbf{u}}^n)\mathbf{g}_L - (2\hat{f}_R^I - 2\mathbf{r}^T\hat{\mathbf{u}}^n)\mathbf{g}_R, \quad (5.7)$$

where $\hat{\mathbf{u}}_i^n = \hat{u}(\hat{x}_i)$, $\mathbf{D}_{ij} = \frac{\mathrm{d}l_j}{\mathrm{d}\hat{x}}(\hat{x}_i)$, $\mathbf{g}_i^{L/R} = \frac{\mathrm{d}g_{L/R}}{\mathrm{d}\hat{x}}(\hat{x}_i)$ and $\mathbf{r}_i = l_i(1)$, $\mathbf{l}_i = l_i(-1)$.

Within the set of approximate solutions in the form of Eq. (5.2), Bloch wave-like functions are considered, namely:

$$\hat{\mathbf{u}}^n = e^{\iota(\tilde{\theta}x_n/h - \tilde{\omega}t)}\hat{\mathbf{v}}, \quad (5.8)$$

where tilde accent denotes the numerical counterparts of continuum variables and x_n indicates the left boundary of the element n in the global reference frame. Once $\hat{\mathbf{u}}^n$ is defined in this way, due to periodicity, it is straightforward to obtain a closed form for all the fluxes expressed in Eq. (5.4). In fact,

$$\hat{\mathbf{u}}^{n-1} = e^{\iota(\tilde{\theta}x_{n-1}/h - \tilde{\omega}t)}\hat{\mathbf{v}} = e^{\iota(\tilde{\theta}(x_n-h)/h - \tilde{\omega}t)}\hat{\mathbf{v}} = e^{-\iota\tilde{\theta}}\hat{\mathbf{u}}^n \quad (5.9)$$

and

$$\hat{\mathbf{u}}^{n+1} = e^{\iota(\tilde{\theta}x_{n+1}/h - \tilde{\omega}t)}\hat{\mathbf{v}} = e^{\iota(\tilde{\theta}(x_n+h)/h - \tilde{\omega}t)}\hat{\mathbf{v}} = e^{\iota\tilde{\theta}}\hat{\mathbf{u}}^n, \quad (5.10)$$

which leads to an explicit expression for the fluxes in vector form as:

$$\begin{aligned} \hat{f}_L^I &= (1-\alpha)e^{-\iota\tilde{\theta}} \quad \mathbf{r}^T\hat{\mathbf{u}}^n + \alpha\mathbf{l}^T \qquad \hat{\mathbf{u}}^n, \\ \hat{f}_R^I &= (1-\alpha) \qquad\quad \mathbf{r}^T\hat{\mathbf{u}}^n + \alpha\mathbf{l}^T e^{\iota\tilde{\theta}} \quad \hat{\mathbf{u}}^n. \end{aligned} \quad (5.11)$$

It is also easy to notice that $\mathrm{d}\hat{\mathbf{u}}^n/\mathrm{dt} = -\iota\tilde{\omega}\hat{\mathbf{u}}^n$.

Finally, it can be seen that, due to solution periodicity, the infinite dimensional problem has now been reduced to a simpler element-wise formulation, *i.e.*, numerical fluxes now depend only on the local solution $\hat{\mathbf{u}}^n$. Hence the apex n can be dropped and the final discretised equation can be written as

$$\begin{aligned} -\frac{\iota}{2}\tilde{\omega}\hat{\mathbf{u}} = \mathbf{D}\hat{\mathbf{u}} &- ((1-\alpha)e^{-\iota\tilde{\theta}}\mathbf{r}^T\hat{\mathbf{u}} + \alpha\mathbf{l}^T\hat{\mathbf{u}} - \mathbf{l}^T\hat{\mathbf{u}})\mathbf{g}_L \\ &- ((1-\alpha)\mathbf{r}^T\hat{\mathbf{u}} + \alpha\mathbf{l}^T e^{\iota\tilde{\theta}}\hat{\mathbf{u}} - \mathbf{r}^T\hat{\mathbf{u}})\mathbf{g}_R, \end{aligned} \tag{5.12}$$

or, in a more compact way:

$$\tilde{\omega}\hat{\mathbf{u}} = -2\iota(\mathbf{C}^- e^{-\iota\tilde{\theta}} + \mathbf{C}^0 + \mathbf{C}^+ e^{\iota\tilde{\theta}})\hat{\mathbf{u}}, \tag{5.13}$$

where $\mathbf{C}^0 = \mathbf{D} - (\alpha-1)\mathbf{g}_L\mathbf{l}^T - \alpha\mathbf{g}_R\mathbf{r}^T$, $\mathbf{C}^- = (1-\alpha)\mathbf{g}_L\mathbf{r}^T$ and $\mathbf{C}^+ = \alpha\mathbf{g}_R\mathbf{l}^T$.

Following the same steps presented above, the following expression can be obtained for the SD scheme:

$$\tilde{\omega}\hat{\mathbf{u}} = -2\iota\mathbf{D}(\mathbf{M}^- e^{-\iota\tilde{\theta}} + \mathbf{M}^0 + \mathbf{M}^+ e^{\iota\tilde{\theta}})\hat{\mathbf{u}}, \tag{5.14}$$

with

$$\mathbf{M}^-_{ij} = \begin{cases} (1-\alpha)l^s_j(1) & \text{for} \quad i = 0 \\ 0 & \text{for} \quad i \neq 0 \end{cases}, \qquad \mathbf{M}^+_{ij} = \begin{cases} 0 & \text{for} \quad i \neq N+1 \\ \alpha l^s_j(-1) & \text{for} \quad i = N+1 \end{cases} \tag{5.15}$$

and

$$\mathbf{M}^0_{ij} = \begin{cases} \alpha l^s_j(-1) & \text{for} \quad i = 0, \\ (1-\alpha)l^s_j(1) & \text{for} \quad i = N+1, \\ l^s_j(\hat{x}^f_i) & \text{otherwise.} \end{cases} \tag{5.16}$$

Notice that, by setting $\mathbf{N}^{0,+,-} = \mathbf{D}\mathbf{M}^{0,+,-}$, a mathematical form similar to Eq. (5.13) can be easily recovered:

$$\tilde{\omega}\hat{\mathbf{u}} = -2\iota(\mathbf{N}^- e^{-\iota\tilde{\theta}} + \mathbf{N}^0 + \mathbf{N}^+ e^{\iota\tilde{\theta}})\hat{\mathbf{u}}. \tag{5.17}$$

For both schemes, the discretised system is now reduced to an eigenvalue problem of dimensions $(N+1)\times(N+1)$:

$$\tilde{\omega}\mathbf{I}\hat{\mathbf{u}} = \mathbf{H}(\tilde{\theta})\hat{\mathbf{u}}. \tag{5.18}$$

For both the FR and SD schemes (Eqs. (5.13) and (5.17), respectively), the algebraic structure of the problem is almost identical: the middle term, indicator of the influence of the interior part of element ($\mathbf{C}^0$ and $\mathbf{N}^0$ for the FR and the SD schemes, respectively) and the two boundary terms representing the influence of the interface numerical fluxes from the left ($\mathbf{C}^-$ and $\mathbf{N}^-$) and right boundaries ($\mathbf{C}^+$ and $\mathbf{N}^+$).

The classical approach normally imposes a real number for the phase $\tilde{\theta} \in [-\pi, \pi]$ and, for each value of $\tilde{\theta}$, the eigenvalue problem is solved to obtain, as output, $N+1$ values for $\tilde{w}$, commonly called *modes*. Only one of these will be denoted as the *primary* mode: this is the only mode which is characterised by the convergence property

$$\tilde{\omega} \to \theta \quad \text{for} \quad N \to \infty. \tag{5.19}$$

The remaining eigenvalues are considered spurious and are referred as secondary modes [72]. As a consequence, all propagation properties are contained in the primary mode, which will be the main focus in the remaining part of the presented temporal analysis.

Given a null phase, the primary mode will assume a value equal to zero but, moving away from the origin, the identification of the primary curve becomes less straightforward due to the possible presence of complex distribution patterns of the eigenvalues. Nevertheless, considering low order discretisations, this issue is less problematic due to the smaller number of eigenvalues per phase value and an intuitive behaviour of the primary curve can be easily recognised. By analogy, it is possible to construct primary curves also for higher orders of approximation. Otherwise, a more methodical procedure to identify the primary mode has been proposed by Vincent, et al. [71], involving an energy evaluation of the eigensolution coefficients in the Legendre polynomial basis. In the present work, a simple geometrical interpretation of the eigenvalue distribution has been used to construct the primary curve.

The technique presented here is commonly known as *temporal* eigenanalysis. In fact, for any given value of *spatial* phase, the capability of the numerical scheme to describe them over *time* can be evaluated. In mathematical terms, a real number for $\tilde{\theta}$ is assumed and $\tilde{\omega} = \tilde{\omega}(\tilde{\theta})$ is consequently calculated. The numerically solved dispersion relation will give informations on the velocity of propagation of discretised waves within the domain, while the diffusion counterpart will quantify dissipation of spatial oscillations along time. In order to highlight the link between the imaginary part of $\tilde{\omega}$ and numerical diffusion, it is useful to observe that

$$u \propto e^{\iota(\tilde{\theta}x - \tilde{\omega}t)} = e^{\mathrm{Im}(\tilde{\omega})t} e^{\iota(\tilde{\theta}x - \mathrm{Re}(\tilde{\omega})t)}. \tag{5.20}$$

Therefore, for negative values of $\mathrm{Im}(\tilde{\omega})$, the coefficient $e^{\mathrm{Im}(\tilde{\omega})t}$ represents a damping coefficient over time. Some level of numerical diffusion can be very useful whenever spatial under-resolution is expected. In fact, a well-distributed amount of dissipation in the high wavenumbers region is very convenient in high-order methods. This property can be helpful in terms of stability and a valuable feature in the perspective of sub-grid scale (SGS) modelling. In Fig. 5.1, some examples of dispersion-diffusion relations are shown for the DG-FR scheme using a full-upwind numerical flux.

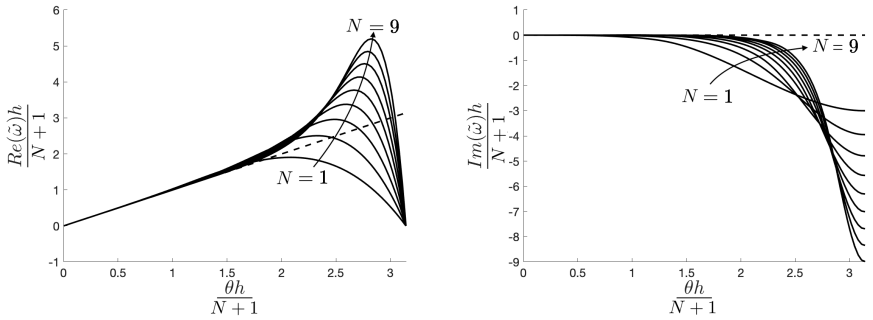

(a) Dispersion (b) Diffusion

Figure 5.1: DG-FR numerical dispersion and diffusion using temporal approach: influence of the approximation order.

5.3 Spatial eigenanalysis

The relation between $\tilde{\omega}$ and $\tilde{\theta}$ is intrinsically defined by Eq. (5.13) which, except for some very particular cases, cannot be analytically inverted. In order to obtain non-trivial solutions the condition $\hat{\mathbf{u}} \neq \mathbf{0}$ is needed. In other words, an equivalent equation which defines the relation between $\tilde{\omega}$ and $\tilde{\theta}$ can be expressed as

$$\det(\iota\tilde{\omega}\mathbf{I} - 2(\mathbf{C}^{-1}e^{-\iota\tilde{\theta}} + \mathbf{C}^{0} + \mathbf{C}^{+}e^{\iota\tilde{\theta}})) = 0, \tag{5.21}$$

that can be seen as an equation in $z = e^{\iota\tilde{\theta}}$:

$$\det(\iota\tilde{\omega}\mathbf{I} - 2(\mathbf{C}^{-}z^{-1} + \mathbf{C}^{0} + \mathbf{C}^{+}z)) = 0. \tag{5.22}$$

The same exact form can be obtained using the SD discretisation simply by replacing the matrices $\mathbf{C}^{0,+,-}$ with the previously defined $\mathbf{N}^{0,+,-}$. It can be proven that this approach leads to a second order characteristic equation in z which admits, consequently, two (in general complex) roots.

Usually, like in the temporal approach, one root is considered physical and the other spurious. Given a fixed value of $\tilde{\omega}$, Eq. (5.22) can be solved numerically in terms of z and, consequently, $\tilde{\theta}$ can be evaluated. In the most general case $\tilde{\omega} \in \mathbb{C}$, however, as in the temporal approach, where a real value is assumed for $\tilde{\theta}$, in the spatial approach, this assumption is applied to $\tilde{\omega}$. Once Eq. (5.22) is solved, a criterion to distinguish physical and spurious solutions is needed. In this work the same idea proposed by Mengaldo, et al. [80] has been exploited: the amplification behaviour of a wave-like solution is embedded in the imaginary part of the eigensolution and, as a consequence, positive values of $\mathrm{Im}(\tilde{\theta})$ are expected for physical solutions and, vice versa, negative values of $\mathrm{Im}(\tilde{\theta})$ are expected for spurious ones.

This can be clearly noticed giving a different interpretation of Eq. (5.20), where roles of $\tilde{\theta}$ and $\tilde{\omega}$ are simply inverted:

$$u \propto e^{\iota(\tilde{\theta}x-\tilde{\omega}t)} = e^{-\mathrm{Im}(\tilde{\theta})x} e^{\iota(\mathrm{Re}(\tilde{\theta})x-\tilde{\omega}t)}. \tag{5.23}$$

Consequently, positive values of $\mathrm{Im}(\tilde{\theta})$ produce a damping factor in *space*. Notice the change of sign with respect to temporal analysis.

Since $z = \exp(\iota\tilde{\theta})$, one has:

$$z = \exp(\iota \mathrm{Re}(\tilde{\theta}))\exp(-\mathrm{Im}(\tilde{\theta})). \tag{5.24}$$

Furthermore, the sign of $\mathrm{Im}(\tilde{\theta})$ is strictly related to the absolute value of z:

$$\mathrm{Im}(\tilde{\theta}) \lesseqgtr 0 \Leftrightarrow |z| \gtreqless 1. \tag{5.25}$$

Therefore, in order to see if a numerical solution z is either spurious or physical, a fast evaluation of its absolute value will give an efficient algorithm to discard the spurious solution. The same idea can also be used to compute an initial guess z_0 for Newton-like methods in the numerical resolution of Eq. (5.22). In particular, an initial physical guess can be expressed as $z_0 = r_1 \exp(2\pi r_2)$ with both r_1 and r_2 real numbers in $[0, 1]$. Then, the second solution is automatically identified as spurious.

Once the physical solution z is identified, it is easy to invert the expression $z = e^{\iota\tilde{\theta}}$ in order to obtain the final value of $\tilde{\theta}$, namely:

$$\mathrm{Re}(\tilde{\theta}) = -\iota \ln(z/|z|) \qquad \text{and} \qquad \mathrm{Im}(\tilde{\theta}) = -\ln(|z|). \tag{5.26}$$

Finally, considering the real part, *i.e.*, dispersion curves, periodicity of $\tilde{\theta}$ needs to be taken into account. A simple check on the variation of the real part with respect to $\tilde{\theta}$ will give a valid indicator to solve the problem: whenever the numerical derivative $d(\mathrm{Re}(\tilde{\theta}))/d\tilde{\omega}$ is negative, a vertical translation of $\tilde{\theta}$ of 2π is imposed. The exact wave-like solution can be trivially re-written in terms of ω as:

$$\mathrm{Re}(\omega) = \theta \quad \text{and} \quad \mathrm{Im}(\omega) = 0. \tag{5.27}$$

In Fig. 5.2 examples of dispersion-diffusion relations are shown for the DG-FR scheme using a full-upwind numerical flux. Complementary features with respect to the classical temporal analysis can be observed. The increase of the approximation order produces smaller dispersion errors (left figure), in analogy with temporal eigenanalysis. On the contrary, higher approximation orders provide smaller levels of spatial diffusion for *any* value of $\tilde{\omega}$ (right figure), whereas in temporal eigenanalysis a stronger level of numerical diffusion is usually present in the high wavenumbers region (compare with Fig. 5.1). Furthermore, notice that in Fig. 5.2 the imaginary part of $\tilde{\theta}$ assumes only positive values, whereas in Fig. 5.1 the imaginary part of $\tilde{\omega}$ is always negative.

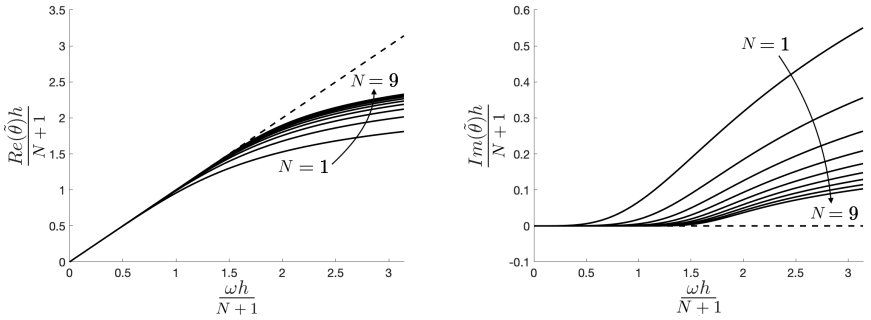

(a) Dispersion (b) Diffusion

Figure 5.2: DG-FR numerical dispersion and diffusion using spatial approach: influence of the approximation order.

5.4 Non-Modal analysis

Recently, a completely different approach to study numerical diffusion has been proposed by Fernandez, et al. [88] called *non-modal analysis*. The principal aim of such analysis originates from the following proposition: given an initial condition characterised by a certain spatial frequency, how does the magnitude of oscillations evolve over time? Standard temporal eigenanalysis answers this question though a spectral analysis of the discretised differential operator. Using temporal analysis, each eigenvalue is considered individually. In particular, only the *primary* mode is examined while all the others are supposed spurious. Non-modal analysis proposes a formulation in which the influence of the whole spectrum is taken into account. In this regard, the theoretical framework is exactly the same until the discretised linear dynamical system is obtained. In fact, if the explicit dependency on time by the Bloch-wave solutions is not exploited, classical temporal analysis leads to the local linear dynamical system:

$$\dot{\mathbf{u}} = \mathbf{H}(\tilde{\theta})\mathbf{u}. \tag{5.28}$$

Once the system is expressed in this form, the very wide literature of dynamical systems can be used to study the influence of numerics on the solution behaviour.

Let us define the so-called *short-term diffusion* as:

$$\bar{\omega}^* := \left.\frac{\mathrm{d}\log(||\mathbf{u}_h||)}{\mathrm{d}\tau^*}\right|_{\tau^*=0}, \tag{5.29}$$

where $||\cdot||$ denotes the L^2 norm and $\tau^* = \tau(N+1) = ta(N+1)/h$ is a characteristic non-dimensional time scale (which is simply $\tau^* = t(N+1)/2$ with the assumptions introduced before).

It can be noticed that the previous equation can be re-written as:

$$\bar{\omega}^* := \lim_{\tau^* \to 0} \frac{1}{\tau^*} \log \left(\frac{||\mathbf{u}_h||}{||\mathbf{u}_{h,0}||} \right). \tag{5.30}$$

This expression is more useful in terms of physical interpretation: as it will be explained later, the quantity $\bar{\omega}^*$ depends on the wavenumber $\tilde{\theta}$ and on the numerics (namely, the type of scheme, the order of approximation and the upwinding parameter). Intuitively, $\bar{\omega}^*$ gives an estimate of the initial decay rate (per unit convection time) of the numerical solution between degrees of freedom (DoF), starting from the initial condition $\exp(\iota\theta x)$.

In fact, inverting Eq. (5.30):

$$||\mathbf{u}_h(\tau^*)|| \approx ||\mathbf{u}_{h,0}|| \exp(\bar{\omega}^* \tau^*). \tag{5.31}$$

At early times, the term $\exp(\bar{\omega}^* \tau^*)$ can be seen as a damping factor per DoF, giving an alternative interpretation of numerical diffusion not based on an eigenanalysis of the matrix $\mathbf{H}$.

Finally, it can be noticed that, using the Legendre polynomials basis, the following expression can be obtained:

$$\bar{\omega}^* := \frac{1}{N+1} \mathrm{Re} \left(\frac{\mathbf{u}_{h,0}^\dagger \mathbf{H} \mathbf{u}_{h,0}}{\mathbf{u}_{h,0}^\dagger \mathbf{u}_{h,0}} \right), \tag{5.32}$$

where $(\cdot)^\dagger$ denotes conjugate transpose. The final form involves the Rayleigh quotient of the linear dynamical system. The Rayleigh quotient gives useful informations regarding the dynamics of the system and it is particularly popular in non-modal hydrodynamic instability theory [83, 84, 85].

In the original work by Fernandez, et al. [88], a classical DG scheme has been employed and explicit formulas to evaluate Eq. (5.32) have been used. In a collocation setting, instead, norms can be alternatively evaluated using proper quadrature formulas:

$$\int_{-1}^{1} u^2 dx = \sum_{j=0}^{N} u^2(x_j^s) w_j,$$

where x_j^s denotes the set of solution points with the corresponding integration weights w_j. Accordingly, Eq. (5.32) can be actually computed as

$$\bar{\omega}^* := \frac{1}{N+1} \mathrm{Re} \left(\frac{\mathbf{u}_{h,0}^\dagger \mathbf{W} \mathbf{H} \mathbf{u}_{h,0}}{\mathbf{u}_{h,0}^\dagger \mathbf{W} \mathbf{u}_{h,0}} \right), \tag{5.33}$$

with $\mathbf{W}_{ik} = w_j \delta_{ik}$. Formally the L^2 norm should be evaluated in $(-\infty, \infty)$, but, thanks to the periodicity condition, the integral is simply n_{el} times

the element-wise one and, since only quotients of norms are considered, the proportionality constant n_{el} simplifies.

It is easy to notice that the matrix $\mathbf{H}$ is the exact same matrix of the temporal approach (except for the complex sign). Then, the difference between the classical temporal analysis and the present analysis is precisely linked to the modal/non-modal character. The classic temporal eigenanalysis studies the eigenvalues of the matrix $\mathbf{H}$ in order to evaluate whether the Fourier modes in the initial solution grow or are dissipated over time. Non-modal analysis, instead, considers all the eigenvalues simultaneously for each wavenumber. Notice that non-modal analysis does not necessitate distinguishing between primary and secondary modes exactly because all of them are considered simultaneously. Finally, notice that, if the primary eigenvectors of $\mathbf{H}$ are selected as initial condition, the Rayleigh quotient coincides with the corresponding eigenvalue and the classical temporal eigenanalysis is then recovered.

5.5 Non-constant advection velocities

A generalisation of the classical temporal approach for non-constant advection velocities has been recently proposed by Manzanero, et al. [86, 87].

For the sake of simplicity, positive advection velocities, periodic within the reference element, have been considered. Without any loss of generality, the inter-element value of the advection velocity has been set equal to 1. These conditions strongly simplify the numerical analysis and are equivalent to apply the following approach to one element only. It is possible to define generalised Bloch wave solutions of the form:

$$u(x,t) = e^{\iota(\theta G(x) - \omega t)}, \tag{5.34}$$

where non-homogeneity in the advection velocity is taken into account by the function $G(x)$.
For an appropriate choice of this function, classical dispersion/diffusion relations can be obtained:

$$\omega = \bar{a}\theta. \tag{5.35}$$

where $\bar{a}$ denotes the average advection speed. Finally, in order to compare relevant results for constant and non-constant advection velocities, scaled wavenumber and frequency are usually considered:

$$\hat{\theta} = \frac{\theta}{\bar{g}} \qquad \text{and} \qquad \hat{\omega} = \bar{a}\hat{\theta} = \frac{\bar{a}\theta}{\bar{g}},$$

where

$$\bar{g} = \frac{1}{2}\int_{-1}^{1} \bar{a}/a(\hat{x})d\hat{x}.$$

The $\mathbf{C}^0$ matrix in Eq. (5.13) will be simply replaced by

$$\mathbf{C}^0 = \mathbf{DA} - \mathbf{B} - (\alpha - 1)\mathbf{g}_L\mathbf{l}^T\mathbf{A} - \alpha\mathbf{g}_R\mathbf{r}^T\mathbf{A}, \tag{5.36}$$

where $A_{ij} = a(x_i)\delta_{ij}$ and $B_{ij} = (D_{ik}a(x_k))\delta_{ij}$. The term involving the matrix $\mathbf{A}$ represents the derivative of the conservative part, namely, $\partial(au)/\partial x$, while the term involving the matrix $\mathbf{B}$ is the discrete version of the operator $u\partial a/\partial x$. Then, a generalisation of the present approach to the full scalar conservation

$$\frac{\partial u}{\partial t} + \frac{\partial(a(x)u)}{\partial x} = 0 \tag{5.37}$$

can be obtained simply by neglecting the term $\mathbf{B}$. The final expression of the $\mathbf{C}_0$ matrix will be:

$$\mathbf{C}^0 = \mathbf{DA} - (\alpha - 1)\mathbf{g}_L\mathbf{l}^T\mathbf{A} - \alpha\mathbf{g}_R\mathbf{r}^T\mathbf{A}. \tag{5.38}$$

The same reasoning can be applied to the SD discretisation, where only the central term in Eq. (5.17) needs to be modified:

$$\mathbf{N}^0 = \mathbf{DA}^f\mathbf{M}^0, \tag{5.39}$$

where matrix $\mathbf{A}^f$ represents the values of the advection velocity at the flux points: $A^f_{ij} = a(x^f_i)\delta_{ij}$.

In this way, both temporal and spatial analyses can be easily generalised to non-constant advection velocity conservation laws. Non-modal analysis can be generalised for non-homogeneous cases as well. The difference is implicitly defined within Eqs. (5.38) and (5.39): the central block of the matrix $\mathbf{H}$ in Eq. (5.28) will change and, consequently, the short-term diffusion of the dynamical system will change accordingly.

While linear stability has been mathematically proven for all the numerical schemes herein considered [89, 48, 70], in the case of non-constant advection velocities, numerical stability is not ensured. In this particular case, the functional form of the advection velocity can lead to what are commonly known as *aliasing* errors. Such numerical errors are caused by an under-sampling of the advection velocity nodal values. In the context of FR schemes, the use of an exact L_2 projection in the flux approximation can eliminate aliasing errors [47]. Nevertheless, such approach is computational expensive and it can strongly affect efficiency and simplicity of the FR scheme. Similarly, split form coefficient in DG method with summation by parts and simultaneous-approximation-term properties have shown to be of significant importance in non-linear stability analysis [87]. In particular, the conservative form of the DG scheme is capable of removing aliasing errors, preventing exponential growth of the solution. Such result suggests the possibility of similar proofs for FR and SD schemes, which rely on the conservative form of the equation. Nevertheless, a mathematical proof of

non-linear stability is out of the scope of the present study and it will not be discussed. Finally, most of the works studying non-constant advection velocities have been primarily focused on DG schemes whereas, to the authors' knowledge, such techniques have never been applied to FR and SD schemes. Furthermore, the non-homogeneous case has never been studied through spatial and non-modal analysis for any spectral element method.

5.6 Theoretical results

The large variety of spectral analysis techniques presented in the previous sections allows a vast number of useful comparisons for each of them. Changing the order of approximation, the numerical scheme and the upwinding parameter, a comprehensive study can be easily performed. The generalisation to non-constant advection velocities provides an extra degree of freedom that can be used to analyse more complex flow configurations.

Most of the numerical analysis results available in the literature are focused on nodal DG methods and, in particular, temporal analysis is performed considering constant advection velocity. Hence the interest in performing a comparative study between SD and DG schemes. In particular, the FR recovered versions, SD-FR and DG-FR, respectively, will be considered in the present analysis whenever the solved equation is of linear advection type. This is justified by the fact that, as already mentioned, for linear advection problems, the SD-FR (resp. DG-FR) scheme coincides with the SD (resp. DG) scheme (*cf.* Appendix B). It shall be noted that, although the temporal analysis has been already performed on both methods, to the authors' knowledge, no spatial or non-modal analysis has ever been performed on the SD scheme.

The present section will be organised as follows: in the first subsection, a simple comparison between DG-FR and SD-FR is performed using temporal and spatial analysis; in the second subsection, non-modal analysis is applied to both schemes; finally, non-homogeneous advection velocity cases are analysed and DG-FR, SD-FR and SD schemes are compared. In particular, two different type of advection velocities are considered: (a) a sinusoidal velocity profile and (b) a random velocity signal. Concerning the interface fluxes, full-upwind, centered and hyper-upwind fluxes will be adopted depending on the performed analysis.

In all the figures presented in the following sections, imposed values of frequency and wavenumber are denoted as ω and θ, respectively, whereas, computed values are indicated as $\tilde{\omega}$ and $\tilde{\theta}$, respectively.

5.6.1 Temporal and spatial analyses

In order to give a solid background, a first comparison of dispersion/diffusion properties of DG-FR and SD-FR is here presented. Once this basic analy-

sis is performed, complexity will be added by considering non-homogeneous advection velocities. It is worthwhile pointing out that, the present analysis being concerned with the linear advection case, the relevant results are expected to hold true for the DG and SD schemes as well.

A full-upwind numerical flux has been considered first. This is also a convenient choice in spatial analysis where no spurious solutions are expected, as already proved by Hu, et al. [79]. Spatial and temporal analyses have been performed for both schemes. Numerical diffusion curves are shown in Figs. 5.3 (temporal analysis) and 5.4 (spatial analysis).

It can be noticed that the diffusive role of the two methods are inverted: according to temporal analysis, for high wavenumber, DG-FR schemes are more dissipative than SD-FR, whereas, in spatial analysis, the opposite happens. In other words, DG-FR has a stronger tendency to damp *temporal* developing high frequencies while SD-FR tends to dissipate more high wavenumber *spatial* disturbances.

Dispersion counterparts are shown in Figs. 5.5 and 5.6. As already observed in other papers [71, 90], according to temporal analysis, SD-FR schemes are more accurate than DG-FR (in particular for high-order approximations). The classical peak in the high wavenumber region is, in fact, less marked. Nevertheless, the wavenumbers responsible for such deviations from the exact solution are supposedly sufficiently dissipated not to influence the overall accuracy of the scheme. On the other hand, spatial dispersion analysis gives almost indistinguishable results between the two schemes.

It is interesting to notice such evident differences between spatial and temporal approaches. The mathematical formulation would suggest *specular* results, *i.e.*, a simple exchange of x and y axis. The eigenvalue problems, Eqs. (5.18) and (5.22), are in fact mathematically equivalent and the roles of $\tilde{\theta}$ and $\tilde{\omega}$ are simply inverted. Nevertheless, in the temporal analysis, a real number is assumed for $\tilde{\theta}$ and $\tilde{\omega} \in \mathbb{C}$ is evaluated whereas, in the spatial analysis, a real number is assumed for $\tilde{\omega}$ and $\tilde{\theta} \in \mathbb{C}$ is computed. Most likely, dropping the assumption of real values for $\tilde{\theta}$ and $\tilde{\omega}$ and consider more general complex values for both would give the expected symmetry between the two procedures.

In order to assess the influence of the numerical flux, a quasi-centered numerical flux has been considered by setting $\alpha = 0.49$ in Eqs. (5.5) and (5.6).

In the following analysis, and in the relevant figures, only physical modes are considered.

Temporal analysis using quasi-centered (see Fig. 5.7) provides some different trends: dispersion curves are characterised by high accuracy in the first region following, instead, large deviations from the exact solution for high wavenumbers. Numerical diffusion, on the other hand, is extremely low for both schemes. In other words, quasi-centered fluxes provide very small numerical diffusion at the cost of sensible dispersion errors. Furthermore, as already mentioned, lack of numerical diffusion in the high wavenumbers

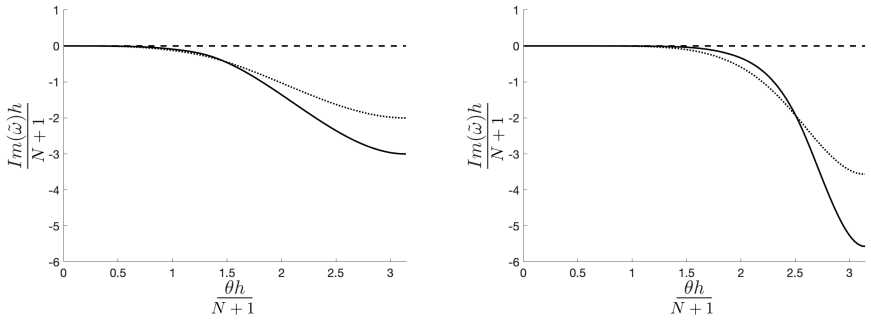

(a) $N = 1$ (b) $N = 4$

Figure 5.3: Numerical diffusion using temporal analysis: solid line, DG-FR; dotted line, SD-FR; dashed line, exact wave-like solution.

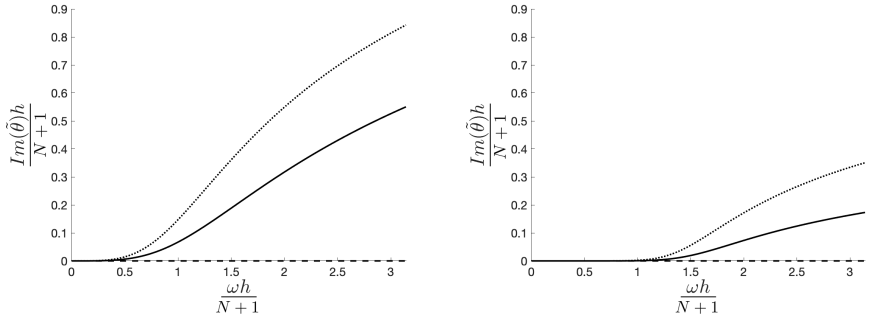

(a) $N = 1$ (b) $N = 4$

Figure 5.4: Numerical diffusion using spatial analysis: solid line, DG-FR; dotted line, SD-FR; dashed line, exact wave-like solution.

region can lead to numerical instability and damage the robustness of the scheme.

Small differences are observed between DG-FR and SD-FR in spatial numerical dispersion and diffusion (see Fig. 5.8). As already noticed by Mengaldo, et al. [80], dissipative bubbles are observed for certain frequencies with both methods, as clearly evident in Fig. 5.8(b). Bubbles seem to be slightly translated and enlarged when using the SD-FR scheme. This fact further suggests that the SD-FR scheme is more dissipative according to the spatial eigenanalysis.

5.6.2 Non-modal analysis

In this subsection a comparison between DG-FR and SD-FR is presented using the non-modal analysis introduced by Fernandez, et al. [88]. The

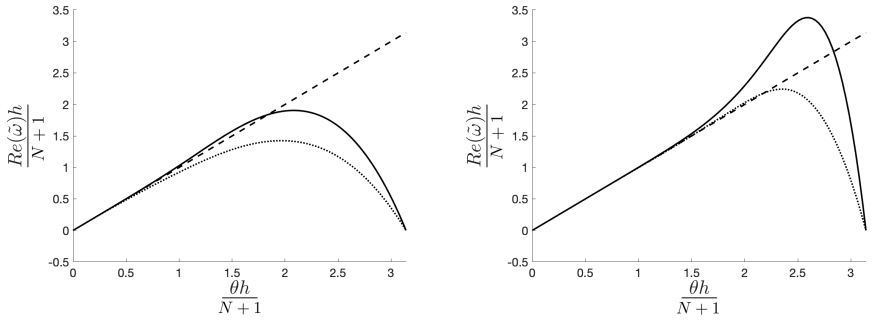

(a) $N = 1$ (b) $N = 4$

Figure 5.5: Numerical dispersion using temporal analysis: solid line, DG-FR; dotted line, SD-FR; dashed line, exact wave-like solution.

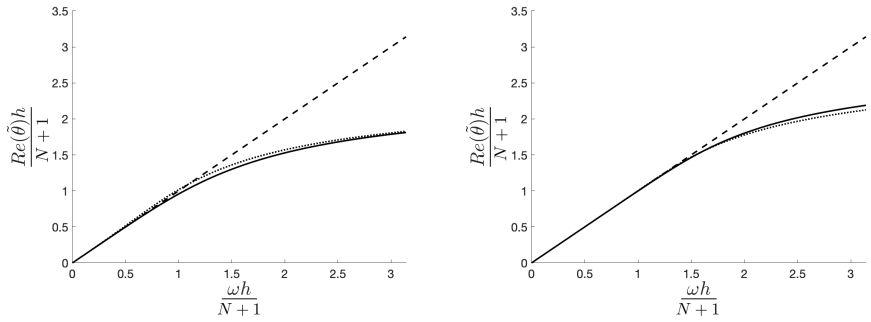

(a) $N = 1$ (b) $N = 4$

Figure 5.6: Numerical dispersion using spatial analysis: solid line, DG-FR; dotted line, SD-FR; dashed line, exact wave-like solution.

application of non-modal analysis to FR and SD schemes, to the authors' knowledge, have never been studied in previous works on spectral analyses of spectral element methods.

The influence of the order of approximation is shown in Fig. 5.9. According to Fernandez, et al. [88], desirable features of the short-term diffusion are monotonicity ($d\bar{\omega}^*/d\theta < 0$) and slowly varying curves. Both properties should imply a more stable discretisation, in particular for strongly non-linear systems, where the interaction between scales plays a more central role. It can be clearly noticed that the SD-FR diffusive curves are, from this point of view, slightly flatter, which suggests higher accuracy. This is particularly evident whenever very high polynomial orders are used as shown in Fig. 5.10. In agreement with [88], polynomial orders around 2–3 are the most promising in the ILES framework, while higher approximation orders tend to introduce insufficient levels of dissipation for high wavenumbers and

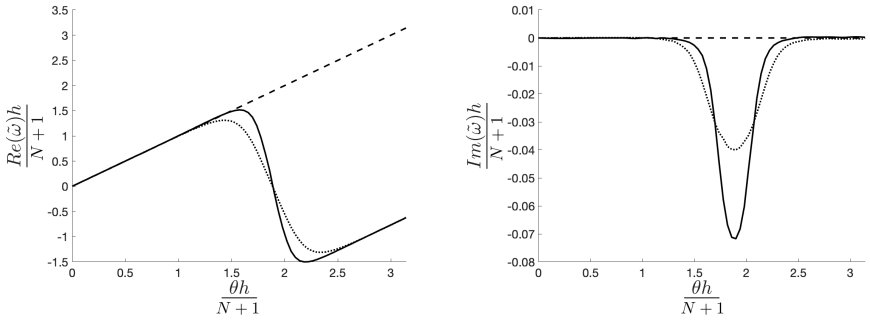

(a) Dispersion (b) Diffusion

Figure 5.7: Numerical dispersion and diffusion for $N = 4$ using quasi-centered fluxes $\alpha = 0.49$ (temporal analysis): solid line, DG-FR; dotted line, SD-FR; dashed line, exact wave-like solution.

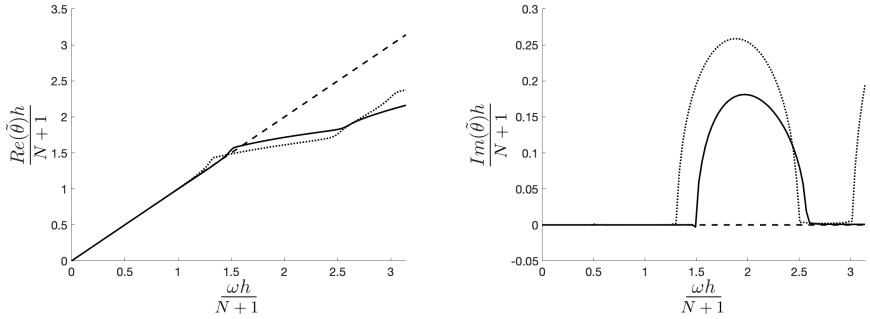

(a) Dispersion (b) Diffusion

Figure 5.8: Numerical dispersion and diffusion for $N = 4$ using quasi-centered fluxes $\alpha = 0.49$ (spatial analysis): solid line, DG-FR; dotted line, SD-FR; dashed line, exact wave-like solution.

are hence characterised by a more non-monotonic behaviour.

As a final note, some positive values of $\bar{\omega}^*$ are observed when using the SD-FR scheme, which could lead to a numerically induced growth of oscillations. Nevertheless, these are still quite small even for very high polynomial order.

5.6.3 Comparison between methods for non-constant advection velocity

In order to consider more realistic conditions, previous analyses are here generalised to the case of non-constant advection velocities. Departing from the linear advection case, the improved SD method by Liang and Jame-

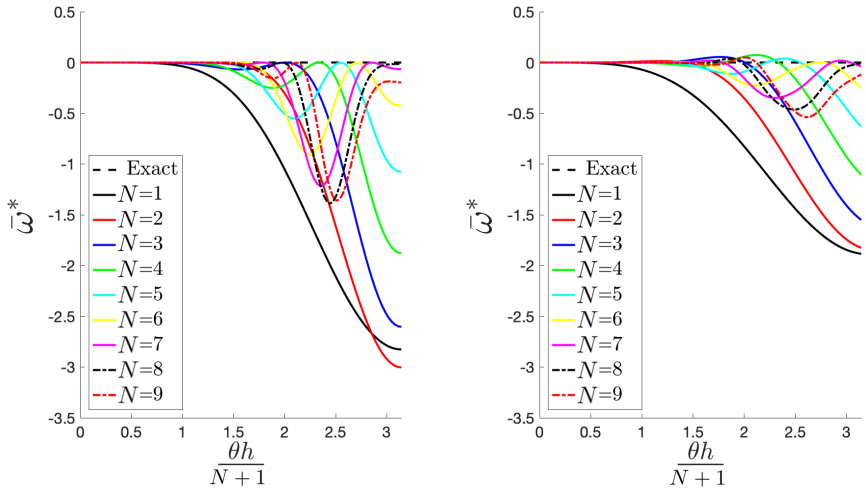

(a) DG-FR (b) SD-FR

Figure 5.9: Short-term diffusion term using nodal DG-FR and SD-FR schemes.

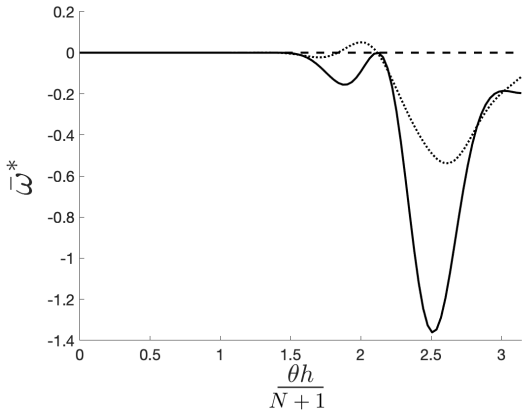

Figure 5.10: Comparison of diffusive curves using DG-FR and SD-FR scheme for $N = 8$.

son [91, 92, 48] will be considered as well. In fact, as explained in Appendix B, for a non-linear flux function, the SD-FR scheme does not coincides anymore with the SD approach. As a consequence, common spectral analyses based on linear equations are insufficient to properly study and highlight differences between these schemes and more advanced techniques are needed.

Concerning the numerical flux and the order of accuracy, a full-upwind flux and an approximation order $N + 1 = 6$ have been chosen. Two different prescribed spatial profiles are considered for the advection velocity. The for-

mer and simplest is a sinusoidal velocity profile, while the latter is a random velocity signal with prescribed variance around the mean value (taken equal to 1); see Fig. 5.11.

Deviations from the constant case $a = 1$ are defined through the parameter σ. In particular, for the two advection velocities herein considered:

$$a(x) = 1 + \sigma \sin(\pi x) \quad \text{and} \quad a(x) = 1 + \sigma W(x) \tag{5.40}$$

where W is a particular realisation of a random field with null mean and unitary variance such that $W(\pm 1) = 0$. In the present subsection a value of $\sigma = 0.6$ has been chosen, imposing a relatively high level of inhomogeneity. The two selected profiles are deemed to be sufficiently representative of a wide range of applications where numerics play a key role in the physical description of the phenomenon and in the computation outcome. The sinusoidal function is the classical simple form of perturbation, which can be considered as the building block of more complex perturbations. For instance, depending on the form of the flux, a sinusoidal perturbation can lead to shock formation and, as a result, characterising the behaviour of the numerical scheme is of paramount importance to ensure the necessary robustness of the simulation.

Concerning the random signal, this can be viewed as a first approximation of a turbulent flow. Differently from the simple sinusoidal profile, the random signal has a rather broad spectrum. Characterising the behaviour of the numerical scheme in such a case can promote a better understanding concerning the suitability of spectral element methods for ILES or, conversely, highlight the necessity of explicit SGS modeling.

In agreement with the continuous theory presented in Section 5.5, for non-constant advection velocity computations, numerical dissipation and dispersion have been conveniently scaled by $\bar{g}$.

Temporal eigenanalysis

A comparison of the results from temporal analysis obtained using the mentioned forms of advection velocity profile is presented in this section. In particular, dispersion and diffusion plots are shown in Fig. 5.12.

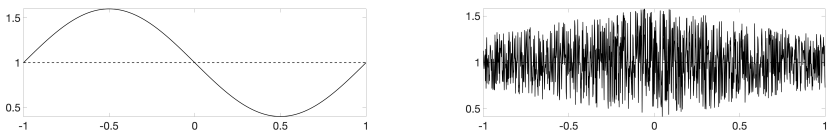

(a) Sinusoidal profile (b) Random profile

Figure 5.11: Advection velocities.

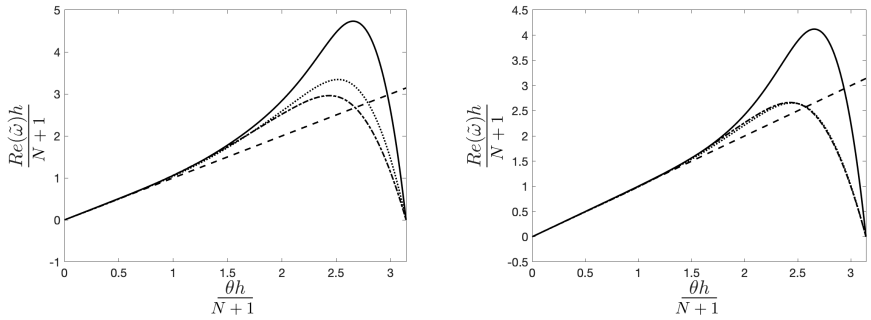

(a) Sinusoidal advection

(b) Random advection

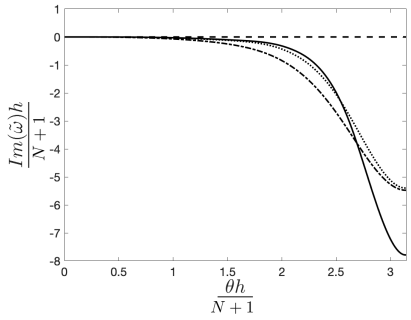

(c) Sinusoidal advection

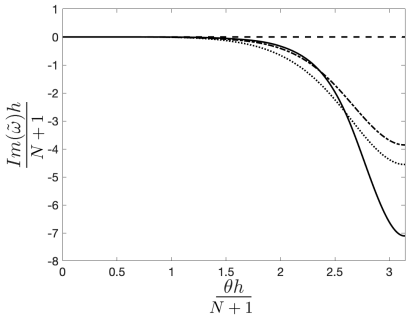

(d) Random advection

Figure 5.12: Temporal dispersion (a, b) and diffusion (c, d) plots: solid line, DG-FR; dotted line, SD-FR; dash-dotted line, SD; dashed line, exact wave-like solution.

Diffusion curves from the temporal analysis (Figs. 5.12 (c) and (d)) do not differ significantly from those obtained in the linear case: the SD and the SD-FR schemes have quite similar behaviours and they are characterised by a lower dissipation for high wavenumbers compared to the DG-FR scheme. In particular, in the sinusoidal velocity case, the SD scheme is always more dissipative than the SD-FR method for any given value of θ, whereas in the random advection case their roles are inverted and the SD-FR is more diffusive. Temporal dispersion shown in Figs. 5.12 (a) and (b) display well-know features: the DG-FR scheme is characterised by a visible peak for high wavenumbers (see also Fig. 5.1 (a)) while the SD and SD-FR schemes follow more accurately the exact wave-like solution. Due to the inhomogeneity in the advection velocity, small differences between the SD-FR and the SD schemes can be noticed, in particular for the sinusoidal profile where the SD scheme appears to be slightly more accurate with respect to the SD-FR method (Fig. 5.12 (a)).

Spatial eigenanalysis

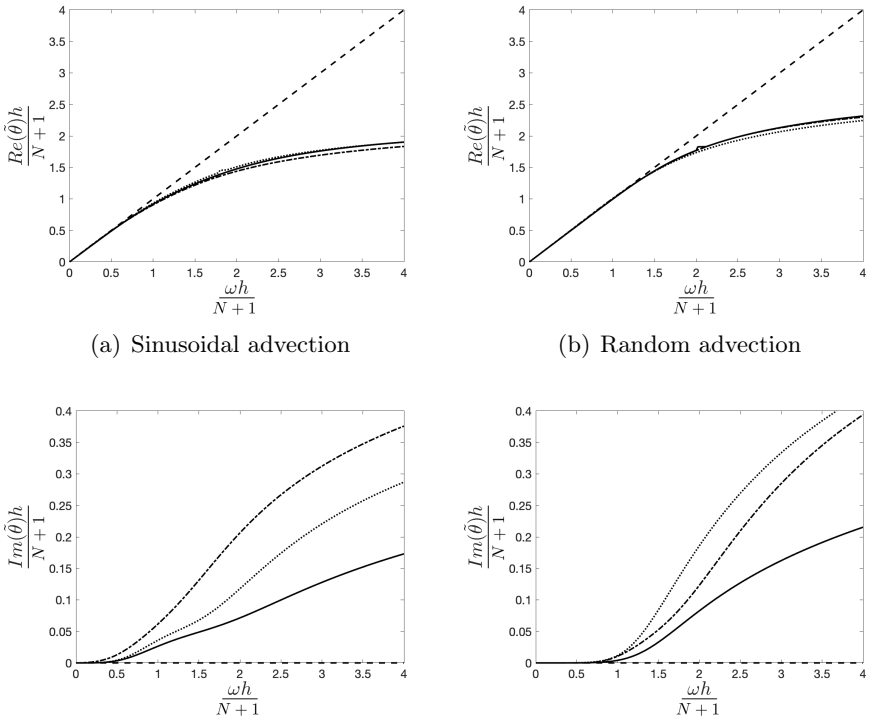

(a) Sinusoidal advection (b) Random advection

(c) Sinusoidal advection (d) Random advection

Figure 5.13: Spatial dispersion (a, b) and diffusion (c, d) plots: solid line, DG-FR; dotted line, SD-FR; dash-dotted line, SD; dashed line, exact wave-like solution.

Diffusion and dispersion curves from the spatial analysis are reported in Fig. 5.13. Noticeable differences are observed in the diffusive curves only, where it appears that the SD and the SD-FR schemes are overall more dissipative than the DG-FR method. Nonetheless, in a similar way as in the temporal analysis, the roles of the SD and the SD-FR are inverted in terms of their diffusive character for the two prescribed advection velocities: in the sinusoidal case, the SD is more dissipative than the SD-FR, whereas the opposite behaviour is observed when a random signal advection velocity is used. Consequently, the influence of the functional form of the advection velocity can significantly affect the numerical diffusion and highlight, for example, noticeable differences between the SD and the SD-FR schemes.

As a representative example of non-upwind fluxes, spatial numerical diffusion for the FR and the SD schemes has been evaluated in the case of sinusoidal advection velocity and strongly upwind fluxes ($\alpha = -50$). In particular, increasing values of σ can be selected to promote a stronger deviation

from the homogeneous case.

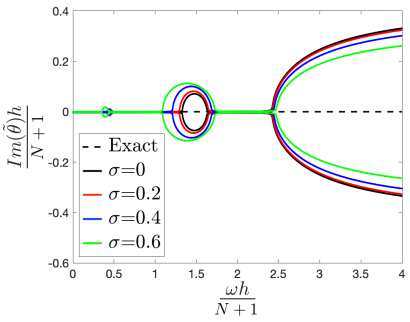

(a) DG-FR

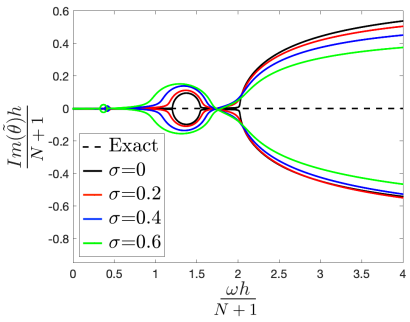

(b) SD-FR

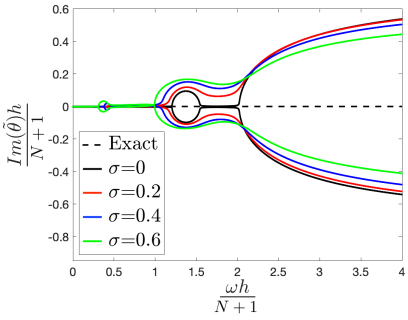

(c) SD

Figure 5.14: Numerical diffusion from DG-FR (a), SD-FR (b), and SD (c) schemes (spatial approach).

In order to understand the role played by the numerical dissipation for increasingly complex advection velocities, the spatial numerical diffusion of the FR and SD schemes has been plotted in Fig. 5.14 for different values of the parameter σ. It is worth recalling that, whenever non-constant advection velocities are considered there is no simple way to distinguish between the physical and the spurious modes; therefore, for this case, both modes have been plotted.

Particular attention should be payed to the medium frequencies region separating the two subsequent dissipative bubbles. With regards to the SD and SD-FR schemes, for increasing values of σ, dissipative bubbles tend to blend together as they flatten along the horizontal direction. Such tendency is even more pronounced for the SD scheme (Fig. 5.14 (c)). The DG-FR scheme, on the other hand, is characterised by bubbles of similar shape and only slightly shifted toward smaller frequencies.

It is important to stress out that the interpretation of diffusive curves lies in essentially two complementary aspects. The magnitude of $\mathrm{Im}(\tilde{\omega})$ indicates

the strength of numerical dissipation and it represents the primary measure to differentiate between more or less dissipative schemes. Nevertheless, how numerical dissipation is distributed along the different frequencies can be as much as relevant. Sharp profiles for such curves are in fact generally not advisable and monotonic behaviours are preferable. Rapid variations of numerical diffusion within a limited range of frequencies could in fact trigger unpredictable energy transfers between scales in realistic simulations.

Non-modal analysis

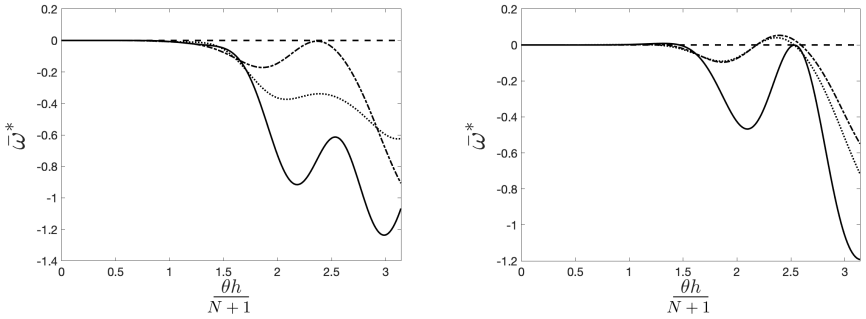

(a) Sinusoidal advection (b) Random advection

Figure 5.15: Short-term diffusion curves: solid line, DG-FR; dotted line, SD-FR; dash-dotted line, SD; dashed line, exact wave-like solution.

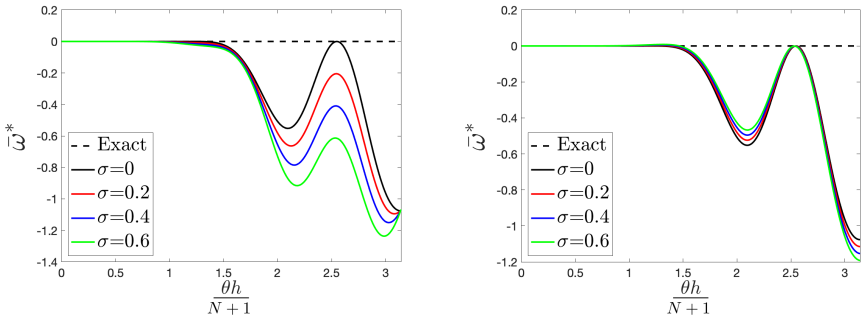

(a) Sinusoidal advection (b) Random advection

Figure 5.16: Short-term diffusion for increasing values of σ (DG-FR).

Diffusion curves from non-modal analysis are depicted in Figs. 5.15–5.17. Positive values (*i.e.*, anti-diffusion behaviour) are observed employing only the SD and the SD-FR methods in the random signal case. As already observed for the linear advection case, the SD-FR and SD curves are charac-

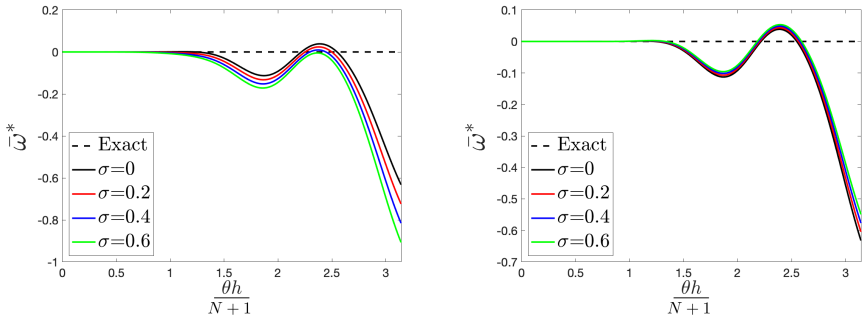

(a) Sinusoidal advection (b) Random advection

Figure 5.17: Short-term diffusion for increasing values of σ (SD).

terised by more regular profiles with respect to the DG-FR scheme, for which some larger variations can be observed in the high wavenumbers region in Figs. 5.15 and 5.16. It is interesting to notice that the sinusoidal advection velocity profile produces larger differences between the SD and the SD-FR methods with respect to the random signal advection velocity.

Concerning the influence of the σ parameter, diffusion plots for the DG-FR and the SD schemes are reported in Figs 5.16 and 5.17. Considering the sinusoidal advection velocity case first, when σ is increased, the DG-FR method tends to be more dissipative for all wavenumbers (the same behaviour is observed for the SD scheme). On the other hand, in terms of overall smoothness, an extra local minimum appears in the high wavenumbers region, reducing the regularity of diffusion curves, whereas no relevant profile variations are noticed for the SD scheme. In general, sensitivity to σ is milder when using the SD scheme, which is a desirable feature in term of outcome predictability. Considering the random advection velocity case, variations in the diffusion curves for different values of σ are smaller for both the SD and the DG-FR schemes.

5.6.4 Summary

The use of non-homogeneous advection velocities, as shown in this section, can lead to some differences between the SD and SD-FR schemes. According to temporal analysis, the deviations between the SD and the SD-FR are noticeable in both dispersion and diffusion curves, whereas, in the spatial analysis, differences are mostly present in the diffusion curves. Spatial dispersive errors are in fact less affected by the inhomogeneity of the advection velocity (Figs. 5.13 (a) and (b)) compared to their temporal counterparts (Figs. 5.12 (a) and (b)).

The importance of the parameter σ has been studied through non-modal analysis in the case of fully-upwind fluxes. The overall influence of the inho-

mogeneity parameter appears to be milder using the SD scheme with respect to the DG-FR, in particular for the sinusoidal advection velocity (Figs. 5.16 (a) and 5.17 (a)). For increasing values of σ the DG-FR develops additional oscillations on the diffusive curves whereas the behaviour of the SD diffusive curves are more regular.

In general, the SD and the SD-FR schemes behave similarly in the well-resolved regions, both in terms of spatial and temporal eigenanalysis. Differences are in fact larger for high wavenumbers, which are particularly important in under-resolved turbulent simulations. In this wavenumber region, even little discrepancies between the two methods could ultimately lead to complete different results in practical applications. This is certainly one of the most limiting factors when performing ILES with these kind of numerical methods: the combination between mesh size, numerical flux and order of approximation needs to be carefully chosen in order to obtain a level of dissipation which mimics the influence of unresolved scales on the large scale dynamics. Although, in the literature, third- and fourth-order ILES with discontinuous finite element methods generally provide satisfactory results, higher orders will certainly need additional dissipation in the high-wavenumbers region. This kind of analysis is therefore a useful tool for the design of dynamic SGS models which should be active only for high wavenumbers. It is then relevant to highlight how numerical diffusion, in general, has neither a positive nor negative connotation in the present discussions. In some cases, for very specific choices, it can be used as an implicit SGS model able to efficiently dissipate small scale fluctuations. On the other hand, if insufficient, can otherwise lead to unstable computations. Thus, the objective of a broad comparative study of spectral techniques applied to different numerical schemes should not be interpreted as a precise recipe to determine which numerical method is best. The final aim, instead, is a deeper knowledge on *each* specific numerical scheme, providing a rich set of tools that can be used to design tailored SGS models for high-order discretisations.

5.7 Numerical results

5.7.1 Temporally evolving turbulence: Taylor-Green Vortex

The Taylor-Green Vortex (TGV) constitutes a well-established test case to study vortex dynamics, turbulent transition, turbulent decay and energy dissipation processes in a three-dimensional setting [93]. It represents a perfect example of temporally evolving turbulence where classical temporal eigenanalysis can be tested. The problem consist of a cubic domain $[-L\pi, L\pi]^3$ with periodic boundary conditions applied to all faces starting from the

smooth initial condition

$$\begin{aligned}
&\rho = \rho_0, \\
&\mathbf{u} = U_0 \begin{pmatrix} \sin(\xi)\cos(\eta)\cos(\zeta) \\ -\cos(\xi)\sin(\eta)\cos(\zeta) \\ 0 \end{pmatrix}, \\
&p = P_0 + \frac{\rho_0 U_0^2}{16}\left[\cos(2\xi) + \cos(2\eta)\right]\left[\cos(2\zeta) + 2\right],
\end{aligned}$$

where $\xi = x/L$, $\eta = y/L$ and $\zeta = z/L$. Unity has been assigned to both U_0 and ρ_0, the reference velocity and density, respectively, and the initial value of the pressure P_0 has been chosen such that the corresponding initial Mach number is equal to 0.1. For this value of the Mach number, the flow is practically incompressible. The flow domain is subdivided in 64^3 uniform cubic elements and discretised with a third-order SD scheme.

Despite the rather idealised and simple initial flow field, the TGV problem contains many different interesting features of turbulence. As the time advances, the vortex stretching process leads to a natural transition to isotropic turbulence, giving a perfect example of temporally evolving turbulence. Due to the absence of physical viscosity (inviscid flow), the energy of the fluctuating field cascades into smaller scales without any viscous dissipation, making the TGV a stringent test case for evaluating numerical dissipation [94].

Different phases of turbulence transition and development can be recognised. Before reaching the characteristic time $t \approx 4L/U_0$, the flow is laminar and it is fully resolved by the mesh and the numerical discretisation. After a transitional period, at $t \approx 7L/U_0$, the vortex stretching process breaks down and sub-grid scales mechanisms start to affect the solution. As predicted by the spectral analysis, the particular choice of the numerical flux employed will strongly affect the solution in the under-resolved phases (after $t \approx 7L/U_0$). In order to assess the influence of the numerical flux, ILES have been performed using Roe and Rusanov fluxes.

As pointed out in the previous test case, the former will lead to an upwind flux and the latter, under almost incompressible regime, to a strong upwinding. Therefore, in Figs. 5.18 numerical dissipation from temporal analysis is shown using upwind ($\alpha = 0$) and strong upwind fluxes ($\alpha = -50$); see Eqs. (5.5)–(5.6). As already observed by Manzanero, et al. [54], varying the upwind parameter α, the maximum level of dissipation is achieved around $\alpha = 0$ (upwind fluxes), while strongly negative values of α yields the opposite effect. In fact, very negligible levels of numerical dissipation can be observed using strongly upwinding fluxes, whereas upwind fluxes follow the classical behaviour already discussed in the previous theoretical sections.

To understand the influence of the Riemann solver on the different scales of the TGV flow, kinetic energy spectra have been computed in the fully

turbulent phase (namely, at $t = 9L/U_0$). As observed in multiple pa-

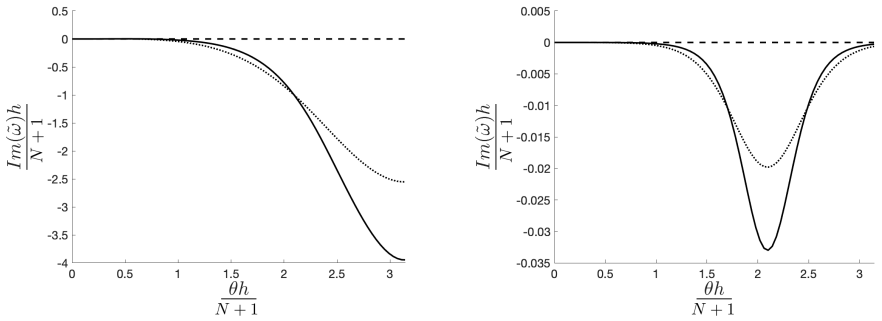

(a) $\alpha = 0.0$ (b) $\alpha = -50.0$

Figure 5.18: Numerical diffusion with standard upwind (left) and strong upwind (right): solid line, DG-FR; dotted line, SD-FR; dashed line, exact wave-like solution.

pers [62, 88, 95], and in total agreement with the herein presented analysis, the particular choice of numerical flux does not affect the large scales of the flow field. Closer to the inertial and dissipation range, instead, numerical diffusion plays a more important role. In this case, substantial differences between the two fluxes can be noticed: as shown in Fig. 5.19 the Roe flux is more dissipative for a wide range of scales while the Rusanov flux extends the inertial range till very close to the Nyquist wavenumber. These characteristics are well predicted by temporal eigenanalysis as shown in Figs. 5.18.

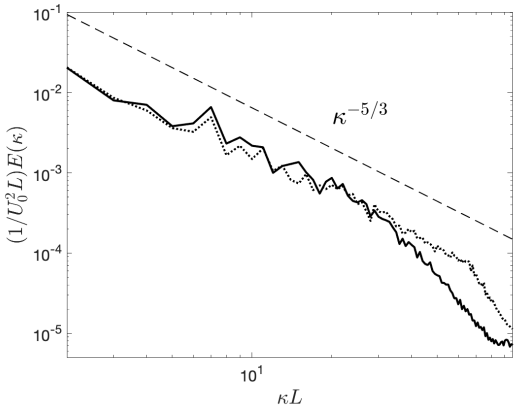

Figure 5.19: Kinetic energy spectra at $t = 9L/U_0$: solid line, Roe flux; dotted line, Rusanov flux.

A more detailed look of the high-wavenumber region is shown in Figs. 6.26 to emphasise such behaviour. Notice the similarity between Figs. 5.18 and

the corresponding spectra in Fig. 6.26. When the Rusanov flux is adopted, an extended inertial range can be observed till $\kappa \approx 70L$, where a weak dissipative region begins. On the other hand, using the Roe solver, dissipation is more well-distributed, providing a smother dissipative range till almost the Nyquist wavenumber. In the very high wavenumbers region, some kinetic energy accumulation can be noticed. This is a clear indication that, for the actual discretisation order and mesh resolution, additional diffusion via a SGS model is advisable.

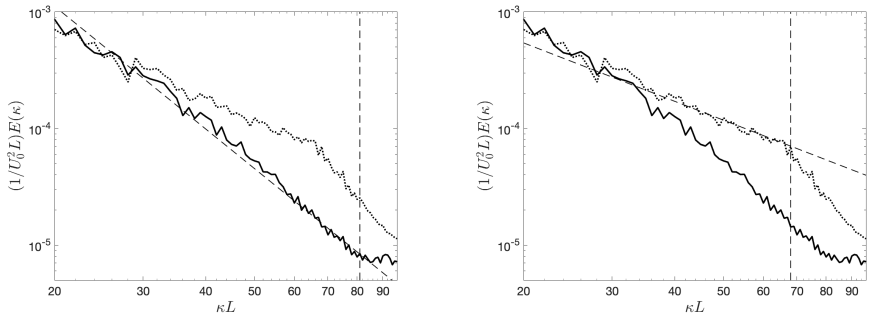

(a) Roe (b) Rusanov

Figure 5.20: Detailed look of Fig. 5.19: solid line, Roe flux; dotted line, Rusanov flux. Dashed lines have been used to highlight the different slopes in the high-wavenumber region.

5.7.2 Spatially evolving turbulence: duct flow

Duct flow simulations have been performed using SD scheme and then compared with DG simulations presented in [80]. The computational domain consists of a rectangular domain of dimensions $[L_x, L_y] = [20\pi, 2\pi]$. It could be argued that an inviscid, two-dimensional simulation provides an unphysical, under-resolved manufactured turbulence. Nevertheless, in order to understand the dissipative role of the numerical scheme, the current setting gives the same macro-behaviour expected in more realistic three-dimensional and viscous configurations. Moreover, the use of Euler equations is a common technique to study the influence of numerics, as the numerical method itself is the only dissipative mechanism acting on the flow. In this way, it can be isolated from molecular viscosity and SGS modelling (if present).

Free slip boundary conditions are applied to $y = \pm\pi$ and inlet conditions

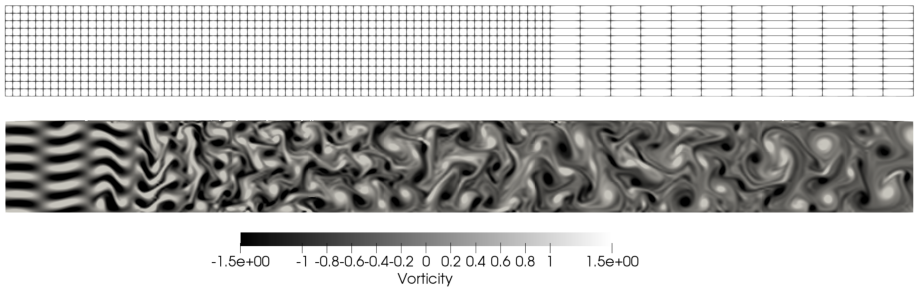

Figure 5.21: Example of mesh and flow configuration adopted.

are prescribed as:

$$\begin{aligned} \rho &= \rho_\infty, \\ \mathbf{u} &= u_\infty \begin{pmatrix} 1 + A\sin(Ky)\sin(\Omega t) \\ 0 \end{pmatrix}, \\ p &= p_\infty, \end{aligned}$$

where $\rho_\infty = 1$, $u_\infty = 1$ and p_∞ is set in order to get a desired value of inflow Mach number, $p_\infty = (\rho_\infty u_\infty^2)/(\gamma \mathrm{Ma}^2)$. The parameters defining the inflow perturbations have been set as $A = 1/2$, $K = 5$, $\Omega = 1$. Finally, in agreement with the simulations presented by Mengaldo, et al. [80], far-field conditions (ρ_∞, u_∞ and p_∞) have been used to compute numerical fluxes at the outlet boundary.

In the following simulations two different Riemann solvers have been used: the Roe's solver, representative of the classical upwinding approach, and the Rusanov solver, which can lead to hyper-upwinding for low Mach number simulations.

In order to trigger a sufficiently wide range of scales, two meshes have been considered: one consists of a homogeneous rectangular mesh of 120×12 elements and a second non-homogeneous mesh is modified with coarsening in the final part of the domain. Mesh coarsening starts at $x = 12\pi$, the first block is discretised with 72×12 elements while the second with 12×12 elements imposing a severe under-resolution. A sketch of the flow configuration is shown in Fig. 5.21. The simulations here considered use a 6th-order accurate SD scheme. Of course, being the main objective the evaluation of numerical dissipation, no SGS modelling has been added to the set of equations.

The results obtained with the SD solver using the Rusanov and Roe fluxes are reported, respectively, in Figs. 5.22 and 5.23. As already observed in [80], the Rusanov flux is less accurate than the Roe flux due to the presence of spurious modes and numerical oscillations are clearly visible close to the outlet and (to a minor extent) at the mesh coarsening interface. The Roe

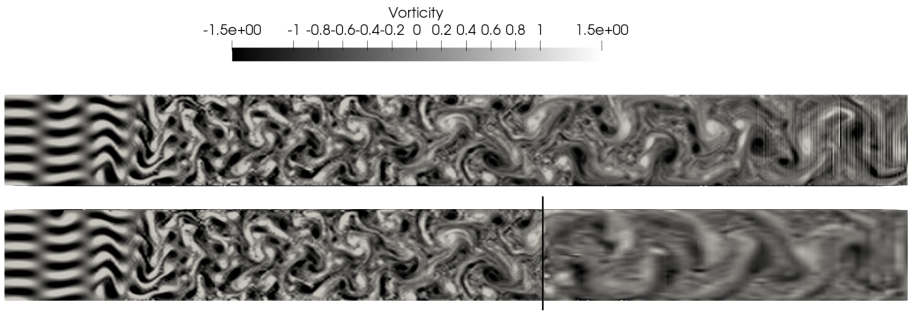

Figure 5.22: Vorticity magnitude using Rusanov Flux with and without mesh coarsening (Ma = 0.03). Black vertical line denotes the beginning of the second block.

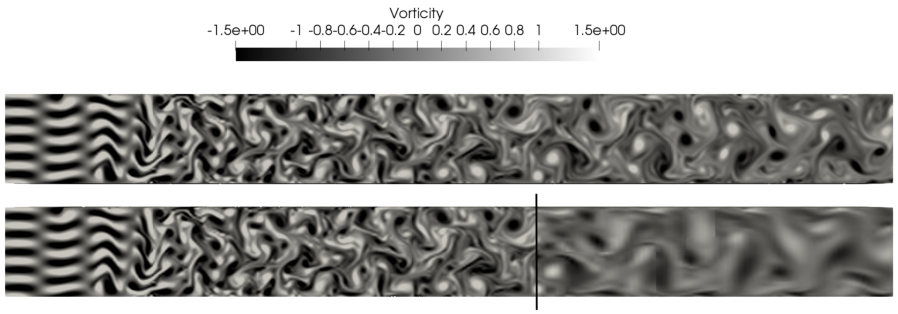

Figure 5.23: Vorticity magnitude using Roe Flux with and without mesh coarsening (Ma = 0.03). Black vertical line denotes the beginning of the second block.

flux, instead, thanks to the absence of spurious modes, gives good results also with the coarse mesh. Moreover, the smooth variation of dissipation across frequencies shown in the previous sections, as opposed to the dissipative bubbles observed using central fluxes, suggests a smoother energy transition between scales, providing better results.

For higher Mach numbers, the hyper-upwinding character of Rusanov flux should be less pronounced and results are expected to be similar to those obtained using the Roe flux. In order to verify such behaviour, the same test has been performed at a higher Mach number (Ma = 0.3). As clearly visible in Figs. 5.24 and 5.25, results do not differ excessively.

Finally, a direct comparison between SD3D and Nektar++ simulations is presented. Nektar++ [96] is a tensor product-based finite element package, based on the DG method formulation, designed to allow the construction of efficient classical low polynomial order h-type solvers as well as higher p-order piecewise polynomial order solvers. The test case simulation at

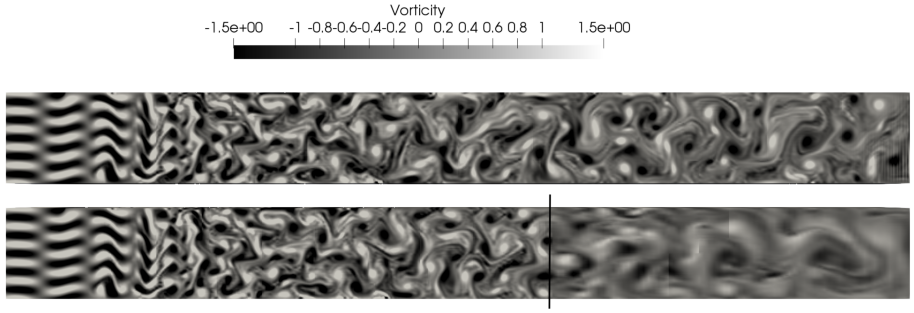

Figure 5.24: Vorticity magnitude using Rusanov Flux with and without mesh coarsening (Ma = 0.3). Black vertical line denotes the beginning of the second block.

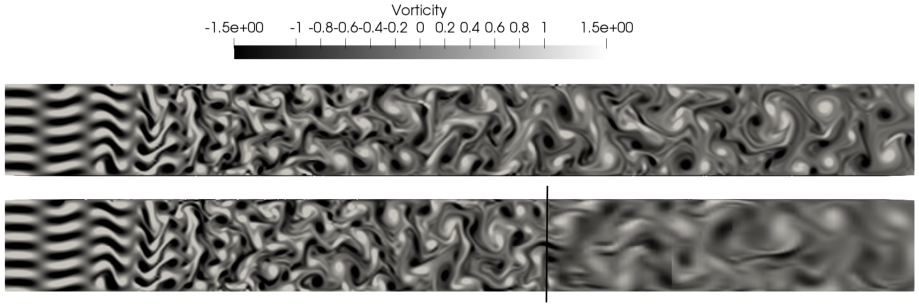

Figure 5.25: Vorticity magnitude using Roe Flux with and without mesh coarsening (Ma = 0.3). Black vertical line denotes the beginning of the second block.

Ma = 0.03 has been here considered using the Rusanov numerical flux. As already said, spurious reflections are expected at the mesh coarsening interface and at the outlet boundary. From Figs. 5.26 and 5.27, weaker reflections are observed using the SD scheme, compared to the DG method. Different interpretations can arise from such results. From the theoretical dispersion/diffusion analysis, a stronger spatial dissipation has been observed using the SD scheme compared to the DG scheme (*cf.* Fig. 5.4), in particular in the high-wavenumbers region. Accordingly, high-frequency oscillations are smoothed out more efficiently by the dissipation of the SD numerical scheme. A different interpretation can instead be sought in the non-constant advection velocity analysis. In previous sections, spatial diffusion curves using hyper-upwind have shown relevant differences between the DG-FR and the SD schemes (see Fig. 5.14). Indeed, a smoother distribution has been noticed using the SD method for increasing levels of inhomogeneity in the advection velocity. A higher regularity of spatial diffusive curves could then partially explain the reduced presence of spurious oscillations in the SD sim-

ulations. The results reported in this section demonstrates how the spectral analysis can provide some useful hints to the role of numerics in computing under-resolved turbulent flows. Indeed, assumptions such as homogeneity, linearity and one-dimensionality are certainly unsuitable to fully describe complex turbulent flows. Nevertheless, such a simple modelling can still well predict the macro-behaviour of the numerical scheme, so relevant for the physical description of the problem.

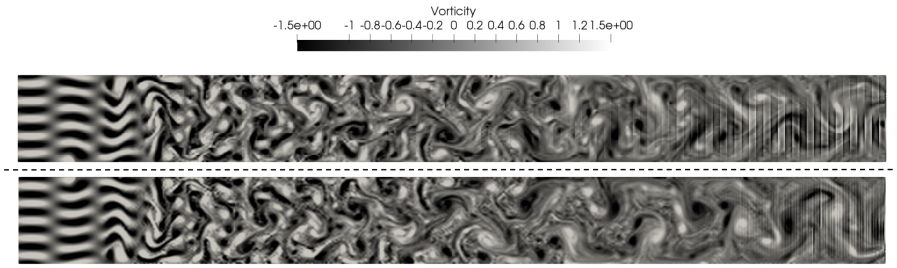

Figure 5.26: Vorticity magnitude using Rusanov Flux with Ma = 0.03 using DG (up) and SD (down). Black vertical line denotes the beginning of the second block and the horizontal dashed line indicates a symmetry axis to facilitate the comparison.

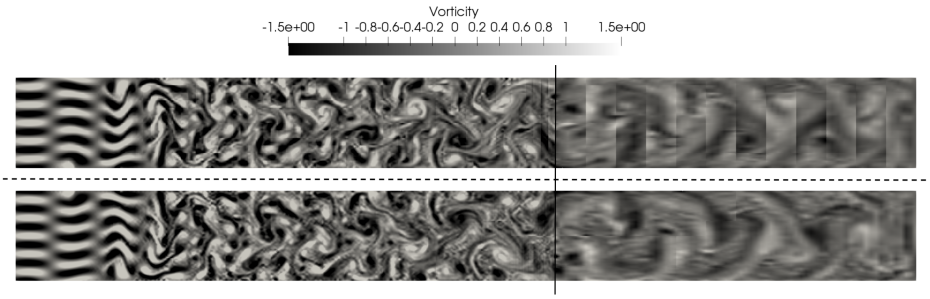

Figure 5.27: Vorticity magnitude using Rusanov Flux with Ma = 0.03 using DG (up) and SD (down) with mesh coarsening. Black vertical line denotes the beginning of the second block and the horizontal dashed line indicates a symmetry axis to facilitate the comparison.

5.8 Conclusions

A comprehensive spectral analysis of high-order schemes has been here performed and numerically tested. In particular, the classical temporal approach [77] has been presented along with the more recent spatial and non-modal analyses [79, 80, 88]. All these techniques have been applied to the

Flux Reconstruction methods [77, 89], in particular, those recovering the nodal Discontinuous Galerkin and the Spectral Difference schemes for linear advection, as well as to the improved Spectral Difference scheme by Liang and Jameson [91, 92, 48]. A generalisation to the non-constant, one-dimensional conservation law has been presented, following the guidelines proposed by Manzanero et al. [86, 87] for non-homogeneous linear advection equations. Classical spectral analyses applied to the standard constant-velocity advection equation provide useful insights in the role of the numerical scheme in the simulation of complex physical systems. Each analysis contributes singularly, highlighting different aspects of the interaction between physics and numerics. Nevertheless, such a simplified approximation can be sometimes inappropriate. The generalisation to non-constant advection velocities yields deeper informations on dispersion and dissipation errors induced by the numerical scheme in more realistic conditions, leading, eventually, to a better understanding of the reliability of high-order ILES. Furthermore, non-constant advection velocities allow to study a larger set of numerical schemes which would act identically for the most simple linear advection case (for example, SD-FR and SD).

In the comparison of numerical dispersion and diffusion errors produced by such schemes, it has been observed a stronger temporal dissipation using the DG-FR scheme, compared to the SD-FR scheme, while this particular behaviour is inverted considering spatial eigenanalysis, where SD-FR appears to be more dissipative. Furthermore, the DG-FR is more dissipative for temporally evolving spatial oscillations, whereas the SD-FR is more dissipative for spatially evolving temporal oscillations. Considering non-constant advection velocities, two different functional forms have been considered: a sinusoidal function and a random signal with unitary mean and prescribed variance. Although they may be considered oversimplified choices to describe realistic flows, the proposed advection velocities are sufficiently complex to give important hints in the role played by numerics in such conditions. Varying the level of inhomogeneity, the SD scheme has shown weaker sensitivity to advection velocity variations with respect to FR methods. Temporal eigenanalysis has show similar behaviours between the SD and the SD-FR schemes both in terms of dispersion and diffusion. In the spatial analysis, instead, deviations between the two schemes have been mainly noticed in the diffusive curves, which have been studied in the case of standard and strongly upwind numerical fluxes. The general observation is that the SD scheme seems to be more dissipative. Additionally, in the case of non-upwind fluxes, smoother profiles of numerical diffusion has been reported. Typical dissipative bubbles tend in fact to blend together for increasing levels of inhomogeneity in the advection velocity. Such behaviour suggest a more robust discretisation for complex flows.

Theoretical findings have been verified through a series of numerical experiments. The constant-velocity advection equation with a prescribed inlet

condition has been discretised using the SD scheme in order to verify spatial eigenanalysis results. Dissipative bubbles, typical of central fluxes, have been observed as in [80], in accordance with spatial eigenanalysis theory.

Considering more complex configurations, the SD scheme has shown stronger dissipation for spatially evolving turbulence. A duct flow with time-dependent inlet boundary condition has been modelled using Euler equations and two different type of numerical fluxes have been employed: Roe and Rusanov fluxes. For low Mach numbers the latter produces fluxes which mimic strong upwinding. In such conditions, spurious reflections due to grid coarsening and outlet boundary conditions, already observed in [80], have been noticed in the present simulations too. Nevertheless, the magnitude of these spurious perturbations appears to be smaller, and in good agreement with spatial eigenanalysis theoretical results, where the SD scheme is expected to be more dissipative.

As an example of temporally evolving turbulence, simulations of Taylor-Green vortex have been performed. Energy transfers between scales have been evaluated through the kinetic energy spectrum in the fully-turbulent phase ($t = 9L/U_0$). Results show a good agreement with temporal eigenanalysis. The use of hyper-upwinding (Rusanov flux) provides a long inertial range suddenly interrupted by a weak dissipative region at very small scales. Classical upwinding (Roe flux), instead, is characterised by a smoother transition between the inertial and the dissipative ranges. In agreement with the temporal eigenanalysis, excessive upwinding (Rusanov flux) produces counterintuitive results, leading to lower dissipation compared to the classical upwinding (Roe flux). Nevertheless, using the Roe flux, a slight accumulation of kinetic energy for high wavenumbers has been noticed due to the insufficient level of numerical dissipation in this region.

It is then clearly evident that upwind fluxes are the most suitable choice for ILES computations. In spite of this, the order of approximation and, consequently, the level of accuracy of the approximation, plays a very important role and can easily lead to insufficient or excessive levels of dissipation. High-order discretisations, typically of order three to four, employing upwind fluxes are commonly used in the literature to perform ILES (mostly using DG-based solvers). Higher orders are instead unfeasible due to the insufficient level of numerical dissipation at the smallest scales. Spectral analyses, like those herein presented, can then be used as a very useful tool in the design of dynamical explicit SGS models which adapt the level of dissipation based on the order of approximation.

Chapter 6

Explicit high-order Sub-Grid Scales modelling

Contents

6.1 Introduction: Implicit vs Explicit LES

In the previous chapter the general problem of turbulence has been treated from a mathematical point of view. More specifically, the approach commonly known as "Large-Eddy Simulations" has been introduced in chapter 3. Concepts such as "filtered equations" and "eddy-viscosity models" have been discussed from a theoretical perspective. Chapter 4, instead, was focused on

the numerical set-up. The high-order Spectral Difference scheme was analysed in detail, starting from the interpolation and differentiation operators to the definition of inviscid and viscous numerical fluxes. Sub-Grid Scales modelling and the Spectral Difference method have been presented separately to simplify the discussion. Nonetheless, in practical under-resolved flows, the interaction between spatial discretisation and turbulence modelling often represent a crucial point in the reliability of the numerical simulation. In chapter 5, the influence of the numerical scheme for under-resolved flows was analysed using spectral eigen-analsysis and relevant numerical experiments. In the present chapter, instead, the discussion will take one more step forward, analysing how intrinsic numerical properties such as numerical dissipation and dispersion can be taken into account in the development of SGS models.

In the practice of numerical simulations, truncation errors associated to discretisation schemes can not be fully avoided whenever under-resolution is present [21]. These errors can significantly perturb the flow physics expected from the solution of the first principle equations. Normally, low order spectral element methods lead to a strong, numerically-induced, dissipation injected in the system. High robustness and implementational simplicity are then paid at the price of a poor description of a non-negligible part of the flow scales, which are irreversibly dissipated. High-order methods, instead, introduce a very low level of numerical dissipation which, on the one hand, implies a better representation of small scales and, on the other, makes the computation more susceptible to undergo stability issues. Accordingly, one of the stumbling-block in the high-order Large Eddy Simulations community lies in the development of a robust theoretical framework, which would relate truncation errors of the numerical discretisation scheme and turbulence under-resolution.

In the context of the so-called Implicit Large Eddy Simulations, the numerical dissipation associated to the scheme is calibrated to model energy transfers along scales [97, 62, 63, 64, 65, 66]. However, the choice of order of accuracy, mesh resolution, and numerical flux may influence strongly the success or failure of these approaches. This is particularly true for certain classes of high-order methods, such as the spectral element methods [67], for which the order of accuracy is a user-selectable parameter of the computation.

The shortcomings and advantages of ILES have been widely discussed in the last decades [98, 99, 100], with a rising interest in the theoretical relation between upwinding/non-oscillatory high-order schemes and numerical dissipation in under-resolved turbulent flows. Nevertheless, a fully generic and clear connection between them is not yet fully understood for complex flows.

Within the framework of high-order discontinuous finite element methods, in particular, recent works on LES modeling strategies for the spectral difference scheme [44, 45, 46], have highlighted the inability of the ILES to

provide consistent and controlled reproduction of sub-grid scale interactions when different orders of accuracy are selected [101, 102, 103]. This, in turn, is a major drawback in view of applications of high-order methods as predictive tools for engineering.

The present chapter will start the discussion on this point. The Spectral Element Dynamic Model, which was just briefly mentioned in chapter 3, will be herein fully analysed and discussed. Firstly, the main concepts of the original work by Chapelier & Lodato [1] will be introduced. Secondly, a series of Large-Eddy Simulations using the SEDM will be considered with a special focus on transition to turbulence. Part of the work presented in this chapter has been published in two different "Flow, Turbulence and Combustion" papers [17, 16] (https://doi.org/10.1007/s10494-021-00273-y, https://doi.org/10.1007/s10494-021-00262-1).

6.2 Spectral Element Dynamic Model

The Spectral Element Dynamic Model [1] defines a constant kinematic eddy-viscosity within the element of the SD discretisation as:

$$\nu_t^n = C_{\mathrm{SEDM}}^2 f(\sigma_n) \Delta_n \sqrt{k_n}\,, \tag{6.1}$$

where Δ_n is an estimate of the local cutoff length scale, $f(\sigma_n)$ is a spectral turbulence sensor, C_{SEDM} is a model constant and k_n is an estimate of the SGS turbulent kinetic energy within the element defined as:

$$k_n = \frac{1}{2}\Big(\langle \widetilde{\mathbf{u}}_n \cdot \widetilde{\mathbf{u}}_n \rangle - \langle \widetilde{\mathbf{u}}_n \rangle \cdot \langle \widetilde{\mathbf{u}}_n \rangle \Big), \tag{6.2}$$

where $\langle \cdot \rangle$ denotes spatial averaging within the element.

6.2.1 Turbulence sensor

In chapter 3, the Spectral Element Dynamic was only briefly introduced because the concept of numerical diffusion/dispersion had not been presented yet. The functional form of the SEDM is, in fact, quite simple and straightforward, whereas the delicate point in terms of interpretation and calibration is represented by the turbulence sensor. This particular object plays a fundamental role in the connection between the SGS model dissipation, which is essentially not particularly different with respect to other classical SGS models, and the numerical dissipation associated to numerical scheme.

The turbulence sensor, denoted as $f(\sigma_n)$, is a smooth function varying from 0 to 1 designed to quantify the local level of resolution of the LES

filtered field. The expression for $f(\sigma_n)$ reads:

$$f(\sigma_n) = \begin{cases} 1 & \text{for } \sigma_n < \sigma_{\text{thr}}, \\ \frac{1}{2}\left\{1 + \sin\left[\frac{\pi(\sigma_{\text{t}} + \zeta - \sigma_n)}{2\zeta}\right]\right\} & \text{for } \sigma_{\text{thr}} \leq \sigma_n \leq \sigma_{\text{thr}} + 2\zeta\,, \\ 0 & \text{for } \sigma_n > \sigma_{\text{thr}} + 2\zeta\,, \end{cases} \tag{6.3}$$

The form of the turbulence sensor resembles the classical discontinuity sensor used by [7] for sub-sell shock-capturing. Defining a turbulence sensor which shares similarities with shock-capturing techniques can be an interesting feature in the development of a generalised SGS models for compressible flows, where both shocks and turbulence under-resolution are treated in a similar manner. More details and a deeper discussion on the connection between these two aspects will be furnished in chapter 8.

The calibration of the parameters involved is based on *a-priori* studies of isotropic turbulence decay. Details on the calibration procedure can be found in the original work by Chapelier & Lodato [1].

On the other hand, in order to better understand the behaviour of the SEDM, some further details will be provided on the computation of σ_n. The power decay σ_n is evaluated using the modal representation of the resolved velocity $\widetilde{\mathbf{u}}$. In particular, starting from the nodal values available from the simulation, the modes within the functional space spanned by Legendre polynomials are evaluated. Subsequently, one-dimensional spectra are computed along each direction and later averaged to give a sense of three-dimensionality. The final output of such procedure is a single kinetic energy spectrum representative of the velocity field within the spectral element. In more details, the modal projection can be very easily computed using the Vandermonde matrix. A pseudo kinetic energy spectrum along each direction can be computed as:

$$\mathbb{E}^m_{\hat{x}}(\hat{y}_j, \hat{z}_k) = \frac{1}{2}\sum_{d=1}^{3}\left(\sum_{s=0}^{N}\mathbb{V}^{-1}_{ms}\widetilde{u}_d(\hat{x}_s, \hat{y}_j, \hat{z}_k)\right)^2, \tag{6.4}$$

$$\mathbb{E}^m_{\hat{y}}(\hat{x}_i, \hat{z}_k) = \frac{1}{2}\sum_{d=1}^{3}\left(\sum_{s=0}^{N}\mathbb{V}^{-1}_{ms}\widetilde{u}_d(\hat{x}_i, \hat{y}_s, \hat{z}_k)\right)^2, \tag{6.5}$$

$$\mathbb{E}^m_{\hat{z}}(\hat{x}_i, \hat{y}_j) = \frac{1}{2}\sum_{d=1}^{3}\left(\sum_{s=0}^{N}\mathbb{V}^{-1}_{ms}\widetilde{u}_d(\hat{x}_i, \hat{y}_j, \hat{z}_s)\right)^2, \tag{6.6}$$

where $\mathbb{V}$ represents the Vandermonde matrix for the Legendre polynomials basis, and $\mathbb{E}^m$ indicate the m-th modal component of the kinetic energy spectrum along a given direction. Subsequently, the kinetic energy spectra along each direction are averaged within the element as follows:

$$\mathbb{E}^m_{\Omega_n} = \frac{1}{3(N+1)^2}\left[\sum_{j,k=0}^{N}\mathbb{E}^m_{\hat{x}}(\hat{y}_j, \hat{z}_k) + \sum_{i,k=0}^{N}\mathbb{E}^m_{\hat{y}}(\hat{x}_i, \hat{z}_k) + \sum_{i,j=0}^{N}\mathbb{E}^m_{\hat{z}}(\hat{x}_i, \hat{y}_j)\right]. \tag{6.7}$$

An exponential representation is then assumed for the averaged kinetic energy spectrum on the element Ω_n in the form $\mathbb{E}_{\Omega_n} \propto m^{-\sigma_n}$ $(m = 1, ..., N)$. The zero-th mode, which corresponds to the mean kinetic energy, is not considered for the evaluation of the modal energetic decay in order to evaluate only the fluctuating component of the velocity field. Finally, the exponent σ_n is estimated using a least square expression:

$$\sigma_n = \frac{N \sum_{m=1}^{N} \ln(m) \ln(\mathbb{E}^m_{\Omega_n}) - \sum_{m=1}^{N} \ln(m) \sum_{m=1}^{N} \ln(\mathbb{E}^m_{\Omega_n})}{N \sum_{m=1}^{N} \Big(\ln(m) \Big)^2 - \Big(\sum_{m=1}^{N} \ln(m) \Big)^2}. \tag{6.8}$$

6.2.2 Taylor-Green Vortex

In the original paper, both for the calibration and validation purposes, a very useful canonical flow has been considered: the Taylor-Green Vortex [93]. Such test case is particularly useful to study transition to turbulence as it is characterised by a first laminar phase which ends in a fully turbulent configuration after approximately 10 characteristic time steps. Such configuration is therefore appealing to evaluate the ability of SGS models to accurately represent laminar-to-turbulent transition. In the framework of Large-Eddy Simulation of the Taylor-Green Vortex, the balance of total kinetic energy averaged on the domain can be a useful source of informations on the dissipative character of SGS model. For low Mach numbers, the balance of the normalised integrated kinetic energy reads

$$-\frac{\mathrm{d}E_k}{\mathrm{d}t} = \varepsilon_{\mathrm{vis}} + \varepsilon_{\mathrm{SGS}} + \varepsilon_{\mathrm{num}}, \tag{6.9}$$

where

$$E_k = \frac{1}{\Omega} \int_\Omega \frac{1}{2} \rho \widetilde{u}_i \widetilde{u}_i d\Omega, \tag{6.10}$$

$$\varepsilon_{\mathrm{vis}} = \frac{2\nu}{\Omega} \int_\Omega \widetilde{S}_{ij} \widetilde{S}_{ij} d\Omega, \tag{6.11}$$

$$\varepsilon_{\mathrm{SGS}} = \frac{2}{\Omega} \int_\Omega \nu_t \widetilde{S}_{ij} \widetilde{S}_{ij} d\Omega, \tag{6.12}$$

and $\varepsilon_{\mathrm{num}} = -\frac{\mathrm{d}E_k}{\mathrm{d}t} - \varepsilon_{\mathrm{vis}} - \varepsilon_{\mathrm{SGS}}$. Particular attention is also focused on the combined effect of both numerical and SGS dissipation:

$$\varepsilon^{\mathrm{tot}}_{\mathrm{SGS}} = \varepsilon_{\mathrm{SGS}} + \varepsilon_{\mathrm{num}}. \tag{6.13}$$

As already introduced in chapter 5, larger order of approximations are associated to a reduced level of numerical dissipation. How numerical dissipation is distributed in the wavenumber domain can vary significantly depending on the numerical scheme used for discretisation. This tendency applies

also in more complex conditions such as in the case of the fully viscous Navier-Stokes equations. In Fig. 6.1, numerical dissipation, evaluated as in Eq. (6.13), is shown for the TGV case for different orders of approximation. The magnitude of ε_{num} is larger for low orders whereas it gets smaller and smaller increasing the order of approximation. Furthermore, numerical dissipation follows the very desirable feature of null dissipation in the first laminar/transient phase for $t < 4$. It is then clear that the levels of dissipation injected by the SGS model need to vary consistently with the order. In other words, for low orders of approximation, numerical dissipation can be sufficiently large to mimic the dissipative nature of unresolved scales. On the other hand, for higher orders, numerical diffusion gets weaker and explicit SGS modelling is necessary to maintain the simulation stable and accurate. At the same time, an hypothetical SGS model for the TGV flow should ideally preserve the ability of numerical dissipation to grow significantly only when the flow becomes under-resolved. In this sense, for the same simula-

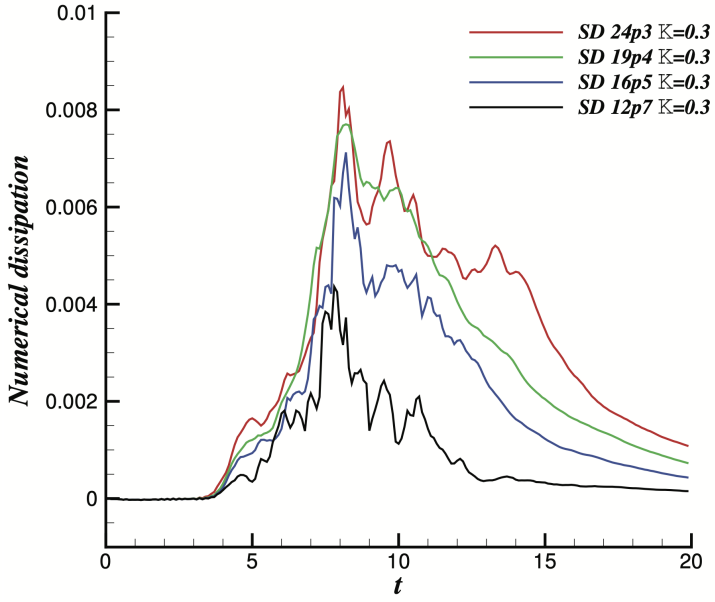

Figure 6.1: Numerical dissipation of resolved kinetic energy ε_{num} for varying order of approximation. (Fig. from [1]).

tions, in Fig. 6.2 the explicit dissipation of the SEDM model is shown. As already anticipated, the SEDM is capable of dynamically adapt the levels of dissipation injected in the system. In the case of low order, the model is essentially inactive, leaving to numerical diffusion the role of build-in SGS model, whereas, for higher orders, the model dissipation gets stronger and stronger to maintain the simulation stable. Furthermore, for any order, the use of a turbulence sensor able to detect under-resolution makes the model

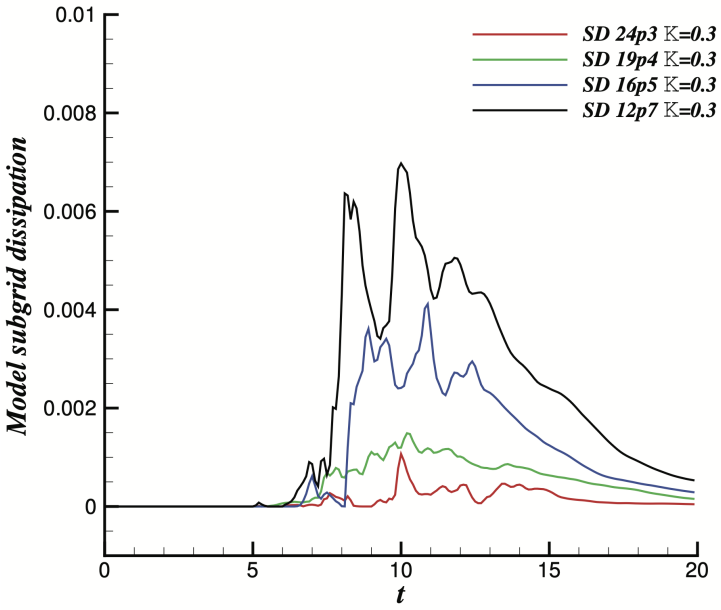

Figure 6.2: Explicit SGS dissipation of resolved kinetic energy ε_{SGS} for varying order of approximation. (Fig. from [1]).

always inactive for times smaller $t < 4$. Classical models such as Smagorinsky model, for example, are active also in the laminar/transient phase, causing an over-dissipation of the flow field. Of course, for some intermediate orders of approximation, numerical dissipation can be sufficiently large to keep the simulation stable and, at the same time, small enough not to over-dissipate the small scale fluctuations. Finding such equilibrium point can be a very difficult task to achieve. The SEDM tries to circumnavigate the issue providing adapting levels of dissipation based on the order of approximation and on the local resolution of the numerical scheme.

6.3 Bypass transition on a zero-pressure-gradient flat plate

The prediction of laminar to turbulent transition is an important problem in the field of aerodynamics and turbo-machinery. One of the most extensively studied cases of transition, is the transition of a zero-pressure-gradient smooth flat-plate boundary layer (ZPGSFPBL). Two principle transition mechanisms exist in nature. At low levels of freestream turbulence intensity ($Tu < 1\%$), natural transition occurs [104]. This is characterised by the development of two-dimensional Tollmien-Schlichting (TS) waves (primary instability), which grow in amplitude along the streamwise direction.

When the amplitude of the TS waves reaches a certain magnitude (usually at Reynolds numbers of $\mathcal{O}(10^6)$), three-dimensional secondary instabilities develop, which finally breakdown into fully turbulent flow. It is possible to trigger transition further upstream simply by increasing the freestream turbulence intensity. This produces bypass transition [105], in which the mechanism of the TS waves is skipped and instead, the flow goes from laminar to turbulent over a relatively narrow range of Reynolds numbers, usually of $\mathcal{O}(10^5)$.

Transitional flows have received a lot of attention in the recent past and as a result the mechanism of transition is relatively well understood. The predominant numerical approach to study bypass transition has been via DNS studies which are computationally quite expensive. Alternative numerical methods do exists in the form of Reynolds averaged Navier-Stokes modelling, which is widely prevalent in the industry. However, RANS models require extensive tuning to produce acceptable results for transitional cases. In recent years, large-eddy simulation in conjunction with high-order solvers have shown much potential in being a truly predictive tool for transition. Thus, in keeping with this theme, the present work focusses entirely upon the application and evaluation of LES models to bypass transition, specifically the experimental ERCOFTAC T3A test case (EXP-T3A), which is a well known example of ZPGSFPBL bypass transition. Although we work with a variety of LES models, our primary objective is to evaluate the spectral-element dynamic model (SEDM) of Ref. [1], since it exhibits several properties which are known to be useful in transitional flows.

The LES of ZPGSFPBL bypass transition was first undertaken in Ref. [106], using freestream turbulence of intensity 6%, in an attempt to reproduce the ERCOFTAC T3B test case. The model employed by them was the dynamic Smagorinsky model. They also performed implicit large eddy simulations by discarding the sub-grid model and instead using a significantly finer mesh. These simulations were termed as low-resolution simulations (LRS). Despite the low resolution, good qualitative agreement was achieved. They also demonstrated the importance of the wall-normal component of the velocity of the freestream turbulence in provoking the transition. The localized version of the dynamic Smagorinsky model was made use of in Ref. [107] on swept-wing boundary layers. Subsequently, [108] carried out one of the earliest controlled transition studies using the filtered-structure-function (FSF) model and a second-order finite difference code. This was a modified version of the original structure function model in Ref. [109], which was found to be too dissipative for transitional flows. They produced good results even with the limited grid resolution available. A more recent study on the ERCOFTAC T3A test case, which used a freestream turbulence of intensity 3%, was performed in Ref. [4]. A second-order finite volume scheme served as the numerical solver and a residual-based variational multi-scale (RB-VMS) style LES model was used. In this work the grid-convergence properties

of the VMS approach were clearly highlighted. More recently, several LES models were tested in Ref. [110] on controlled H-type and K-type transition using a 5^{th}-order accurate finite-difference code. A detailed comparison was made against the DNS. It was found that all the models exhibited an under-prediction of the skin-friction coefficient in both transitional and turbulent regions. Their conclusion was that only those models which introduced negligible sub-grid viscosity prior to transition were capable of allowing the transition process to occur. This is an important point whose effects are deeply discussed in this work. Finally, we mention the work in Ref. [111], on bypass transition over an adverse pressure gradient flat plate, wherein numerous LES models (dynamic Smagorinsky, mixed-time scale and WALE) were tested. They sought to test out the transition-prediction capabilities of various models and found that only the mixed-time scale model could successfully capture all the physical features and bore the strongest similarity to the DNS data.

The key conclusion of several of these studies was that negligible amounts of dissipation are required within the pre-transitional region of the flow. This is because the primary disturbances, called the 'Klebanoff modes', which are usually well resolved even on coarse grids, must be allowed to grow in amplitude until they reach the stage at which secondary instabilities may begin to develop. It is only within the transitional region, where the unresolved scales begin to grow rapidly, that the sub-grid models must begin to act. Thus in general, for flows which exhibit a high-degree of intermittency, the sub-grid eddy-viscosity must be applied in a manner which is local, both in physical and in wavenumber space. A distinct preference exists towards the application of the sub-grid eddy-viscosity within regions of low-resolution in physical space and upon the high wave-numbers. The bypass transition test case is ideal for testing these behaviours in LES models, since there exists two distinct regions of flow, one well-resolved and dominated by low wave-numbers (laminar region) and the other poorly-resolved and dominated by high wave-numbers (turbulent region).

The well documented behaviour of the ZPGSFPBL bypass transition [112, 113, 114, 2, 115, 116], makes an accurate comparison and evaluation possible. Despite this, LES studies of transition are quite rare in literature [111] since they tend to give rise to numerous complications. The primary complication is the interaction between the numerical dissipation and the sub-grid model dissipation, making it difficult to truly evaluate the model behaviour. To overcome this obstacle we make use of a high-order Spectral Difference solver [117] which introduces low levels of numerical dissipation and dispersion errors [118, 73] and hence allows the model's effects to dominate. A secondary concern, pertains to the specification of the inflow and means of forcing transition. When forcing transition by means of freestream disturbances, this difficulty encompasses not only the generation of synthetic turbulence, on an auxiliary mesh, with a behaviour comparable with that of

the experiment, but also the transfer of the synthetic turbulence to a highly under-resolved, and non-uniform LES mesh. We have utilised the technique put forth in Ref. [3]. The present approach makes use of synthetic turbulence, generated by the digital filter method in Ref. [119], of specific length-scale and intensity, injected at the inflow, at a certain height above the flat plate. The resulting freestream disturbance exhibits a streamwise behaviour very similar to that of the T3A case. Furthermore, the primary disturbance, induced within the pre-transitional boundary layer, closely matches the experimental data. Thus with grid refinement, the overall transition behaviour converges strongly towards the T3A experiment.

Thus with the tools outlined above, we seek to carry out LES studies of ZPGSFPBL bypass transition with settings designed to reproduce the conditions of the ERCOFTAC T3A test case. Our objective is to test the transition-prediction capabilities of SEDM. We also utilise the WALE and SIGMA models as reference. Direct comparisons are made between the LES simulations and the experimental T3A data for quantities such as the skin-friction coefficient, fluctuating stresses and sub-grid eddy-viscosity. A grid-convergence study is also performed to reveal the convergence characteristics of the models.

6.3.1 Computational domain and boundary conditions

The simulations are carried out within a hexahedral computational domain, starting downstream of the flat plate leading edge. The domain extension is such that $10^4 \leq Re_x \leq 5 \times 10^5$, x being the distance from the flat plate leading edge. Transition for the T3A case, generally occurs for $1.1 \times 10^5 \leq Re_x \leq 3.1 \times 10^5$. The domain height is three times the height of the turbulent boundary layer at the outflow and the width of the domain is equal to the height of the turbulent boundary layer at the outflow. While the streamwise and wall-normal dimensions are nearly identical to the domain used in the DNS in Ref. [2], the spanwise width is only half that of the DNS. This was done primarily to keep down computational costs, however it is widely accepted that the spanwise scale of even the largest eddies in a turbulent boundary layer are generally smaller than turbulent boundary layer height [120]. The dimensions of the domain, normalised by the inflow boundary layer displacement thickness (δ^*_{in}), are presented in Tab. 6.1. A characteristic boundary condition is used at the inflow and a characteristic-based boundary condition, using extrapolated variables for the ghost state and exit pressure specified, is used at the outflow and freestream boundary. Finally, in the spanwise direction, periodic boundary conditions are employed and an adiabatic no-slip boundary condition is applied to the wall. The SD discretisation of the domain with these boundary conditions has been observed to be stable, consistent and convergent using a laminar Blasius profile test case.

Reynolds number range	$1.0 \times 10^4 - 5.0 \times 10^5$		
Fluid properties	Freestream density	ρ_∞	1.0 kg/m^3
	Kinematic Viscosity	ν	10^{-5} m^2/s
	Specific heat capacity (const. pressure)	c_p	1.006 kJ/kgK
	Specific heat ratio	γ	1.4
	Prandtl number	Pr	0.72
Domain details	Displacement thickness at inflow	δ^*_{in}	9.5×10^{-6} m
	Domain dimensions	H_x	$2847\delta^*_{\text{in}}$
		H_y	$214\delta^*_{\text{in}}$
		H_z	$71\delta^*_{\text{in}}$
Flow properties	Freestream Mach number	Ma_∞	0.5
	Freestream velocity	U_∞	188.0 m/s
	Bulk velocity (laminar flow)	U_{bulk}	187.0 m/s
	Freestream turbulence intensity	Tu	$3.0 - 3.5\%$
	Freestream turbulence integral length scale	L_{ii}	$10.92\delta^*_{\text{in}}$

Table 6.1: Parameters used in this study for the reproduction of the T3A experiment.

Grids

The domain is discretised by hexahedral elements, kept uniform in the streamwise and spanwise direction and stretched in the wall-normal direction using

Name	No. elements $(E_x \times E_y \times E_z)$	Stretching factor C_{str}	Scheme order (N+1)	Δx^+	Δy^+	Δz^+
Coarse	$40 \times 6 \times 3$	0.03	6	70	$\simeq 1$	24
Medium	$60 \times 8 \times 5$	0.04	6	47	$\simeq 1$	14
Fine	$80 \times 10 \times 6$	0.06	6	35	$\simeq 1$	11

Table 6.2: Computational grid details (the friction velocity, u_τ, used for normalisation is computed at $Re = 3.1 \times 10^5$, which is the skin-friction peak. An equidistant distribution of solution points within the element was assumed.)

an algebraic stretching function [108], defined as:

$$\epsilon_j = j/Ne_y, \quad \forall \ 0 \leq j \leq Ne_y, \tag{6.14}$$

$$y_j = H_y \frac{C_{\text{str}} \times \epsilon_j}{1 + C_{\text{str}} - \epsilon_j}, \tag{6.15}$$

where Ne_y is the number of elements in the wall-normal direction, C_{str} is the user specified stretching factor, H_y is the domain height and y_j is the co-ordinate of the upper boundary of element number j. The stretching factor has been adjusted for all grids, such that the first element has its upper boundary located at $y^+ \simeq 7$. Thus, with the use of a 6^{th}-order SD scheme, the first solution point is always located at $y^+ < 1$ and at least 10 points are present below $y^+ = 10$, thus providing sufficient wall resolution. It must be noted that since the distribution of the solution points, interior to the element, is unknown during the grid-generation process, we have calculated $\Delta x^+, \Delta y^+, \Delta z^+$ assuming equidistant interior solution points. However, in general due to the clustering of the solution points near the element boundaries, the true values are usually lower.

Three sets of grids are used for the LES computations, one coarse, one medium and one fine. Their nomenclature may be justified by comparing them with the DNS grid in Ref. [2] which utilises $2048 \times 180 \times 192$ points. Thus, as can be seen from Tab. 6.2, the coarse grid has approximately one-tenth the number of points of the DNS in the streamwise and spanwise dimension while having one-fifth the number of points in the wall-normal direction, with the medium grid having one and a half times and the fine grid having two times the number of elements as the coarse grid, along each direction. Thus overall the coarse grid contains nearly 500 times fewer number of points and the fine grid possesses nearly 70 times fewer number of points as compared to the DNS grid in Ref. [2]. This level of under-resolution is significantly greater than that used in prior studies of this case. For the sake of comparison, it must be pointed out, that the fine grid used in this study is nearly equivalent to the coarse grid used in the LES study in Ref. [4].

Freestream Disturbance

The properties of the freestream turbulence are crucial to obtain the correct behaviour of the ZPGSFPBL bypass transition case. Earlier studies in Ref. [3] have shown that it is possible to obtain a close agreement with the experimental T3A data by injecting synthetic turbulence of specific length-scale, L_{ii}, and turbulent intensity, Tu, over the laminar boundary layer at the inflow. This synthetic turbulence is produced, upon an auxiliary grid at the inflow plane, by the method put forth in Ref. [119]. This method makes use of digital filters in order to correlate three random fields of data, $R_\alpha, \alpha = x, y, z$, to produce a field at the inflow plane, $u'_\alpha(j, k)$, whose prop-

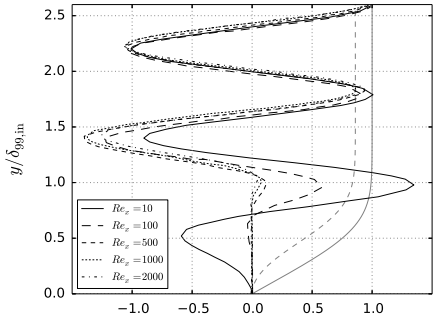

(a) Continuous modes of the Orr-Sommerfeld equation plotted at different Reynolds numbers (reproduced from Ref. [2]).

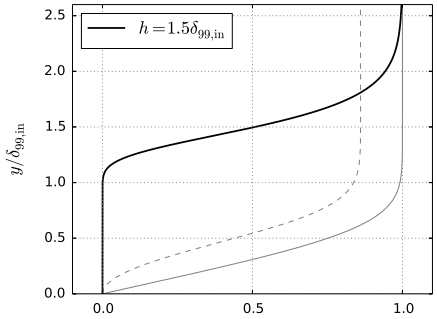

(b) Damping function behaviour with parameter $h = 1.5\delta_{99,\text{in}}$ plotted at $Re_x = 10^4$.

Figure 6.3: A comparison between the wall-normal basis used in the synthetic turbulence in Ref. [2] (figure on the left) and the damping function used to suppress fluctuations within the boundary layer (figure on the right). Blasius streamwise velocity component, u/U_∞ (——) and wall-normal velocity component, $v/U_\infty \times \sqrt{U_\infty x/\mu}$ (- - -), also shown for reference.

erties closely resemble those of the desired turbulent field:

$$u'_\alpha(j,k) = \sum_{i'=-N_x}^{N_x} \sum_{j'=-N_y}^{N_y} \sum_{k'=-N_z}^{N_z} b_{i'j'k'} R_\alpha(i', j+j', k+k'), \tag{6.16}$$

with $\overline{u'}_i = 0$ and $\overline{u'_i \cdot u'_j} = \delta_{ij}$ and where N_x, N_y, N_z represent the stencil of the filter $b_{i'j'k'}$. In order to account for the cross-correlations between the various velocity components, the method proposed in Ref. [121] is used. We define $u_i = \overline{u}_i + a_{ij}u'_j$ where:

$$a_{ij} = \begin{pmatrix} (R_{11})^{1/2} & 0 & 0 \\ R_{21}/a_{11} & (R_{22} - a_{21}^2)^{1/2} & 0 \\ R_{31}/a_{11} & (R_{32} - a_{21}a_{31})/a_{22} & (R_{33} - a_{31}^2 - a_{32}^2)^{1/2} \end{pmatrix}, \tag{6.17}$$

and where R_{ij} is the correlation tensor known *a priori* such as from experimental or DNS data. By setting the cross-correlation coefficients to zero in R_{ij}, homogeneous-isotropic synthetic turbulence may be obtained.

Finally, we can ensure that the fluctuations are confined solely within the freestream by making use of a van Driest type damping functions, given by

$$(1 - e^{-y/(0.137 \times h)})^{1000},$$

which is multiplied by all three components of the synthetic turbulent fluctuations at the inflow plane. This function, as seen in Fig. 6.3(b), undergoes

Name	Tu	$L_{11}/\delta^*_{\text{in}} = L_{22}/\delta^*_{\text{in}} = L_{33}/\delta^*_{\text{in}}$	$h/\delta_{99,\text{in}}$
COARSE	3.75%	10.92	1.5
MEDIUM	3.65%	10.92	1.5
FINE	3.5%	10.92	1.5

Table 6.3: Parameters for the generation of freestream turbulence for each grid used within this study.

a smooth change in value from 0 to 1. More specifically, it achieves a value of 0.5 at a height of h. This parameter, h, is user specified and strongly determines the transition behaviour as it controls the depth to which the freestream disturbance penetrates into the boundary layer at the inflow. It must be kept in mind that the choice of this function was completely arbitrary and its behaviour merely designed to mimic the continuous modes of the Orr-Sommerfeld spectrum as shown in Fig. 6.3(a). Experiments in Ref. [3] have provided us with suitable values for the turbulence intensity ($3.5\% \leq Tu \leq 3.75\%$), the length-scale ($L_{ii} = 10.92\delta^*_{\text{in}}$) and the height of injection of the synthetic turbulence ($h = 1.5\delta_{99,\text{in}}$). These values are presented within Table. 6.3. By using these parameters and a 6^{th}-order ILES approach, there is a strong trend of convergence towards the T3A experimental data. Finally, by making use of a grid with $780 \times 120 \times 48$ solution points (which we call U-FINE since it has better resolution than the FINE grid used within this study), a very close agreement is achieved with the T3A experimental data as can be observed from the comparison of the skin-friction coefficient and the streamwise component of the fluctuating stress (Fig. 6.4).

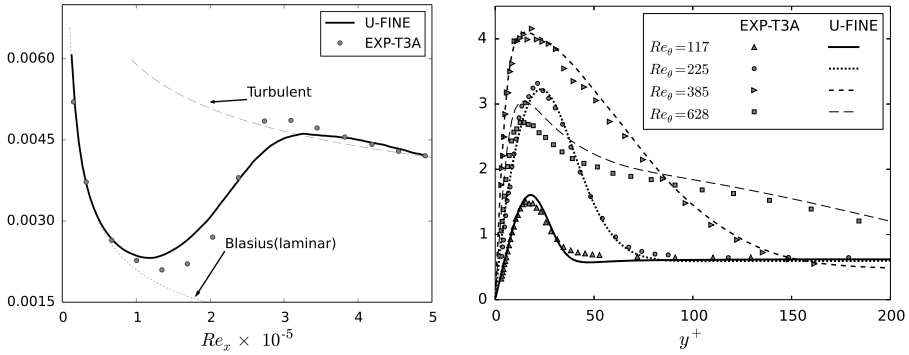

(a) C_f.

(b) u'_{rms}/u_τ at several streamwise locations.

Figure 6.4: T3A reproduction upon the ultra-fine grid using synthetic turbulence within the freestream (selected results from Ref. [3]).

6.3.2 Results and Discussion

The results presented within this section contain data from the simulations carried out with the three different LES models (WALE, SIGMA and SEDM), as well as the ILES, upon the three different LES grids (coarse, medium and fine). The data presented within this work represents the time-averaged quantities over the course of forty flow turn-over times, similar to that used in the study in Refs. [108] and [4] followed by a single spanwise averaging of the quantities of interest at the solution points. The statistical averaging has been commenced after a period of five flow turn-over times used to flush out any transients.

Behaviour of freestream intensity and fluctuating stresses close to inflow

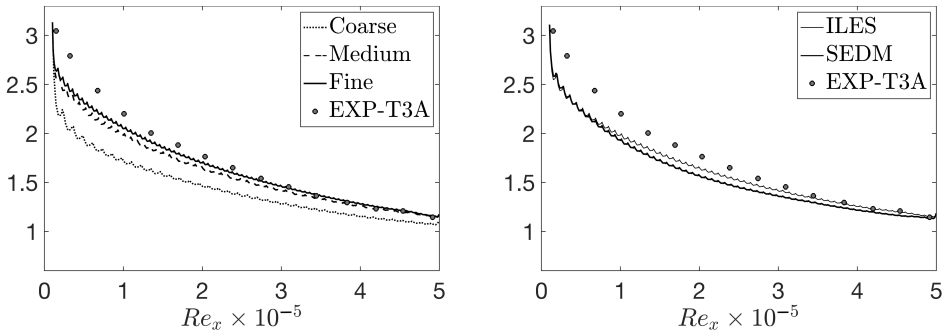

(a) Variation with grid resolution.

(b) Variation with sub-grid model (medium grid).

Figure 6.5: $\%Tu$ streamwise behaviour.

The grid and the numerical scheme have a strong influence upon the freestream behaviour. Once the parameters for the generation of the turbulence upon the auxiliary grid have been set, there is very little that can be done to control its streamwise evolution. The grid and numerical scheme affect, not only the total intensity, but also the homogeneity and isotropy of the freestream turbulence.

The curves in Fig. 6.5(a) show the freestream turbulence intensity upon the three different LES grids. The simulation is an ILES. We can easily observe the influence of the grid resolution upon the freestream turbulence intensity. In general, there appears to be a sharp initial drop in the freestream turbulence intensity, followed by slower decay. With grid refinement, the magnitude of the initial drop decreases, while the decay rate downstream of the drop increases (approaching the reference decay rate). This phenomenon tends to make it appear as if the freestream turbulence upon the coarser grid

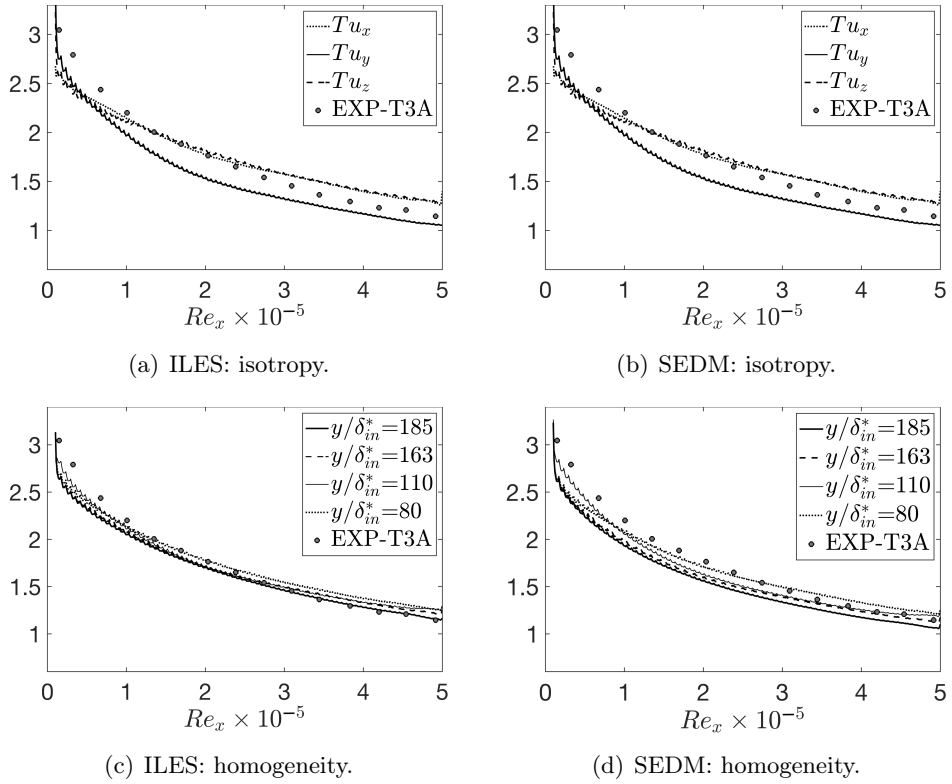

(a) ILES: isotropy.

(b) SEDM: isotropy.

(c) ILES: homogeneity.

(d) SEDM: homogeneity.

Figure 6.6: $\%Tu$ comparison between the ILES and SEDM (medium grid).

possesses a length-scale greater than the prescribed one. This behaviour has been well documented in Ref. [3], and grid convergence produces a distinctive trend towards the reference T3A data. We now look at the influence of the model upon the freestream behaviour. A comparison of the freestream turbulence intensity of the ILES and the SEDM on the medium grid is shown in Fig. 6.5(b). In general, the model effect is dissipative in nature, thus many of the trends for the ILES, described in the previous paragraph, are expected to be exaggerated for an LES using the model. The comparison between the curves of the freestream turbulence intensity of the ILES and the SEDM, as seen in Fig. 6.5(b), reveal that the sharp drop in intensity, near the inflow, is a bit more severe in the case where the model is applied. In general, this drop in the turbulence intensity can be directly attributed to the drop in the wall-normal intensity, Tu_y, which is quite apparent when examining the behaviour of the individual components of the freestream turbulence in Figs. 6.6(a) and 6.6(b).

The reason for this behaviour is relatively simple to explain. Within the turbulence injection technique, perturbations are firstly evaluated on an auxiliary cartesian grid. Subsequently, the same quantities are interpolated

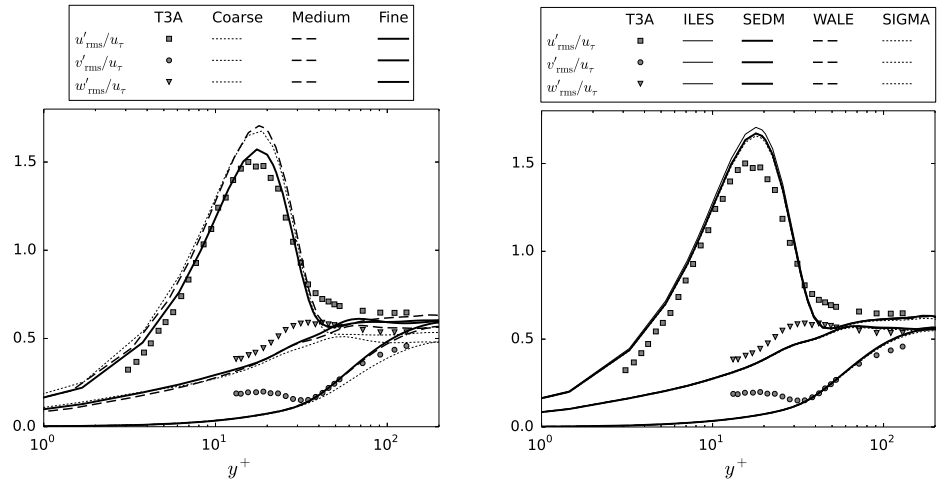

(a) Variation with grid resolution.

(b) Variation with sub-grid model (medium grid).

Figure 6.7: $u'_{i,\mathrm{rms}}/u_\tau$ at location $Re_x = 3.2 \times 10^5$.

on the high-order SD discretisation. Although such procedure is straightforward in the case of isotropic grids, it can be more complex whenever one of the direction is stretched, like in the wall-normal direction for this particular case. Velocity fluctuations along this direction can then be affected by the anisotropy of the grid.
Furthermore, the presence of a model tends to exacerbate this trend, as seen in the case of the SEDM in Fig. 6.6(b). This overall trend is indicative of a relative loss in the isotropy of the freestream turbulence in the case of ILES as seen in Fig. 6.6(a), with the situation being even more severe for the case with a model Fig. 6.6(b), with deviations between the individual components of the stresses as large as 20% being seen. Moreover, when viewing the turbulence intensities at several different wall-normal locations, in Figs. 6.6(c) and 6.6(d), it becomes apparent that there is a relative loss in the homogeneity as well. In general, at any given streamwise location, the freestream turbulence intensity is lower the further we move away from the boundary layer due to the coarsening of the grid due to stretching, with the effect being more significant for the SEDM than the ILES.

Despite the relatively large variations in the freestream behaviour due to the grid and model, the effect upon the fluctuating stresses, within the boundary layer, close to the inflow is relatively minor, as seen in Fig. 6.7. A comparison of the boundary layer fluctuating stresses among the three different grids is shown in Fig. 6.7(a), for the ILES simulation. A similar figure, showing a comparison of the boundary layer fluctuating stresses, on the medium grid, among the various models is shown in Fig. 6.7(b). We

can observe in Fig. 6.7(a), that the effect of the grid is relatively small and, in general, the disturbance is well predicted. As can be expected, the prediction upon the coarsest mesh is the least accurate, with the streamwise fluctuating stress exhibiting higher values than the T3A reference and the other two components exhibiting lower values. However, on the medium and fine grids, a much improved agreement is achieved. In a similar manner, the curves in Fig. 6.7(b), show that the use of the LES models results only in a minor deviation as compared to the ILES. A prominent discrepancy between simulation and experiment is visible within the wall-normal and spanwise components of the fluctuating stresses close to the wall ($y^+ < 40$). This discrepancy was visible even within the simulations using the U-FINE mesh, previously described in Sec. 6.3.1, within the study in Ref. [3]. It is also present within the reference DNS [2] and to the best of our knowledge, no simulation has been able to match these experimental curves exactly. However, within the realm of existing literature, our representation of the fluctuating stresses close to the inflow is quite acceptable and thus, it is with these conditions within the boundary layer and freestream that the following LES transition studies will be carried out.

Transition behaviour

The transitional zone extends between $1.1 \times 10^5 \leq Re_x \leq 3.1 \times 10^5$ and it represents our main region of interest. However, in order to understand the onset of the transition, it is important to study the trends present within the pre-transitional zone, which occupies $Re_x < 1.1 \times 10^5$. A discussion concerning this zone as well as the early portion of the transition zone ($1.1 \times 10^5 \leq Re_x \leq 2 \times 10^5$) is presented in Sec. 6.3.2. A discussion concerning the remainder of the transitional zone as well as the fully turbulent region is subsequently presented within Sec. 6.3.2. Finally, a detailed look at the trends of the sub-grid eddy-viscosity, useful for understanding the transition behaviour, is presented within Sec. 6.3.2.

Pre-transitional region

Transition typically occurs when the amplitude of the fluctuating stresses (primary disturbance) within the boundary layer grows sufficiently large so that breakdown of the structures of the pre-transitional region into fully turbulent flow can occur [2]. This growth, which should occur linearly with respect to the square-root of Reynolds number, is presented in Fig. 6.8, for the medium and fine grids. The figures indicate that, in general, the coarser the grid, the lower is the rate at which the disturbance tends to grow. This trend was seen in Ref. [3] and observations regarding its relevance to the transition onset were made.

The influence of the sub-grid dissipation upon the growth rate of the

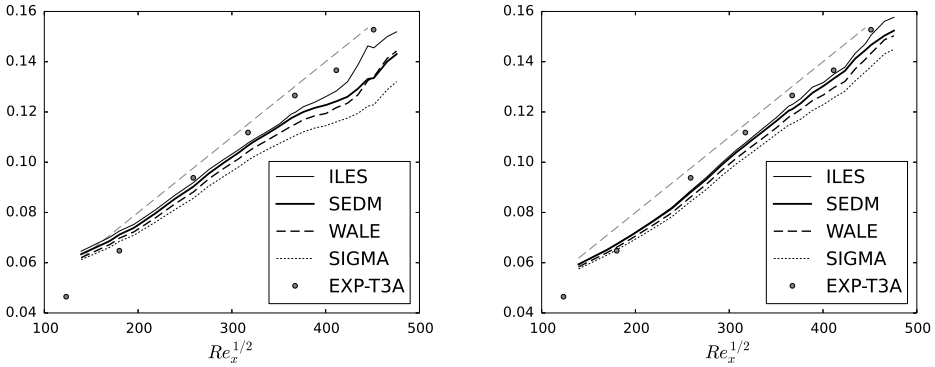

(a) Medium grid.

(b) Fine grid.

Figure 6.8: $u'_{\mathrm{rms,max}}/U_\infty$ behaviour along the streamwise direction. Linear growth with respect to $Re_x^{1/2}$ (– – –) shown for reference.

disturbance is what is of interest here. As pointed out in Ref. [110], models which input minimal sub-grid dissipation within the pre-transitional region tend to predict higher growth rates. In our simulations we do observe a dependency of the growth rate upon the model type. Across all the grids used, the growth rates of the disturbance were the highest for the ILES, followed by the SEDM, then the WALE and finally the SIGMA model. Since all the models used, introduce a dissipative effect, it is to be expected that the ILES will exhibit the highest growth rate. However, among the various LES models used, the curves in Figs. 6.8(a) and 6.8(b) seem to indicate that the SEDM is the least dissipative while the SIGMA is the most dissipative within this region, with the behaviour of the WALE falling neatly between the two. Evidence in support of this claim will be presented within Sec. 6.3.2, where the eddy-viscosity behaviour at several streamwise stations has been plotted. The graphs therein, do show that the SEDM has lower levels of eddy-viscosity than either WALE or SIGMA models.

This influence is felt not only upon the streamwise component of the fluctuating stress, but to a greater extent upon the wall-normal and spanwise components. This can be observed in the behaviour of the fluctuating stresses, just downstream of the pre-transitional region, upon the medium grid, as shown in Fig. 6.9. Three different streamwise locations are shown which best exhibit the effect of the sub-grid dissipation. We can observe that although at the first location there is not much of a distinction between the curves of the various models, as we move downstream, large differences begin to evolve. This effect is most apparent in the curves of the wall-normal and spanwise components of the fluctuating stresses as seen in Figs. 6.9(b) and 6.9(c) respectively. In general, the ILES and the SEDM exhibit a higher prediction of the peak stress, in keeping with the T3A reference, while the

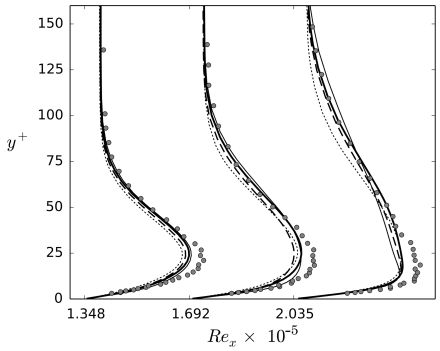

(a) Streamwise stress: $0.1(u'_{\text{rms}}/u_\tau) + Re_x$.

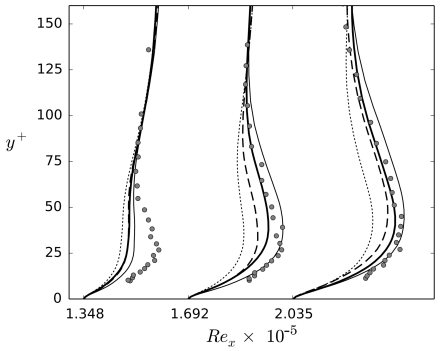

(b) Wall-normal stress: $0.5(v'_{\text{rms}}/u_\tau)+Re_x$.

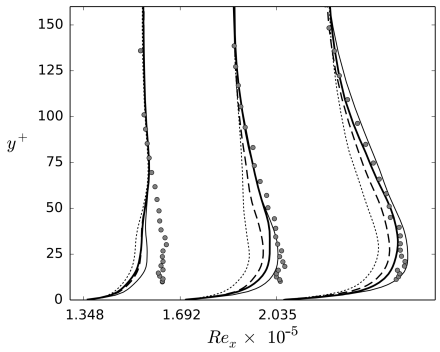

(c) Spanwise stress: $0.4(w'_{\text{rms}}/u_\tau) + Re_x$.

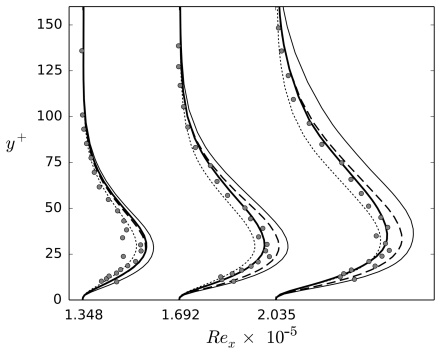

(d) Cross stress: $0.5(\overline{u'v'}/u_\tau^2) + Re_x$.

Figure 6.9: Behaviour of the fluctuating stresses within the pre-transitional region of the boundary layer. ILES (—), SEDM (▬), WALE (- - -), SIGMA (·····) and T3A reference (●).

WALE and SIGMA exhibit a much lower value. This trend is different for the curves representing the cross-stress shown in Fig. 6.9(d), where the ILES and WALE tend to exhibit strong over-predictions deviating far from the T3A reference, while the SEDM and SIGMA stay relatively close to the reference.

However, in general the ILES and SEDM tend to maintain higher rates of disturbance growth, which leads to them exhibiting an earlier transition as compared to the WALE and SIGMA. The skin-friction coefficient, the quantity most sensitive to the transition behaviour, is shown, for the three different models as well as the ILES, for the medium and fine grids, in Fig. 6.10. In keeping with the trend seen for the disturbance growth, the transition onset takes place first in the ILES simulation, followed by the SEDM, next by the WALE model and, finally, by the SIGMA model.

Transitional and fully turbulent region

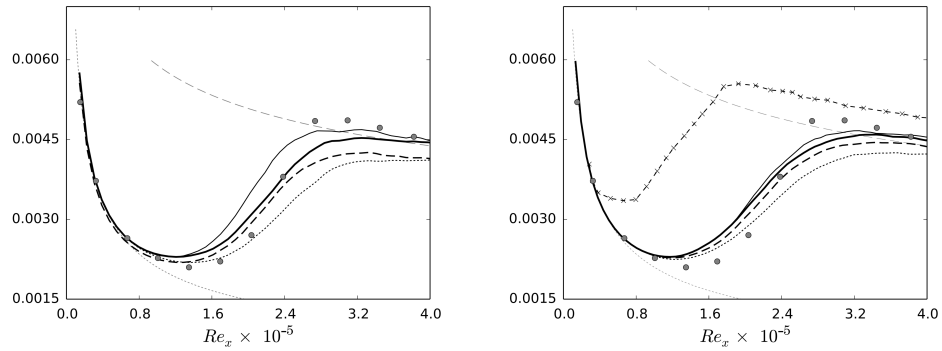

(a) Medium grid.

(b) Fine grid.

Figure 6.10: Friction coefficient behaviour for various grids and models. ILES (—), SEDM (—), WALE (– – –), SIGMA (·····) and T3A reference (•). The equivalent simulation in Ref. [4] (-×-) is also shown in the figure on the right.

The results of the skin-friction, presented within Fig. 6.10, demonstrate well the capabilities of the ILES computations when carried out with high-order schemes. The computations upon the medium and fine grids are quite accurate despite their poor resolution (relative to the DNS). The relative power of the ILES computations performed here, are visible in Fig. 6.10(b), when making a comparison with the ILES on the coarse grid in Ref. [4] (a grid with an equivalent resolutions to the fine grid used in this study). The relative difference between the two curves indicates a dramatic improvement in the prediction of the location of the transition onset as well as the magnitude of the skin-friction coefficient between the two. While the ILES simulations are relatively accurate, we seek to examine the influence of the LES models on the transition behaviour. Of the three LES models used within this study, it was observed that the WALE and the SIGMA model exhibited relatively similar behaviours to each other, while the SEDM exhibited rather different behaviour, falling somewhere in between the behaviour of the ILES and the WALE model. In general, on a given grid, the use of a model tends to push the transition onset downstream while increasing the range over which the transition occurs, as compared to the ILES (Fig. 6.10). This effect is the strongest in the case of the SIGMA model followed by the WALE and finally the SEDM. For the medium grid ILES, the onset of transition occurs far upstream of the reference and is completed slightly upstream of the reference, as seen in Fig. 6.10(a) . In the case of the SEDM while the transition also commences close to the ILES, the transition range overlaps that of the reference in a manner which provides a good matching between the two. However, for the WALE and SIGMA models, despite the

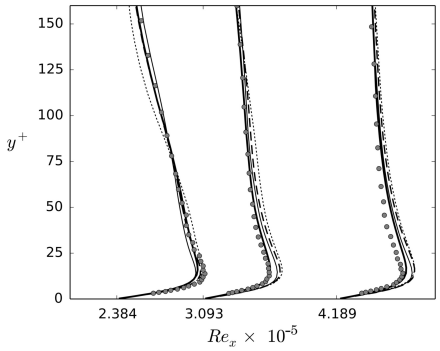

(a) Streamwise stress: $0.2(u'_{\text{rms}}/u_\tau) + Re_x$.

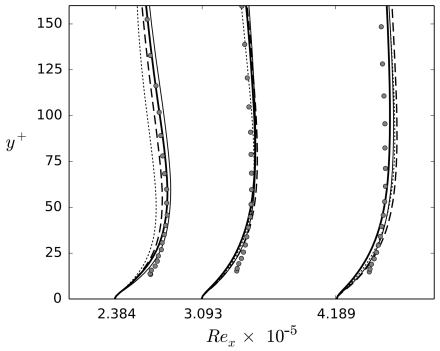

(b) Wall-normal stress: $0.5(v'_{\text{rms}}/u_\tau)+Re_x$.

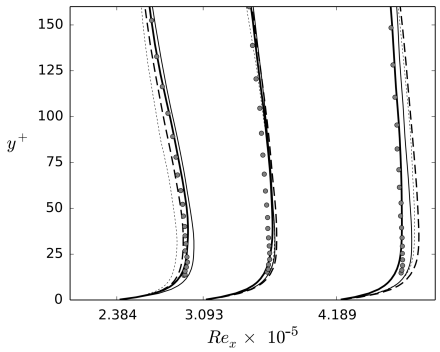

(c) Spanwise stress: $0.5(w'_{\text{rms}}/u_\tau) + Re_x$.

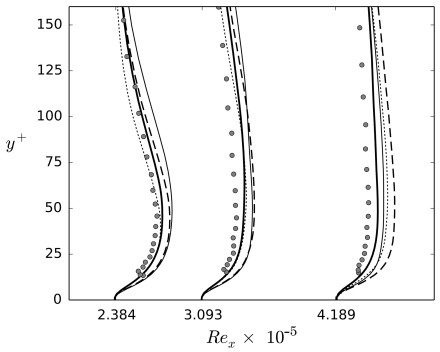

(d) Cross stress: $0.5(\overline{u'v'}/u_\tau^2) + Re_x$.

Figure 6.11: Behaviour of the fluctuating stresses within the transitional and fully turbulent region of the boundary layer. ILES (—), SEDM (—), WALE (– – –), SIGMA (·····) and T3A reference (•).

location of the transition onset being roughly similar to that of the SEDM, the transition range is longer and as a result the matching of the WALE and SIGMA, with the reference is noticeably worse. The differences between these models, within the transition region, may be related to the interaction between the eddy-viscosity and the mechanism of transition. A more dissipative model tends to inhibit the transition mechanism as compared to a less dissipative model. The previous section, Sec. 6.3.2, had shown that, based upon the growth-rate of the disturbance, the SEDM is the least dissipative model followed by the WALE and finally the SIGMA model. Thus, the length of the transition range progressively increases in this order. We will elaborate upon this trend in Sec. 6.3.2, where the profiles of eddy-viscosity in the wall-normal direction lend support to this reasoning.

Finally, we observe a discrepancy in the level of the skin-friction coefficient, within the fully turbulent region, for the WALE and SIGMA models on both medium and fine grids (Fig. 6.10). We can see that for the medium grid,

the simulation using the SEDM achieves a level of the skin-friction coefficient close to that of the reference within the fully turbulent region (Fig. 6.10(a)). However, this is clearly not the case for the WALE and SIGMA models. Even upon the fine grid, although there is a definite trend towards the reference, the true level of the skin-friction coefficient in the fully turbulent region is not achieved (Fig. 6.10(b)). The cause for this discrepancy is unknown.

The relatively poorer performance of the WALE and SIGMA models as compared with the SEDM is also apparent in the behaviour of the fluctuating stresses at three different streamwise locations within the transitional and fully turbulent regions. To illustrate this point, four components of the fluctuating stresses, on the medium grid, are shown in Fig. 6.11. A common feature of all the curves is the relative over-prediction of the stress levels by the ILES at all three streamwise locations. While the WALE and SIGMA models usually under-predict the stresses at the downstream location, they tend to also exhibit an over-prediction at the upstream location. It is interesting that the SEDM exhibits the most consistent behaviour in mitigating the over and under-prediction at all three streamwise locations.

Eddy-viscosity behaviour

With the impact of the sub-grid dissipation quite apparent within the results presented above, it is of interest to examine this behaviour in detail. In order to do this, we view directly the spatial behaviour of the sub-grid eddy-viscosity, the physical manifestation of the sub-grid dissipation. In order to achieve this, the wall-normal behaviour of the eddy-viscosity, for all three sub-grid models, upon all three LES grids, at several streamwise locations, are plotted in Fig. 6.12. The trends of the sub-grid eddy-viscosity, described in the following sections, help in interpreting and understanding the results presented in the sections above.

Wall-normal behaviour of eddy-viscosity at streamwise locations

In general, the behaviour of the sub-grid eddy-viscosity, as shown in Fig. 6.12, differentiates clearly between two different flow regions: the freestream and the boundary layer. The magnitude of the sub-grid eddy-viscosity is very strong within the freestream, while it is noticeably weaker within the boundary layer. This is primarily because the freestream is a region with large gradients and thus activates the WALE and SIGMA models, while the under-resolution of the grid within this region (due to wall-normal stretching) activates the SEDM. However, the behaviour of the sub-grid eddy-viscosity at the edge of, as well as within the boundary layer, is of greater importance as it dictates the transition behaviour. As we have pointed out previously in Sec. 6.3.2, the boundary layer may be split into the pre-transitional, transitional and fully turbulent regions.

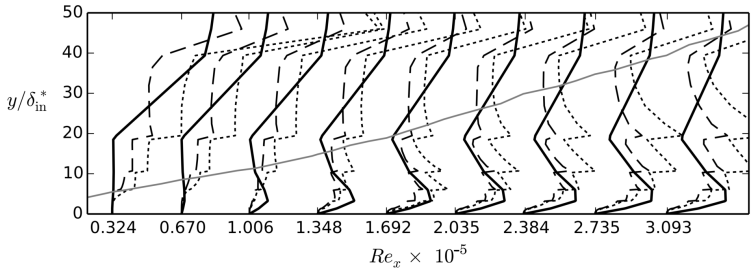

[ht!]

(a) Coarse grid (scale = 0.5).

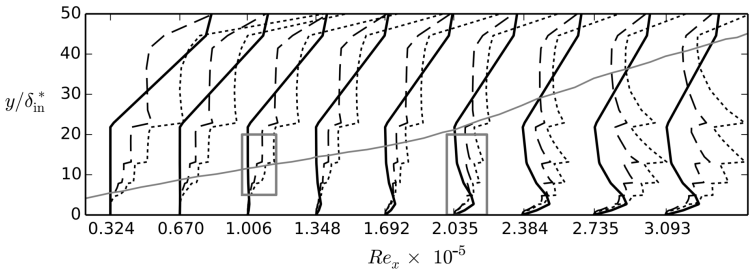

(b) Medium grid (scale = 0.5). Closeup regions in Figs. 6.13(a) and 6.14(a).

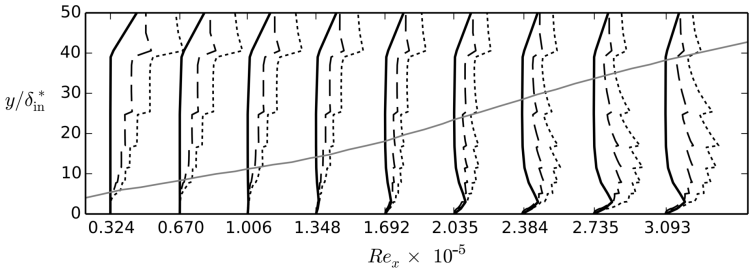

(c) Fine grid (scale = 0.5).

Figure 6.12: Behaviour of the eddy-viscosity ratio, ν_{sgs}/ν, at several streamwise locations for the SEDM (—), WALE (- - -), SIGMA (·····). Also shown, with a grey line, the boundary layer 99% thickness.

Ideally, we would like to have zero eddy-viscosity within the pre-transitional region to allow for the undamped growth of the primary disturbance. Models such as the SIGMA and the WALE do vanish when the flow field is two-dimensional in nature. However, the pre-transitional region is not a region of strictly two-dimensional flow, as can be seen from the fluctuating stresses close to the inflow, in Fig. 6.7. Thus, as can be observed, upon all three grids, shown in Fig. 6.12, starting from the edge of the boundary layer and progressively moving towards the wall there is a strong growth in the mag-

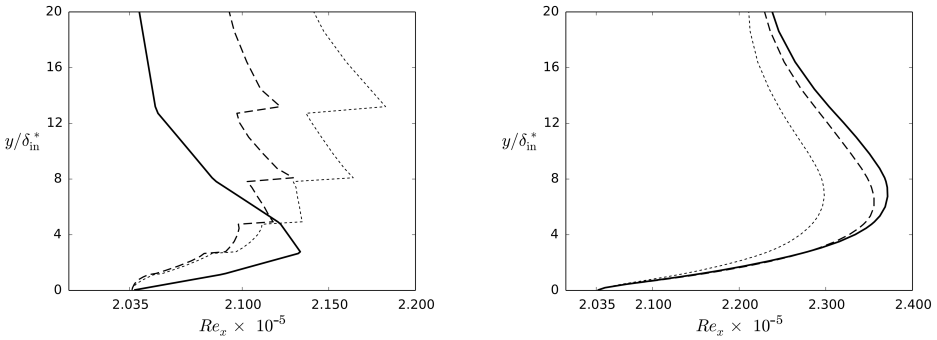

(a) $0.5\nu_{\text{sgs}}/\nu$ (b) $0.5(v'_{\text{rms}}/u_\tau)$

Figure 6.13: Near-wall behaviour showing the peaks in sub-grid eddy-viscosity and fluctuating stress for the SEDM (—), WALE (– – –) and SIGMA (·····) at the streamwise location $Re_x = 2.035 \times 10^5$ upon the medium grid.

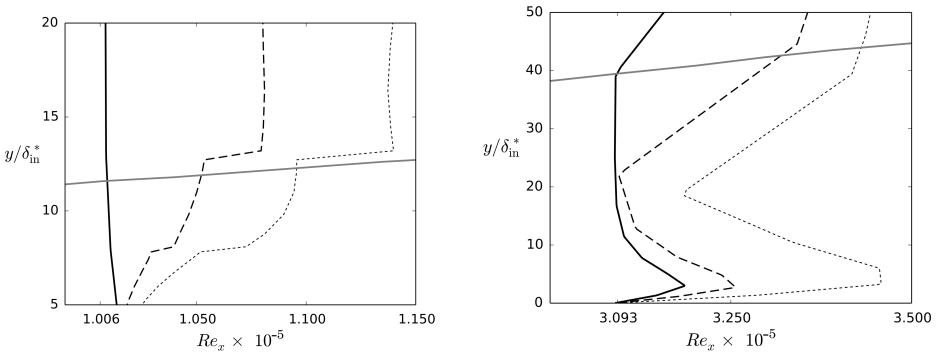

(a) SEDM (—), WALE (– – –), SIGMA (·····). (b) Coarse grid (·····), Medium grid (– – –) and Fine grid (—).

Figure 6.14: Behaviour of $0.5\nu_{\text{sgs}}/\nu$ at the streamwise locations $Re_x = 1.006 \times 10^5$ (a) and $Re_x = 3.093 \times 10^5$ (b). In (a), model comparison close to the edge of the boundary layer; in (b), grid convergence when using the SEDM.

nitude of the sub-grid eddy-viscosity. By comparison, the pre-transitional region is one where, except upon the coarse grid, the eddy-viscosity of the SEDM is kept quite close to zero (Figs. 6.12(b) and 6.12(c)). This is due to the fact that the grid in this region is quite fine due to the wall-normal stretching and the fluctuating stresses are of a sufficiently low magnitude such that they can be well resolved. The results of this are demonstrated in growth of the fluctuating stress as shown in Fig. 6.8 which for the SEDM are closer to the ILES than those of either the WALE or SIGMA model.

When comparing the eddy-viscosity behaviour of the SEDM with the

WALE and SIGMA models, we observe that the growth in the eddy-viscosity of the SEDM occurs near the wall and subsequently remaining close to zero over the bulk of the boundary layer, as can be seen in Fig. 6.12. This behaviour can be understood by observing the correlations between the fluctuating stress and the eddy-viscosity. This has been highlighted in Fig. 6.13, by plotting the eddy-viscosity (Fig. 6.13(a)) and the wall-normal component of the fluctuating stress (Fig. 6.13(b)) at a single streamwise location within the transitional region. As can be observed, for the case of the SEDM, there is a strong correlation between the position of the peak stress and the peak eddy-viscosity. Furthermore, as the stress begins to decay away from the wall, so does the sub-grid eddy-viscosity. This behaviour indicates that the spectral sensor in the model is indeed being triggered by the behaviour of the fluctuating stress, within the boundary layer.

By comparison, the behaviour of the eddy-viscosity of the WALE and SIGMA models are quite different from that of the SEDM as seen in Fig. 6.12. They are noticeably non-zero over much of the boundary layer height, and particularly at the interface between the boundary layer and freestream, where the sub-grid eddy-viscosity levels of the WALE and the SIGMA are noticeably higher than that of the SEDM. This behaviour has been highlighted in Fig. 6.14(a), which contains the plots of the eddy-viscosity behaviour near the edge of the boundary layer at a single streamwise station within the transitional zone. Based upon the transition behaviour described in Ref. [2], it is this region of the boundary layer that plays an important role in the transition mechanism. Once the primary disturbances have acquired a certain amplitude, high-frequency and high-wavenumber modes within the freestream, normally damped within the boundary layer, may interact with them to produce secondary instabilities which produce fully turbulent flow. It is thus apparent that the eddy-viscosity behaviour in this region will strongly influence this interaction. As we have observed in the behaviour of the skin-friction coefficient, in Fig. 6.10, the transition range of all the models appears longer than that of the ILES. Furthermore, the transition range of the WALE and SIGMA models are noticeably longer than that of the SEDM. We speculate that this difference is due to the behaviour of the eddy-viscosity within this region. One possible explanation is that the higher levels of the sub-grid eddy-viscosity in this region, introduced by the WALE and SIGMA models, suppresses the high-frequency, high-wavenumber modes close to the edge of the boundary layer, thus inhibiting transition and prolonging the range of the transitional region.

Grid convergence of the eddy-viscosity

The grid convergence study also highlights an interesting trend in the eddy-viscosity behaviour. That of the convergence of the sub-grid eddy-viscosity to zero with grid refinement. For the WALE and SIGMA models, approaching

to convergence, non-null values of the eddy-viscosity will be locally found also for $\Delta_{\text{sgs}} \ll \eta_k$ (where η_k represents the Kolmogorov length scale). Such behaviour is clearly undesirable, since no model would be necessary under these conditions. Instead, the dynamic nature of the SEDM, provided by the spectral decay sensor, $f(\zeta_{K_j})$, allows the model to be inactive whenever the velocity field is sufficiently well-resolved. Then, at least in a qualitative way, a different type of convergence is expected for the SEDM with respect to the more classical SGS models.

This trend is visible when comparing at any given streamwise location, the eddy-viscosity behaviour across the the coarse, medium and fine grids, in Fig. 6.12(a), Fig. 6.12(b) and Fig. 6.12(c), respectively. By doing so we observe, that with grid refinement, there is a strong trend of the eddy-viscosity of the SEDM to vanish, within the bulk of the boundary layer. This has been highlighted in Fig. 6.14(b), which shows the eddy-viscosity behaviour for all the grids at a single streamwise location within the fully turbulent zone. As the figure shows, upon the fine grid, except at locations very close to the wall (due to the large fluctuating stress peaks) the eddy-viscosity is nearly zero throughout the entire boundary layer. By comparison, although some convergence is observed in the eddy-viscosity of the WALE and SIGMA models (particularly within the freestream), the rate at which the eddy-viscosity vanishes is noticeably slower overall.

Since high-order schemes, such as the SD, typically converge rapidly in space. It appears to be desirable to have sub-grid models that can match this rate of convergence. The failure to do so, as is the case for the WALE and SIGMA models, may be responsible for the discrepancy in the prediction of the skin-friction coefficient in the fully turbulent region (Fig. 6.10). This situation is not ideal since in most practical situations our grid resolution is always limited and thus a slowly converging sub-grid model appears to produces a sub-optimal solution at a given resolution.

Near-wall eddy-viscosity scaling behaviour

We had mentioned previously, that the ideal sub-grid eddy-viscosity must exhibit a near-wall scaling of $\mathcal{O}(y^3)$. The WALE and SIGMA models exhibit a theoretical scaling of of $\mathcal{O}(y^3)$, while the SEDM exhibits a theoretical scaling of $\mathcal{O}(y)$. We now look to see whether, the theoretical behaviours are reproduced within the simulations.

In order to do this, we have plotted the wall-normal behaviour of the sub-grid eddy-viscosity and fluctuating stresses at a single streamwise location, placed within the fully turbulent region, for the simulations on the fine grid, in Fig. 6.15. We observe from Fig. 6.15(a), that while the SEDM exhibits a linear scaling $\mathcal{O}(y)$, just like the theoretical scaling law, the WALE and SIGMA models exhibit only a quadratic scaling $\mathcal{O}(y^2)$, which is a departure from the theoretical cubic scaling $\mathcal{O}(y^3)$. This behaviour persists throughout

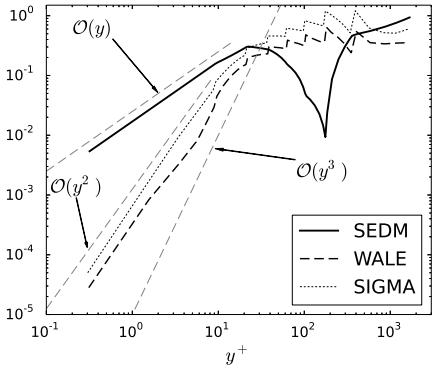

(a) Eddy-viscosity ratio (ν_{sgs}/ν).

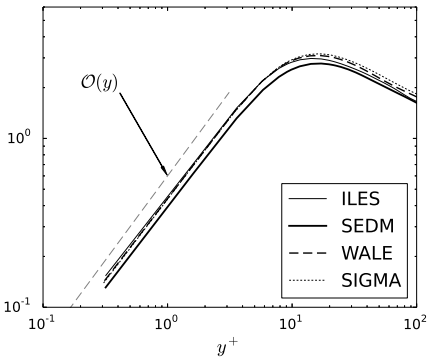

(b) Streamwise fluctuating stress.

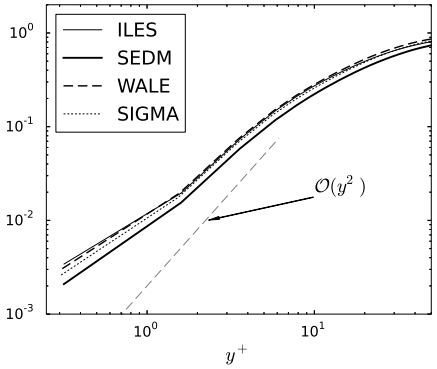

(c) Wall-normal fluctuating stress.

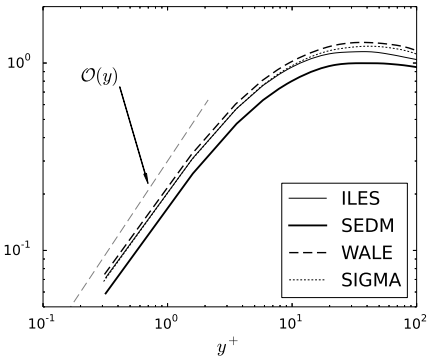

(d) Spanwise fluctuating stress.

Figure 6.15: Near-wall scaling behaviour of relative sub-grid eddy viscosity and fluctuating stresses at streamwise station $Re_x = 4.189 \times 10^5$. Also shown are the theoretical rates.

the transitional and turbulent regimes of all grids. The cause of the departure between the practical and theoretical scaling for the WALE and SIGMA models is unknown.

However, we observe that despite the deviation of the eddy-viscosity, for all three models, from the ideal scaling behaviour, the near-wall scaling of the fluctuating stresses is unaffected. To demonstrate this, we have presented the fluctuating streamwise, wall-normal and spanwise stresses in Figs. 6.15(b), 6.15(c) and 6.15(d) respectively at the same streamwise station. The slopes of the fluctuating stresses are identical to their theoretical values, taken from Ref. [122], and shown alongside in the figures. As yet, we are unable to explain the reason why the fluctuating stresses retain their theoretical scaling behaviour, while the eddy-viscosity does not.

6.4 SD7003 airfoil

6.4.1 Introduction

Accurate simulations of turbulent flow over airfoils and wings are of fundamental importance in modern aeronautical process design. Flow conditions and geometrical parameters lead to a wide range of challenging situations to be numerically modelled. Ultimately, CFD tools should address these concerns with robustness and accuracy for efficient virtual prototyping of advanced aerodynamical systems.

The SD7003 low Reynolds airfoil simulation is a classical test for transitional flows [123, 124, 125, 126], in particular for spectral element high-order methods [127, 128, 129, 130, 131]. In such conditions, dynamic turbulence models should distinguish between smooth and under-resolved regions of the flow and act accordingly. The capability of a turbulence model to remain inactive in laminar flows is of fundamental importance for such complex applications. Classical RANS (Reynolds Averaged Navier-Stokes) approaches may lack this property and additional models to detect/trigger transition are needed [132, 133, 134, 135]. These are normally based on user-defined parameters or on simplified theories (two-dimensional flows and thin boundary layers). Here, the Spectral Element Dynamic Model [1] is used, which is based on a direct modal analysis of the simulated velocity signal.

The total simulated time is of $50c/u_\infty$ convective times (with $c = 1$ chord length). Statistics collection starts after $20c/u_\infty$. The most relevant quantities to be evaluated are pressure and skin friction coefficients due to the large amount of reference data. Notice that spectral element methods, due to their intrinsic flux-based formulation, return automatically pressure and viscous fluxes on the elements' faces, including wall boundaries. Such values can then be easily combined with the local geometric informations, such as the wall normal direction, to compute pressure and friction coefficients.

Finally, averaged streamwise velocity and streamwise fluctuations are computed along the airfoil surface normal direction. Vortex structures are visualised by means of the Q-criterion isosurfaces at $t \approx 50c/u_\infty$ in Fig. 6.16. The flow is characterised by a laminar region close to the leading edge of the airfoil, followed by a rapid transition to turbulence in the detached boundary layer. The vortical structures are then smoothed out in the first region, whereas they break up to smaller and smaller vortices in the second part of the airfoil, where the local turbulent Reynolds number increases.

In order to better quantify the influence of the SEDM, Implicit Large Eddy Simulations have been performed on the same computational grid and with identical solver's parameters. Unfortunately, for both orders of accuracy, the ILES have shown to be unstable. More precisely, starting from the prescribed, uniform, initial condition, the two implicit LES fail right before the transition to turbulence. Such behaviour is not totally unexpected as it

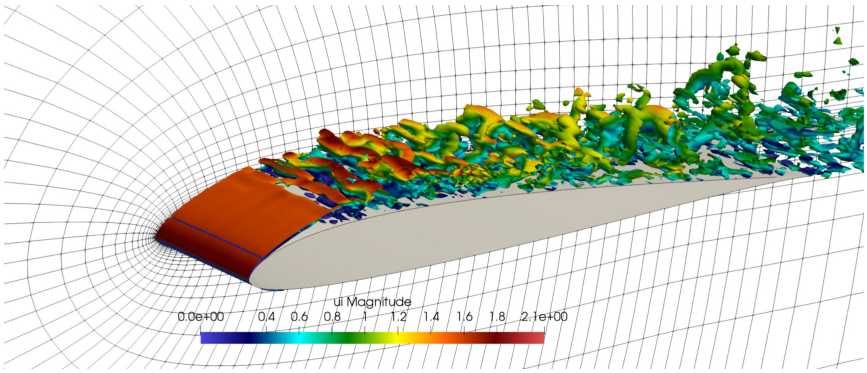

Figure 6.16: Isosurface of the Q-criterion ($Q = 200$) colored with instantaneous velocity field magnitude.

is typical of such high-order turbulent simulations. In the authors' experience, in fact, similar unstable ILES have been observed both in free shear and wall bounded flows [1, 136]. In particular, as in this case, the simulations tend to fail just before the transition phase, when large-scale kinetic energy starts flowing toward the smallest (unresolved) scales. The failure of ILES is, in fact, directly caused by the insufficient level of numerical dissipation at such scales and the consequent buildup of energy at the highest wavenumbers. Even restarting the simulation from a fully-established turbulent flow field, obtained from explicit LES computations, has lead to numerical failure soon after. Such behaviours are even more exacerbated by high orders of approximation and strongly anisotropic grids. Thus, despite of their appealing efficiency, ILES are often very delicate in terms of both stability and accuracy. It is quite well-established that for relatively low orders (3-rd or 4-th) and proper choices of the numerical flux, spatial discretisation and grid size, ILES can provide satisfactory results in a fairly wide range of turbulent flows. Nevertheless, such conditions can be rather specific and, more importantly, in large part uncertain, in particular for complex configurations like the ones herein considered.

6.4.2 Simulation Setup

All relevant informations regarding present simulations are listed in Table 6.4. Both grids have been generated on a two-dimensional geometry and subsequently extruded along spanwise direction z. The first solution point along the wall-normal direction has been located such that $y^+ < 1$, in order to achieve a wall-resolved LES. In particular, in Table 1, y^+ has been evaluated at at $x/c = 0.7$ as reference. Nonetheless, the condition $y^+ < 1$ is satisfied along the whole surface of both profiles.

The wing span to chord ratio is set to 0.2 for both cases, the same as in Galibraith and Visbal [5] simulations of SD7003 profile. In both con-

		SD7003	
Reynolds number	Re	6×10^4	
Mach number	Ma	0.1	
Angle of attack	AoA	8°	
Wall BC	-	$T_{wall} = 1.002 \cdot T_\infty$	
Number of elements	$N_t \times N_n \times N_z$	$128 \times 24 \times 2$	
Polynomial degree	N	5	7
Degrees of freedom	DoF	1.3×10^6	3.1×10^6
Wall distance	$\langle h \rangle$	1.08×10^{-5}	6.35×10^{-6}
Wall scaling	y^+ at $x/c = 0.7$	≈ 0.05	≈ 0.03
Probe 1 location	(x_1, y_1, z_1)	$(0.5, 0.11, 0)$	
Probe 2 location	(x_2, y_2, z_2)	$(0.5, 0.05, 0)$	
Probe 3 location	(x_3, y_3, z_3)	$(1.3, 0.00, 0)$	

Table 6.4: Physical and computational set-up. All quantities are made dimensionless with respect to the chord length and free-stream values. A nominal value $c = 1$ has been assigned to the airfoil length. Reference frame is centred on the leading edge. In y^+ calculations the closest solution point to the wall has been considered. In particular, the notation $\langle h \rangle$ denotes the averaged value of wall-distance along the whole profile.

figurations the airfoil has been located approximately 15 chords away from boundaries. For the SD7003 simulations two different polynomial degree have been considered ($N = 5$ and $N = 7$) to evaluate the influence of the scheme's accuracy on the numerical results.

The response of the shear viscosity versus temperature is expressed according to Sutherland's law:

$$\mu(T) = \mu_0 \left(\frac{T}{T_0} \right)^{3/2} \frac{T_0 + T_S}{T + T_S}, \tag{6.18}$$

where $\mu_0 = 1.827 \times 10^{-5}\,\mathrm{kg\,m^{-1}s^{-1}}$, $T_S = 120\,\mathrm{K}$ and $T_0 = 291.15\,\mathrm{K}$. Finally, a specific heat ratio $\gamma = 1.4$ and a $\mathrm{Pr} = \mu_0 c_P / \kappa = 0.71$ are assumed. The flow is initialised homogeneously in the whole domain according to the far-field conditions.

Notice that in both computations high-orders of approximation are chosen ($N = 6$ and 8). The reason for such choice is twofold. First of all, the SGS model described in the previous section is based on a modal turbulence sensor which is more suitable for high orders of approximation (at least $N = 3$) for which the decay exponent can be estimated more accurately. The same applies to the shock-capturing scheme, whose modal sensor needs a sufficiently high order of approximation as well. Secondly, the use of the SEDM model would be of very little interest for low order discretisations since it would be almost constantly inactive, leading, in the end, to a low or-

der implicit LES. For a deeper discussion on the SEDM and its relationship with numerical dissipation see [1].

Notice that the reduced number of elements along the spanwise can have a misleading interpretation. Of course, due to the high-order approximation, the total number of degrees of freedom along z is considerably larger. Moreover, the use of high-order spectral element methods has often shown superconvergence properties (see [77]). In each element, the smallest resolved scale can then be even smaller than the classical estimation $\Delta z/(N+1)$.

6.4.3 Pressure and skin friction coefficients

In Fig. 6.17, it can be clearly noticed how the Laminar Separation Bubble (LSB) is the most difficult region of the flow to be predicted accurately. Only in this zone, noticeable differences can be identified with respect to the reference data. Such deviations may be explained, to some extent, by the different size of the domain, or by the different numerical discretisation employed (order of approximation, numerical flux, scheme, etc.). In particular, in [137], a considerable influence due to farfield boundary conditions has been observed, along with some evident discrepancies using different orders of approximation, while keeping the same number of degrees of freedom (DoF). The latter observation highlight the importance of the implicit features of the spatial discretisation such as numerical dissipation and dispersion. These observed differences, with the consequential uncertainties, underline the general need for reliable and robust theoretical studies on numerical diffusion and dispersion of high-order schemes in order to accurately predict the levels of dissipation introduced in ILES. A minor influence of the approximation order has been observed in the present simulations too. For $N = 8$, the peak of friction coefficient at $x \approx 0.4$ is slightly higher and the location of the LSB is closer to the leading edge. In particular, the reattachment point is moved upstream with respect to the 6-th order simulation, whereas no relevant differences have been noticed for the separation point location. It is also interesting to notice that the minimum value of the friction coefficient is located at $x \approx 0.25$ for both simulations and it coincides with the pressure peak on the left Fig. 6.17. Finally, it is worthwhile mentioning that most of reference simulations used a compressible Navier-Stokes solver, whereas, only Catalano and Tognaccini [138] used an incompressible solver. Averaged quantities have a good agreement with respect to previously published works, even though a considerably smaller number of DoF is used.

It is interesting to notice that all the reference simulations predict accurately the location of the separation bubble, except for the computation by Boom and Zingg [139], where the LSB is significantly shifted toward the leading edge. Furthermore, considering the friction coefficient, shown on the right of Fig. 6.17, only the present 6-th order simulation along with the computation by Catalano and Tognaccini [138] show slightly positive values of

C_f around $x \approx 0.2$.

The capability of the Spectral Element Dynamic Model to distinguish between smooth and turbulent regions appears here as a key factor for a good description of laminar, fully turbulent, and more importantly, transitional regions. This can be noticed, in particular, in Fig. 6.18, where the ratio between eddy-viscosity and molecular viscosity is shown. Very small values are observed in the first laminar region close to the leading edge, followed by a gradual increase, up to the fully turbulent boundary layer. In the separated flow the eddy-viscosity ratio takes values up to ≈ 4 indicating a non-negligible influence of the SGS model in this particular test case.

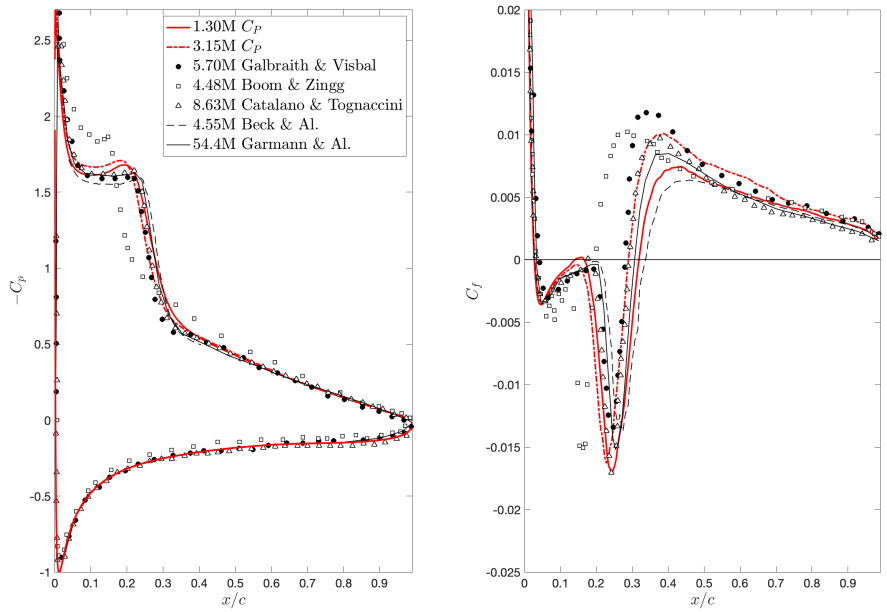

(a) Pressure coefficient (b) Skin friction coefficient (suction side)

Figure 6.17: Pressure and Skin friction coefficients.

In Table 6.5, the mean aerodynamic loads and separation bubble dimensions are listed. The data extracted from the present simulation appear to be in good agreement with respect to other reference simulations. All of them, in agreement with the present analysis, are formally categorised as Large-Eddy simulations. In particular, the most refined computation by Garmann and Visbal will be considered as reference. A fairly good grid convergence was, in fact, reported in [5, 6].

Notice that high-order methods, such as Spectral Difference used here, Flux Reconstruction or Discontinuous Galerkin schemes, locate the solution

Author	C_L	C_D	x_s/x_r	Order	DoF
Galbraith and Visbal [123]	0.910	0.043	0.040/0.280	6	5.70M
Catalano and Tognaccini [138]	0.940	0.044	0.030/0.290	2	8.63M
Boom and Zingg [139]	0.968	0.034	0.037/0.200	4	4.48M
Beck et al. [137]	0.923	0.045	0.027/0.310	3	4.26M
Beck et al. [137]	0.932	0.050	0.030/0.336	7	4.55M
Garmann and Visbal [5]	0.917	0.045	0.031/0.303	6	54.4M
Selig et al. (exp) [140]	≈ 0.920	≈ 0.029	-	-	-
Current ($N = 5$)	0.947	0.048	0.027/0.316	6	1.30M
Current ($N = 7$)	0.943	0.046	0.028/0.288	8	3.10M

Table 6.5: Mean Aerodynamic loads and separation (x_s) and reattachment (x_r) locations and computational details.

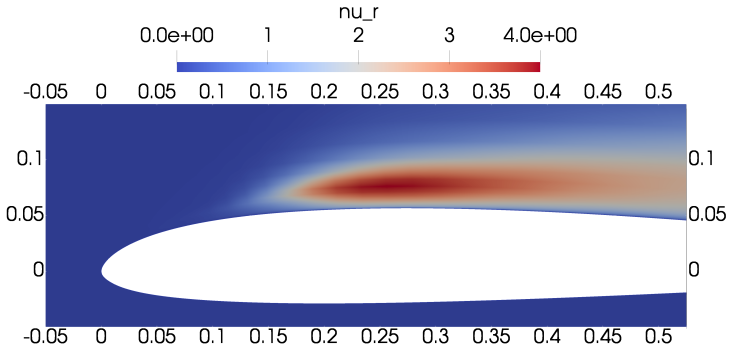

Figure 6.18: Averaged eddy-viscosity ratio ($N = 5$).

points in the inner part of the element while fluxes are evaluated on a different set of nodes (flux nodes) including the element's edges. Pressure values and viscous fluxes are then directly available at the wall boundaries and can be used to compute the pressure and friction coefficient, respectively.

To quantify the dynamic nature of the SEDM, the turbulence sensor (the function $f(\sigma_n)$ in Eq. 6.3) has been computed on a fully-developed flow field in a post-processing fashion. In particular, a snapshot of the 8-th order simulation has been chosen. In Fig. 6.19 the instantaneous flow field and the turbulence sensor applied to it are consequently shown. Firstly, it can be noticed that the turbulence sensor is almost completely inactive on the lower side of the airfoil, where the flow does not separate. In fact, the numerical algorithm correctly recognises such region of the flow as well-resolved due to the negligible small scale fluctuations. On the upper side, instead, a much higher activation can be observed due to the detached flow characterising this region. In particular, the very narrow shear layer developed closely after the leading edge is detected by the turbulence sensor has a partially

under-resolved region ($f \approx 0.5$). A detailed view of such region is shown in Fig. 6.20. Subsequently, downstream the separation bubble, the flow completely separates and the turbulence sensor frequently assumes a unitary value, indicating fully-developed turbulence. However, the turbulence sensor can also occasionally take much smaller values in the detached region, highlighting the presence of locally well-resolved structures even within the separated flow.

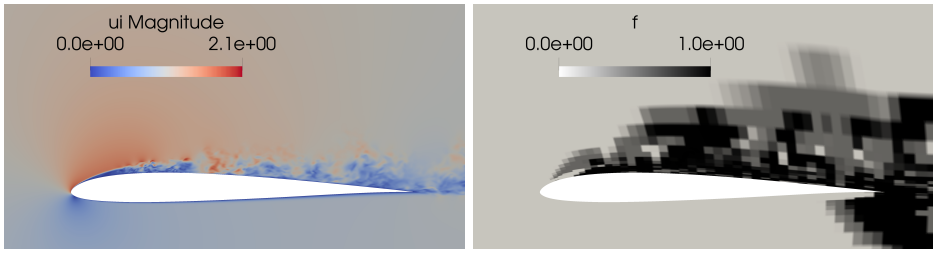

(a) Instantaneous flow field. (b) Turbulence sensor f.

Figure 6.19: Instantaneous flow field (left) and spectral turbulence sensor applied to the velocity field (right).

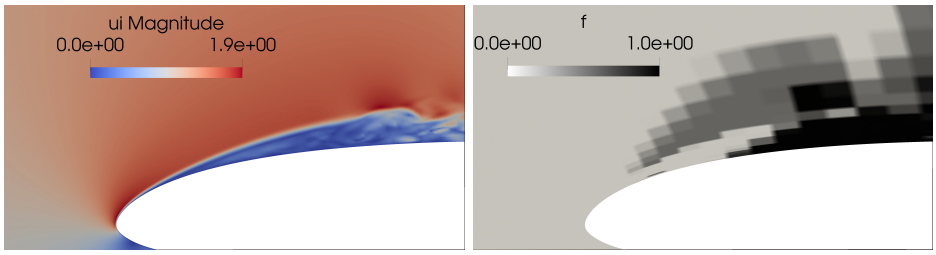

(a) Instantaneous flow field. (b) Turbulence sensor f.

Figure 6.20: Detailed view of Fig. 6.19 in proximity of the shear layer developed closely after the leading edge.

6.4.4 Averaged normal profiles

In addition to wall values, like pressure and viscous stresses, a set of wall-normal slices are extracted and main variables are compared against those of the most refined simulation [5, 6] (the locations of the planes of measure are shown in Fig. 6.21).

In Fig. 6.22, the averaged streamwise velocity is shown. It can be clearly noticed that the fully turbulent and laminar regions are well described by the SEDM model. Some discrepancies are still present in the transition region, however such differences are reasonably expected due to the very large

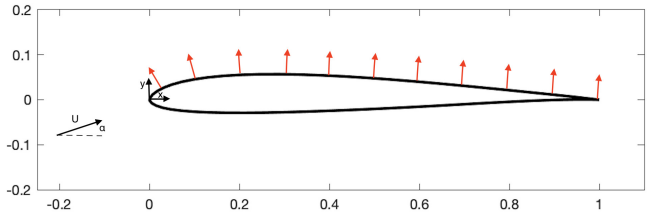

Figure 6.21: Profile lines normal to the airfoil surface. These have been taken every 10% of the chord except for the first point located at $x/c = 0.025$.

resolution difference between the two simulations (more than one order of magnitude in terms of DoF). The 6-th order simulation is marginally more accurate in the transitional region, in particular at $x = 0.2$ and $x = 0.3$. At $x = 0.3$, all the velocity profiles have almost null normal derivative, indicating the proximity with the reattachment point. In particular, in the 6-th order simulation, the normal derivative assumes small negative values, followed by the reference data and finally the 8-th order simulation, with slightly positive values. In other words, the 6-th order simulation anticipates the separation, while the 8-th order simulation delays it. The same conclusions can be drawn from Fig. 6.17 and Table 6.5.

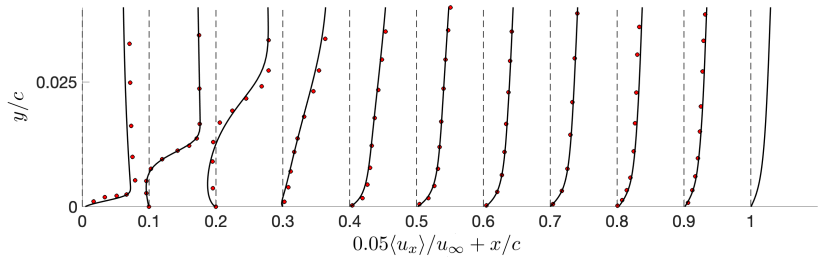

Figure 6.22: Averaged streamwise velocity along normal direction ($N = 5$, solid line, $N = 7$, dot-dashed line). Red dots represent streamwise velocity by the most accurate simulation [5, 6].

Analogous observations can be made from the streamwise velocity fluctuations shown in Fig. 6.23, where the two simulations show similar trends. At $x = 0.2$, the predicted fluctuations are larger than the reference whereas at $x = 0.3$, both simulations show smaller fluctuations, indicating a faster transition with respect to the reference data. Namely, the largest fluctuations occur more upstream with respect to the DNS data in both simulations. Nevertheless, for this level of resolution, results are sufficiently satisfying.

Finally, in Fig. 6.24, the eddy-viscosity ratio is plotted. The ability of the sensor to activate only in the transitional and fully turbulent regions, leaving practically untouched the laminar part of the flow, is particularly evident. In

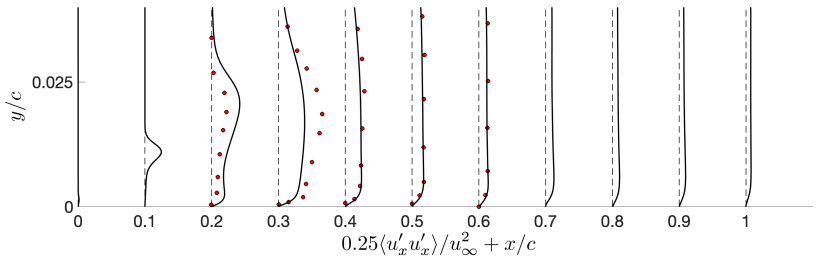

Figure 6.23: Streamwise velocity fluctuations along normal direction ($N = 5$, solid line, $N = 7$, dot-dashed line). Red dots represent streamwise velocity fluctuations by the most accurate simulation [5, 6].

the fully turbulent region of the airfoil, the eddy viscosity reaches an almost constant value along the streamwise direction, suggesting an expected self similar behaviour of the flow field. It is finally interesting to notice a peculiar characteristic of the SEDM: considering the 8-th order simulation, the eddy viscosity values are smaller with respect to the 6-th order case. in fact, since the level of resolution has been increased, the amount of kinetic energy to be dissipated is smaller and the model is naturally tending to a progressive deactivation. Such behaviour is a very desirable feature of turbulence models, which should turn completely off in both laminar and sufficiently resolved turbulent regions of the flow.

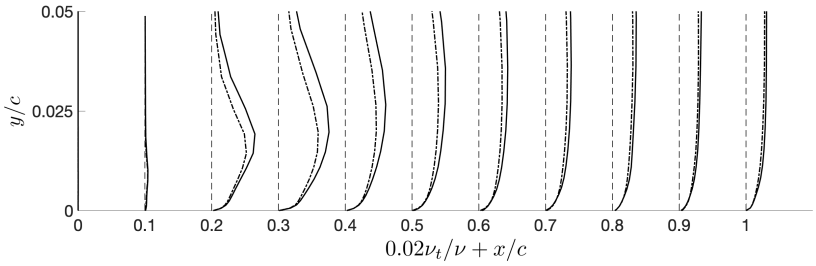

Figure 6.24: Averaged eddy-viscosity ratio along normal direction ($N = 5$, solid line, $N = 7$, dot-dashed line).

6.4.5 Kinetic energy spectra

In order to assess the energy transfers and content in fully turbulent regions, velocity data have been stored over time using virtual probes located in different zones of the boundary layer and wake regions, as shown in Fig. 6.25. Fast Fourier transform (FFT) has then been applied to time signals and energy spectra are computed. It is then possible to relate the temporal energy spectra with the spatial one assuming the applicability of the Taylor's

hypothesis [141]. In the present section only the 6-th order simulation has been considered.

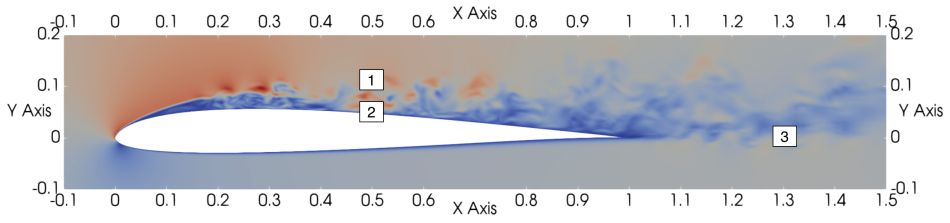

Figure 6.25: Instantaneous velocity magnitude. Numbers mark probes locations.

Once the full time signal processing is done, a possible estimate of the wavenumber is provided as:

$$\kappa = \frac{2\pi\mathcal{F}}{\langle ||\mathbf{u}|| \rangle} , \tag{6.19}$$

where $\mathcal{F}$ is the temporal frequency and $\langle \cdot \rangle$ denotes temporal averaging operation. Subsequently, the dissipation rate can be directly computed in phase space according to the well known relation:

$$\epsilon(\kappa) = 2\nu\kappa^2\mathbb{E}(\kappa) , \tag{6.20}$$

where $\mathbb{E}(\kappa)$ denotes the kinetic energy spectrum.

In Fig. 6.26, the energy spectrum of two different probes is shown. Probes 1 and 2 are chosen in order to validate the applicability of Taylor's hypothesis.

A transition to spectral decay is expected right after the inertial range for high wavenumbers, located approximately within the range $\pi/2 < \kappa^* < \pi$ with $\kappa^* = \kappa\Delta x/(N+1)$. A good alignment between advection velocity and the x-direction has been here assumed with the use of the streamwise grid size Δx. Due to very high velocity fluctuations, in the second probe, the expected dissipative region close to the Nyqvist grid wavenumber is shifted. On the other hand, analysing the spectrum of probe number 1, the natural transition to the smooth region is located close to the maximum resolved wavenumber. In Fig. 6.26, both curves are characterised by a very short inertial range, typical for such small Reynolds numbers turbulence. Finally, no energy accumulation has been observed in proximity of the Nyqvist grid wavenumber, providing a smooth transition from inertial to dissipative range. The SGS model is then capable of properly mimicking energy transfers between scales.

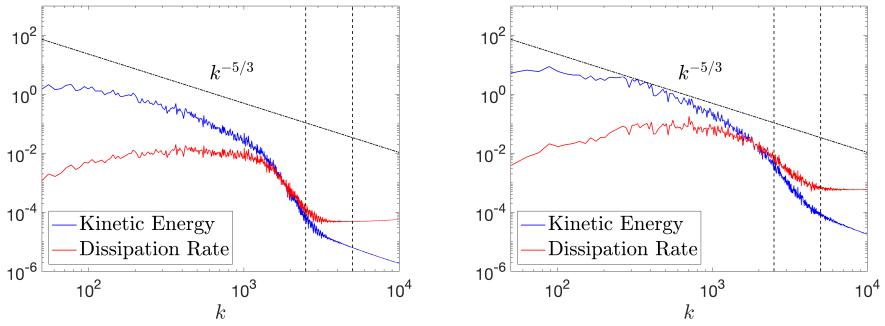

(a) Probe 1 (b) Probe 2

Figure 6.26: Kinetic energy spectra in probe 1 and 2. Vertical lines denotes an estimate of the dissipation region: $\pi/2 < \kappa^* < \pi$.

6.5 Conclusions

This work has presented the behaviour of various LES models, the WALE, SIGMA and particularly the SEDM, upon a numerical reproduction of the experimental ERCOFTAC T3A, ZPGSFPBL bypass transition test case. In general, we conclude that at the finest grid resolutions (although coarser than those of previous studies) the performance of all the models is acceptable. In fact for the current test case, the sensitivity of the transition behaviour to the grid far exceeds the sensitivity to the LES models used. However, when we compare the behaviour of the models among each other we observe that the SEDM performs better than either the WALE or SIGMA models. We elaborate upon these conclusions and lay out a path for future work below.

As pointed out above, the quality of the LES simulation was quite sensitive to the grid used. This is due to the use of the high-order spectral difference schemes. These schemes possess high-rates of convergence and thus the results change dramatically in moving from coarse to fine grid as the scheme exhibits rapid grid-convergence. The ILES computation on the fine grid is quite revealing of this trend. The fine grid used by us is close, in terms of the number of solution points used, to the coarse grid utilised in Ref. [4]. This notwithstanding, better agreement with reference data is shown in the present study. While it is quite possible that the different synthetic turbulence used in the two cases may have played a role, it is more likely that the difference is due to the use of different numerical schemes, low-order schemes (2^{nd}-order finite volume) in Ref. [4] as compared to high-order (6^{th}-order SD) in our case. Thus it appears, that an ILES using a high-order scheme will tend to produce better results than an LES using a low-order scheme, irrespective of the type of model used, due to the rapid grid-convergence of the high-order schemes. The strong dependency of the

solution quality on the numerical scheme as compared to the sub-grid model, leads us to believe that perhaps a test case must be chosen, for which the influence of the sub-grid model is comparable to that of the scheme. The natural transition of the T3A- case ($Tu \simeq 0.9\%$) appears to be a suitable candidate as the transition occurs at Reynolds numbers an order of magnitude higher than either the T3A or T3B cases. To our knowledge there does not appear to have been any simulation upon the T3A- case and perhaps it may be used in future to obtain large differences between the models.

We now focus upon the behaviour of the LES models. All three models, WALE, SIGMA and SEDM, allow for transition to occur, but with varying behaviour. In general, the WALE and SIGMA model are relatively more dissipative than the SEDM. Within the pre-transitional region, the sub-grid eddy-viscosity introduced by the WALE and SIGMA is significant. This damps out the growth of the primary disturbance in the streamwise direction and hence delays the onset of transition. For the SEDM however, particularly on the medium and fine grids, the eddy-viscosity within this region is noticeably lower. This in turn allows the disturbance to grow in a manner similar to the ILES and thus the onset of transition is further upstream as compared to the WALE or SIGMA models. Thus, from this fact we can conclude that it is indeed a desirable property to have vanishing or low-levels of sub-grid eddy-viscosity in the pre-transitional region.

The grid convergence property of the SEDM is a property which has proven to be quite useful in our simulations. With the rapid decrease in the eddy-viscosity in the well-resolved regions of the domain (such as the freestream-boundary layer interface), a proper transition range and skin-friction level can be attained. With the rapid spread of high-order methods, the property of super-linear grid convergence of the eddy-viscosity is likely to become a more attractive feature in future LES modelling approaches. This feature was also highlighted as one of the major advantages of the variational multi-scale models (VMS), a technique specific to the high-order FEM type discretizations [142]. By comparison, for the WALE and SIGMA models, the rate at which the eddy-viscosity vanishes is linear and the consequences of this are quite apparent with a poorer prediction of the skin-friction in the fully turbulent region as well as the transition range. At this point we must bear in mind that the WALE and SIGMA models were developed during a period when low-order methods dominated numerical simulations and thus the need for the sub-grid eddy-viscosity to converge at high rates was never considered.

Despite what was stated in the paragraph above, the WALE and SIGMA models do provide reasonable accuracy. However, what is troubling is the fact that the near-wall scaling of the eddy-viscosity is quadratic rather than the cubic as is the theoretical rate. While we have been unable to identify cause of this problem, it does not appear to affect the scaling behaviour of the fluctuating stress. By comparison the eddy-viscosity of the SEDM scales

linearly and since it is based upon the scaling of the fluctuating stress, this is the best scaling behaviour possible. Future work could be focused in different combinations of functional forms of the eddy-viscosity operator multiplied by the turbulence sensor in order to reproduce the correct scaling. Finally, we recall the simulations in Ref. [111] involving the transition over a flat plate subjected to an adverse pressure gradient. In their simulations, they noticed that only the mixed-time-scale (MTS) model [143] was capable of predicting the presence of a recirculation zone, with the dynamic Smagorinsky and WALE model being too dissipative. We have come to a similar conclusion, about the WALE and SIGMA model, within this work as well. However, what is interesting is that the MTS model scales its eddy-viscosity with a test-filtered sub-grid scale energy and a time-scale and thus its overall formulation bears a strong resemblance to the SEDM. Perhaps, these test may point towards the benefits of using sub-grid kinetic energy as part of the eddy-viscosity formulation in the development of future turbulence models.

Considering the flow over the SD7003 airfoil, transition to turbulence has been well predicted by the proposed dynamic turbulence model, both in terms of bubble location and wall-normal profiles. A good agreement with previously published experimental and computational results has been observed, despite the use of a fairly coarse mesh. Kinetic energy spectra have been computed in both cases using the Taylor's hypothesis. Despite the high order selected for the simulation and the associated very low numerical dissipation introduced by the discretisation, no energy accumulation has been observed in the proximity of the Nyqvist grid wavenumber, providing a smooth transition from inertial to dissipative range.

Implicit large eddy simulation performed on the same computational grid have been performed to better quantify the overall influence of the Spectral Element Dynamic Model on the resolved field. However, all the implicit computations have shown to be unstable due to the insufficient numerical dissipation at the smallest scales. Implicit large eddy simulations, in fact, despite the appealing computational efficiency, are often inaccurate and/or unstable for a wide range of computational grids, numerical fluxes, especially when high orders of approximation are adopted on under-resolved meshes (i.e., typical LES resolutions). Therefore, adaptive dynamic SGS models, able to operate only in presence of insufficient numerical dissipation, represent a crucial step in the development of reliable and robust high-order schemes for complex turbulent flows.

Chapter 7

Bulk artificial viscosity

Contents

7.1 Introduction

Compressible gas dynamics has motivated many studies [144] and shock capturing techniques have been developed since the very beginning of the application of computational fluid dynamics. This research field is still extremely active due to the necessity of a proper description of compressibility effects in various complex engineering applications. Many different available numerical schemes are particularly susceptible to the treatment of discontinuous solutions, especially when high-order approximations are employed. In this case, the persistency of numerical oscillations in the proximity of a shock (commonly known as Gibbs phenomenon) can lead to unstable solutions implying accuracy and robustness reduction. Within the framework of high-order Discontinuous Finite Element (DFE) methods, many different procedures have been constructed to mitigate this issue. In particular, two of the most utilised approaches involve the use of limiters [145, 146, 147, 148]—including weighted essentially non-oscillatory (WENO) schemes [149, 150, 151, 152, 153]—or the injection of artificial viscosity (AV) [154, 155, 7, 156]. The former approach is based on the proper numerical limitation of the amplitude of the gradients of the solution, whereas the latter consists in the local addition of an ad-hoc amount of numerical dissipation. Both methods intend to limit or damp the presence of oscillatory behaviours near shocks and discontinuities.

Depending on the geometrical, physical and mathematical setting, one approach can be more suitable than the other: artificial viscosities terms are usually highly compact and can be easily computed even in higher dimensions, whereas limiters and WENO schemes cannot preserve the DFE scheme compactness and an appropriate and efficient generalisation to multiple dimensions on unstructured grids can be extremely cumbersome, both theoretically and computationally. On the other hand, the use of artificial viscosity does not provide full control on local minima and maxima of the solution and can lead to the occurrence of negative densities or pressures. Under such circumstances, it is necessary to couple the artificial viscosity with a positivity preserving scheme [157].

Regardless of which class of methods is employed, the identification and localisation of sharp features in the fluid flow is of fundamental importance for the correct description of the physical system. To this end, the use of shock sensors is widely diffused: these are designed to detect if a discontinuity is present or not in a certain region of the domain. Shock development and dynamics could sometimes be extremely difficult to predict, leading to a strong interest in the development of very accurate and highly automated sensors. The detection of such structures can be directly performed using nodal values of the solution (for example the divergence of the velocity [158]) or it can rely on modal sensors, which are based on the decay rate of the expansion coefficients of the approximated solution [7, 8]. In the context of

high-order approximations, the latter procedure is clearly more attractive, as it basically exploits intrinsic information provided by the spatial discretisation itself. Possible approaches include the use of the ratio between the energy of highest mode and the energy of the whole spectrum [7], or a least-square power fit of the modal coefficients decay [156]. It is worthwhile noting that an obvious limitation of the use of modal sensors is the necessity of a sufficiently high order approximation to get a meaningful modal spectrum. In the present work, the recently proposed characteristic-based sensor is implemented [159].

Once the discontinuity is identified the operative procedure to smooth out or limit the shock can be applied locally, stabilising the solution. However a careful attention should be paid on how spurious terms or numerical manipulations could affect the physical phenomena. Different shock capturing methods could lead to a similar mean behaviour of the solution but damage, or eventually completely destroy, some key characteristic of the governing equations.

On this particular regard, in the present work, a detailed comparison is presented between shock capturing approaches based either on the addition of Laplacian terms in the Navier-Stokes equations or on the addition of an amount of bulk viscosity in the stress tensor. Five canonical compressible flows are considered, namely: the one-dimensional shock collision; the two-dimensional inviscid strong-vortex/shock-wave interaction; the inviscid Taylor-Green vortex; the decaying compressible isotropic turbulence and the shock/wavy-wall interaction. Both direct numerical simulation and large-eddy simulation are performed depending on the selected test case.

The novelty of the work lies in the particular emphasis put in the assessment of the shock capturing procedure in correctly reproducing the theoretically expected non-monotonic behaviour of the entropy across the shock and on the capacity of the artificial viscosity to deal with turbulence, when present, and to interact with relevant models—*i.e.*, the sub-grid scale model in the case of LES—such as to provide physically accurate results.

The results of the present chapter have been published in "Computers and Fluids" [18] (https://doi.org/10.1016/j.compfluid.2019.104357).

7.2 Shock capturing in high-order discretisations

The usual Navier-Stokes equations [160] for the density ρ, the momentum $\rho\mathbf{u}$, $\mathbf{u}$ being the velocity vector, and the specific total energy E (internal + kinetic) are solved in their compressible form using the high-order Spectral Difference method [161, 162, 48]. The SD scheme enables arbitrary high-order computations over unstructured meshes and provides high resolution of the flow with minimal numerical dissipation [163, 94]. It is worthwhile noting that, the shock capturing formalisms discussed herein is based on the original

work of Persson and Peraire [7] and subsequent developments [8, 164, 159], and can be applied to any discretisation relying on a modal approximation of the solution.

7.2.1 Laplacian viscosity

The Laplacian viscosity represents a very robust approach [7, 8, 165, 166, 167, 164, 168, 159] in which the right-hand-side of each advection-diffusion equation (including mass conservation) is augmented by a Laplacian term in the form

$$\boldsymbol{\nabla} \cdot (\varepsilon_{\mathrm{AV}} \boldsymbol{\nabla} \phi) \,, \tag{7.1}$$

where ϕ is the relevant transported quantity—either the density, the momentum, or the total energy—and $\varepsilon_{\mathrm{AV}}$ is the added artificial viscosity by the shock capturing scheme. It is worth stressing that this approach treats each equation in the same way and the same amount of diffusion is added to every transported quantity.

7.2.2 Physical artificial viscosity

The physical artificial viscosity approach, on the other end, formally introduces artificial viscous fluxes in strict analogy to those representing molecular viscosity. An artificial viscosity μ_{AV}, an artificial bulk viscosity β_{AV} and an artificial thermal conductivity λ_{AV} are then added to the molecular viscosities and to the flow thermal conductivity.[1] In particular, according to previous works on physical models for the artificial viscosity [169, 170], in the present study an additional bulk viscosity is applied without any artificial shear viscosity. Hence, using index notation and Einstein summation convention, the viscous tensor and heat flux vector read, respectively,

$$A_{ij} = \mu \left[\left(\frac{\partial u_i}{\partial x_j} + \frac{\partial u_j}{\partial x_i} \right) - \frac{2}{3} \frac{\partial u_k}{\partial x_k} \delta_{ij} \right] + \beta_{\mathrm{AV}} \frac{\partial u_k}{\partial x_k} \delta_{ij} H \left(-\frac{\partial u_k}{\partial x_k} \right) , \tag{7.2}$$

$$Q_j = -(\lambda + \lambda_{\mathrm{AV}}) \frac{\partial T}{\partial x_j}, \quad \text{with} \quad \lambda_{\mathrm{AV}} = \frac{\beta_{\mathrm{AV}} c_p}{\mathrm{Pr}_\beta}, \tag{7.3}$$

[1] It is worth noting that a previous work on modal detection approaches for discontinuous Galerkin schemes [7] seem to suggest the use of the artificial shear viscosity only, μ_{AV}, while keeping the Stokes's hypothesis valid for the artificial viscous stresses ($\beta_{\mathrm{AV}} = 0$). Such a choice, which would prevent any artificial dissipation in the momentum equation in the one-dimensional case, appears—to the authors—to be in conflict with the one-dimensional results presented in the same paper, where the physical model provides sufficient robustness even at relatively high Mach numbers. Indeed, in a subsequent recent works [169, 170], not only the artificial bulk viscosity is retained, but it is the artificial shear viscosity which is set to zero because, as the authors emphasise, "shock waves are stabilized through β^* and λ^* only" (the * superscript is adopted therein for artificial viscosity terms).

where Pr_β is the artificial viscosity Prandtl number and c_p the constant-pressure heat capacity. Notice that, to prevent the artificial viscosity from being triggered in flow regions undergoing expansions (*i.e.*, where the divergence of the velocity is positive), an additional switch based on $H(\cdot)$, the Heaviside function, is embedded in the artificial bulk viscosity expressed by (7.2) [171, 172].

For the majority of the presented simulations, a constant value of $\mathrm{Pr}_\beta = \mathrm{Pr} = 0.71$ is used, whereas, for the three-dimensional cases featuring quite strong fluctuations of the local Mach numbers, the expression proposed in [170] is adopted:

$$\mathrm{Pr}_\beta = \mathrm{Pr}\left\{1 + \exp\left[-4\left(\mathrm{Ma} - \mathrm{Ma}_{\mathrm{thr}}\right)\right]\right\}, \tag{7.4}$$

where Ma is the local Mach number computed from the velocity magnitude and $\mathrm{Ma}_{\mathrm{thr}} = 3$ is a fixed threshold. This formulation avoids adding unnecessary thermal dissipation for low Mach number regions of the flow and provides a value of Pr_β that would tend asymptotically to Pr, the flow Prandtl number for hypersonic problems. Concerning the suppression of the shear AV term in favour of a bulk viscosity only, as it will be discussed in more details in the results section, the addition of a shear viscosity implies an extra dissipative term on vorticity equation, whereas the bulk viscosity adds a similar term in the dilatation equation only. As a result, the former affects vorticity modes, while the latter acts on dilatational modes. The use of bulk viscosity only appears to be very well suited for shock capturing for two main reasons. First of all because, being multiplied by the divergence of velocity, its functional form has an intrinsic compressible nature: even if shock detection is not perfect, the additional bulk viscosity is still proportional to a term which is big only in presence of strong compressibility effects. Secondly, the shear viscosity being linked to vorticity, it is more suited for turbulence modelling, as it is well established by widely popular eddy-viscosity models for LES. In this sense an additional artificial shear viscosity would lead to unnecessary vorticity dissipation and, more importantly, it could lead to unexpected interactions between an eddy-viscosity SGS model and the AV model.

7.2.3 Discontinuity sensor

Within the context of high-order methods, discontinuities are usually detected from the decay rate of the expansion coefficients of the solved signals (the reader is referred to the original works in [7, 8, 159] for additional details). In the current implementation, a recently proposed modal sensor based on the acoustic characteristics and the density is used [159]. Let ψ and $\overline{\psi}$ be, respectively, the signal adopted for shock detection and its truncated

polynomial expansion:

$$\psi(\xi) = \sum_{i=0}^{N} \hat{\psi}_i P_i(\xi), \quad \overline{\psi}(\xi) = \sum_{i=0}^{N-1} \hat{\psi}_i P_i(\xi), \tag{7.5}$$

where P_k is a polynomial of degree k from a suitable polynomial basis and $\hat{\psi}_k$ is the relevant kth mode. Then, the modal sensor s_e can be computed as:

$$s_e(\psi) = \log_{10}\left[\frac{(\psi - \bar{\psi}, \psi - \bar{\psi})_{L^2}}{(\psi, \psi)_{L^2}}\right], \tag{7.6}$$

where $(\cdot,\cdot)_{L^2}$ is the standard L^2 inner product within the element.[2]

Depending on the adopted approach—namely, Laplacian or physical model—the artificial viscosities, ε_{AV} or β_{AV}, are triggered in the neighbourhood of discontinuities using a sinusoidal function of the modal sensor s_e:

$$f(s_e) = \begin{cases} 0 & \text{for} \quad s_e < s_0 - l, \\ \dfrac{\varepsilon_0}{2}\left\{1 + \sin\left[\dfrac{\pi(s_e - s_0)}{2l}\right]\right\} & \text{for} \quad s_0 - l \leq s_e \leq s_0 + l, \\ \varepsilon_0 & \text{for} \quad s_e > s_0 + l, \end{cases} \tag{7.8}$$

with f being either ε_{AV} or β_{AV}/ρ in the case of Laplacian or physical model, respectively. The quantities s_0 and l are, respectively, a threshold and the sensor tolerance, whereas the nominal maximum value of the artificial viscosity, ε_0, is computed from the spectral radius of the flux Jacobian and the mesh element size h as

$$\varepsilon_0 = C_\varepsilon a_{\max} h/(N+1), \tag{7.9}$$

where $a_{\max}$ is the maximum wave speed in the whole domain. Unless explicitly stated otherwise, in the following computations, an automatic calibration algorithm based on manufactured solutions [164, 159] is adopted to determine optimal values of the shock capturing parameters (s_0, l, C_ε).

7.3 On non-monotonicity of entropy profile across an inviscid shock

Back in 1949, Morduchow and Libby [173] used an analytic solution for the profile of a weak shock in a viscous, heat-conducting, compressible flow to

[2] In the case an orthonormal polynomial base is adopted (*e.g.*, normalised Legendre polynomials), the inner products in the sensor definition assume the particularly simple form

$$(\psi, \psi)_e = \sum_{i=0}^{N} \hat{\psi}_i^2 \quad \text{and} \quad (\psi - \overline{\psi}, \psi - \overline{\psi})_{L^2} = \hat{\psi}_N^2, \tag{7.7}$$

where the modes are obtained from nodal values via matrix multiplication with the inverse Vandermonde matrix of the selected polynomial basis [52].

demonstrate that the equilibrium thermodynamic entropy has a maximum inside the propagating wave. Such overshoot of entropy within a shock layer was then further investigated for inviscid flows using weak solutions of partial differential equations based on distribution theory and integral conservation form of the equations [174, 175, 176, 177].

In the context of the Euler equations and Hugoniot jump conditions [178], the underlying idea is that, since the (normalised) entropy $s = \ln(p/\rho^\gamma)$ is defined using two functions (pressure and density) which are discontinuous across the shock, it cannot be defined by a single jump for, in such a case, some information would be unavoidably lost. Along these lines, Salas and Iollo [175] have discussed a more adequate form for the entropy function built from two Heaviside functions (Fig. 7.1)

$$s(\xi) = s_l + (s^* - s_l)H(\xi) + (s_r - s^*)H(\xi), \tag{7.10}$$

where ξ is the coordinate in a frame moving with the shock. The subscript 'r' denotes the shocked (compressed) gases and 'l' the gases upstream of the propagating interface, whereas s^* is the maximum level of entropy approximated as

$$s^* = \left[\ln(p_r)\left(\frac{p_r}{p_r - 1}\right) - 1\right] + \gamma\left[\ln(v_r)\left(\frac{v_r}{v_r - 1}\right) - 1\right], \tag{7.11}$$

where p denotes the pressure and $v = 1/\rho$ is the specific volume and the left relevant values of p_l and v_l, without any loss of generality, have been set equal to unity. The above relation provides the value of the theoretical peak

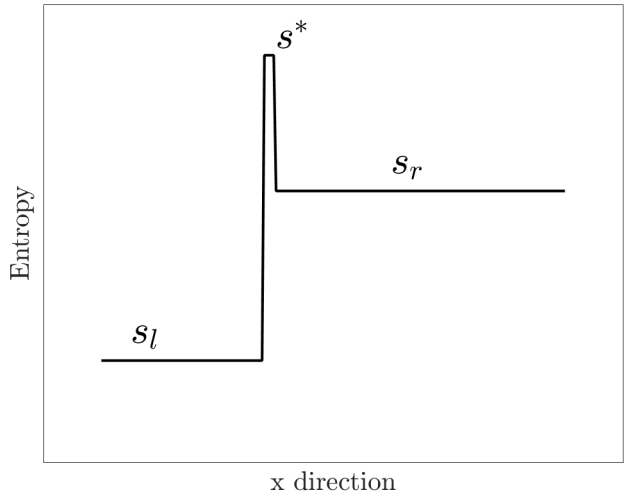

Figure 7.1: Sketch of the entropy profile across an inviscid shock layer.

of entropy which is expected in the case of a shock in the inviscid limit.

Such entropy peak is practically unattainable when the Euler equations are numerically solved because, no matter how accurate is the scheme or how fine is the mesh, a certain amount of numerical dissipation is unavoidable. Such (numerical) departure from the inviscid limit is even more pronounced when an artificial viscosity is adopted in the neighbourhood of shocks and discontinuities to guarantee a sufficient resolution of the solution. Under such circumstances and in the absence of a viscous counterpart of Eq. (7.11), this last can be used to asses the entropy preserving nature of the numerical scheme and the artificial viscosity approach, the most performing ones being those that provide the best approximation of the theoretical entropy profile across the shock. This is a crucial point which, to the authors' knowledge, has not been considered in detail so far in the archival literature. On this regard, however, it is worth noting that non-monotonic profiles in the entropy across one-dimensional shocks were reported in [7] when using the physical artificial viscosity model with non-zero artificial thermal conductivity λ_{AV}, whereas, this behaviour was lost when $\lambda_{\mathrm{AV}} = 0$ or in the case the Laplacian viscosity model was used. In view of the present analysis, these two particular choices in dealing with shocks would rise questions concerning their physical consistency in terms of entropy.

It is finally worth pointing out that overheating errors which were observed in [159] when performing one-dimensional shock collisions—and for which no remedy could be identified—are indeed, as it will be shown in the next sections, a direct consequence of the use of a Laplacian viscosity model and the resulting error in the entropy across the shocks.

7.4 Flow configurations and computational set-up

Five canonical test cases are considered to evaluate the two shock capturing approaches and their physical consistency in term of entropy behaviour: (a) stationary one-dimensional weak shock; (b) the collision of one-dimensional shocks; (c) the interaction between a two-dimensional strong-vortex and a shock-wave; (d) the inviscid Taylor-Green vortex; (e) the compressible, decaying, homogeneous, isotropic turbulence and (f) the interaction between a shock and a wavy-wall. Time integration is performed using a three step explicit Runge-Kutta scheme. The order of accuracy of the SD spatial discretisation varies with the cases. Whenever needed depending on the test cases, the Spectral-Element Dynamic Model (SEDM) for turbulence modelling has been employed [1]. It is worth noting that this SGS model features a modal turbulence sensor to detect flow under-resolution and locally activate the eddy-viscosity when needed.

7.4.1 Stationary one-dimensional weak shock

The simulation of a weak one-dimensional shock of Ma = 1.1 is here considered. The domain is 0.02 units long, equivalent to approximately 650λ, with λ the mean free path. The initial value of density, pressure and velocities are defined through Rankine-Hugoniot conditions and the system is let evolve toward the expected stationary solution. A very refined, shock-resolving simulation is here considered as reference: a uniform grid of 405 8th-order elements has been used, leading to approximately 90 solutions points located within the shock. For this level of resolution, shock capturing models are not needed. A dynamic behaviour of shear viscosity according to Sutherland's law has been assumed:

$$\mu(T) = \mu_0 \left(\frac{T}{T_0} \right)^{3/2} \frac{T_0 + T_S}{T + T_S}, \tag{7.12}$$

where $\mu_0 = 1.827 \times 10^{-5}\,\mathrm{kg\,m^{-1}s^{-1}}$, $T_S = 120\,\mathrm{K}$ and $T_0 = 291.15\,\mathrm{K}$. Finally, a Specific heat ratio $\gamma = 1.4$ and a $\mathrm{Pr} = \mu_0 c_P/\lambda = 0.71$ are assumed. Coarser 8-th order inviscid simulations have been performed on a 45 element grid with the two models active. For this discretization, approximately 8 solutions points are located in the inner part of the shock.

7.4.2 One-dimensional shock collision

Let a unitary long one-dimensional domain be initialised with two identical shocks moving towards each other, initialised respectively at $x = 0.2$ and $x = 0.8$. Two Mach numbers, Ma = 5 and Ma = 10 are considered. The domain is discretised in 60 uniformly distributed elements and Euler equations are solved using a 6th-order SD scheme. The initial values of density, pressure and velocity upstream the shocks, defined by the Rankine-Hugoniot conditions, along with the reflected shocks properties are summarised in Table 7.1. For all one-dimensional test cases, a slightly higher activation value has been chosen for the physical model in order to make it more sensitive to shock detection and, consequently, more aggressive in damping oscillations. Regarding the Laplacian approach, nominal parameters have been used.

7.4.3 Two-dimensional inviscid strong-vortex/shock-wave interaction

The physical domain is $\Omega = (0, 2L) \times (0, L)$ and a stationary shock is located at $x_s = L/2$, where L is a reference length scale (unity in the present case). The inflow Mach number is $\mathrm{Ma}_\infty = 1.5$ and a compressible, isothermal, zero-circulation vortex with external radius $b = 0.175L$ and inner core $a = 0.075L$ is initially centred at $(x, y) = (L/4, L/2)$. The initialisation procedure of velocity, temperature, density and pressure can be found in

	Ma	5	10
Incident	ρ	5.000	5.714
	$\lvert u\rvert$	4.733	9.762
	p	29.000	116.500
Reflected	Ma_r	2.408	2.579
	ρ_r	16.110	19.550
	$\lvert u_s\rvert$	5.916	10.946
	p_r	191.400	884.500

Table 7.1: One-dimensional shock collision (all the quantities are normalised with respect to the initial density and pressure of the fluid at rest between the initial shocks).

multiple articles [179, 180, 181, 170], based on isothermal, isochoric or isentropic conditions. As in [179], an isothermal initial condition is prescribed and the vortex Mach number Ma_v is set to 0.9 (based on the maximum tangential velocity in the vortex' inner core). Considering a reference frame with the origin in the initial position of the vortex centre, the initial velocity vector field upstream of the shock is obtained as the superposition of a uniform horizontal velocity corresponding to upstream shock conditions and the vortex velocity field, namely, $\mathbf{u}(r) = u_\theta(r)\hat{\mathbf{e}}_\theta + u_\infty \hat{\mathbf{e}}_x$, where $\hat{\mathbf{e}}_\theta$ is a unitary vector in the tangential direction around the centre and u_θ is the relevant tangential velocity component. The velocity components then read

$$u_\infty = \mathrm{Ma}_\infty \sqrt{\gamma R T_0}, \tag{7.13}$$

$$u_\theta(r) = \mathrm{Ma}_v \sqrt{\gamma R T_0} \begin{cases} r/a & \text{for} \quad r \leq a, \\ \dfrac{\eta}{2}\left(\dfrac{r}{b} - \dfrac{b}{r}\right) & \text{for} \quad a \leq r \leq b, \\ 0 & \text{for} \quad r > b, \end{cases} \tag{7.14}$$

where

$$\eta = 2(b/a)/[1 - (b/a)^2].$$

The thermodynamic variables in the vortex zone are evaluated combining the balance of the pressure gradients with the centripetal force and isothermal condition for ideal gases,

$$\frac{\mathrm{d}p}{\mathrm{d}r} = \rho \frac{u_\theta^2}{r}, \quad p = \rho R T_0, \tag{7.15}$$

leading to

$$\ln\left(\frac{p}{p_\infty}\right) = \begin{cases} \dfrac{\gamma \mathrm{Ma}_v^2}{2}\left[\left(\dfrac{r}{a}\right)^2 + \eta\dfrac{b}{a} + \eta^2 \ln\left(\dfrac{b}{a}\right)\right] & \text{for} \quad r \leq a, \\ \dfrac{\gamma \mathrm{Ma}_v^2}{2}\eta^2\left[\dfrac{(r/b)^4 - 1}{4(r/b)^2} - \ln\left(\dfrac{r}{b}\right)\right] & \text{for} \quad a \leq r \leq b, \\ 1 & \text{for} \quad r > b, \end{cases} \tag{7.16}$$

The spatial domain is subdivided in 256×128 uniform quadrilateral elements with a 5th-order SD discretisation. Free-slip and adiabatic walls are imposed on the top and bottom sides of the domain and characteristic-based, non-reflecting boundary conditions are applied on the inflow and outflow [182, 183].

7.4.4 Inviscid Taylor-Green vortex

The Taylor-Green Vortex constitutes a well-established test case to study vortex dynamics, turbulent transition, turbulent decay and energy dissipation processes in a three-dimensional setting [93]. The problem consist of a cubic domain $[-L\pi, L\pi]^3$ with periodic boundary conditions applied to all faces starting from the smooth initial condition

$$\begin{cases} \rho = \rho_0, \\ u_1 = U_0 \sin\left(\dfrac{x}{L}\right) \cos\left(\dfrac{y}{L}\right) \cos\left(\dfrac{z}{L}\right), \\ u_2 = -U_0 \cos\left(\dfrac{x}{L}\right) \sin\left(\dfrac{y}{L}\right) \cos\left(\dfrac{z}{L}\right), \\ u_3 = 0, \\ p = P_0 + \dfrac{\rho_0 U_0}{16}\left[\cos\left(\dfrac{2x}{L}\right) + \cos\left(\dfrac{2y}{L}\right)\right]\left[\cos\left(\dfrac{2z}{L}\right) + 2\right]. \end{cases} \tag{7.17}$$

Unity has been assigned to both U_0 and ρ_0, the reference velocity and density, respectively, and the initial value of the pressure P_0 has been chosen such that the corresponding initial Mach number is equal to 0.1. For this value of the Mach number, the flow is practically incompressible. The objective of the present simulation is thus to evaluate how dissipative are the two artificial viscosity models discussed in Section 7.2 when they are applied to an inviscid flow free from shocks. The flow domain is subdivided in 32^3 uniform cubic elements and discretised with a 6th-order SD scheme. The solution obtained without artificial viscosity will serve as reference. In all the simulations, considering the actual resolution of the employed mesh, the SEDM model has been activated due to turbulent nature of the developed flow field in later times of the simulation.

7.4.5 Under-resolved compressible isotropic turbulence

The objective of this test case is to investigate the performance of Laplacian and physical shock capturing models when shocks and turbulence coexist and both the SGS model and the shock capturing viscosity are activated. The computational domain consists in a periodic cube $\Omega = [-L\pi, L\pi]^3$ containing decaying homogeneous and isotropic turbulence. Pressure, temperature and density fields are initially constant and the velocity is solenoidal with

a turbulent kinetic energy spectrum $E(k) \sim k^4 \exp[-2(k/k_M)^2]$, where k is the wavenumber and k_M corresponds to the most energetic wavenumber (in this case $k_M = 4/L$). The initial turbulent Mach number and Taylor-scale Reynolds number are evaluated on the initial flow filed as:

$$\mathrm{Ma}_{t,0} = \frac{u_{\mathrm{rms},0}\sqrt{3}}{\langle a \rangle} = 0.6, \quad \text{and} \quad \mathrm{Re}_{\lambda,0} = \frac{\langle \rho \rangle u_{\mathrm{rms},0} \lambda_0}{\langle \mu \rangle} = 100, \tag{7.18}$$

where a is the speed of sound and $\langle \cdot \rangle$ denotes spatial averaging, whereas

$$u_{\mathrm{rms},0} = \sqrt{\tfrac{1}{3}\langle u_i u_i \rangle}\Big|_{t=0} \quad \text{and} \quad \lambda_0 = \sqrt{\frac{\langle {u_1}^2 \rangle}{\langle (\partial u_1/\partial x_1)^2 \rangle}}\Big|_{t=0} \tag{7.19}$$

are, respectively, the initial root-mean-square velocity fluctuations and the Taylor micro-scale. A power-law is assumed for the dynamic viscosity,

$$\mu = \mu_0 (T/T_0)^{3/4}.$$

It's easy to show that the initial condition is such that $\lambda_0 = 1/k_M$. The domain has been discretised using 16^3 hexahedra elements with a 6-th order polynomial approximation. Considering state-of-the-art LES of compressible isotropic turbulence [169] [184] [185] this resolution gives a purposely slightly under-resolved simulation in order to enhance the impact of numerical dissipation, this last including the dissipation coming from the numerical discretization, the artificial shock capturing viscosity and the SGS modeling viscosity. Defining the Nyquist wavenumber as $\tilde{k}_N = \pi/h$, corresponding to the smallest resolvable scales, the chosen grid gives $\tilde{k}_N = 48/L$, which is in good agreement with commonly used values for LES of this configuration. The value h has been approximated as $2\pi L/N$ where N is the number of degrees of freedom (DoF) along one direction. It shall be noticed that this resolution corresponds, in terms of DoF, to the one used in [170] for 3rd-order computation of the same test case. Results have been compared with a DNS on 256^3 DoF [186]. According to [186], higher resolution data (384^3 DoF) have been employed to evaluate kinetic energy contributions. The simulation is performed from $t = 0$ to $t = 4A_0$, with $A_0 = \lambda_0/u_{\mathrm{rms},0}$.

7.4.6 Shock/wavy-wall interaction

The interaction between a shock wave and a sinusoidal wavy wall is a more challenging test case, simultaneously featuring complex shock reflections and a background low-Mach number flow with very specific small scale patterns [187, 188, 168]. The problem has been chosen to match the experiment reported in [187]. In this experiment, a vertical planar shock propagating at Mach number 1.5 in air is reflected on a sinusoidal wall with amplitude 1.0 mm and wavelength 2.0 cm. The Navier-Stokes equations are integrated

Figure 7.2: Geometrical set-up and initial conditions for shock/wavy-wall interaction.

over a computational domain 10 cm long and 2 cm high with 600×140 unstructured quadrilateral elements. A 5th-order SD scheme is adopted and the total number of degrees of freedom is 2.1×10^6. The left wall is characterised by a no-slip condition while top and bottom boundaries are set as periodic. The initial setup is schematically represented in Fig. 7.2. The typical properties for air have been used in the simulation, hence the specific heat ratio γ is set equal to 1.4, while the Prandtl number is set equal to 0.72. The dynamic viscosity is modelled using a Sutherland's law, namely,

$$\mu(T) = \mu_0 \left(\frac{T}{T_0} \right)^{3/2} \frac{T_0 + T_S}{T + T_S}, \tag{7.20}$$

where $\mu_0 = 1.827 \times 10^{-5}\,\mathrm{kg\,m^{-1}s^{-1}}$, $T_S = 120\,\mathrm{K}$ and $T_0 = 291.15\,\mathrm{K}$. A second, more challenging, situation has been considered where the incident shock Mach number is increased up to 5.0 and the specific heat ratio γ is reduced down to 1.15, thus approaching the Newtonian limit [168]. The other physical parameters are the same as in the Mach 1.5 case. All the main computational and physical parameters are listed in Table 7.2 for convenience.

7.5 Results and discussion

7.5.1 Stationary one-dimensional weak shock

This particular test case is focused on the shock-shape across a viscous weak shock. It is well-known that a non-monotonic behaviour should be observed whenever a viscous-thermal conductive fluid is considered [173]. Moreover, even if this property can be observed for strong shocks as well, a weak shock allows to easily run shock-resolved simulations, which do not need any shock capturing procedure. Accordingly, a highly resolved simulation of a weak shock has been performed and considered here as a reference. In order to evaluate the capability of the two shock capturing models to describe the physical properties of the shock, two coarser inviscid simulations have been tested. An example of coarse grid solution is shown in Fig. 7.3, where approximately 8 solution points are contained within the shock. The density

Domain size	$L \times H$	10.0×2.0		cm^2
Number of elements	$N_x \times N_y$	600×140		–
Discretisation order	n	5		–
Degrees of freedom	DoF	2.1×10^6		–
Wavy-wall amplitude	A_{ww}	1.0		mm
Wavy-wall wavelength	λ_{ww}	2.0		cm
Specific heat ratio	γ	1.4	1.15	–
Incident shock Mach	$\mathrm{Ma_i}$	1.5	5.0	–
Incident shock speed	$\mathcal{D}_\mathrm{i}$	-514.0	-1553.0	$\mathrm{m\,s^{-1}}$
Reflected shock Mach	$\mathrm{Ma_i}$	1.43	3.16	–
Incident shock speed	$\mathcal{D}_\mathrm{r}$	324.9	271.5	$\mathrm{m\,s^{-1}}$
Initial left state	ρ_1	1.208		$\mathrm{kg\,m^{-3}}$
	u_1	0.0		$\mathrm{m\,s^{-1}}$
	p_1	101.325		kPa
Initial right state	ρ_2	2.25	11.29	$\mathrm{kg\,m^{-3}}$
	u_2	-237.96	-1386.88	$\mathrm{m\,s^{-1}}$
	p_2	249.091	2703.344	kPa

Table 7.2: Physical and computational set-up of shock wavy-wall interaction. Velocities are indicated on the laboratory reference frame.

and the entropy profiles from the coarse grid computations are compared to the reference solution in Fig. 7.4 From the observation of the reference solution, the non-monotonic behaviour of the entropy is clearly evident, with a very strong overshoot located almost exactly at $x/\lambda = 0$; *cf.* Fig. 7.4(b). It can be noted how the relative jump in the entropy overshoot is extremely large compared to the shock-generated entropy, $\Delta s = s_r - s_l$. In particular, $s_{max} - s_l \approx 23\Delta s$, which is slightly higher than the expected value given by Eq. (7.11), namely, $s_{max} - s_l \approx 15\Delta s$. This is not really surprising: the presence of thermal conductivity gives an additional increase of entropy within the shock, which adds to the inviscid overshoot. Regarding the two coarser simulations, non-monotonicity is preserved by the physical model while the Laplacian AV gives an almost flat profile. Moreover, concerning the Laplacian approach, the small, persisting, numerical oscillations close to the shock force the entropy to take values smaller than s_l. In other words, the use of the Laplacian model leads, for this test case, to a local decrease of entropy, which is clearly unphysical. The Physical artificial viscosity gives the expected behaviour of entropy across the shock, even if it is not able to reach the exact peak of entropy production.

7.5.2 One-dimensional shock collision

The present analysis focuses mainly on three aspects which are strictly connected to the accuracy and reliability of the shock capturing scheme:

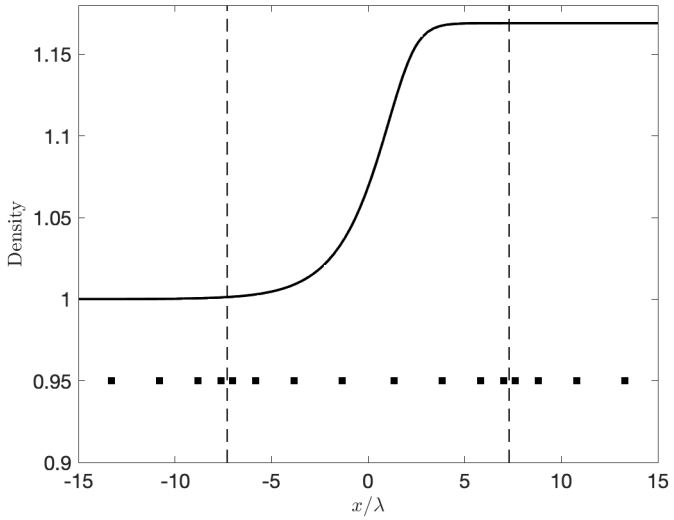

Figure 7.3: Example of coarse grid with ≈ 8 solution points in the shock region. The x-axis is normalized with respect to the mean free path λ. Dashed lines indicate element interfaces; symbols indicate the location of the solution points.

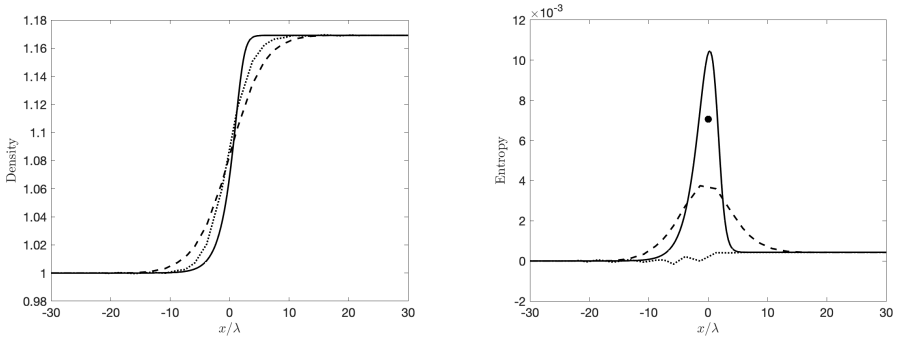

(a) density (b) entropy

Figure 7.4: Density and entropy shock profiles: solid line, reference solution; dashed line, physical AV model; dotted line, Laplacian AV model; the black dot on the entropy profile indicates the theoretical maximum in the inviscid limit (*cf.* Eq. (7.11)).

(a) the correct reproduction of the theoretically expected behaviour of entropy across the shock front, (b) the presence of spurious post-collision oscillations and (c) the onset of overheating errors in the solution and their connection to entropy preservation. In Fig. 7.5(a), the density field is shown before collision. No particular difference is present between the Laplacian

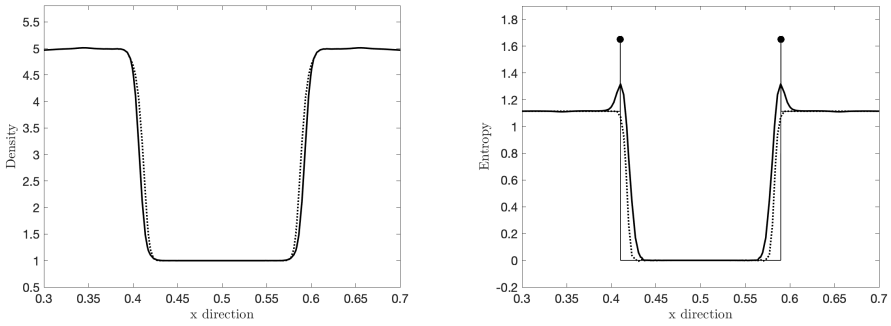

(a) density (b) entropy

Figure 7.5: Ma = 5 shocks before collision: solid line, physical artificial viscosity model; dotted line, Laplacian AV model; the black dot on the entropy profile indicates the theoretical maximum in the inviscid limit (*cf.* Eq. (7.11)).

and physical models, which both smooth adequately the shocks. Looking at the normalised entropy profile in Fig. 7.5(b), however, more marked differences between the two approaches appear. Using the physical model, the behaviour of the entropy across the shock is non-monotonic, whereas the Laplacian artificial viscosity produces a simple entropy jump. Hence, the expected non-monotonic theoretical profile of entropy is preserved by the physical model due to its capability to secure the proper physical coupling between the viscous work, the thermal dissipation and the entropy itself. In Fig. 7.5(b) the entropy jump is compared with the theoretical value obtained from the inviscid Eq. (7.11). The purely numerical nature of the Laplacian approach becomes evident, with the lack of knowledge on the energy transfers within the shock (without mentioning the artificial diffusion of density). Turning the attention to the behaviour of the two models after the shock collide, the relevant density and entropy profiles are depicted in Figs. 7.6(a) and 7.6(b), respectively. At the location of the impact between the shocks, another notable difference between physical and Laplacian viscosities is visible. In particular, when the Laplacian approach is adopted, an unphysical decrease of density is generated. This phenomena is commonly known as *overheating* error, which motivated multiple studies [189, 190, 191, 192, 193, 194]. It was concluded that the onset of overheating errors is directly related to the numerical scheme and its inability to preserve exactly the entropy convection at the moment of collision. The consequent increase in entropy would then be the main responsible of these spurious effects. This is readily confirmed by looking at Fig. 7.6(b), where the two shock capturing approaches report very different entropy behaviours. As already mentioned, the same type of overheating errors were observed in [159] for the same test case when using the

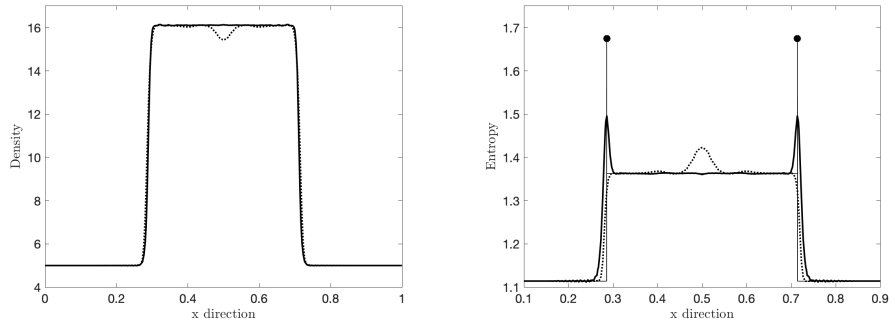

(a) density (b) entropy

Figure 7.6: Ma = 5 shocks after collision: solid line, physical AV model; dotted line, Laplacian AV model; the black dot on the entropy profile indicates the theoretical maximum in the inviscid limit (*cf.* Eq. (7.11)).

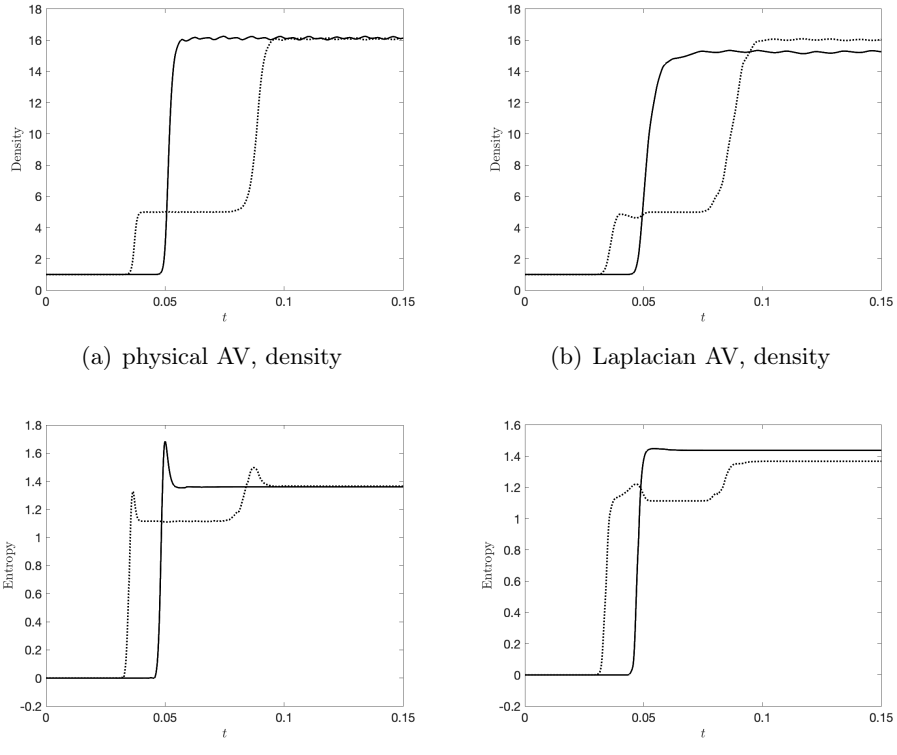

(a) physical AV, density (b) Laplacian AV, density

(c) physical AV, entropy (d) Laplacian AV, entropy

Figure 7.7: Mach = 5 shock collision. Density (a, b) and entropy (c, d) time history profiles. Solid line, $x = 0.5$; dotted line $x = 0.58$

Laplacian model. However, overheating errors can be observed in multiple other test cases, even in absence of shocks, such as in the case, for example, of the receding flow [191, 193]. This phenomenon is not directly related to the shock capturing procedure unless, of course, this last impacts, negatively, entropy conservation. On the contrary, a wise choice of artificial viscosity can lead to the mitigation, or even to the complete removal, of overheating errors. It is clear from Fig. 7.6(b) that the physical approach appears as a better option, simply because the physical model uses an artificial thermal conductivity related to the bulk viscosity, which features an elliptic/diffusive nature. Therefore, every temperature gradient (in the absence of any forcing term) tends to be dissipated due to thermal conduction.

The damping of the overheating error is quantitatively evaluated in Fig. 7.7, where the time history of the density and the entropy at two different locations ($x = 0.5$ and $x = 0.58$) is shown. These plots provide additional evidence of differences in the value of the density and the entropy at the point of impact ($x = 0.5$) and away from it ($x = 0.58$). A gap between the two lines can be clearly noticed when using the Laplacian model: underestimation of the density and over-estimation of the entropy. The physical model, on the other hand, does not produce overheating errors and no difference is visible between the relevant values recorded at $x = 0.5$ and $x = 0.58$.

Finally, a more challenging situation is considered increasing the Mach number up to 10. Results are reported in Fig. 7.8, where the density and entropy profiles after collision are shown. Overall, no major differences between the Ma = 5 and the Ma = 10 test cases are found.

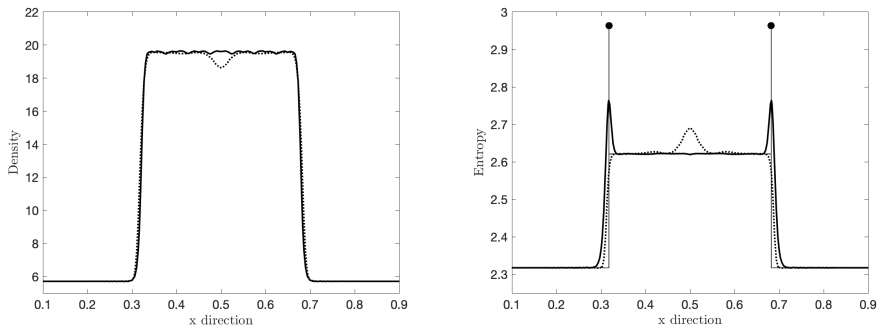

(a) Density (b) Entropy

Figure 7.8: Ma = 10 shocks after collision: solid line, physical AV model; dotted line, Laplacian AV model; the black dot on the entropy profile indicates the theoretical maximum in the inviscid limit (*cf.* Eq. (7.11)).

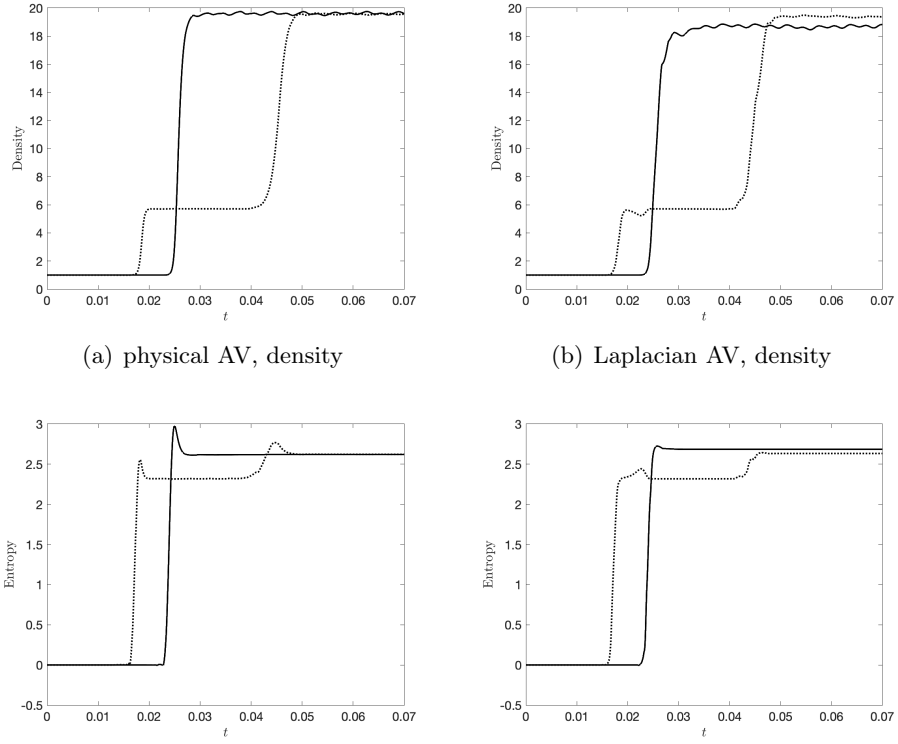

(a) physical AV, density

(b) Laplacian AV, density

(c) physical AV, entropy

(d) Laplacian AV, entropy

Figure 7.9: $M = 10$ shock collision. Density (a, b) and entropy (c, d) time history profiles. Solid line, $x = 0.5$; dotted line $x = 0.58$.

7.5.3 Two-dimensional inviscid strong-vortex/shock-wave interaction

In the shock-vortex interaction, particular attention will be paid on the locality of the artificial viscosity and on the low dissipative character of the physical model. To evaluate the accuracy of the shock capturing procedure, snapshots of the density field are shown in Fig. 7.10(a), right after the vortex traverses the shock, and in Fig. 7.10(b), when the vortex splits into two smaller vortices as a result of its interaction with the shock front. After the interaction, complex acoustic structures arise. Some interesting differences between the two AV approaches are observed in Fig. 8.9. The higher dissipation of the Laplacian approach does not allow for the vortex to breakdown, whereas the physical artificial viscosity captures this feature. In other words, when the Laplacian viscosity is used, the fluid behaves as a more viscous gas, thereby jeopardising the development of the smallest flow structures. Concerning the localization of the artificial viscosity when using the physical model, Figs. 7.12(a) and 7.12(b) show the contours of artificial bulk viscos-

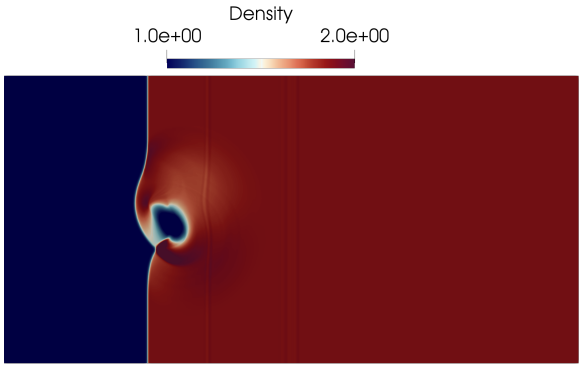

(a) $t_1 = 0.085s$

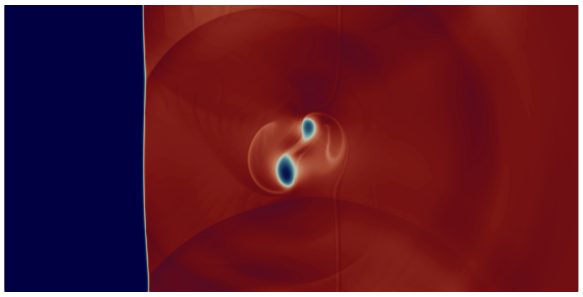

(b) $t_2 = 0.245s$

Figure 7.10: Shock-vortex interaction. Density field.

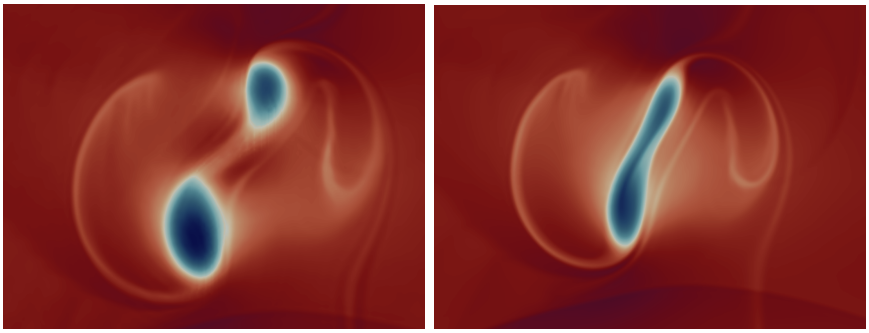

(a) physical (b) Laplacian

Figure 7.11: Shock-vortex interaction. Density field detail at $t_2 = 0.245s$.

ity right after interaction and at the moment the vortex breaks down. As it can be seen, the artificial bulk viscosity is zero almost everywhere, except in the shock region. This is, of course, of paramount importance to avoid the injection of unnecessary dissipation in the system away from the shock. Finally, as already mentioned in the mono-dimensional test case, entropy

(a) $t_1 = 0.085s$

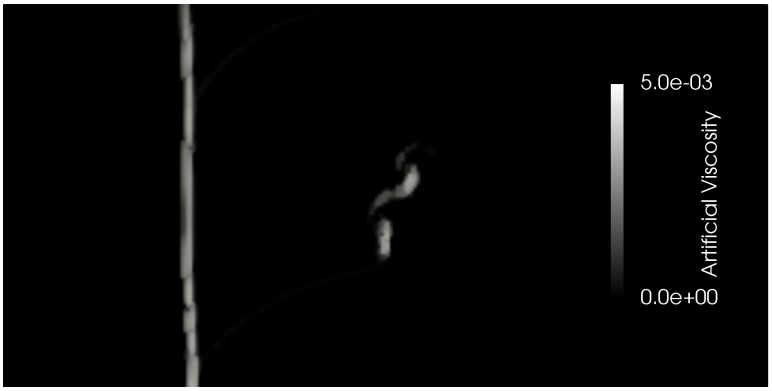

(b) $t_2 = 0.245s$

Figure 7.12: Shock-vortex interaction. Physical artificial viscosity. Image resolution is low due to the lack of smoothness of the artificial viscosity itself (which is only linear).

shocks should be non-monotonic. This characteristic property is clearly satisfied by the physical model in this two-dimensional case too (see Fig. 7.13).

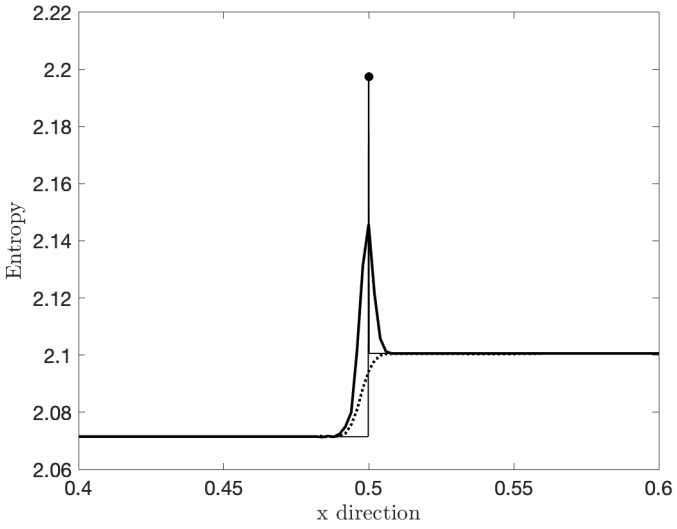

Figure 7.13: Shock-vortex interaction. Entropy field at $t_1 = 0.085s$ (see Fig. 7.10(a) for vortex position) along the line y=0.4L. Solid line, physical AV model; dotted line, Laplacian AV model; the black dot on the entropy profile indicates the theoretical maximum in the inviscid limit (*cf.* Eq. (7.11)).

7.5.4 Inviscid Taylor-Green Vortex

Despite the rather idealized and simple initial flow field, the TGV problem contains many different interesting features of turbulence. As the time advances, the vortex stretching process leads to a natural transition to isotropic turbulence. Due to the absence of physical viscosity (inviscid flow), the energy of the fluctuating field cascades to smaller and smaller scales without any viscous dissipation, making it a stringent test case for calibrating artificial numerical dissipation.

Different phases of turbulence transition and development can be recognised. Before reaching the characteristic time $t \approx 4L/U_0$, the flow is laminar and it is fully resolved by the mesh. After a transitional period, at $t \approx 7L/U_0$ the vortex stretching process breaks down and sub-grid scales mechanisms start to affect the solution.

Figs. 7.14 and 7.15 show the time evolutions of four main quantities, namely the mean kinetic energy ratio $k = (1/2)\rho u_i u_i / k_{\text{ref}}$ (where k_{ref} is the mean kinetic energy theoretically present in the flow), the mean square vorticity $\Omega = L^2 \omega_i \omega_i / U_0^2$, the temperature variance $c_v^2 \langle T'T' \rangle / U_0^2$ (where c_v is

the specific heat at constant volume) and the dilatation variance $L^2\langle\theta'\theta'\rangle/U_0^2$ with $\theta = \partial u_i/\partial x_i$. Note that the prime denotes deviations from the mean value over the whole domain, namely, given any generic quantity ϕ, $\phi' = \phi - \langle\phi\rangle$.

In this inviscid flow, the mean kinetic energy should stay constant. As it can be seen in Fig. 7.14(a), this is observed when the physical artificial viscosity is used. The Laplacian model, on the other hand, is found to be too dissipative and promotes a rapid decay of the kinetic energy. Similarly, applying the Laplacian artificial viscosity, the mean-square vorticity is not increasing as it should in this inviscid flow (*cf.* Fig. 7.14(b)), whereas the physical artificial viscosity allows for the vorticity to raise as expected. The temperature variance also suffers from a too rapid decay with the Laplacian formulation, which is not the case with the physical formulation (Fig. 7.15(a)). Turning to the compressible character of the flow (*cf.* Fig. 7.15(b)), the Laplacian form of the artificial viscosity does not allow for the variance of dilatation to grow in a significant manner. Because of the bulk character of the physical model for the artificial viscosity, part of this variance is unavoidably damped; nonetheless, a significant growth is yet captured.

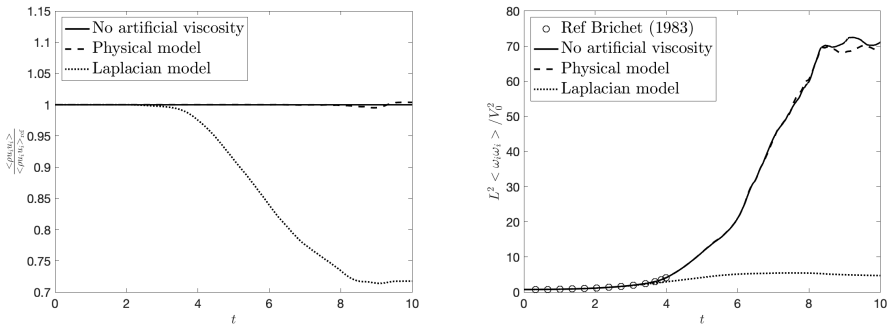

(a) Normalised mean kinetic energy (b) Normalised mean-square vorticity

Figure 7.14: Inviscid Taylor-Green Vortex. Kinetic energy and vorticity.

7.5.5 Under-resolved compressible isotropic turbulence

To further progress on the evaluation of artificial viscosity in the presence of both turbulence and compressibility effects, results with the compressible isotropic turbulent test case are now examined. The unstable initial configuration leads quickly to the development of strong vortical, entropy and acoustic modes in the whole domain. Weak shock waves, commonly known as eddy shocklets [195], appear spontaneously from the turbulent motions as well. An example of a shocklet is shown in Fig. 7.16, where the relevant profiles of dilatation, density and Mach number are plotted. Simulations

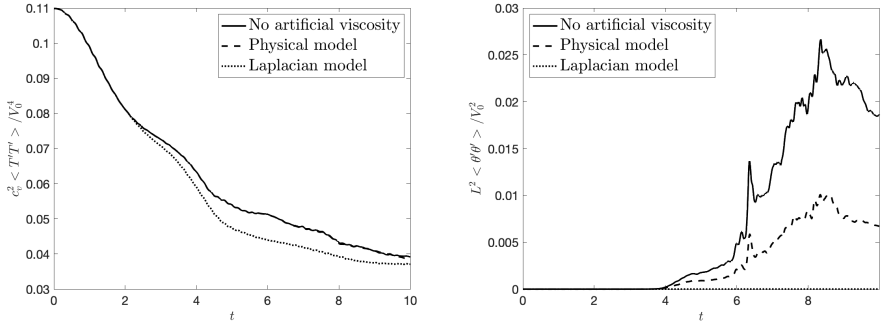

(a) Variance of temperature (b) Variance of dilatation

Figure 7.15: Inviscid Taylor-Green Vortex. Variance of temperature and dilatation.

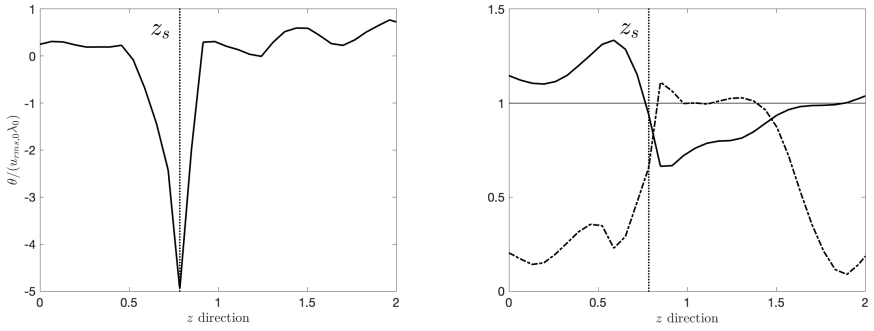

(a) Normalised dilatation (b) Normalised density (solid line) and Mach number (dash-dotted)

Figure 7.16: Example of shocklet occurring at normalised time $t \approx 0.557$ at $(x, y) \approx (4.3, \pi)$ plotted along z direction.

performed without artificial viscosity and using the Laplacian or physical models are compared to DNS results. The relevant results are reported in Figs 7.17–7.19. It shall be noted that the simulation performed without artificial viscosity, due to the accumulation of kinetic energy at the unresolved scales, became unstable at a normalised time of about 0.56. This notwithstanding, the relevant (partial) curves are retained for reference in all plots. Concerning the SEDM model, it is worth pointing out that, due to the actual order of accuracy of the employed discretization and due to the relevant enhanced resolution of the SD scheme, the SEDM turbulence sensor seldom detected any appreciable under-resolution. As a consequence, negligible amounts of eddy-viscosity were injected throughout the computation. This indicates that the numerical dissipation from the spatial discretization

operators sufficiently describes the energy transfers between resolved and under-resolved scales.

Using the physical artificial viscosity, the time evolution of the normalised mean kinetic energy (Fig. 7.17(a)) is in perfect agreement with the reference DNS [186], while the Laplacian form overestimates the dissipation, which confirms once again the over-dissipative character of the Laplacian model. The mean-square vorticity is also well reproduced with the physical artificial viscosity (dashed line in Fig. 7.17(b)), while the Laplacian form misses the vorticity response and returns a constant decay (dotted line in Fig. 7.17(b)). Turning the attention to quantities more related to compressibility effects,

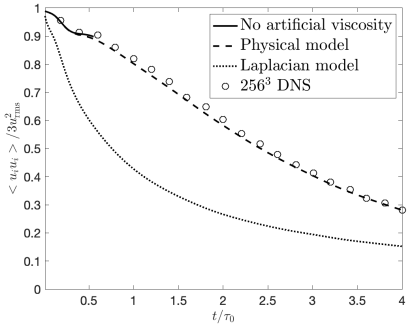

(a) Normalised mean kinetic energy

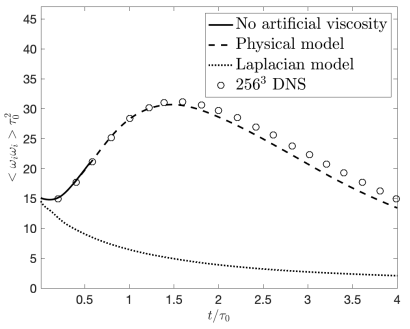

(b) Normalised mean-square vorticity

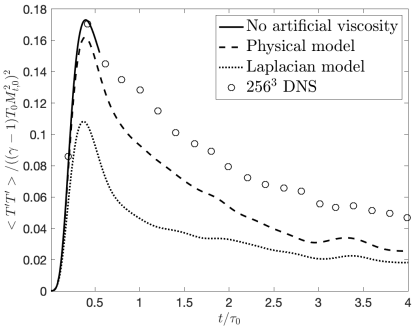

(c) Normalised variance of temperature

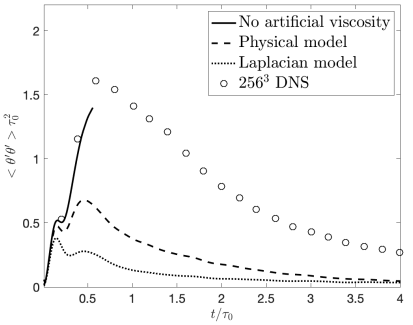

(d) Normalised variance of dilatation

Figure 7.17: Under-resolved isotropic compressible turbulence.

such as the variance of temperature (Fig. 7.17(c)) and the variance of dilatation (Fig. 7.17(d)), the Laplacian AV yields results which depart significantly from the DNS, yet some weakness of the physical AV model become also apparent. The variance of temperature from the physical model is slightly underestimated, which suggests a slight overestimation of thermal dissipation. Unfortunately, the bulk viscosity is known to damp acoustic modes [171] and this is clearly visible in Fig. 7.17(d). The use of divergence-based sen-

sors should improve the results [170, 171].

The kinetic energy balance (under the periodic boundary condition applied here) can be written as

$$\overbrace{-\frac{d}{dt}\left(\frac{1}{2}\int \rho u_i u_i dV\right)}^{\text{Variation of kinetic energy}} = \overbrace{\int \left(2\mu S_{ij}S_{ij} - \frac{2}{3}\mu\left(\frac{\partial u_j}{\partial x_j}\right)^2\right)dV}^{\text{Viscous dissipation}} \underbrace{-\int p\left(\frac{\partial u_j}{\partial x_j}\right)dV}_{\text{Dilatation work}} + \varepsilon, \tag{7.21}$$

where the dissipation term ε contains the three contributions stemming from the sub-grid scale model, the artificial viscosity and the numerical dissipation:

$$\varepsilon = \varepsilon_{\text{SGS}} + \varepsilon_{\text{AV}} + \varepsilon_{\text{num}}. \tag{7.22}$$

Fig. 7.18(a) shows the viscous dissipation from Eq. (7.21), which is well

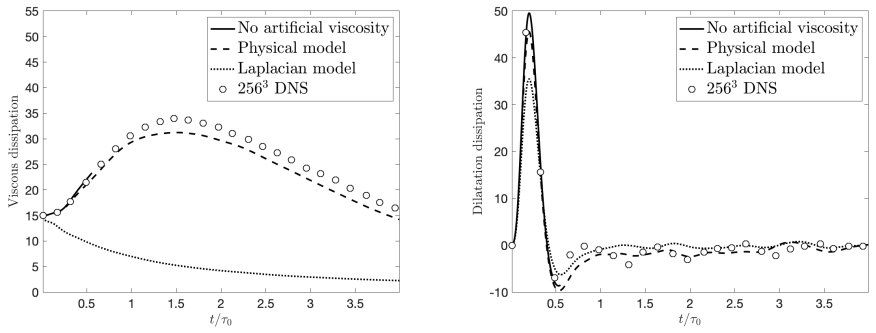

(a) Viscous dissipation (b) Dilatation dissipation

Figure 7.18: Under-resolved isotropic compressible turbulence.

reproduced by the physical artificial viscosity due to the small damping of vortical modes, which is not the case when using the Laplacian form. As far as the dilatation term is concerned (see Fig. 7.18(b)), this is not perfectly reproduced due to the use of the bulk viscosity. Even if acoustic damping using bulk viscosity is clearly visible and theoretically known, it is worth noticing that using a Laplacian approach gives no advantage at all for this test case. In Fig. 7.19, the additional spurious dissipation is analysed. The difference in energy, which is artificially dissipated in the system between Laplacian and physical approach, becomes here clearly evident and further confirms the lower dissipation overall promoted by the use of the physical model. Concerning the influence of the shock capturing parameters, these can be changed within reasonable limits, yet the main results of our discussion remain unchanged: the Laplacian viscosity tends to be more dissipative overall and cannot preserve the expected entropy behaviour. Finally it

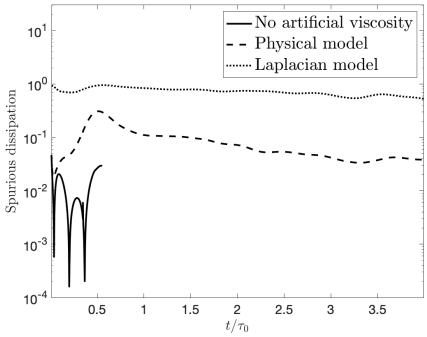

Figure 7.19: Under-resolved isotropic compressible turbulence. Spurious dissipation (in absolute value scaled by $-\dot{E}_k$).

should be pointed out that similar results have been shown in [184], where some drawbacks when using an artificial bulk viscosity were pointed out. The presence of a bulk viscosity implies a certain amount of dissipation on dilatational modes. Such dissipation is more or less strong depending on the specific parameters chosen, as clearly confirmed in Fig. 7.17(d). Nonetheless, whenever moderately compressible turbulent flows are considered, the use of a bulk viscosity over a shear viscosity shall be preferred, as the latter could lead to an excessive dissipation on vorticity modes, affecting energy transfers of turbulence. Moreover, the coexistence of a shear artificial viscosity and an eddy-viscosity SGS model could lead to unpredictable outcomes in both shock stabilization and turbulence modelling.

7.5.6 Shock/wavy-wall interaction in the Newtonian limit

The interaction between a shock wave and a wavy-wall involves a rather broad range of scales: the complex flow patterns arising in proximity of the wall are characterised by velocities many order of magnitudes smaller than the macroscopic shock speed. This wide spectrum of scales implies challenging difficulties in the experimental detection of such structures. On the other hand, numerical experiments are computationally very expensive in order to get a sufficient level of detail. A more detailed analysis on the peculiar physical features of this particular test case at an initial Mach number of 1.5, based on the companion experiment by Biamino [187], can be found in [188]. Other similar computations at higher Mach numbers (3.0 and 5.0) are reported in [168]. The present study focuses on the 1.5 and 5.0 Mach number tests only. Compared to the results reported in [188, 168] the present simulation has been performed with the physical shock capturing procedure instead of the Laplacian based approach.

A first validation for the lower Mach number case is reported in Fig. 7.20, where experimental Schlieren photography images are compared with nu-

merical results at times 120μs, 200μs and 280μs giving a qualitatively good agreement with respect to experimental data. Clearly, even the physical model for the shock capturing procedure is able to stabilise the numerical simulation without damaging the complex pattern of reflections arising from the collision with the wavy wall. As in the one-dimensional case no particular difference can be noticed between the two models: they both represent accurately shocks reflection and collision. The only characteristic feature preserved by the physical approach is the shape of entropy across the shocks both before the impact, at $t = 0s$ (Fig. 7.21) and after, at $t = 120\,\mu$s (Fig. 7.22). A more challenging situation as been studied as well, consider-

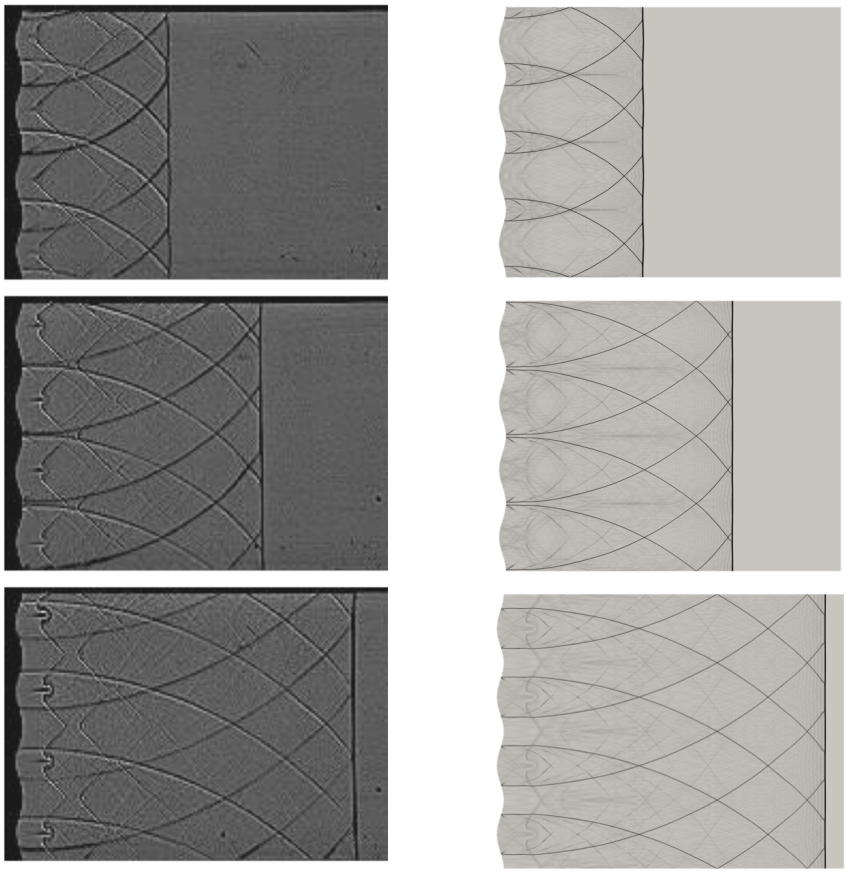

Figure 7.20: Qualitative comparison between experimental (left) and numerical Schileren using physical AV model (right) at times 120μs, 200μs and 280μs (up to bottom).

ing an incident Mach number $\mathrm{Ma_i} = 5.0$ and a specific heat ratio $\gamma = 1.15$. These choices lead to stronger reflected shocks and to even more complex patterns into the shocked gas region. In these extreme conditions the divergence switch has been turned off while instead all the other AV parameters

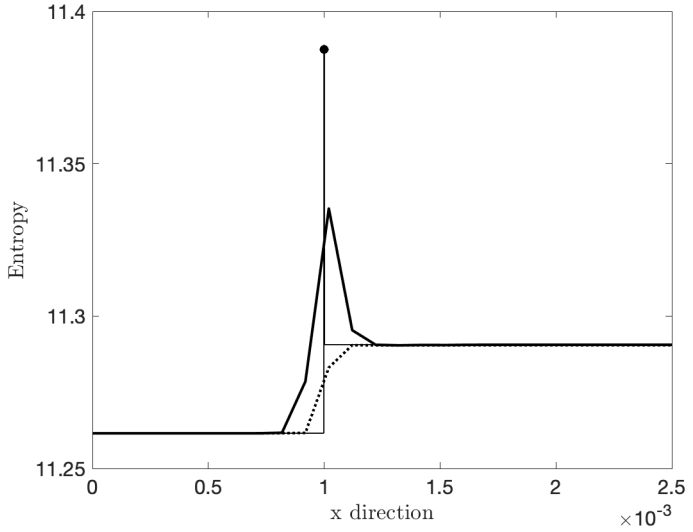

Figure 7.21: Entropy field at $t = 0.0$s along y=0. Solid line, physical AV model; dotted line, Laplacian AV model; the black dot on the entropy profile indicates the theoretical maximum in the inviscid limit (*cf.* Eq. (7.11)).

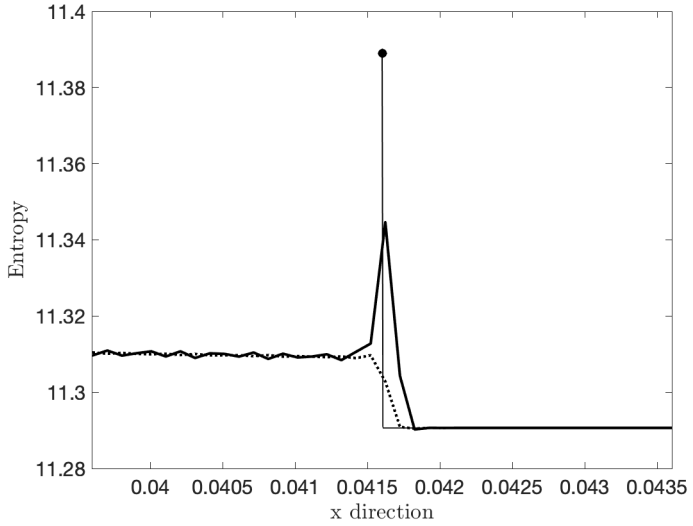

Figure 7.22: Entropy field at $t = 120\mu$s along y=0. Solid line, physical AV model; dotted line, Laplacian AV model; the black dot on the entropy profile indicates the theoretical maximum in the inviscid limit (*cf.* Eq. (7.11)).

are the same as in one-dimensional tests. It is worth mentioning that the additional divergence check affects only partially the results: it implies less dilatational modes dissipation but other quantities are only slightly affected.

In this particular test case, more marked differences between Laplacian and physical approaches can be noticed. First of all, in Fig. 7.23 it is evident the tendency of the Laplacian approach to englobe many smaller vorticity structures and over-smooth the velocity field while instead the physical artificial viscosity gives sharper profiles. Furthermore, higher values of vorticity have been computed using the physical approach in agreement with previous tests results, indicating a different influence on vortical modes. More interesting, is the peculiar loss of symmetry in the shocked gas: in the very first instants after the impact the boundary layer near the wall gets unstable and a strong burst of vorticity is injected in the far-wall region (Fig. 7.24). This phenomenon propagates in time affecting larger and larger regions of the domain. Both numerical and laboratory experiments of this particular test case are very rare so the detailed physics is still not completely known. In this sense, it is still premature to say if this phenomenon is just a numerical artefact or rather a physically realistic hydrodynamic instability of the flow. On the other hand, results exposed in this paper suggest a certain level of physical reliability regarding the proposed artificial viscosity procedure.

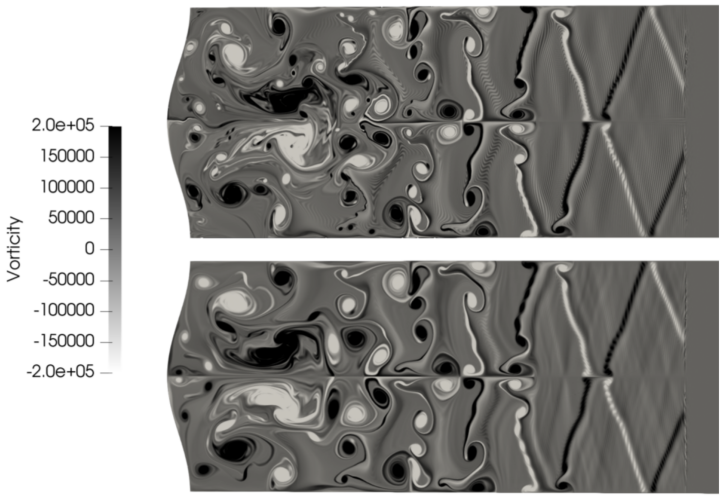

Figure 7.23: Wavy Wall (M=5.0): vorticity field at $t = 160\mu s$. Up, physical approach, bottom Laplacian approach.

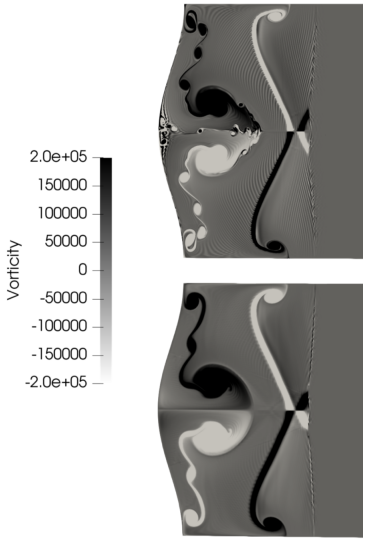

Figure 7.24: Wavy Wall (M=5.0): vorticity field at $t = 40\mu s$. Up, physical approach, bottom Laplacian approach.

Chapter 8

Compressible turbulent flows

Contents

8.1 Introduction

In the first chapter of the present work the problem of turbulence was introduced and the main techniques to tackle it were presented, with particular

attention to Large Eddy Simulations. Subsequently, the role played by the numerical scheme was taken into account, highlighting the important link between physics and numerics in SGS modelling. The interaction between the numerical scheme and sub-grid modelling lead to the presentation of the SEDM, which has been used in this work. Finally, a chapter has been dedicated to a characteristic-based low dissipative bulk artificial viscosity as shock-capturing technique.

Considering compressible turbulent flows, each of these three aspects are of major importance for the reliability of numerical simulations. In this chapter, then, attention will be particularly focused on the interaction between SGS modelling and AV techniques. The combined presence of both models will be not only analysed in terms of dissipative contributions to resolved quantities such as kinetic or internal energy, but also in terms of their interpretation as under-resolved quantities in a filtered LES formalism. In this sense, similarities between these two aspects will be presented and discussed thoroughly.

Following the same concept, the interaction between turbulence and shock-waves will be analysed in terms of coexistence of SGS and AV modelling. A series of increasingly complex numerical simulations have been considered. In particular, as representative example of shock-induced boundary layer separation, the transonic flow over a RAE2822 airfoil has been simulated using both SEDM and AV models active. Secondly, the interaction between a fully-developed turbulent boundary layer and a shock-wave has been simulated considering a classic compression ramp configuration. The former case is characterised by a less complex physics since turbulence is essentially generated downstream the shock-wave and no real superposition of turbulent and shocked regions is present. In the latter case, instead, the interaction is stronger as it triggers a richer range of physical phenomena characterising shock wave-turbulence interaction. Considering the compression ramp geometry, both *a-posteriori* LES and *a-priori* analyses on DNS data have been performed.

8.2 RAE2822 airfoil

8.2.1 Ducros modification

With the increasing popularity of high-order methods in CFD, the development of efficient, low-dissipative shock-capturing techniques gained a lot of interest in recent years. As a matter of fact, the influence of shock-capturing algorithms on the overall accuracy of compressible flow simulations has shown to be far from negligible. For example, WENO schemes, if not carefully designed, can seriously damage the quality of the solution due to excessive numerical dissipation [184]. In a similar way, Laplacian artificial viscosity has shown to be extremely dissipative if applied to under-

resolved turbulent flows [18, 170]. Therefore, the methodical design of shock-capturing techniques, specifically tailored for spectral element methods, represents a key feature in the development of reliable and robust numerical solvers for compressible turbulent flows. Artificial viscosity approaches are more common in spectral element methods, as, in a similar way, WENO techniques are more suited for compact finite differences schemes. Even if spectral element methods and compact finite differences have a comparable computational cost [196], the geometrical flexibility of the former can be particularly attractive for the simulation of complex geometries such as external flows around airfoils. The shock-capturing procedure herein considered is based on the concept of modal decay by Persson and Peraire [7, 8] for Discontinuous Galerkin schemes, combined with the recently proposed characteristic-based sensor by Lodato [159]. The specifics on the artificial viscosity technique have been presented in chapter 7.

A further improvement of the present AV model in the case of wall bounded flows is employed. While eddy viscosity needs to be set to zero at the wall, as dictated by turbulent boundary layer theory, artificial viscosity has no constraint from this point of view. Nevertheless, it is common practise turning off the AV model at wall boundaries [172]. There are two main reasons to do so. First of all, high values of the artificial viscosity in the inner layer (where grid spacing is necessarily small) would impose extremely small time-steps due to viscous Courant-Friedrichs-Lewy conditions. This problem is even more accentuated by bulk artificial viscosity, which usually assumes quite high values with respect to its shear counterpart. Secondly, due to the strong mesh anisotropy close to the wall, the approximation of the cell grid size, and consequently of the CFL stable time-step, can be particularly inaccurate. High values of the artificial viscosity exacerbate even more such numerical issue.

To avoid unnecessary artificial viscosity activation, it is proposed to couple a Ducros-type of sensor [158] with the standard modal shock detection. The local element shock sensor by Persson and Peraire [7] is thus modified as follows:

$$\tilde{s}_e = s_e \cdot \frac{[0.5(|\langle \nabla \cdot \mathbf{u} \rangle| - \langle \nabla \cdot \mathbf{u} \rangle)]^2}{\langle \nabla \cdot \mathbf{u} \rangle^2 + \langle ||\nabla \times \mathbf{u}|| \rangle^2 + \varepsilon}, \tag{8.1}$$

where $\langle \cdot \rangle$ denotes element averaging and ε is usually a constant of order machine epsilon squared. However, in the following simulations the correction proposed by Pirozzoli [197] has been employed, namely,

$$\varepsilon = (u_\infty / l)^2, \tag{8.2}$$

which is a global measure of a large scale velocity gradient squared. In the present work, the chord of the airfoil has been used as characteristic length scale l.

The gain in such generalisation is twofold. It provides a smooth transition to null values of AV at the wall boundaries, increasing stability and efficiency.

Furthermore, the Ducros sensor avoids the injection of unnecessary artificial dissipation in strongly vortical regions of the flow characterised by negligible compressibility effects. Finally, the numerator in Eq. (8.1) has been modified in order to be zero in expansion regions ($\nabla \cdot \mathbf{u} > 0$). The additional modifications applied to the modal sensor can surely increase the computational expense of the baseline shock-capturing scheme. Nonetheless, achieving a simple and yet efficient shock-capturing algorithm for high-order turbulent simulations has always been a very elusive goal to reach [184, 172]. Handling shock-waves, in fact, similarly to turbulence modeling, is a task intrinsically numerical and physical at the same time. Finding a reasonable equilibrium between these two aspects is a crucial challenge for shock-capturing techniques. The combined use of modal [7, 8] and physical [158] sensors is then representative of the delicate balance between numerics and physics. A physical correction have been deemed essential to differentiate between turbulence under-resolution and shock waves, which are often undistinguishable from a merely numerical point of view. In particular, a modal decay sensor would likely be active in both cases, even for different choices of target variables. The application of the Ducros sensor, instead, offers a more physical insight on the nature itself of under-resolved quantities, providing better shock detection and consequently reduced levels of artificial dissipation.

8.2.2 Simulation setup

The features of a turbulent boundary layer can be strongly affected by the interaction with shock waves. A wide range of coupled length and time scales are then involved and either sufficiently high resolution or precise modeling is necessary. For example, the interaction with a fully developed boundary layer and a compression corner presents an unsteady oscillation of the shock wave, which involves time scales much larger than the ones characterising turbulent fluctuations. RANS models have been widely tested for this particular case with evident limitations [198, 199, 200, 201], whereas LES [202, 203, 204] and of course DNS [14, 205] show a better agreement with experimental data. With respect to a compression corner, the present configuration is less challenging since the boundary layer interacting with the shock wave has been forced to be laminar. However, the inherent unsteadiness of the detached flow generated by the interaction has a non-negligible influence on the shock wave itself, which oscillates around a mean location [206, 207]. The combined action of SGS and AV model is then particularly important in terms of dissipation injected in the system: over-dissipation would damp excessively the shock motion whereas insufficient energy draining could cause spurious oscillations. Like in the SD7003 simulation, statistics are collected between 20 and 50 convective times. Probes locations are the same as in the previous case (Table 8.1).

The response of the shear viscosity versus temperature is expressed ac-

		RAE 2822
Reynolds number	Re	6.5×10^6
Mach number	Ma	0.729
Angle of attack	AoA	2.31°
Wall BC	-	adiabatic
Number of elements	$N_t \times N_n \times N_z$	$166 \times 30 \times 2$
Polynomial degree	N	5
Degrees of freedom	DoF	2.15×10^6
Wall distance	$\langle h \rangle$	8.16×10^{-6}
Wall scaling	y^+ at $x/c = 0.7$	≈ 0.2
Probe 1 location	(x_1, y_1, z_1)	$(0.5, 0.11, 0)$
Probe 2 location	(x_2, y_2, z_2)	$(0.5, 0.05, 0)$
Probe 3 location	(x_3, y_3, z_3)	$(1.3, 0.00, 0)$

Table 8.1: Physical and computational set-up. All quantities are made dimensionless with respect to the chord length and free-stream values. A nominal value $c = 1$ has been assigned to the airfoil length. Reference frame is centred on the leading edge. In y^+ calculations the closest solution point to the wall has been considered. In particular, the notation $\langle h \rangle$ denotes the averaged value of wall-distance along the whole profile.

cording to Sutherland's law:

$$\mu(T) = \mu_0 \left(\frac{T}{T_0} \right)^{3/2} \frac{T_0 + T_S}{T + T_S}, \tag{8.3}$$

where $\mu_0 = 1.827 \times 10^{-5}\,\mathrm{kg\,m^{-1}s^{-1}}$, $T_S = 120\,\mathrm{K}$ and $T_0 = 291.15\,\mathrm{K}$. Finally, a specific heat ratio $\gamma = 1.4$ and a $\mathrm{Pr} = \mu_0 c_P / \kappa = 0.71$ are assumed. The flow is initialised homogeneously in the whole domain according to the far-field conditions.

8.2.3 Pressure coefficient

For this particular case, an extensive set of experimental measurements are present in the literature [208]. The pressure coefficient is known to be a good indicator of the reliability of the simulation. From its behaviour, it is possible to evaluate the accuracy of both shock-capturing and turbulence modeling, depending on the flow regions that they affect. A clearly desirable feature of the shock capturing technique is to produce pressure profiles as steep as the numerical scheme can possibly achieve. The width of the shock wave, which is inherently affected by both the AV model and the accuracy of the numerical scheme, can strongly impact on the shock oscillation due to the interaction with the subsequent turbulent region. A very small region of break down turbulence, in fact, is present right after the shock wave. The location of the

shock is then another relevant measure of how well transition to turbulence is captured. In the present simulation the shock location is in good agreement with experiments, implying a good description of transition and a low level of dissipation injected by the artificial viscosity model (*cf.* Eq. 7.2). Fig. 8.1 displays a snapshot of the simulation results. In proximity of the shock wave roll-ups structures start to develop, and finally, downstream of the shock wave, they break up in fully turbulent vortices. Fig. 8.2 shows the

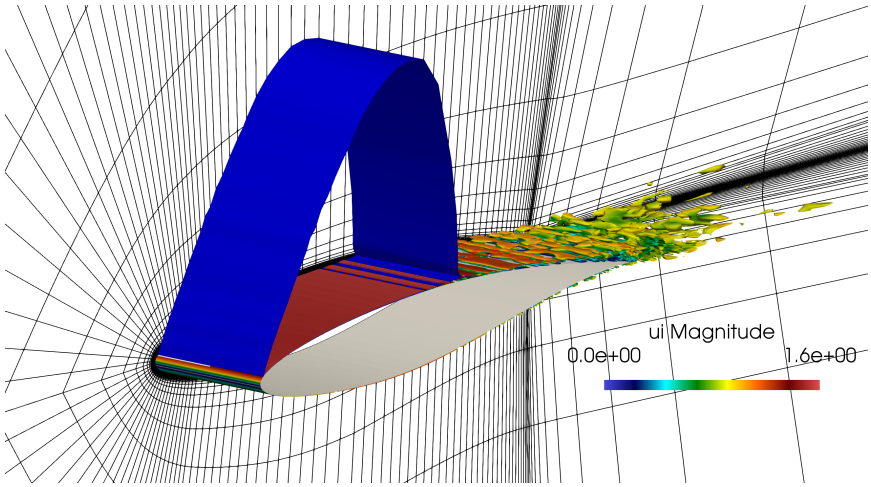

Figure 8.1: Isosurface of the Q-criterion ($Q = 20$) colored with instantaneous velocity field magnitude. The Ma = 1 isosurface has been used to visualise the shock wave on the upper side.

pressure coefficient with a good agreement against experiments along the whole airfoil length. The upstream region and the location of the shock itself are fairly well predicted, despite the absence of a geometrical trip. In the proximity of the leading edge, the small pressure peak on the upper side is not perfectly captured due to lack of transition mechanism. The turbulence generated by this test case is visibly different with respect to the SD7003 simulation (see Fig. 8.1). The thickness of the boundary layer is much smaller due to the higher Reynolds number and the smaller angle of attack. The shock-induced boundary layer separation point near the mid-chord region on the upper surface can be clearly noticed in Fig. 8.3. In fact, as a result of the adverse pressure gradient across the shock, the thickness of the boundary layer increases in the second part of the suction side. Wall-normal slices of the streamwise velocity highlight such behaviour (Fig. 8.4). The boundary layer is very steep in the first, laminar region of the flow, whereas it thickens considerably after the interaction with the shock wave where detachment occurs. Finally, mean aerodynamic loads are listed in Table 8.2 and are in good agreement with the reference data by Cook and Mcdonald [208]. Averaged eddy-viscosity and artificial bulk viscosity are

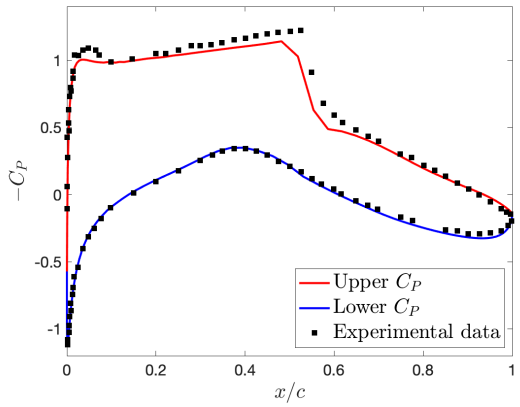

Figure 8.2: Pressure Coefficient.

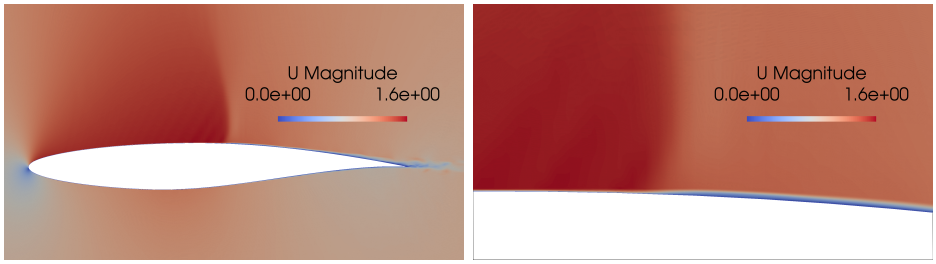

(a) (b)

Figure 8.3: Instantaneous velocity magnitude. On the right, a closer look of the shock wave region (averaged velocity).

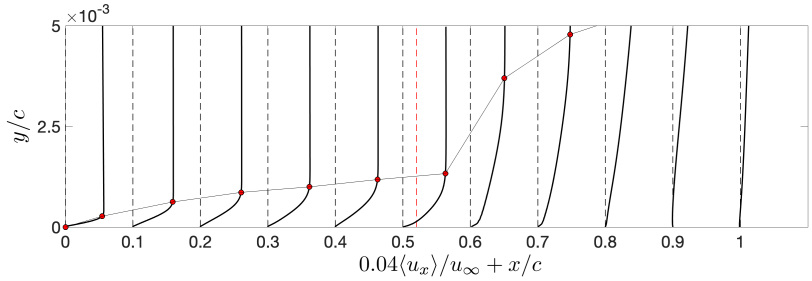

Figure 8.4: Averaged streamwise velocity along normal direction. Red-dashed line denotes the approximate mean location of the shock wave. The 99% boundary layer thickness is shown using red dots to highlight detachment.

shown in Figs. 8.5 and 8.40, respectively, where the different zones in which they are activated can be clearly noticed. As expected, the SGS model is

Author	C_L	C_D
Cook and Mcdonald [208]	0.743	0.0127
Current	0.704	0.0110

Table 8.2: Mean Aerodynamic loads.

mainly active close to the airfoil tail, in the turbulent boundary layer and wake, while the AV assumes nonzero values mostly in proximity of the shock. The eddy viscosity assumes small values in a very narrow region close to the trailing edge, coinciding with an highly refined zone. The SGS model is, in fact, weakly active in this area for multiple reasons related to the local level of resolution. Firstly, the eddy-viscosity is proportional to the grid size (see Eq. 6.1). Secondly, the estimate of turbulent kinetic energy given by Eq. (6.2), for sufficiently small cells, is very close to zero. Finally, in the case of highly refined grids, the decay exponent used in the turbulence sensor's definition is particularly high, indicating well resolved velocity fields. As already discussed by Tonicello et al. [18], the present artificial bulk viscosity without Ducros sensor has a quite high activation. Due to its functional form, nevertheless, the influence is limited to dilatational modes only, whereas vorticity is well preserved. The present modification using the Ducros sensor (Eq. 8.1) improves the AV model providing a much better activation. In fact, in the RAE2822 simulation, excessive levels of AV had been observed inside the boundary layer in absence of the Ducros correction (cf. Fig. 8.12).

It is finally worthwhile mentioning that in multiple works (mainly RANS simulations), a similar behaviour of the eddy-viscosity activation has been observed [209, 210, 211, 212, 213, 214] (see Fig. 8.5). Finally, in Figs. 8.7

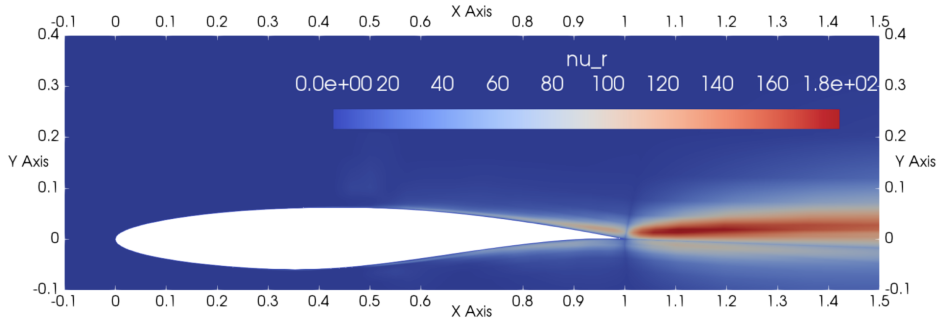

Figure 8.5: Average eddy-viscosity ratio. Notice that, due to the high Reynolds number, the eddy-viscosity ratio is considerably larger than in the previous test case.

and 8.44, Reynolds shear stresses and turbulent kinetic energy are shown. As expected, the turbulence is restricted to a very narrow region close the airfoil tail. The rapid transition to turbulence appears right after the shock

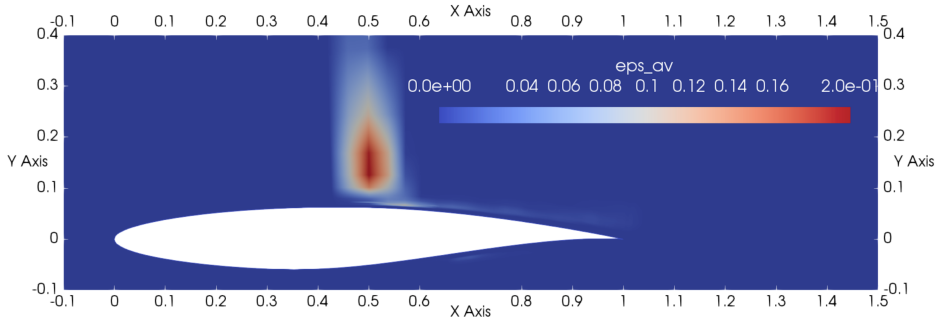

Figure 8.6: Average artificial bulk viscosity.

wave, causing an increase of both turbulent kinetic energy and Reynolds stresses (a detailed look is shown in Fig. 8.9). Supercritical transonic air-

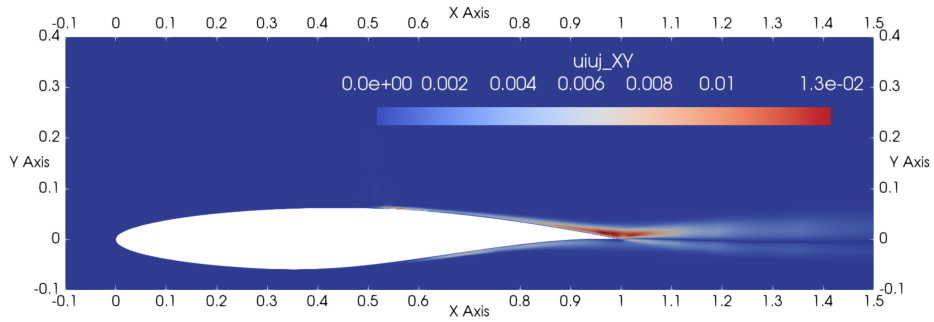

Figure 8.7: Reynolds shear stresses ($|\langle u'v' \rangle|/u_\infty^2$).

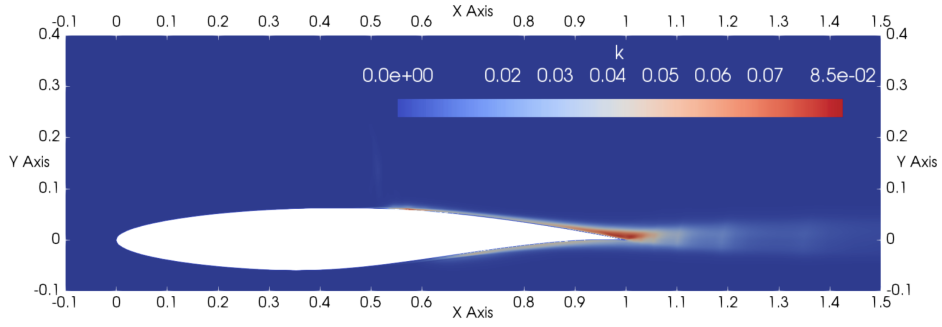

Figure 8.8: Turbulent kinetic energy $(\frac{1}{2}\rho(\langle u'_x u'_x + u'_y u'_y + u'_z u'_z \rangle))/(\frac{1}{2}\rho_\infty u_\infty^2))$.

foils are usually characterised by streamwise shock oscillations (or buffeting) on the upper side of the wing. In the present configuration, however, the flow experiences only a mild buffeting phenomenon, which is expected for very low angles of attack [215] as the one herein considered. The oscillation of the shock wave is then highlighted in Fig. 8.10 through a turbulent kinetic

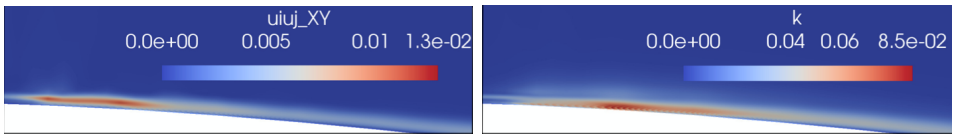

(a) Reynolds stress anisotropic part (b) Turbulent kinetic energy

Figure 8.9: Closeup of Reynolds shear stresses (left) and turbulent kinetic energy (right) in the neighborhood of the shock wave location.

energy closeup in proximity of the shock wave. Outside of the separated boundary layer, the turbulent kinetic energy assumes non-zero values only in a very narrow region around the mean shock location, indicating only mild oscillations of the shock front. The same analysis used for Fig. 6.19

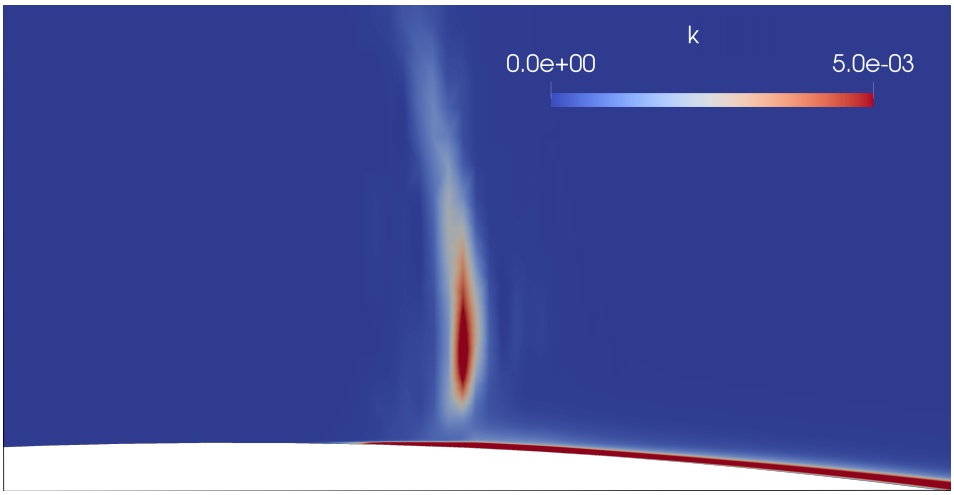

Figure 8.10: Closeup of turbulent kinetic energy in proximity of the shock-wave.

has been applied to the RAE2822 airfoil in Fig. 8.11. Namely, the turbulence sensor has been used as a post-processing tool and computed on a given instantaneous flow field. Similarly to the previous SD7003 case, the turbulence sensor is mostly active in the detached region of the flow, where the velocity field is expected to be under-resolved. It is interesting to notice that the turbulence sensor never reaches a unitary value, indicating that the algorithm recognises the separated flow as only partially under-resolved. A possible explanation of such behaviour could be partially linked to the presence of an additional smoothing mechanism, represented by the artificial viscosity model. In a similar way, in fact, the turbulence sensor is essentially inactive in proximity of the shock wave since the bulk artificial viscosity is sufficiently large not to necessitate any additional shear viscosity. In order to

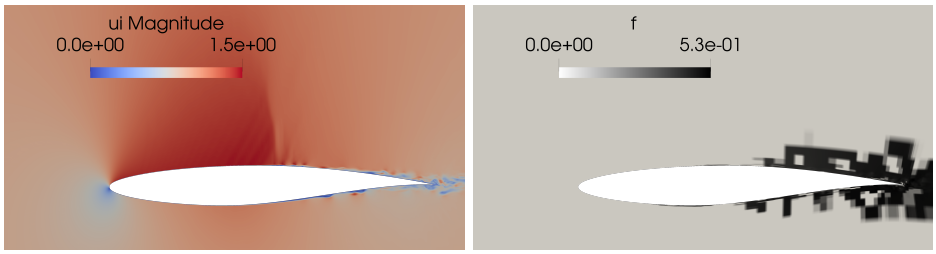

(a) Instantaneous flow field. (b) Turbulence sensor f.

Figure 8.11: Instantaneous flow field (left) and spectral turbulence sensor applied to the velocity field (right).

assess the major impact of the Ducros modification on the shock-capturing technique, a comparison between the baseline modal sensor and its modified version applied to an instantaneous flow field is shown in Fig. 8.12. It can be clearly noticed that the modal sensor is extremely active in the separated region of the flow field. Turbulence under-resolution is in fact erroneously detected as a shock wave discontinuity. The physical information provided by the Ducros sensor represent the key ingredient to distinguish between shock waves and turbulence under-resolution (which can be numerically similar). The modified artificial viscosity model, in fact, as observed also in Fig. 8.40, is active only in proximity of the shock wave. In other words, the Ducros modification is able to remove all the unnecessary artificial viscosity in the detached region preserving, at the same time, the correct detection of the main shock wave. Due to the high complexity of the present transonic sim-

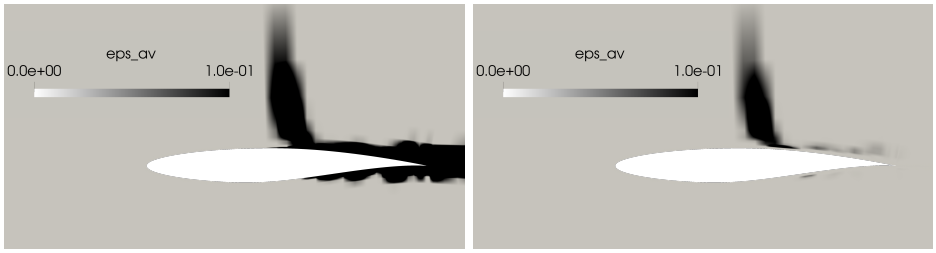

(a) Baseline modal sensor. (b) Ducros-modified sensor.

Figure 8.12: Comparison between the baseline modal sensor [7, 8] (left) and its modified version (Eq. 8.1) using the Ducros correction (right).

ulation, some further discussions are necessary. In particular, the nature of the boundary layer interacting with the shock wave needs to be specified. In the experimental setup, the flow was geometrically tripped at $x/c = 0.03$. However, it is relevant to observe that sufficiently satisfying results have been reported also without an explicit transition mechanism. The ultimate goal

of the present work was in fact to analyse the interaction between a turbulent boundary layer and a large scale shock wave. For such purpose, the accurate prediction of separation-induced transition has been considered adequate to evaluate the combined effects of the two models herein employed. The present setup is meant to highlight the capability of the two models to coexist and influence different regions of the flow field. A more refined simulation, with a more accurate description of transition, would give similar results and conclusions on the interaction between AV and SGS modeling. On the upper side of the airfoil a very narrow region of non-zero values of eddy-viscosity would likely appear, region in which AV would be essentially zero due to the proximity to the wall. In the authors' experience, a coarse mesh as the one herein considered is adequately capable of providing useful insights on the mutual interaction between the two models. Furthermore, such a coarse resolution highlights even more the delicate stability of the numerical computation. In particular, both the Ducros correction on the AV and the explicit SGS modeling have shown to be necessary to keep the computation stable.

8.2.4 Kinetic energy spectra

Using the same technique previously introduced, kinetic energy spectra have been computed for the RAE2822 profile as well. The location of the virtual probes is the same as before. In Fig. 8.13 they are shown in superposition with the instantaneous flow in the fully turbulent regime. There is no real interest in the study of turbulence in probes 1 and 2, where the flow is either laminar (probe 1) or not suitable to Taylor's hypothesis (probe 2). On the other hand, probe 3 gives some insights on compressible turbulence. The

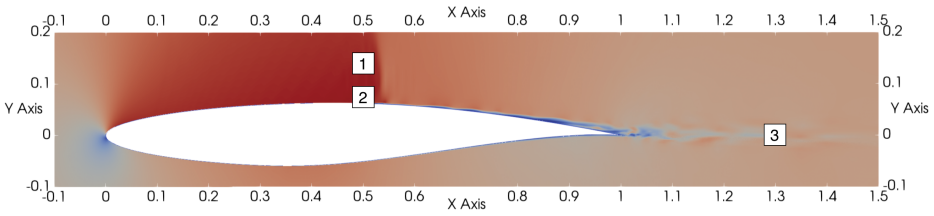

Figure 8.13: Instantaneous velocity magnitude. Numbers mark probes locations.

difference between these flow regimes can be seen in Fig. 8.36(b), where the kinetic energy spectra of probes 1 and 3 are plotted. The difference is clearly evident: the flow field at location 1 is laminar and even if a small transition is seen close to the estimated dissipative region, the whole spectrum undergoes an almost perfect spectral convergence for all wavenumbers. Differently, observing the kinetic energy spectrum of probe 3, the expected turbulent be-

haviour is present. It is interesting to point out that no particular difference can be reported in the spectrum between the SD7003 case and the present one. Both show an inertial range, followed by a spectral convergence region close to the range $\pi/2 < \kappa^* < \pi$. The different levels of smoothness mainly depends on the sampling rate and on the characteristic time scales, which are different in the two airfoil simulations.

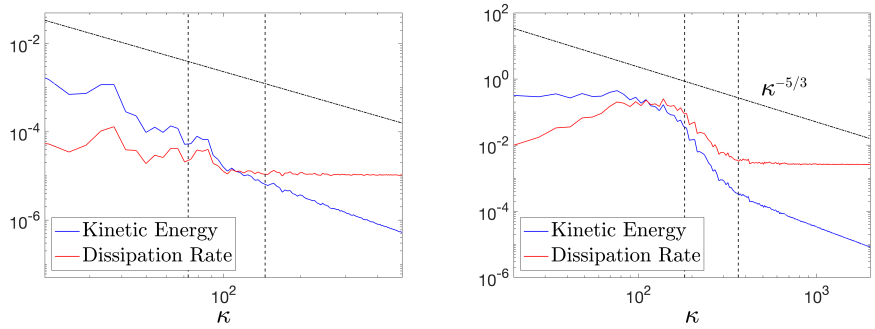

(a) Probe 1 (b) Probe 3

Figure 8.14: Kinetic energy spectra in probe 1 and 3. Vertical lines denotes an estimate of the dissipation region: $\pi/2 < \kappa^* < \pi$.

8.3 Compression ramp: Large-Eddy Simulation

Shock-wave turbulence interaction is of fundamental importance in many different applications of aerospace engineering, such as propulsion and aerodynamic systems. These highly compressible flows are characterised by multi-scale phenomena, which are still highly challenging for numerical simulation. Despite a rapidly increasing interest in the simulation of such complex configurations, fundamental questions on the underlying flow physics, the corresponding modeling and the most appropriate numerical discretisation are still open.

Along these lines, innovative numerical high-order schemes such as the Discontinuous Galerkin [52, 51], the Flux Reconstruction [77, 89], and the Spectral Difference [44, 117], gained a lot of interest in the last few decades. High-order discretisation of convective dominated flows are indeed characterised by many useful features in terms of numerical dissipation and are widely used to simulate turbulent flows [62, 137].

In particular, much interest has been focused on the numerical dissipation and multiple studies tried to use it as a built-in turbulence model for specific choices of numerical fluxes [62, 63, 64, 65, 66] . This approach is commonly known as Implicit Large Eddy Simulation. Despite the advantages in terms of computational efficiency and simplicity of implementation, the choice of

order, grid size, and numerical flux strongly influences the success or failure of such procedures. This is particularly true for certain classes of high-order methods, such as the spectral element methods [67], for which the order of accuracy is a user-selectable parameter of the computation.

Explicit large-eddy simulations using standard SGS models, on the other hand, may inject too high levels of dissipation, ignoring the informations coming from the numerical discretisation. It is then crucial to design explicit turbulence models that take into account not only the flow physics, but also the intrinsic characteristics of the numerical scheme used to solve the equations.

Furthermore, considering high speed flows, performing reliable numerical simulations becomes even more challenging due to the presence of non-negligible compressibility effects, which can eventually lead to the formation of shock waves. Under these conditions, the SGS model needs not only to distinguish between laminar and fully turbulent regions, tuning accurately the level of dissipation, but it also interacts with shock capturing techniques, which can strongly affect in return the turbulence properties.

All these flow modeling features are involved in the simulation of a compression ramp, which is thus a perfect test case to evaluate the capability of the recently developed SEDM [1] to accurately predict the rapid variations of turbulence, typical of the problem, and to study its interaction with the shock capturing technique herein employed.

The following results will be shown in comparison with a DNS by Priebe et al. [12] and a LES at similar conditions by Dawson et al. [216].

8.3.1 Simulation setup

The test case considered has been deeply analysed in many different works, both numerical [202, 203, 217, 205, 204, 14] and experimental [218, 13], with a particular attention to the unsteadiness of the shock-wave front. Most of the numerical simulations rely on WENO-type schemes [219] to handle shock waves, with recycling/rescaling techniques [220, 221] for the incoming turbulent boundary layer. In all the previously cited works, different resolution levels and a large variety of analyses has been performed on the same configuration.

The problem consists in a supersonic, fully-turbulent boundary layer interacting with a 24° degrees compression ramp. The unsteady nature of the boundary layer causes the shock to wrinkle and oscillate near the corner. The adverse pressure gradient, caused by the main shock, creates a separation bubble in proximity of the corner. Such bubble, due to the motion of the shock front, tends to increase and decrease in dimensions with low frequency oscillations. Downstream of the corner, the boundary layer is superiorly bounded by the main shock, while additional shocks arise from the large structures in the wake of the boundary layer, to finally merge with the

Ma	Re_θ	δ^+	U_∞	δ	δ^*	θ	H
2.91	2900	340	610 m/s	7.1 mm	2.58 mm	0.47 mm	5.49

Table 8.3: Characteristic of the incoming boundary layer.

main shock downstream.

The computational domain is parametrised using the 99% thickness of the incoming boundary layer δ, as shown in Fig. 8.30; the main flow properties of the boundary layer are listed in Table 8.5.

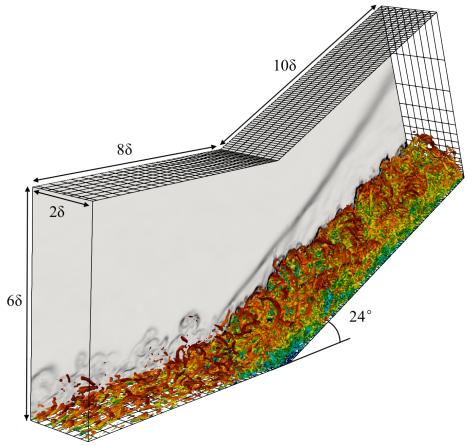

[t]

Figure 8.15: Computational domain. In the background, Q-criterion coloured by velocity magnitude ($Q = 1.0U_\infty^2/\delta^2$).

The Reynolds number is defined as $\mathrm{Re}_\theta = U_\infty\theta/\nu_\infty$, where θ is the momentum thickness, U_∞ the free-stream velocity and ν_∞ is the kinematic viscosity in the free-stream. The Karman number is defined as $\delta^+ = \delta u_\tau/\nu_w$ where u_τ is the friction velocity and ν_w is the kinematic viscosity at the wall. Finally, δ^* is the displacement thickness and $H = \delta^*/\theta$ is the shape factor. Dynamic viscosity has been modelled using the Sutherland's law:

$$\mu = \mu_{ref}\left(\frac{T}{T_{ref}}\right)^{3/2}\frac{(T_{ref}+S)}{(T+S)}, \tag{8.4}$$

where $\mu_{ref} = 1.834\cdot 10^{-5}$ kg m/s, $T_{ref} = 291.15$ K and $S = 120$ K.

No slip, isothermal boundary conditions have been applied to the wall, with a temperature at the wall fixed at $T_w = 307$ K. The free-stream density has been set to the nominal value $\rho_\infty = 7.7\cdot 10^{-2}$ kg /m^3. Consequently, pressure can be evaluated through the mach number, $p_\infty = 2.41678\cdot 10^3$ Pa. The temperature of the free-stream flow is equal to $T_\infty = 109.1$ K. Finally, the reference dynamic viscosity has been chosen in order to provide the

N	N_x	N_y	N_z	Δx^+	Δy^+	Δz^+	DoF
6	$70 + 84$	18	8	$5.5 \sim 40$	$0.18 \sim 43$	13	5.25M

Table 8.4: Grid properties.

prescribed Reynolds number. Since pressure is assumed to be constant, the density at the wall can be evaluated as $\rho_w = 2.736 \cdot 10^{-2}\,\mathrm{kg}/\mathrm{m}^3$, then all the remaining variables can be evaluated:

$$\nu_w = \mu_w/\rho_w = 7.0460 \cdot 10^{-4}\,\mathrm{m}^2/\mathrm{s}, \quad \text{and} \quad u_\tau = \delta^+/\delta\nu_w = 33.741\,\mathrm{m/s}.$$

Many different approaches are present in the literature to prescribe turbulent inflow generation (see Wu [222] for an extensive summary). In the present study, the Klein's digital filter technique [119]—which has been recently generalised and validated to the present numerical setup [223, 16]—has been employed for the turbulent inflow condition. The mean profiles, to which perturbations are superimposed, have been evaluated using closed form relations involving Van Driest transformed velocity profiles as described by Touber [224].

The correlation tensor of the fluid velocity and the characteristic turbulence length scales are the control parameters used to generate the synthetic turbulent boundary layer at the inlet. The technique herein applied is the one proposed by Klein [119], which has been recently generalised and validated to the present numerical setup [223, 16]. A constant value has been chosen for the length scales along y and z (spanwise) equal to $l_{y,z} = 1.3\,\mathrm{mm}$ which is approximately one sixth of the inlet 99% displacement and $l_x = 2.6\,\mathrm{mm}$ (streamwise) for the length scale along x. The values of the correlation tensor have been extrapolated from the DNS by Pirozzoli and Bernardini [225] at a similar Reynolds number.

Regarding the numerical discretisation, grid properties are listed in Table 8.4. The number of total degrees of freedom suits a typical LES resolution for such configurations [202, 204, 216, 226].

The LES solves the Favre-filtered Navier-Stokes on a coarse grid. In particular the system (I) by Vreman [24] has been considered. The deviatoric part of the SGS tensor and the SGS heat flux have been modelled using the SEDM by Chapelier et al. [1] whereas a modification of Yoshizawa model [25] has been used for the isotropic part of the SGS tensor.

The shock capturing technique is based on the modal sensor by Persson and Peraire [7], combined with the physical, bulk-based, artificial viscosity by Fernandez et al. [169], recently generalised to the SD method using characteristic based sensors [159, 18]. Furthermore, to avoid unnecessary artificial viscosity activation in strongly vortical regions, a Ducros-type sensor [158] has been coupled with the standard modal shock detection.

Finally, due to the very high complexity of such test case, a positivity-

preserving scheme [227] has been employed to maintain stability of the simulation.

8.3.2 Validation of turbulent boundary layer injection

The very first step in results analysis consists in a proper validation of the incoming turbulent boundary layer which needs to satisfy the imposed properties at the inlet. In order to evaluate quantities along the wall-normal direction, the plane $x = x_0 - 7\delta$ has been considered. In Fig. 8.34 are shown the Van-Driest transformed streamwise velocity (left) and Reynolds stresses (right). Secondly, in Fig. 8.33 the velocity profiles along wall-normal direction and Reynolds stresses have been evaluated after the interaction with the shock wave ($x = x_0 + 4\delta$).

Incoming velocity profiles are in very good agreement with previous simulations and experiments in this configuration. Velocity fluctuations are reasonably similar to the ones imposed at the inlet. On this particular point, it is important to highlight that Reynolds stresses have been extrapolated by Pirozzoli [225] where different flow parameters have been used. A perfect convergence of Fig. 8.34 is then not expected.

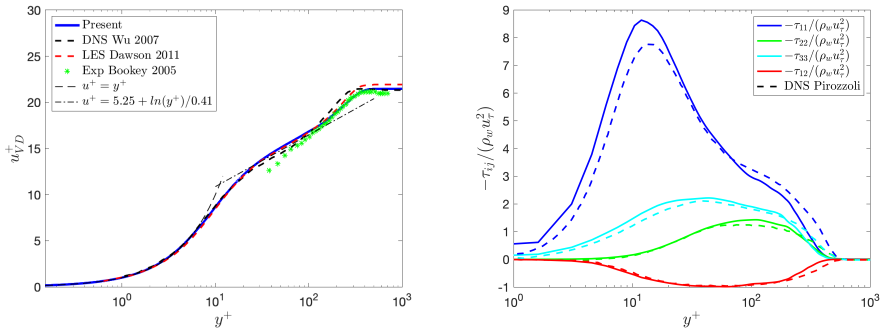

(a) Streamwise velocity.

(b) Reynolds stresses.

Figure 8.16: streamwise velocity and Reynolds stresses at $x = x_0 - 7\delta$.

In Fig. 8.33 the streamwise velocity component and Reynolds stresses have been plotted along the wall-normal direction in the outer region. Both profiles are in good agreement with the reference data. Accurate predictions downstream the interaction with the shock-wave are particularly meaningful, since the turbulent flow, in this particular region, is characterised by even smaller length scales.

As downstream Reynolds stresses reference data, the DNS data by Chen [228] have been used.

Finally, the main properties of the incoming boundary layer are summarised in Table 8.5. Most of them are in fairly good agreement with the

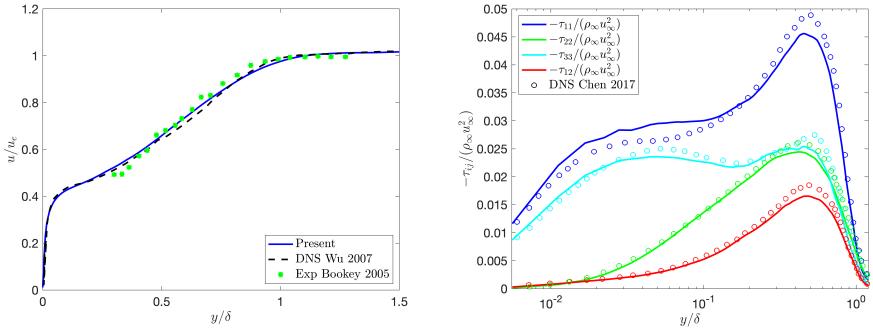

(a) Streamwise velocity. (b) Reynolds stresses..

Figure 8.17: streamwise velocity and Reynolds stresses at $x = x_0 + 4\delta$.

-	Re_θ	δ	δ^+	δ^*	θ	H	$C_f \times 10^3$
ref	2900	7.10 mm	340	2.58 mm	0.47 mm	5.49	2.16
$x_0 - 7\delta$	2907	7.71 mm	362	3.02 mm	0.47 mm	6.42	2.22

Table 8.5: Characteristic of the incoming boundary layer: reference vs computed.

reference values of Priebe's simulation.

The differences observed in Fig. 8.34 affect the properties of the incoming boundary layer, leading, for example, to larger 99% displacement. The momentum thickness θ and consequently the Reynolds number are accurately reproduced.

8.3.3 Friction coefficient & wall pressure

In order to validate the test case here presented, friction coefficient and wall pressure have been compared with previous simulations and experimental data respectively in Figs. 8.18(a) and 8.18(b). Simulations results are in good agreement with the DNS by Priebe et al. [217, 12] and a comparable LES by Dawson et al. [226].

In particular, considering the friction coefficient, the present simulation seems to be located more or less halfway, in terms of accuracy, in between the LES by Dawson and the DNS by Priebe. Analysing the wall pressure, instead, an almost perfect agreement between the DNS reference data and the present LES has been obtained.

The friction coefficient, in agreement with all the reference data, is characterised by 5 local extrema: a minimum right after the separation point, a local maximum at approximately $(x - x_0) = -\delta$, and a rapid sequence of two minimum separated by at maximum located exactly at the corner. Such peak can be explained by the sudden variation of the normal direc-

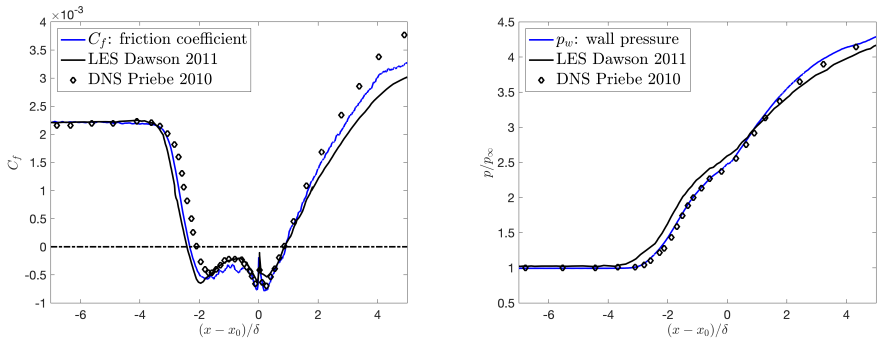

(a) Friction coefficient

(b) Wall pressure

tion, whereas the flow varies smoothly at this location. It is then commonly considered a mere consequence of the inexact geometry description of the problem and it has no relevant physical meaning. Instead, the central increase of friction coefficient can be related to the low-frequency unsteadiness of the shock front [12].

Before proceeding to more complex analysis, it is worthwhile mentioning some relevant results regarding the coexistence of shock-capturing and SGS model. It is reasonable to think that a shock-capturing technique should be as local as possible and inject the exact right amount of dissipation necessary to stabilise numerical description of shock waves. Considering shock-wave/turbulence interaction problems, different type of *under-resolution* can be present: one related to the inability of the numerical scheme to accurately resolve shock waves and another related to turbulence under-resolution. These two aspects should be treated and, more importantly, detected separately. It is, in fact, advisable to have a clear distinction, if the problem allows it, between the two. As already mentioned in previous sections, in order to decrease the activation of the modal AV sensor in turbulent regions, a Ducros type correction has been applied. Hence, for this particular test case, the shock wave is situated mainly far from the wall except for a very narrow region located right before the separation bubble. On the other hand, turbulence is mainly located close to the wall, in the boundary layer. The ratio between eddy and physical viscosity is shown in Fig. 8.18(c) while artificial bulk viscosity is shown in Fig. 8.18(d). The activation regions are almost perfectly complementary one another: AV is active mainly at the shock location, far from the wall, whereas eddy-viscosity assumes non zero values only in the turbulent boundary layer. A small overlapping zone is still present where the interaction occurs, nevertheless, the shock gets weaker and weaker approaching the wall and AV is sensibly smaller in this region. Furthermore, notice that neither AV or SGS model is active in the separation bubble: in this zone, in fact, no shock wave is present and the flow is sufficiently well-resolved to not necessitate the activation of an SGS

model. Finally, the eddy-viscosity is also active in some elements containing the shock wave: the addition of the Ducros sensor is extremely relevant in the present AV since it has been already shown in previous works how considerably deteriorating can be the influence of a bulk viscosity on the levels of compressibility of turbulent flows [18, 184, 229]. On the other hand, the presence of additional shear-viscosity in proximity of a shock-wave, if not extremely high, will only implicate another secondary dissipative mechanism in the smoothing operation of the discontinuity. It is in fact, important to remind that a bulk-viscosity is much more influent in proximity of a shock wave since it acts on the most relevant components of the velocity gradient, *i.e.*, the dilatation.

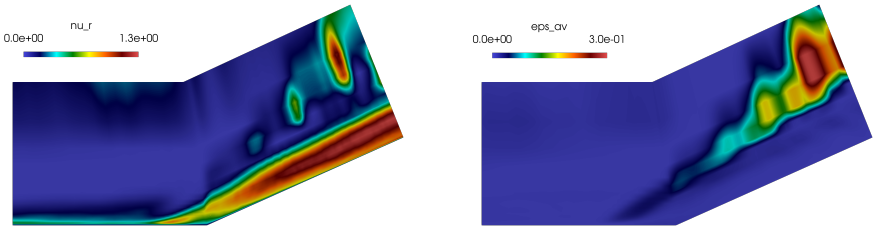

(c) Eddy-viscosity ratio. (d) Artificial viscosity.

It is finally worthwhile mentioning that due to the very high complexity of such test case, a positivity-preserving scheme [227] has been employed to maintain stability of the simulation. The limiter, nevertheless, has a very low and localised activation as shown in Fig. 8.18. To visualise its activation levels it has been introduced an element-wise constant flag which assumes unitary value if the limiter is active and zero if it is not. Consequently, it can be noticed that the maximum value assumed is approximately $2.9 \cdot 10^{-3}$ meaning that the limiter is not only active in a very small region of the flow but it is mostly temporally inactive too. As it is reasonable to expect, the region where the limiter is mostly active is nearby the interaction between the boundary layer and the shock wave.

Finally it is interesting to study the behaviour of the SGS tensor component along the streamwise direction (Fig. 8.19). As predicted from classical Shock Wave-Turbulence Interaction (SWTI) problems, the magnitude of each component should increase across the shock-wave, in particular the streamwise velocity fluctuations get almost 4 times larger in the middle of the interaction. It is also evident the increase of turbulent kinetic energy (which is simply the trace of the SGS tensor with a minus sign).

8.3.4 Probes

Main variables have been collected over time through virtual probes in different locations. Subsequently, temporal and spatial kinetic energy spectra can

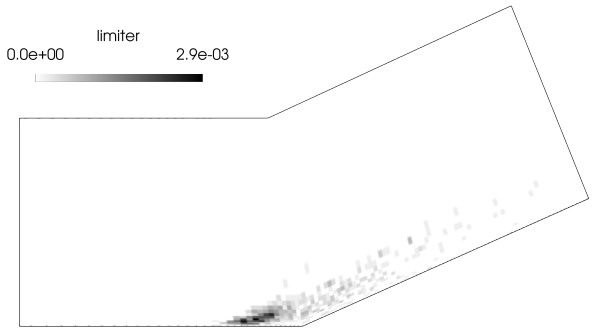

Figure 8.18: Limiter activation.

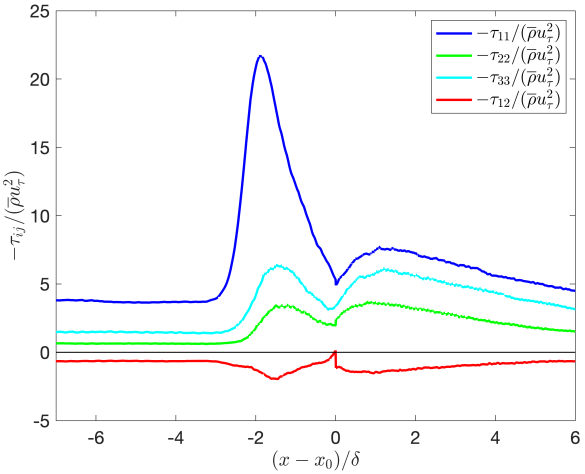

Figure 8.19: Reynolds stresses along x ($y^+ = 30$).

be related through Taylor hypothesis. All the probes have been located far enough from the wall, in order to make such hypothesis reasonably suitable. Probes location are shown in Fig. 8.20. Probes number 1 is located in the log region of the incoming boundary layer, number 2 in the separation bubble and the remaining two (number 3 and 4) in the log region of the turbulent boundary layer developed after the interaction with the shock wave.

As it can clearly understood, probe number 2 is not suitable for Taylor's hypothesis application, in fact, oscillations are comparable to the mean flow in the separation bubble region. So, in order to evaluate the resolution of the present simulation only probes 1 and 3 have been considered. Their kinetic energy spectra are respectively shown in Fig. 8.36(a). Furthermore, due to periodicity along the spanwise direction, kinetic energy spectrum along z has been evaluated too and it is shown in Fig. 8.36(b). Inertial range is clearly visible in all of the kinetic energy spectra, followed by a steeper viscous range

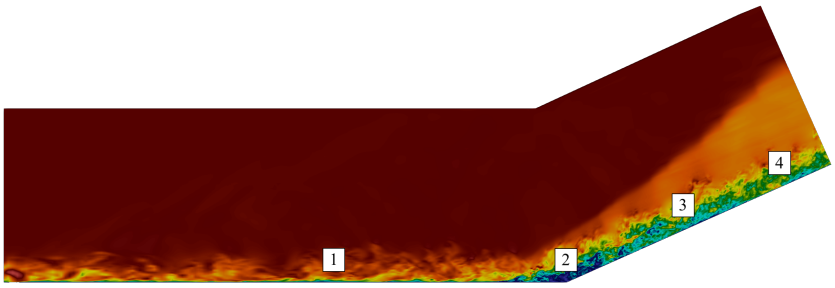

Figure 8.20: Probes location. Velocity magnitude in background.

where dissipation takes place. Notice that no accumulation of kinetic energy in proximity of the Nyquist grid wavenumber is present. The SGS model is then fully capable to dissipate the extra kinetic energy associated to the smallest scales.

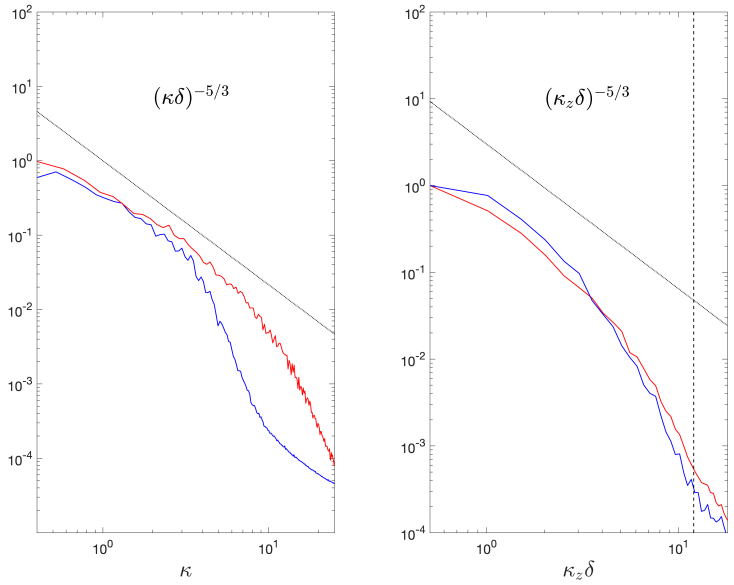

(a) Kinetic energy spectra (temporal).

(b) Kinetic energy spectra along z ($y = 0.7\delta$). Vertical dashed-line indicates the Nyquist grid wavenumber.

Figure 8.21: Kinetic energy spectra. Blue line, probe 1; red line, probe 3.

Observing the kinetic spectra evaluated using the Taylor's hypothesis

some relevant deviations can be noticed looking at the different probes. Firstly, the inertial range occupying the medium wavenumber region is more evident after the interaction with the shock (*i.e.*for probes 3 and 4). In other words, a larger part of kinetic energy is present in the higher wavenumber region, indicator of smaller length scales characterising the downstream turbulence. Moreover, longer inertial range is typically associated with higher Reynolds number flows. In agreement with such observation, in many studies of SWTI, intensity and anisotropy of the incoming turbulence strongly increase after the interaction with the shock wave.

Knowing the time history of main variables it is possible to construct discrete PDF (Probability Density Function) of the main quantities. Furthermore, it has been observed that at location 4 the flow locally passes from subsonic to supersonic frequently. The same PDFs have been consequently conditioned to the local Mach number in order to highlight features typical of such conditions. These are shown in Fig 8.22.

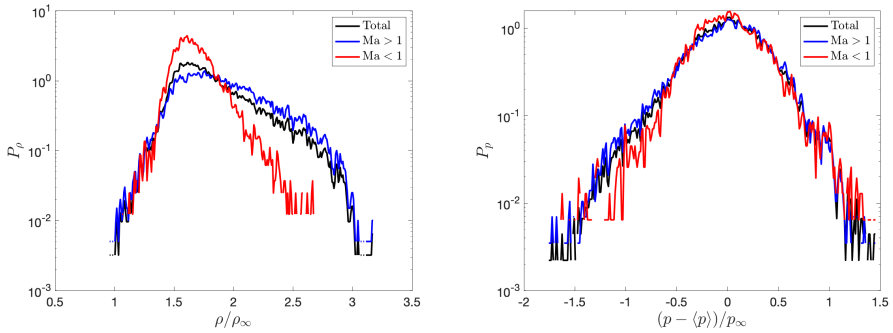

(a) Density PDF.

(b) Pressure PDF.

Figure 8.22: PDF of density and pressure. Dashed vertical lines denote the mean value in the different regimes. Pressure PDFs have been centered around zero because their mean values were practically identical.

It is interesting to notice that the probability density function of the pressure (Fig 8.39(a)) is not particularly influenced by the supersonic/subsonic regime. Its shape follows the classical behaviour of this quantity in compressible flows with a slight tendency to promote negative values. On the other hand, in Fig 8.39(a), a relevant difference is observed in subsonic and supersonic regimes: whenever the Mach number is higher than 1 density PDF tends to extend to higher values, whereas in subsonic conditions it is more symmetric with respect to the mean value. This can be related to the presence of local shocklets in the boundary layer causing local compression events, and, consequently, local increase of density.

8.3.5 Wall-normal profiles

In order to analyse in more detail the behaviour of both SGS and AV model, a series of wall-normal profiles have been evaluated in proximity of the separation point. In particular, in Fig. 8.23, the value of the eddy-viscosity ratio is shown. In agreement with previous simulations using the same turbulence model [1, 136], a local maximum is present in proximity of the wall. Such behaviour is clearly related to the definition of the model itself, where an approximation of the turbulent kinetic energy is used. Consequently, in proximity of high velocity fluctuations the SGS model is more active. It is interesting to stress that such behaviour can be particularly important in the Large Eddy Simulation of wall-bounded flows since the peak of turbulent kinetic energy is usually coinciding with the local maximum of SGS kinetic energy transfer [230, 231] at approximately $y^+ \approx 10$. This is evident

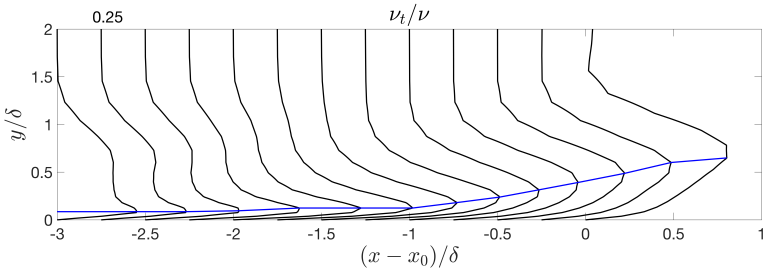

Figure 8.23: Eddy-viscosity ratio along the wall-normal direction. Blue line represents the maximum value of ν_t at each location.

in Fig. 8.24, where the streamwise component of the Reynolds stresses is shown. To facilitate the comparison the location of the maximum value of eddy-viscosity ratio and streamwise component of the Reynolds stresses are respectively represented by the blue and dotted-line.

The superposition between these two lines is visible as higher values of velocity fluctuations lead to larger values of eddy-viscosity.

Likewise, the artificial viscosity is shown in Fig. 8.25. In a similar way with respect to the previous figures, the location of the maximum value of β_{AV} is shown by the red line, whereas the blue line indicates the location of the maximum value of eddy-viscosity. Such representation is useful to highlight the separation between the two regularisation techniques. Close to the interaction the two maxima are close since both turbulence and shock-wave coexist in a very narrow region close to the wall. Moving downstream, the eddy-viscosity is mainly active in the separated flow, where vortical structures develop, whereas a clear departure toward the free-stream region can be noticed for the artificial viscosity.

Such tendency is obviously related to the Ducros correction applied to the present AV technique. In Fig. 8.26, the dilatation is shown following

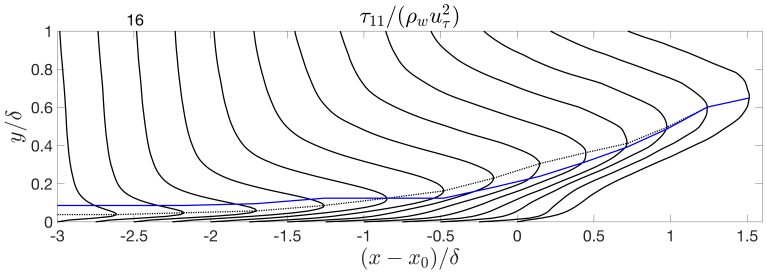

Figure 8.24: Streamwise component of the Reynolds stresses along the wall-normal direction. Dotted-line represents the maximum value of τ_{11} at each location, whereas the blue line indicates the location of maximum value of ν_t.

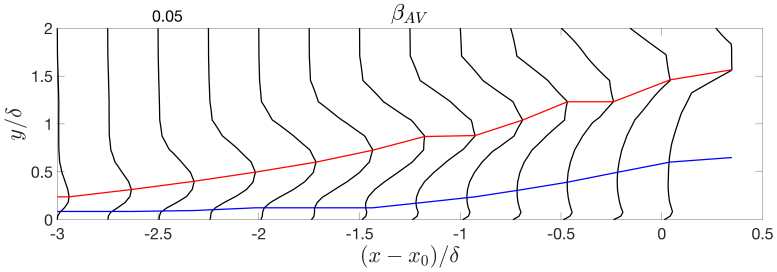

Figure 8.25: Artificial viscosity along the wall-normal direction. Red line represents the maximum value of β_{AV} at each location, whereas the blue line indicates location of the maximum value of ν_t.

the same visualisation paradigm introduced before: the dotted line represents the location of minimum dilatation, whereas the red line indicates the correspondent maximum of AV. The two lines are almost perfectly overlapping, showing that the artificial viscosity is much larger in presence of strong compressions, whereas it assumes very small values in the shear layer, where turbulence is more intense.

8.3.6 Reynolds Stress Anisotropy Invariant Map (RSAIM)

One of the most popular technique to visualise the anisotropic behaviour of Reynolds stresses is commonly known as "Lumley triangle" introduced by Lumley and Newman in 1977 [232]. In the original work and in many followings scientific paper the main objective was identified in a better understanding of isotropic turbulence recovery which is represented by the reference frame's origin of the Lumley triangle map.

The Reynolds stress anisotropy tensor, b_{ij}, is calculated as :

$$b_{ij} = \frac{\tau_{ij}}{\tau_{kk}} - \frac{\delta_{ij}}{3}. \tag{8.5}$$

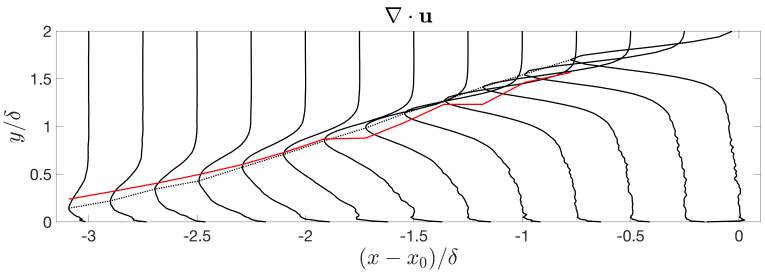

Figure 8.26: Dilatation along the wall-normal direction. Dotted-line represents the maximum value of the dilatation at each location, whereas the red line indicates the location of maximum value of β_{AV}.

Its corresponding second and third invariants can be calculated as:

$$II = b_{ij}b_{ji}/2, \tag{8.6}$$

$$III = b_{ij}b_{jn}b_{ni}/3. \tag{8.7}$$

The states highlighted here as x_1, x_2 and x_3 represent the limit values assumed by the invariants of b_{ij}. The origin, x_3, corresponds to the isotropic case, x_2 the axisymmetric two-component case and x_1 the one-component case.
An example of such representation is shown in Fig. 8.27.

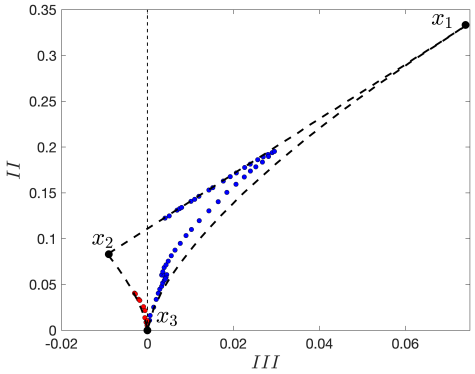

Figure 8.27: Example of Lumley triangle for a channel flow DNS [9] (blue circles) and experimental turbulent mixing layer [10] (red circles).

Due to the rich variety of turbulence topologies characterising the present configuration, RSAIM can be a very useful tool in the physical analysis of SWTI flows. It is then interesting to visualise the Reynolds Stress anisotropy map invariant for a certain set of points such as wall-normal profiles. In Figs. 8.28(a) and 8.28(b) the RSAIM is shown at $x = x_0 - 7\delta$ and $x =$

$x_0+4\delta$ for varying values of wall-normal distance. The resemblances between Fig. 8.28(a) and the classical behaviour of turbulent channel flow shown in Fig. 8.27 are evident. In proximity of the wall, turbulence lies on the two-component line connecting x_1 and x_2. Moving toward the free-stream, instead, turbulence converges toward the expected isotropic state. Considering instead Fig. 8.28(b), the behaviour is considerably different. In proximity of the wall, turbulence state lies very close to the axisymmetric contraction line, it passes through an isotropic state at $y^+ \approx 28$ and it finally moves toward the one-component state through an axisymmetric expansion. The upstream region turbulence structures resemble classical boundary layer turbulence like channel flow simulations, occupying essentially the second quadrant of the RSAIM, whereas, after the interaction negative values of III are observed as well, which are usually associated to mixing layers [233]. The similarity between mixing layers and downstream turbulence has been already reported by Priebe et al. [12]. Finally, within the SWTI framework, similar behaviours of RSAIM has been observed in other previous studies [234, 235, 236].

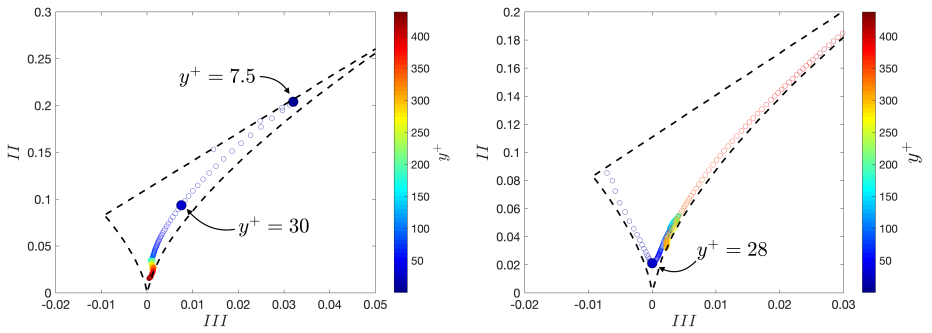

(a) $x = x_0 - 7\delta$. (b) $x = x_0 + 4\delta$.

Figure 8.28: Reynolds Stress Anisotropy Invariant Map along the wall normal direction at two different location upstream and downstream the shock-wave interaction.

In a similar way it is possible to analyse the variation of turbulence across the interaction plotting the RSAIM along x for a fixed value of $y^+ = 30$. Such visualisation is show in Fig. 8.29. As already observed in Fig. 8.19 a strong variation is expected around $x \approx x_0 - 2\delta$ where the shock-wave interacts with the incoming boundary layer. In Fig. 8.29 it can be noticed that such variation is represented as a sharp tendency toward the one-component case, meaning that streamwise fluctuations are considerably larger then the other two components. After the interaction, turbulence rapidly moves toward isotropy due to flow separation.

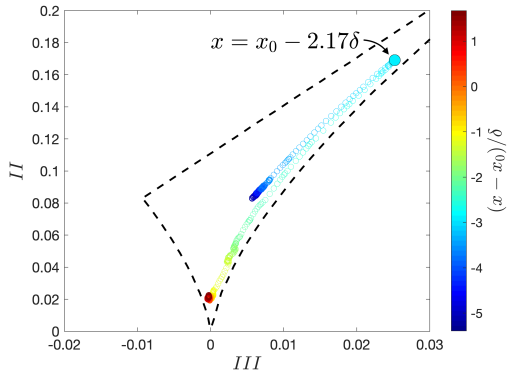

Figure 8.29: Reynolds Stress Anisotropy Invariant Map along the streamwise direction at $y^+ = 30$.

8.3.7 Conclusions

A Large Eddy Simulation of a 24° compression ramp has been performed using a high-order Spectral Difference solver. Turbulence modelling has been handled using the Spectral Element Dynamic model by Chapelier et al. [1], whereas shock capturing has been performed using a low dissipative, bulk-based, artificial viscosity technique [18]. For turbulence inflow generation, Klein's digital filter approach [119] has been used. Numerical results have been compared with both simulations and experimental data available for this particular test case. In particular, mean profiles, variances and wall coefficients have shown to be in fairly good agreement with the references.

The combination of SGS and AV is well balanced thanks to the addition of Ducros sensor [22] to the standard modal sensor by Peraire and Persson [7] within the shock-capturing procedure. The activation of the AV is mainly limited to the outer layer, where the shock is laminar and unaffected by turbulence. The SGS model, in the same way, thanks to its dynamical natural is mainly active in the turbulent boundary layer. An extensive validation of the present test case has been performed, including temporal/spatial kinetic energy spectra, wall-normal profiles and Reynolds Stress Anisotropy Invariant Maps flow representation. The next section will be focused on a series of physical and numerical analyses based on a DNS of a similar configuration.

8.4 Compression/expansion ramp: Direct Numerical Simulation

Shock wave-turbulence interaction is a major challenge in many different applications of aerospace engineering, varying from external flows around supersonic/hypersonic vehicles to rocket nozzles and scramjet engines. The

intrinsic unsteadiness of SWTI problems often imposes severe thermal and mechanical loads, which can strongly affect the structural integrity and efficiency of high-speed vehicles, thus playing a fundamental role in the aeronautical design process. The first attempts of studying the mutual interaction between shock waves and laminar or turbulent boundary layers started with the experimental works by Ackeret [237] and Liepmann [238]. In the following decades, most of the research on SWTI advanced by virtue of experimental data of both compression ramps and impinging shocks (see [239] and references therein for an extensive overview). More recently, the uprising computational power allowed to tackle the flow physics of the compression ramp via direct numerical simulation for reasonably low Reynolds numbers [14, 240, 241, 242].

The interaction between a large scale structure, such as a shock wave, and the small scale turbulence contained in an incoming boundary layer triggers a wide range of length and time scales characterising the physics of the problem. The capability of accurately representing the intricate dynamics of such scales is a fundamental step in the development of high-fidelity computational fluid dynamics simulations of turbulent flows.

The effect of compressibility alone can be particularly challenging in terms of turbulence modelling. It is commonly conjectured that, for incompressible flows, in statistical mean, the influence of the smallest scales on the large scales can be represented as a fully-dissipative process, justifying the widespread use of eddy-viscosity models. In practical applications to compressible turbulent flows, the use of fully-dissipative models can be controversial, specifically when the Reynolds-averaging operator adopted in Reynolds-averaged Navier-Stokes equations is replaced by the filtering operator of large-eddy simulation. The general assumption of similarity between incompressible and compressible turbulence has lead to a series of generalisations of popular turbulence models for the sub-grid scale tensor (in LES) and Reynolds stresses (in RANS). Nevertheless, with the Navier-Stokes equations in their compressible form, a new set of unclosed SGS terms arise from both the RANS and the LES formalisms. Some previous works addressed the importance of such terms in *a-priori* DNS analyses (see for instance [24] and reference therein), however modelling can still be considered significantly under-developed for most of those unclosed terms. Furthermore, even for incompressible contributions, such as the kinetic energy SGS dissipation term, their dependency on compressibility and thermodynamics remains, at this date, in great measure unknown.

Since the very beginning of turbulence modelling, the kinetic energy dynamics has always been identified as one of the primary driving force of turbulent flows. A comprehensive understanding of how kinetic energy is distributed along scales and how turbulent structures interact one another is of fundamental importance to understand turbulent flows physics. In the context of LES, the phenomenon known as kinetic energy backscatter (also

known as inverse energy cascade) has been extensively studied in the last decades [230, 231, 243, 244]. Based on explicitly filtered DNS data, it is in fact possible to directly evaluate the kinetic energy transfer contributions associated to the unresolved scales of the flow. The main results presented by Piomelli et al. [230] highlighted the predominance of a forward energy cascade as the one first conjectured by Richardson [27] and later formalised by Kolmogorov [20] for three-dimensional turbulence. However, a large amount of the flow field is instead characterised by backscatter events, *i.e.*, an inverse energy cascade, where small scales contribute as a source term for the large scale kinetic energy. After these first results, the presence of backscatter has been observed in many different applications [245, 246, 247, 248, 249, 250]. Both *a-posteriori* and *a-priori* analyses of turbulent flows have soon been applied to more complex conditions, such as reactive and compressible flows. In such circumstances, thermodynamics plays a much more relevant role in the total energy balance. Thus, the description of total energy transfers in turbulence soon evolved from the canonical formulation involving kinetic energy only to more generalised forms, where the influence of internal energy cannot be neglected anymore. The interconnection between kinetic and internal energy has been consequently studied in deep, analysing the role played by pressure-dilatation work as the predominant conversion mechanism between the two forms of energy [251, 252, 253, 254, 255]. Along these lines, shock waves represent a conventional process of energy redistribution in compressible flows. Shock waves have been shown to have a major impact on the turbulence characteristics.

The first theoretical attempts to treat SWTI were formulated in the 50's [256, 257, 258, 259] and they were all based on the classical decomposition of disturbances introduced by Kovasznay [260]. Only many years later, as a result of the increasing computational capabilities, DNS of isotropic turbulence-normal shock wave interaction were within reach for relatively weak shocks [261, 262]. It was observed that the interaction was characterised by an abrupt increase in turbulence anisotropy and intensity, triggering strong energy transfers in proximity of the shock-wave. A long series of works followed, analysing the different aspects of SWTI, ranging from the effect of the shock strength [263] to the variations of the upstream turbulence [264, 265, 266].

Many of these computations considered small enough Mach numbers to numerically resolve the inner structure of the viscous shock wave. However, for sufficiently strong shocks, like the ones frequently encountered in complex engineering applications, an accurate resolution of the shock profile is often computationally impossible and an additional regularisation mechanism is needed. The canonical approaches to address such matter in turbulent flows are usually categorised in ENO/WENO/TENO schemes [149, 267, 150], shock-fitting techniques [268, 269, 270, 271] and artificial viscosities [272, 155, 7, 169, 18]. Each of them needs to be properly designed to

regularise shock waves, preserving, at the same time, the delicate properties of turbulence. Each shock-capturing technique is characterised by two main steps: identification and regularisation. In particular, in turbulent flows, the detection of shock waves can be particularly challenging due to the presence of highly unsteady and rapidly varying turbulent structures. An inaccurate identification of flow discontinuities can then easily lead to a significant degradation of small scale fluctuations [184, 172].

The present work addresses the up-mentioned fundamental features of compressible turbulence in a unified setting. The compression/expansion ramp herein considered is, in fact, a particularly interesting setup characterised by complex compressible turbulence dynamics in a self-contained configuration.

8.4.1 Simulation setup

The canonical compression ramp setup features all the ingredients of shock wave-turbulent boundary layer interaction. The arising flow field can be particularly complex, containing many challenging physical phenomena among which shock waves, turbulence, flow separation and unsteady heat transfer. All of these factors have been extensively studied in the literature as each of them requires specific numerical treatments, in particular, if they strongly interact with each other. For example, standard shock-capturing techniques need to be carefully tailored whenever applied to compressible turbulent flows, in order to avoid excessive artificial dissipation [184, 172]. In a similar way, low-dissipative numerical schemes are often essential to reduce as much as possible detrimental effects by numerical dissipation.

The test case herein considered has been extensively studied in many works, both experimental [218, 13] and numerical [14, 12, 202, 204, 203], with particular attention to the unsteady nature of the main shock-wave front. The majority of the up-cited numerical simulations rely on different forms of WENO schemes to handle shock waves [273] and recycling/rescaling techniques to reproduce the incoming turbulent boundary layer [221]. Another relevant simulation of the same configuration, which will be used as an additional reference, has been presented by Li et al. [274]. Starting from this, a series of related studies have been proposed in the following years, including a large number of investigations, such as, wall temperature/turning angle influence, Reynolds stress anisotropy maps and turbulent kinetic energy balance [235, 275, 11]. Most of these works are characterised by the same parameters and techniques used by Martín, except for the turbulent boundary layer inlet condition. In the simulation by Li et al [274], the transition to turbulence has been simulated without any artificial turbulence injection nor recycling/rescaling technique. Instead, a blow-and-suction disturbance has been used to trigger the transition sufficiently far away from the compression corner.

To the authors' knowledge, the interaction between a fully-developed turbulent boundary layer and an oblique shock-wave generated by a compression ramp has never been simulated using the high-order spectral element method [161, 162, 48].

In all the previously cited works, different resolution levels and a large variety of analyses have been performed on the same configuration, providing an extensive framework for validation. The canonical problem consists in a supersonic, fully-turbulent, boundary layer interacting with a 24° degrees compression/expansion ramp. The computational domain (see figure 8.30) has been parametrised using the 99% thickness of the incoming boundary layer (here denoted as δ). The classical geometry of the present configuration is commonly limited to the compression ramp only. The subsequent expansion corner has been added to study the effect of strong expansions on the turbulence.

As geometrical reference, the origin is located at the corner of the compression ramp and the x-coordinates are measured starting from this point following wall-tangent directions. In agreement with the DNS by Priebe & Martín [12], the reference supersonic boundary layer has been evaluated at $x = -8\delta$. Upstream of this location the generation of the turbulent boundary layer itself takes place. In the work by Priebe & Martín [12], a secondary simulation based on recycling/rescaling has been used in order to prescribe a realistic inlet condition at $x = -8\delta$. In the present simulation, instead, an extended domain has been considered, in which the digital filter technique for turbulence generation by Klein et al. [119] has been applied at $x = -20\delta$.

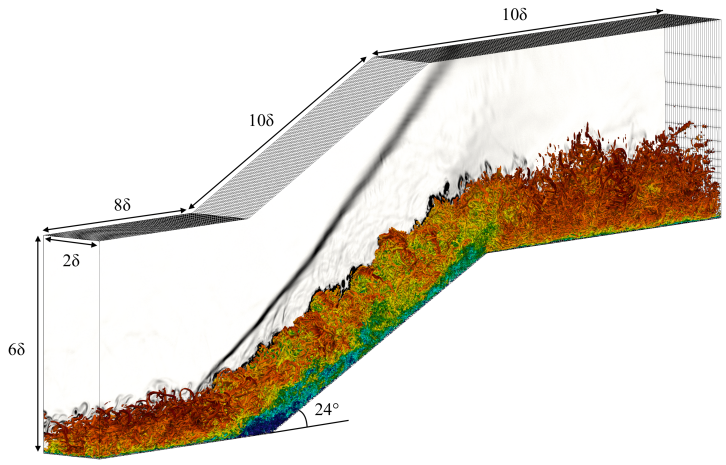

Figure 8.30: Q-criterion contours coloured by velocity magnitude ($Q = 1.0u_\infty^2/\delta^2$). In the background, numerical Schlieren is displayed to highlight the primary shock-wave. δ: incoming boundary layer thickness.

N	N_x	N_y	N_z	δx^+	δy^+	δz^+	DoF
6	$120 + 120 + 120$	28	27	$4.75 \sim 15$	$0.3 \sim 9$	4.2	54M

Table 8.6: Numerical discretisation details. N, order of approximation; N_x, N_y,N_z, number of elements along the stream-wise, wall-normal and span-wise directions respectively; δx^+,δy^+,δz^+, wall-normalised grid spacings.

Regarding the turbulent inlet condition, many different approaches have been proposed in the literature of SWTI to prescribe turbulent inflow generation (see [222] for an extensive summary). Using the digital filter technique by Klein [119], generalised and validated to the present numerical setup [223, 16], the mean profiles, to which perturbations are superposed, have been evaluated using closed form relations involving Van Driest transformed velocity as described by Touber [224]. Given the correlation tensor of the fluid velocity and typical length scales of the desired turbulence field, realistic velocity fluctuations are prescribed at the inlet boundaries, far enough from the flow zone of interest. The values of the correlation tensor have been extrapolated from a turbulent boundary layer DNS performed by Pirozzoli & Bernardini [225] at a similar Reynolds number. Finally, density and temperature fluctuations have been imposed using the strong Reynolds analogy (SRA).

Details regarding the 6th-order accurate numerical discretisation are listed in Table 8.6. The number of total degrees of freedom (DoF) has been chosen in order to match the same accuracy of the DNS by Priebe & Martín [12]. As common practice for high-order spectral element schemes, the grid spacings in Table 8.6 have been evaluated using the length of the elements along each direction divided by the order of approximation (denoted as N). Wall resolution is enforced locating the first solution point at $y^+ \approx 0.3$ and the entire first element within the viscous sub-layer ($y^+ < 10$). The computational domain (figure 8.31) has been enlarged with respect to most of the previously cited works based on recycling/rescaling techniques. Indeed, the inlet forcing method for turbulence injection necessitates of a certain length to develop the desired boundary layer statistical properties, which measures approximately $2/3\delta$ as previously observed by Adler et al [276].

8.4.2 Simulation validation and physical analysis

In this section, a detailed validation of the the main flow features is presented. Once the reliability of the simulation is established, further analyses on the resolved flow field are discussed in subsequent sections.

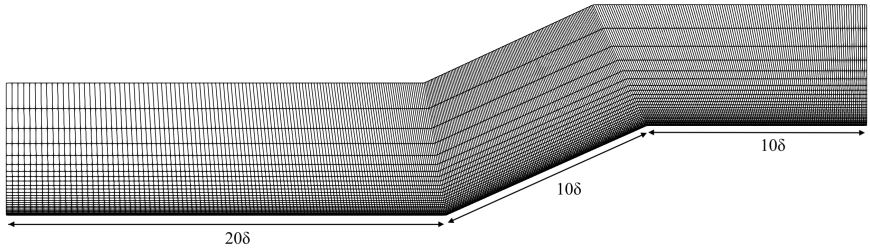

Figure 8.31: Compression/expansion ramp: computational grid. δ: incoming boundary layer thickness.

Wall coefficients and mean profiles

In order to validate the proposed DNS, the averaged friction coefficient and wall pressure have been computed and compared with previous simulations and experimental data of the same configuration in figures 8.32(a) and 8.32(b). In many other works, a perfect agreement within the rich literature of compression ramp simulations has proven to be a very difficult task to achieve. This is commonly true not only in the detached region of the flow, which can be very challenging to be accurately predicted, but also in the upstream region where large deviations of the skin friction coefficient are normally reported in the literature. To highlight such tendency, the DNS by Zhu et al. [11] along with experimental data by Ringuette et al. [13] have been added to figures 8.32(a) and 8.32(b). The simulation by Zhu et al. [11] was performed in the same conditions of the experiments by Ringuette et al. [13] and DNS by Wu & Martín [14], which were characterised by a slightly smaller Reynolds number with respect to the present computation (namely, $\mathrm{Re}_\theta = 2400$). Another relevant difference can be identified in the upstream boundary layer: the DNS performed by Zhu et al. [11] did not rely on any artificial injection of turbulence. In fact, the full laminar-to-turbulent transition of the incoming boundary layer was explicitly simulated using a blow-and-suction disturbance technique.

In figure 8.32(a), in the upstream region, the friction coefficient is slightly higher than the reference DNS by Priebe & Martín [12], whereas the simulation by Zhu et al. [11] reports an even larger value. The experimental separation point is much better predicted by both Zhu et al. [11] and the present simulation rather than by Priebe & Martín [12]. Furthermore, both simulations tend to provide smaller values of the friction coefficient in the downstream region, in agreement with the experimental location of the reattachment point. In figure 8.32(b), the computed wall pressure profile follows nicely the one obtained by Zhu et al. [11], which departs from the DNS by Priebe & Martín [12] within the interaction region around $-3 < x/\delta < 0$.

In order to asses the quality of the incoming boundary layer, mean profiles

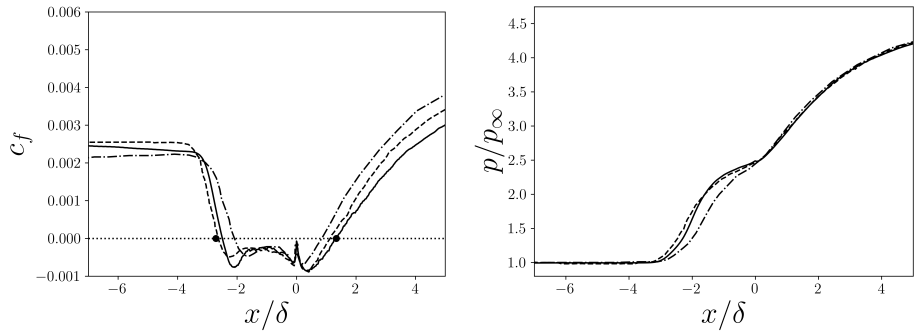

(a) Friction coefficient. (b) Wall pressure.

Figure 8.32: Averaged friction coefficient and wall pressure along the stream-wise direction. Solid line, present simulation; dashed line, DNS by Zhu et al. [11], dashed-dotted line, DNS by Priebe & Martín [12]. Black circles, measurements by Ringuette et al. [13].

along wall-normal planes at different locations have been extracted. First, in figure 8.33, velocity profiles have been evaluated before the interaction with the shock wave ($x = -3\delta$) and after ($x = 4\delta$). Secondly, in figure 8.34, the Van-Driest transformed stream-wise velocity at $x = -8\delta$ is shown. In figure 8.34, the first 6 solution points of the high-order discretisation are shown to highlight wall resolution. Notice that the first element is entirely contained in the viscous sub-layer ($y^+ < 10$). The Van-Driest transformed velocity follows accurately the experimental data in the log-region whereas some small differences with respect to the reference DNS are visible, in particular in the buffer layer.

At $x = -3\delta$ the profile extracted from the present simulation shows a perfect agreement with the reference DNS. Downstream of the shock-interaction region, instead, some discrepancies can be noticed, where a much better agreement with the experimental data by Ringuette et al. [13] has been obtained. Similar results in the detached region have been reported only by Kokkinakis et al. [277] using a 9-th order WENO scheme. In the same work, different schemes were employed and compared. Compared to lower order methods, the 9-th order WENO scheme resulted in higher values of the skin friction in the upstream boundary layer and smaller ones in the downstream region, in agreement with the results shown in Fig 8.32(a).

Finally, the main features of the incoming boundary layer are summarised in Table 8.7. Most of them are in fairly good agreement with the reference values of Priebe's simulation.

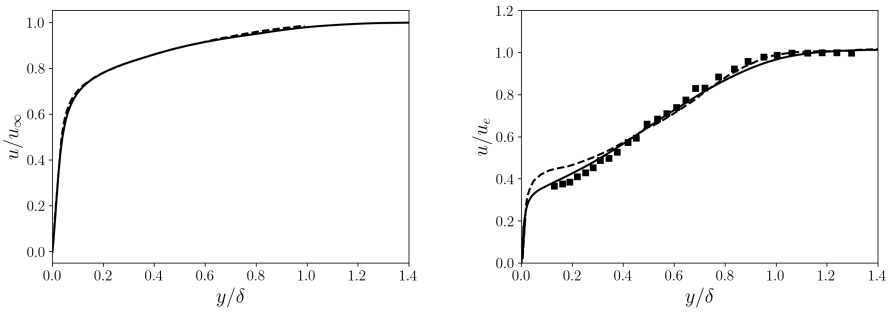

(a) $x = -3\delta$. (b) $x = 4\delta$.

Figure 8.33: Tangential velocity profile along the wall-normal direction at $x = -3\delta$ (left) and $x = 4\delta$ (right). On the left figure, solid line, present simulation; dashed line, DNS by Priebe & Martín [12]. On the right figure, solid line, present simulation; dashed line, DNS by Wu & Martín [14]; symbols, experimental data by Ringuette et al. [13]. On the right figure the stream-wise velocity is normalised by the outer velocity u_e downstream of the main shock.

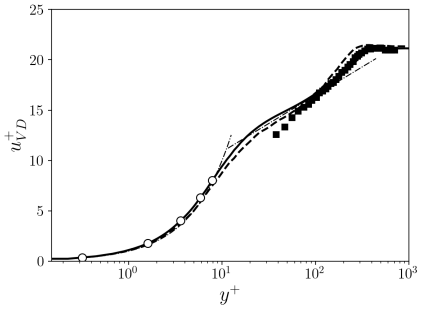

Figure 8.34: Van-Driest transformed stream-wise velocity at $x = -8\delta$. Solid line, present simulation; dashed line, DNS by Wu & Martín [14]; symbols, experimental data by Ringuette et al. [13]; dash-dotted line, $u^+_{VD} = y^+$ and $u^+_{VD} = 5.25 + \log(y^+)/0.41$.

Probes

The main variables have been collected over the simulated time through virtual probes located in regions characterised by different thermodynamic states and turbulence structure (see figure 8.35). Subsequently, temporal and spatial kinetic energy spectra have been related using the Taylor's hypothesis. All the probes have been taken far enough from the wall, in order to make the Taylor's hypothesis reasonably realistic. The first probe has been

-	Re_θ	δ	δ^+	δ^*	θ	H	$c_f \times 10^3$
reference	2900	7.10 mm	340	2.58 mm	0.47 mm	5.49	2.16
$x = -8\delta$	2873	7.43 mm	355	2.72 mm	0.47 mm	5.86	2.17

Table 8.7: Characteristic of the incoming boundary layer: reference vs computed.

located in the log region of the incoming boundary layer and the second in the detached flow downstream of the interaction with the shock wave. The

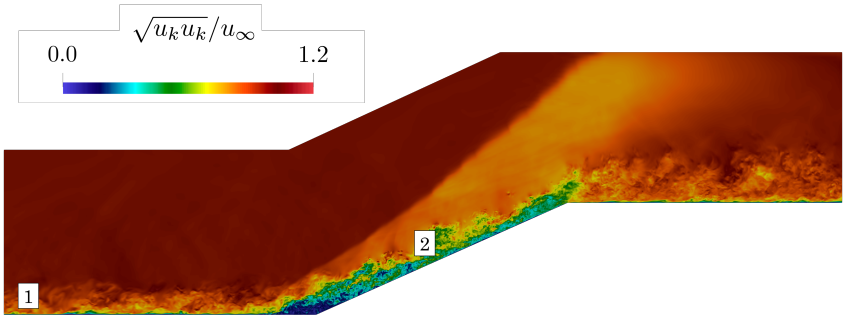

Figure 8.35: Probes location. In the background, instantaneous normalised velocity magnitude field.

kinetic energy spectra, computed using the Taylor's hypothesis, are shown in figure 8.36(a). In addition, due the periodic conditions along z, the kinetic energy spectra in the span-wise direction have been evaluated at the same locations and they are shown in figure 8.36(b). To reduce numerical noise, the spatial kinetic energy spectra have been computed at multiple time steps and subsequently averaged.

The inertial range is clearly visible in all the spectra, followed by a steeper viscous range where viscous dissipation takes place. Notice that no accumulation of kinetic energy in the proximity of the Nyquist grid wavenumber is observed. The molecular viscosity is then sufficiently large to dissipate the kinetic energy associated to the smallest grid size, indicating a fairly good resolution of the dissipative scales. It is interesting to notice that the inertial range is evidently elongated after the interaction with the shock wave. This feature is in good agreement with the widely known evolution of isotropic turbulence across large scale shock waves. The turbulence downstream of the interaction is, in fact, characterised by smaller scales (see also figure 8.37), pushing the dissipative range to larger wave-numbers. Another well-known effect of shock waves on isotropic turbulence is the strong amplification of the transverse vorticity component. As a qualitative visualisation of such

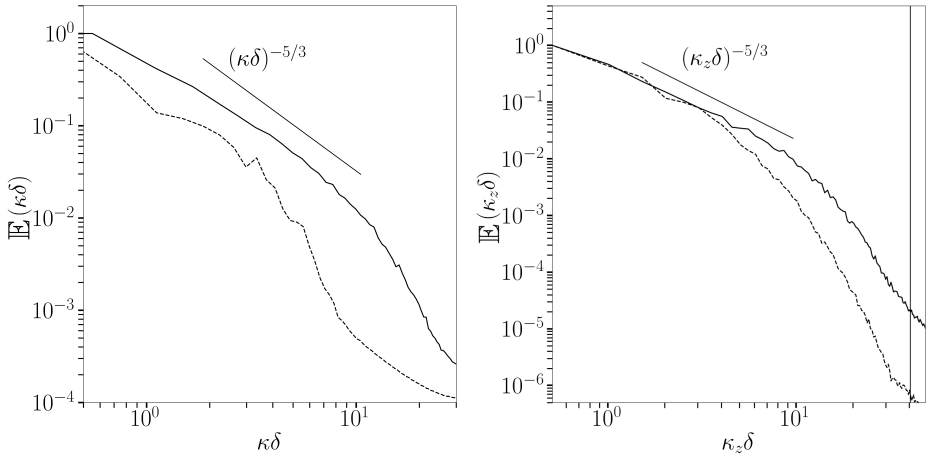

(a) Kinetic energy spectra applying Taylor's hypothesis to temporal signals.

(b) Kinetic energy spectra along z ($y = 0.7\delta$). The vertical dashed line represents the Nyquist grid wavenumber.

Figure 8.36: Kinetic energy spectra. Dashed line, $x = -8\delta$; solid line, $x = 4\delta$. $\mathbb{E}$ denotes the kinetic energy Fourier spectrum of the temporal (left) and span-wise (right) velocity signal. κ represents the wavenumber which is evaluated along the span-wise direction as $\kappa_z = 0.5/z$ and, using Taylor's hypothesis, as $\kappa = 2\pi f/\langle||\mathbf{u}||\rangle$, with f the temporal frequency of the time signal.

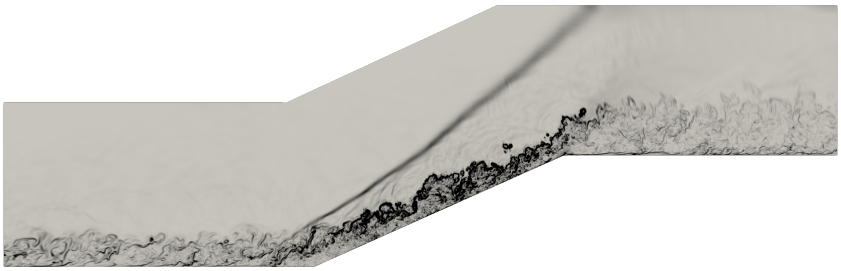

Figure 8.37: Numerical Schlieren.

behaviour, a wall view of the vorticity field is shown in figure 8.38. From this figure, the recovery of velocity fluctuations right after the turbulent inlet condition is also seen.

Knowing the time history of the main variables, the discrete Probability Density Function (PDF) of quantities of interest may be built in a time-averaged statistical sense. At the downstream probe location, the flow regularly oscillates between subsonic and supersonic regimes. Consequently, the PDFs have been conditioned to the local Mach number. The discrete PDFs

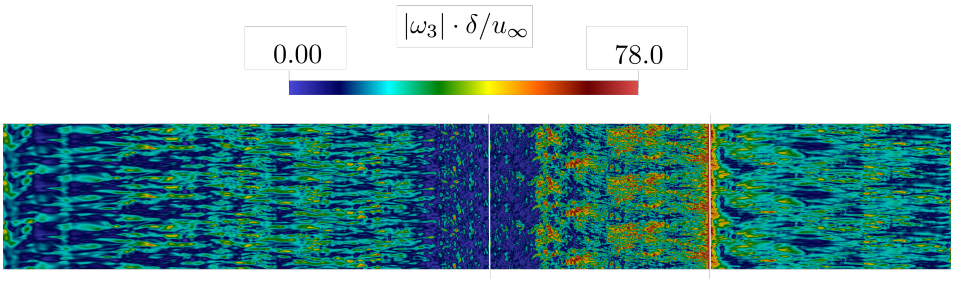

Figure 8.38: Instantaneous absolute value of the normalised span-wise component of the vorticity field (wall view). Vertical white lines represent compression and expansion corners. Three periods along the span-wise direction have been plotted.

of density and pressure are shown in Fig 8.39. The PDF of pressure, shown

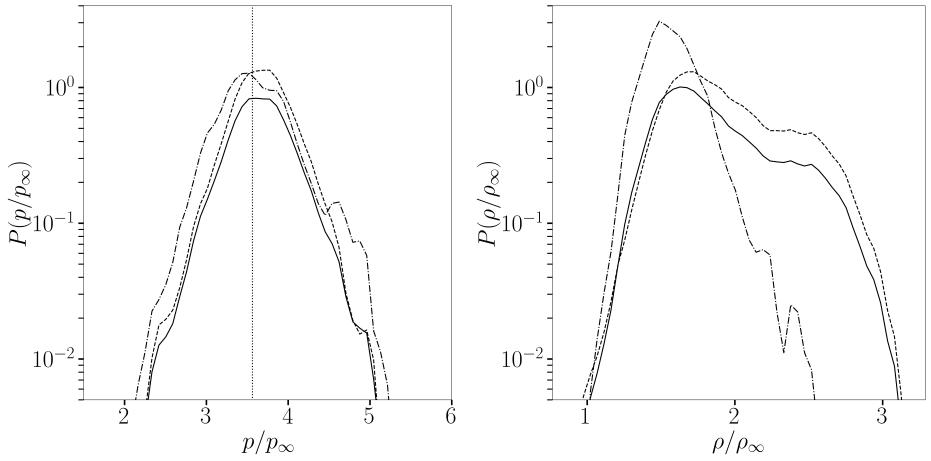

(a) Pressure PDF.

(b) Density PDF.

Figure 8.39: PDF of density and pressure. Dash-dotted line, conditional PDF with Ma < 1; dashed line, conditional PDF with Ma > 1; solid line, total PDF. Vertical dotted line on the left figure represents the pressure mean value.

in figure 8.39(a), is not particularly influenced by the supersonic/subsonic regime. On the other hand, in figure 8.39(b), a significant dependance on the sonic regime is observed for the density: whenever the Mach number exceeds a unitary value, the density PDF tends to extend to larger values, whereas, in subsonic conditions, it is more symmetric with respect to the mean value. This tendency can be partially explained by the presence of shocklets [278] in the detached flow, causing local compressions, and, consequently, an abrupt

increase of the fluid's density.

In these simulations, the shock-capturing artificial viscosity must be essentially inactive in the separated flow, which is characterised by strong vortical structures. This is confirmed in figure 8.40, where the averaged value of the artificial viscosity is shown. The model is active only in the proximity of the shock wave, whereas vanishing values are observed in the rest of the domain. Similarly, the positivity-preserving scheme, has a relatively low and

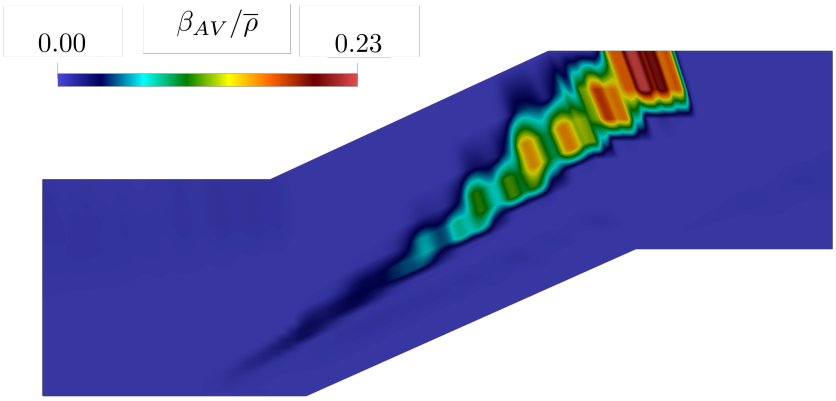

Figure 8.40: Snapshot of averaged artificial viscosity (m^2/s).

localised activation, as shown in figure 8.41. To visualise its activation levels, an element-wise constant flag has been introduced, taking a unitary value if the limiter is active and zero if it is not. Such flag indicator is then averaged in time and along the span-wise direction following the classical paradigm for statistically steady state and span-wise periodic flows. The maximum value assumed by the limiter flag is approximately 1×10^{-4} meaning that the limiter is not only active in a very small region of the flow but also mostly inactive in time as well.

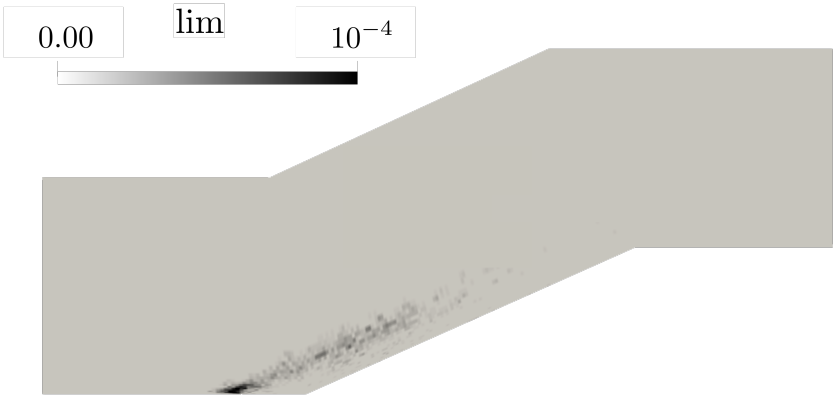

Figure 8.41: Averaged limiter activation.

8.4.3 Analysis of the resolved kinetic energy balance

The space filtered mass and momentum balance equations are obtained applying a density weighted spatial filtering operation $\widetilde{(\cdot)} = \overline{\rho(\cdot)}/\overline{\rho}$ to equations (2.1) and (2.2):

$$\frac{\partial \overline{\rho}}{\partial t} + \frac{\partial}{\partial x_j}(\overline{\rho}\widetilde{u}_j) = 0\,, \tag{8.8}$$

$$\frac{\partial}{\partial t}(\overline{\rho}\widetilde{u}_i) + \frac{\partial}{\partial x_j}(\overline{\rho}\widetilde{u}_i\widetilde{u}_j) = -\frac{\partial \overline{p}}{\partial x_i} + \frac{\partial}{\partial x_j}\left[2\mu(\widetilde{T})\widetilde{S}^d_{ij}\right] + \frac{\partial \tau_{ij}}{\partial x_j} + \frac{\partial \tau^v_{ij}}{\partial x_j}\,, \tag{8.9}$$

where $\widetilde{S}^d_{ij}$ is the deviatoric part of the strain-rate tensor, computed from the resolved velocity field,

$$\widetilde{S}^d_{ij} = \frac{1}{2}\left(\frac{\partial \widetilde{u}_i}{\partial x_j} + \frac{\partial \widetilde{u}_j}{\partial x_i}\right) - \frac{1}{3}\frac{\partial \widetilde{u}_k}{\partial x_k}\delta_{ij}\,, \tag{8.10}$$

and the terms representative of transport by unresolved fluctuations read,

$$\tau_{ij} = \overline{\rho}\widetilde{u}_i\widetilde{u}_j - \overline{\rho u_i u_j}\,, \tag{8.11}$$

$$\tau^v_{ij} = \overline{2\mu S^d_{ij}} - 2\mu(\widetilde{T})\widetilde{S}^d_{ij}\,. \tag{8.12}$$

The total kinetic energy may be written

$$\overline{\rho}E_k = \frac{1}{2}\overline{\rho u_i u_i} = \frac{1}{2}\overline{\rho}\widetilde{u}_i\widetilde{u}_i + \overline{\rho}k\,, \tag{8.13}$$

where $\overline{\rho}k = (\overline{\rho u_i u_i} - \overline{\rho}\widetilde{u}_i\widetilde{u}_i)/2$ denotes the unresolved part of the kinetic energy.

The contribution of τ^v_{ij} (8.12) is often neglected, based on the assumption that terms involving molecular viscosity are mostly restricted to the smallest scales and then weakly affected by the averaging or filtering operations. Most common turbulence models for the unresolved Reynolds stress tensor τ_{ij} rely on the so-called Boussinesq's hypothesis (eddy-viscosity hypothesis):

$$\tau_{ij} = 2\overline{\rho}\nu_t\widetilde{S}^d_{ij} - \frac{2}{3}\overline{\rho}k\delta_{ij}, \tag{8.14}$$

where ν_t is the eddy-viscosity.

The balance equation for the resolved part of the kinetic energy may be written as

$$\frac{\partial(\frac{1}{2}\overline{\rho}\widetilde{u}_k\widetilde{u}_k)}{\partial t} = K_0 + K_1 - K_2 + K_3 - K_4, \tag{8.15}$$

with

$$K_0 = \frac{\partial}{\partial x_j}\left\{-\frac{1}{2}\overline{\rho}\widetilde{u}_k\widetilde{u}_k\widetilde{u}_j - \overline{p}\widetilde{u}_j + \left[2\mu(\widetilde{T})\widetilde{S}^d_{ij} + \tau_{ij} + \tau^v_{ij}\right]\widetilde{u}_i\right\}, \tag{8.16}$$

$$K_1 = \overline{p}\frac{\partial \widetilde{u}_j}{\partial x_j},\ K_2 = 2\mu(\widetilde{T})\widetilde{S}^d_{ij}\frac{\partial \widetilde{u}_i}{\partial x_j},\ K_3 = -\tau_{ij}\frac{\partial \widetilde{u}_i}{\partial x_j},\ K_4 = \tau^v_{ij}\frac{\partial \widetilde{u}_i}{\partial x_j}. \tag{8.17}$$

The first term on the RHS of (8.15) represents a transport term, which only redistributes kinetic energy. The last four terms, instead, act as sources and sinks of the kinetic energy of the resolved scales. K_1 denotes the pressure-dilatation work, which quantifies the exchange of energy between kinetic and internal energy balances. The term K_2 represents the large-scale viscous dissipation. K_3 is the dissipation term of the resolved part of the kinetic energy (*i.e.*, the so-called production term of k, the unresolved kinetic energy) and K_4 denotes the contribution of the unclosed viscous term due to the non-linearity of molecular viscosity.

In a similar manner, the transport equation for the unresolved part of the kinetic energy (*i.e.*, the last term in equation 8.13) reads,

$$\begin{aligned}\frac{\partial\overline{\rho}k}{\partial t}=&\frac{\partial}{\partial x_j}\left[-\overline{\rho}k\widetilde{u}_j-\frac{1}{2}\overline{\rho}(\widetilde{u_k u_k u_j}-\widetilde{u_k u_k}\widetilde{u}_j)\right]\\&+\frac{\partial}{\partial x_j}\left[\left(-\overline{pu_j}+\overline{p}\widetilde{u}_j\right)+\left(\overline{2\mu(T)S^d_{ij}u_i}-\overline{2\mu(T)\widetilde{S}^d_{ij}}\widetilde{u}_i\right)-\tau_{ij}\widetilde{u}_j\right]\\&+\left(\overline{p\frac{\partial u_j}{\partial x_j}}-\overline{p}\frac{\partial\widetilde{u}_j}{\partial x_j}\right)-\left(\overline{2\mu(T)S^d_{ij}\frac{\partial u_i}{\partial x_j}}-\overline{2\mu(T)\widetilde{S}^d_{ij}}\frac{\partial\widetilde{u}_i}{\partial x_j}\right)+\underbrace{\tau_{ij}\frac{\partial\widetilde{u}_i}{\partial x_j}}_{-K_3}.\end{aligned}\tag{8.18}$$

As in the resolved kinetic energy balance, all the terms on the RHS can be cast in flux terms, which only redistribute the turbulent kinetic energy in space, and in source/sink contributions. The most interesting term, for the purposes of the present work, is certainly the last one in equation 8.18, which coincides exactly with the term K_3 of (8.15) with inverted sign. Such term is, in fact, representative of the interchange of kinetic energy between the resolved and unresolved scales within the LES formalism or mean and fluctuating fields in the RANS framework. In other words, the dissipation of the resolved kinetic energy, denoted as K_3, directly coincides with the production of unresolved kinetic energy. Most of the following analyses will be focused on the resolved kinetic energy balance rather than on the unresolved kinetic energy conservation law. Such decision is mainly justified by the fundamental importance of the resolved kinetic energy within the LES framework. The main task of LES is, in fact, providing a generally satisfying description of the large scale motions and only model the influence of the smallest scales on the resolved field.

If not explicitly stated differently, all the terms of the resolved kinetic energy balance will be considered as normalised by the quantity $\rho_\infty u_\infty^3/\delta$.

Averaged fields

In the DNS featuring an homogeneous direction, the density-weighted ensemble-averaging is defined from an integration in time and along the statistically

homogeneous direction:

$$\widetilde{\phi}(x_1, x_2) = \frac{\overline{\rho\phi}}{\overline{\rho}} = \frac{\int_{-L}^{L}\int_{0}^{T} \rho\phi \, \mathrm{d}x_3\mathrm{d}t}{\int_{-L}^{L}\int_{0}^{T} \rho \, \mathrm{d}x_3\mathrm{d}t}, \tag{8.19}$$

for a sufficiently large duration T and where L denotes the length of the x_3 homogeneous direction. The terms K_1 (pressure-dilatation) and K_3 (dissipation) of equation (8.15) are thus first considered in a RANS context, for which the balance equations formally take the exact same form as the filtered ones.

Pressure-dilatation (K_1) represents a quantity which can be directly expressed as a function of the resolved variables, as opposed to the unresolved dissipation (K_3), for which explicit turbulence modelling is needed. The pressure-dilatation term, despite being a large-scale quantity, is particularly important as it represents the primary mechanism of energy exchange between kinetic and internal energies.

Each of these terms is plotted in the whole domain in figures 8.42 and 8.43. In the first figure, showing the dissipation, black and red lines have been added to highlight zones of negative and positive values, respectively. Clearly, most of the flow field is characterised by forward transfer of kinetic energy from the mean flow to the turbulent kinetic energy, as expected in RANS. The dissipation term reaches its smallest values right after the interaction with the shock wave, indicating that most of the unresolved dissipation takes place at this location. The presence of non-zero values of dissipation in proximity of the shock wave is instead caused by the unsteadiness of the shock front which oscillates along the stream-wise direction. As already mentioned, backscatter is rarely observed in mean whereas it is a more common feature in an explicit filtering setup. However, in the present configuration, even in mean, a large portion of the flow experiences an inverse energy transfer, from the fluctuating field to the mean flow, in proximity of the expansion corner. The correlation between expansion/compression motions and inverse/direct energy cascade observed by O'Brien et al. [245] and Wang et al. [246, 279] is then confirmed also in mean. A deeper discussion on the interpretation of such behaviour will be presented in the next sections.

The pressure-dilatation term $\overline{p}(\partial\widetilde{u}_j/\partial x_j)$ is shown in figure 8.43. The large-scale compression and expansion are clearly visible in proximity of the corresponding corners. In the detached region, most of the flow is mildly compressed due to the presence of local shocklets. Closely after the main shock/turbulence interaction, the secondary shocks caused by the separated flow (visible also in figure 8.37) produce a relatively extended compression region downstream of the main shock. The presence of secondary shocks is also responsible for the main shock deflection, coinciding in the figure with the intersection between the two white lines. The pressure-dilatation work interacts only partially with the incoming turbulent boundary layer in

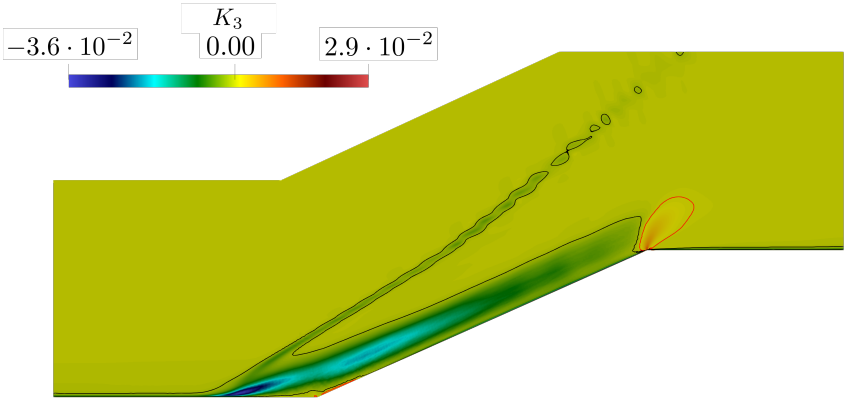

Figure 8.42: Dissipation of the kinetic energy of the resolved scale (K_3 term of equation 8.15).

a very narrow region of the flow, coinciding with the shock in the vicinity of the wall. The Reynolds number is in fact not large enough for the shock wave to penetrate entirely in the turbulent boundary layer. To highlight

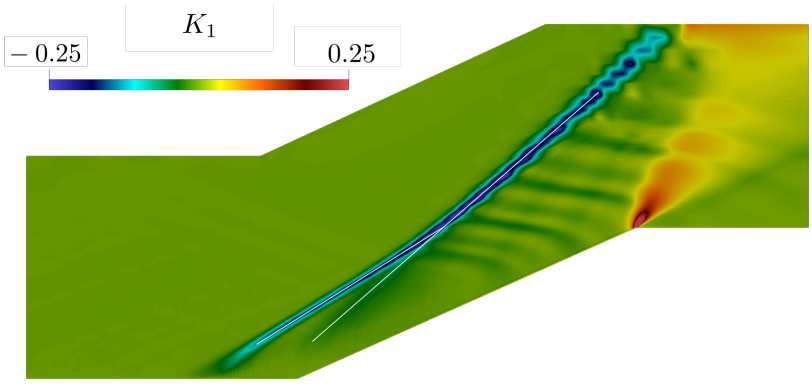

Figure 8.43: Pressure-dilatation term (K_1 term of equation 8.15).

the interaction, the evolution of the most relevant terms of the resolved kinetic energy balance have been computed along the stream-wise direction, at height $y^+ \approx 30$ (figure 8.45). As already observed in figure 8.43, the dissipation reaches its local minimum right after the shock. Upstream of the shock, turbulence interacts with the shock wave generating fluctuations at smaller scales, thereby promoting a large amount of dissipation immediately after. For the same reason, downstream of the primary shock, turbulent ki-

netic energy is locally produced and subsequently advected in the detached region (see figure 8.44). Similarly to the kinetic energy dissipation, non-zero values of turbulent kinetic energy in proximity of the shock wave are mainly caused by the oscillation of the shock wave. It is worth mentioning that the

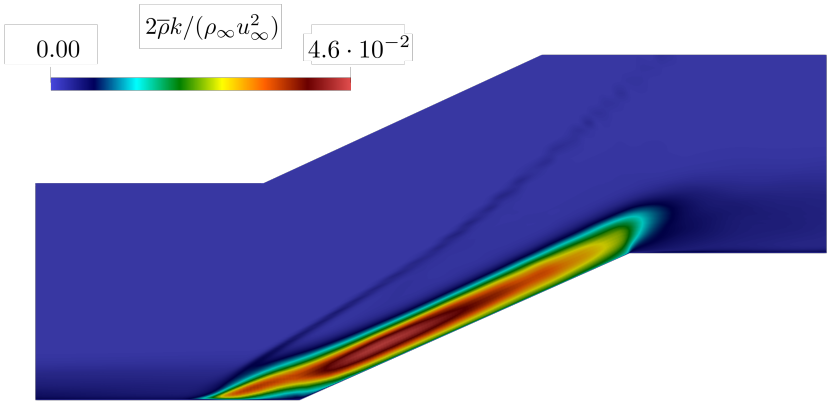

Figure 8.44: Normalised turbulent kinetic energy: $2\overline{\rho}k/(\rho_\infty u_\infty^2)$.

pressure-dilatation work assumes non-negligible values only in proximity of the shock wave. Across the shock, in fact, kinetic energy is locally converted in internal energy, precisely, through the pressure-dilatation term. In terms of resolved kinetic energy balance, the negative values of dissipation and pressure-dilatation work are mainly compensated by the flux term K_0 which assumes mostly positive values along the stream-wise direction. The sum of all the terms on the RHS of (8.15) has been evaluated and it is additionally shown in figure 8.45 as solid black line. The local balance of resolved kinetic energy is very close to zero, indicating an accurate prediction not only of the large-scale terms such as pressure-dilatation and viscous dissipation, but also of the unclosed fluctuating contributions such as the unresolved dissipation term K_3. Furthermore, an accurate local balance of resolved kinetic energy is also indicative of negligible numerical dissipation, confirming the high resolution of the present DNS. An additional term in equation 8.15, representing the contribution of the artificial viscosity model, has been taken into account in the evaluation of the resolved kinetic energy balance shown in figure 8.45. Such term can be written as

$$K_5 = \frac{\partial}{\partial x_j}\left(\beta_{AV}\frac{\partial \widetilde{u}_k}{\partial x_k}\widetilde{u}_j\right) - \beta_{AV}\left(\frac{\partial \widetilde{u}_k}{\partial x_k}\right)^2. \tag{8.20}$$

Its contribution on the total balance of resolved kinetic energy has shown to be quite smaller than the other relevant terms. Nonetheless, it has been found necessary to include it in order to achieve an accurate balance, in

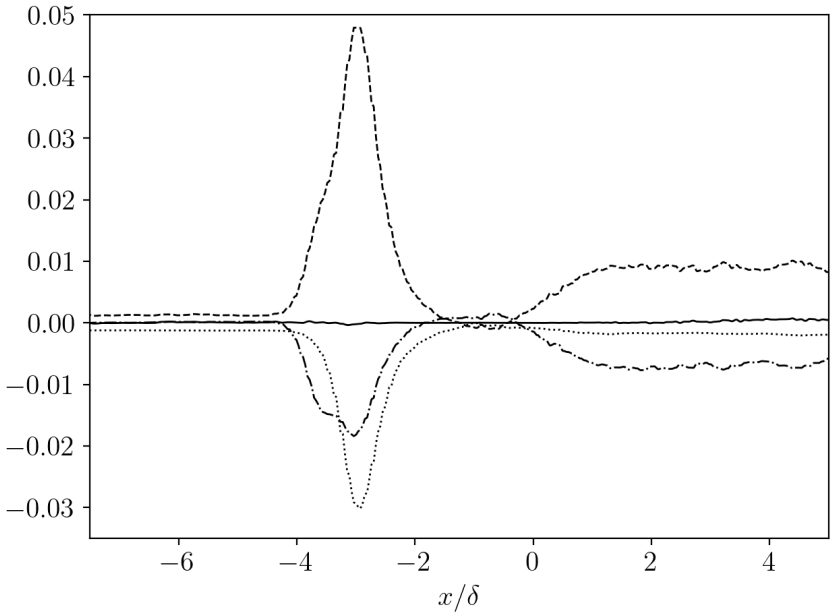

Figure 8.45: Main terms of the resolved kinetic energy balance (equation 8.15) along the stream-wise direction at height $y^+ \approx 30$. Dashed line, flux term K_0; dotted line, pressure-dilatation work K_1; dash-dotted line, dissipation term of the resolved part of the kinetic energy K_3; solid line, local balance of the resolved kinetic energy $\sum_{i=0}^{5} K_i$ (K_5 from equation 8.20). All the terms are normalised by $\rho_\infty u_\infty^3/\delta$.

particular in proximity of the shock wave. (The expression of such term has been omitted in equation (8.15) for clarity purposes.)

Space filtered *vs* averaged fields

The differential filter proposed by Germano [280] is applied, in which the resolution of a heat-type equation is performed with the spectral difference scheme employed for simulating the flow. Filter widths of $\Delta = 2h$, $\Delta = 4h$ and $\Delta = 8h$ have been considered in the following analysis, with h the DNS resolution.

The role of compressibility in kinetic energy transfers has been extensively investigated [279, 281, 282, 246, 283, 284, 245], where the most relevant studies have been focused on the interconnection between large scale dilatation, turbulent Mach number and the dissipation. The first two represent the most relevant indicators of local levels of compressibility and the last one drives the canonical mechanism of kinetic energy redistribution along scales in turbulent flows.

In figure 8.46, the PDF of the dissipation term of the resolved field (term

K_3 in equation 8.15) is shown using both averaging and filtering approaches. Some peculiar differences can be noticed. The first, more relevant, can

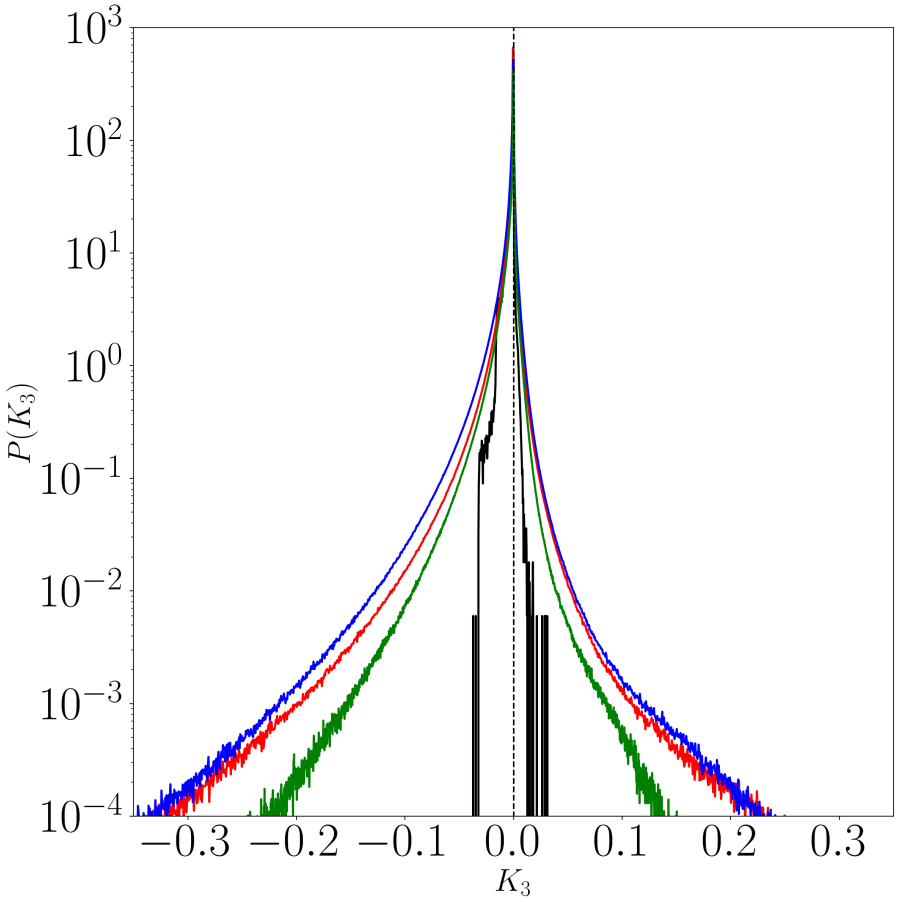

Figure 8.46: PDF of the SGS kinetic energy dissipation term (K_3). Black line, averaging; shades of greys, filtering with $\Delta = 2h$, $\Delta = 4h$, and $\Delta = 8h$ for increasing darkening

.

be identified in an evident prevalence of negative contributions of K_3 using averaged fields (see figure 8.47). In mean, within reasonable bounds, the assumption of classic kinetic energy cascade holds, whereas, using the filtering operation, a much larger amount of both positive and negative values are observed. Still, the left tail of the PDF is clearly longer than the right one, indicating that forward transfer is still more likely to occur than backscatter. Even if the general behaviour of averaged and filtered PDFs is clearly different, mean values are similar. Such observation is in agreement with the suitability of eddy-viscosity models: their dissipative nature is in fact able to represent mean kinetic energy transfers (but not local ones). The influence

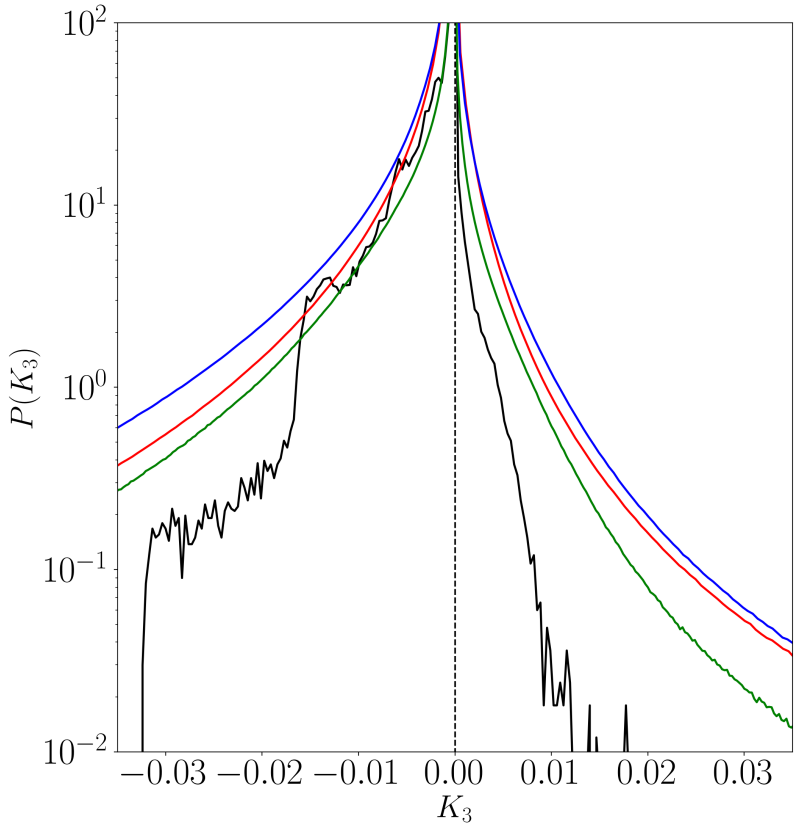

Figure 8.47: Detailed view of figure 8.46.

of the small scales on the resolved flow field is then fairly well approximated, despite the absence of explicit backscatter mechanisms.

Secondly, as expected, local interactions allow much larger values of both inverse and direct energy cascade due to a less regular flow field. Smaller filter widths lead, in fact, to larger gradients and therefore larger values of dissipation. Such behaviour is clearly visible in figure 8.46, where a narrower PDF is observed for the largest filter size ($\Delta = 8h$). Similar trends have been already reported in the case of compressible forced isotropic turbulence by Wang et al. [246]. Finally, the negligible difference between the PDFs for $\Delta = 2h$ and $\Delta = 4h$ is a good accuracy indicator for the present computation. A very small amount of kinetic energy is, in fact, transferred between the two scales, showing that the total kinetic energy can be considered fairly well resolved by the Nyquist grid size (see also figure 8.36(b)).

In the present work, as classical indicator of small scale compressibility activity, the SGS Mach number has been considered. Namely, the SGS Mach

number is defined as:

$$\mathrm{Ma}_{\mathrm{SGS}} = \sqrt{\frac{2\overline{\rho}k}{3\gamma\overline{p}}}\,. \tag{8.21}$$

The averaged SGS Mach number throughout the domain is shown in figure 8.48. In figures 8.49 and 8.50, the filtered SGS Mach number is displayed for increasing filter size. The maximum value of the averaged SGS Mach number is approximately equal to 0.32. Using explicit filtering, instead, slightly higher values can be observed (around 0.42 for $\Delta = 4h$ and $\Delta = 8h$). Non-negligible compressibility effects are expected for values approximately larger than 0.3 [285, 286, 287, 288]. Such values have been reported mainly in the detached region of the flow, where compressibility is expected to have a much stronger influence. Non-zero values of the turbulent kinetic energy

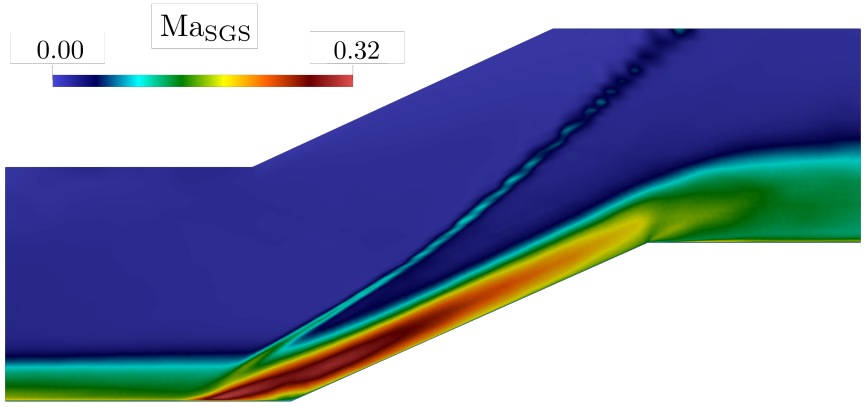

Figure 8.48: Averaged SGS Mach number (equation 8.21).

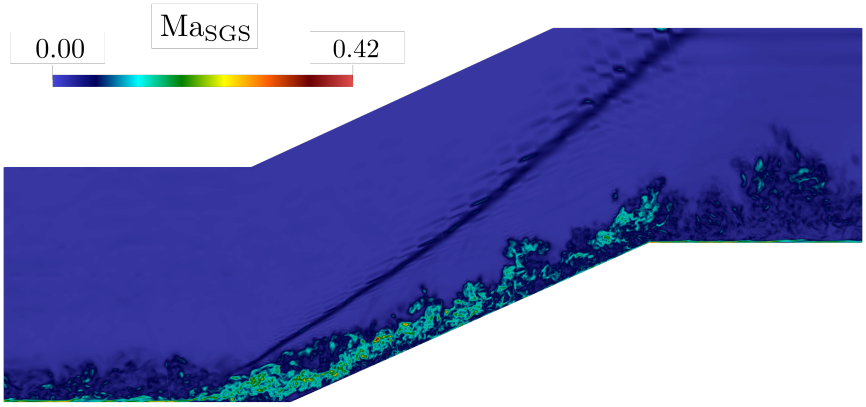

Figure 8.49: Filtered SGS Mach number ($\Delta = 4h$).

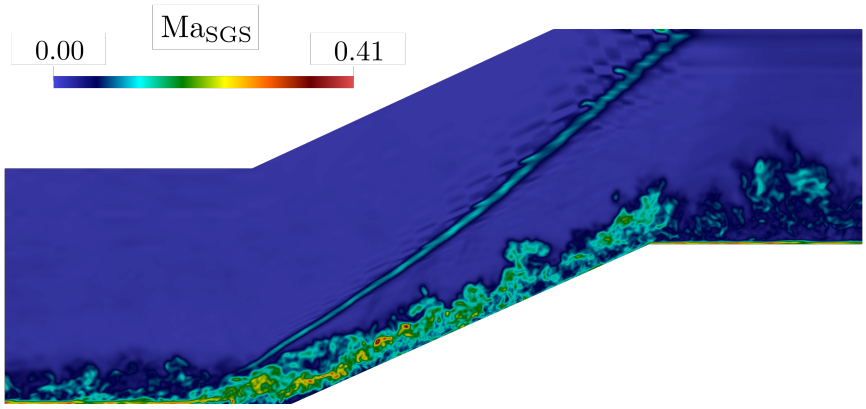

Figure 8.50: Filtered SGS Mach number ($\Delta = 8h$).

are observed not only in the detached region but also in proximity of the shock wave, where the flow is essentially laminar. In average, the generation of turbulent kinetic energy at the shock location is explained by the oscillation of the shock wave in the stream-wise direction. Considering LES space filtering, such tendency is simply caused by the spatial regularisation of the discontinuity.[1]

To focus on the mutual influence between kinetic energy transfers and compressibility, the correlation between large scale pressure-dilation work and SGS kinetic energy dissipation is analysed in figure 8.51, where the joint-PDF (JPDF) of the K_3 and K_1 terms is depicted. In mean, a large amount of the flow field is characterised by a classical direct energy cascade, as the kinetic energy dissipation term is evidently skewed toward negative values. The evident branch of positive values of dissipation in the second quadrant is instead caused by the expansion fan downstream of the compression ramp (see figure 8.42 for comparison). Considering filtered quantities, both differences and analogies can be noticed. Differently with respect to the JPDF of the averaged field, a larger amount of backscatter is present, in particular, in compression regions. Expansion motions are still mainly characterised by backscatter, whereas compressions enhance a direct energy cascade. Such tendency is more evident for larger filter widths and is intrinsically connected to the previous figures 8.49 and 8.50: for larger filter widths the unresolved kinetic energy is higher, leading to larger SGS Mach numbers and a consequently stronger influence of compressibility in kinetic energy transfers.

A more intuitive visualisation of pressure-dilatation work and dissipation of the resolved scales is shown in figure 8.52, where local interactions

[1] A shock wave, from a numerical point of view, will still represent an unresolved feature of the flow even if not directly linked to the classical concept of turbulence under-resolution.

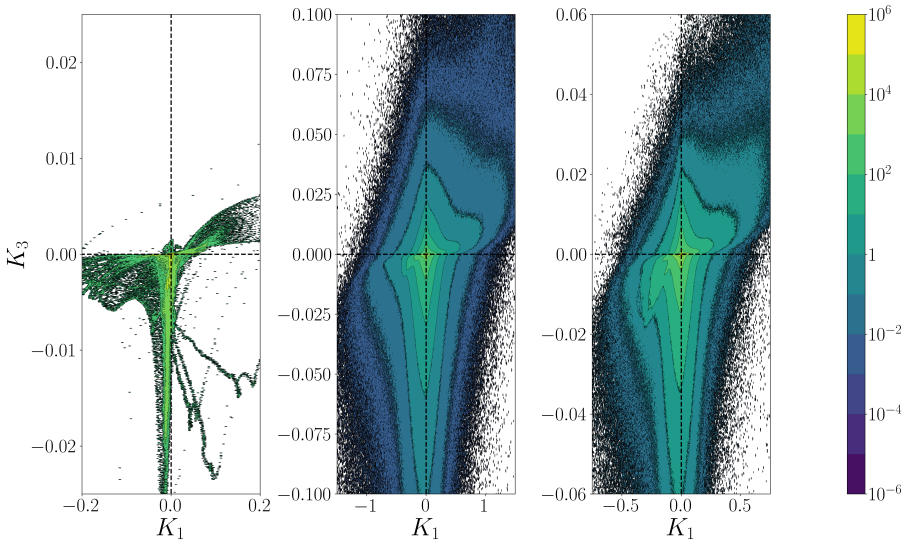

Figure 8.51: JPDF of dissipation of resolved scales (K_3) and resolved pressure-dilatation work (K_1). Left plot, averaged data; middle plot, filtered data with $\Delta = 4h$; right plot, filtered data with $\Delta = 8h$.

are highlighted: compression regions are characterised by classical forward kinetic energy cascade, whereas, vice-versa, expansion regions are more likely to experience backscatter.

Notice that the JPDF of the averaged field in figure 8.51 is in large amount restricted to a very narrow region along the $K_1 = 0$ line, meaning that, in mean, most of the unresolved activity is restricted to regions of negligible pressure dilatation work. The strongest kinetic energy transfers are located right downstream of the interaction with the shock wave, where the flow is only mildly compressed due to the presence of shocklets generated by the detached flow. Considering filtered fields, the JPDFs are much wider and characterised by a large amount of both positive and negative pressure-dilatation work. The shape of the JPDF of the averaged field can be explained by the highly intermittent character of the separated flow. The averaging operation causes an overall compensation between compression and expansion regions. Such effect is an example of the kind of information which is lost studying averaged fields only. It is then relevant to highlight that the importance of compressibility in the modeling is not entirely imposed by the physics of the problem, but it is also strongly influenced by the filter width and thus by the flow resolution chosen for the simulation. Relatively coarse LES are then more likely to experience a stronger influence of compressibility in the modeling rather than well-resolved simulations.

Another way to study the relation between compressibility and kinetic energy transfer is to relate the SGS Mach number with the SGS kinetic

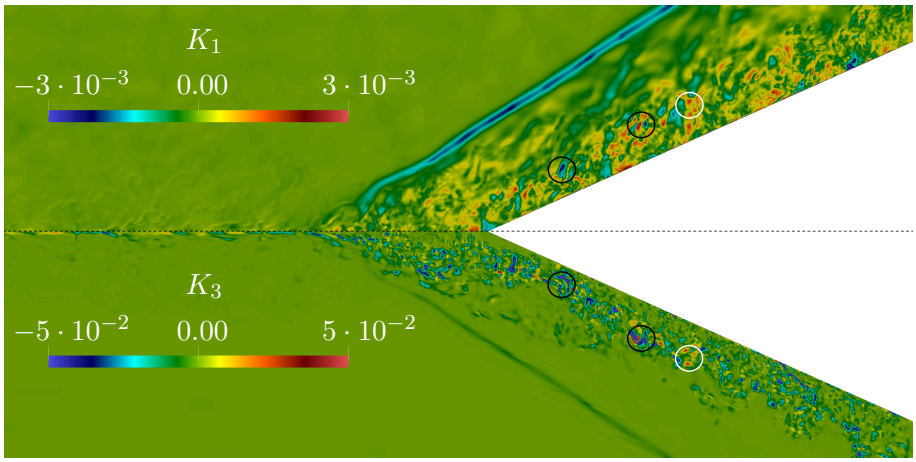

Figure 8.52: Visual comparison of dissipation (bottom, K_3) and pressure-dilatation work (top, K_1) for a given instantaneous filtered field ($\Delta = 4h$). The two quantities are shown in a specular way to ease the comparison. White and black circles highlight regions of intense back and forward scattering respectively.

energy dissipation. In figure 8.53 the JPDFs of these two quantities are shown considering both averaging and filtering approaches. The amount

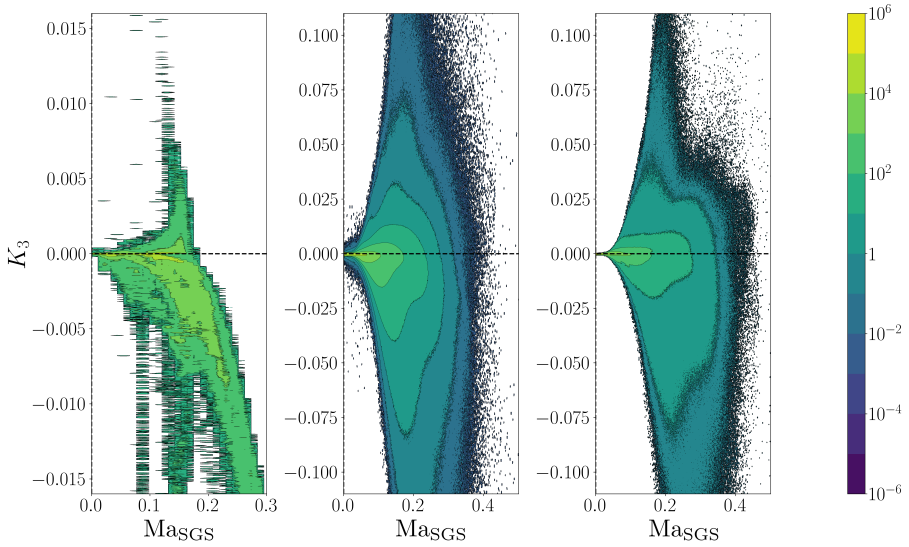

Figure 8.53: JPDF of SGS kinetic energy dissipation and $\mathrm{Ma_{SGS}}$. Left plot, averaged data; middle plot, filtered data with $\Delta = 4h$; right plot, filtered data with $\Delta = 8h$.

of forward kinetic energy transfer gets stronger and stronger for increasing values of $\mathrm{Ma_{SGS}}$, indicating that larger turbulent Mach numbers enhance

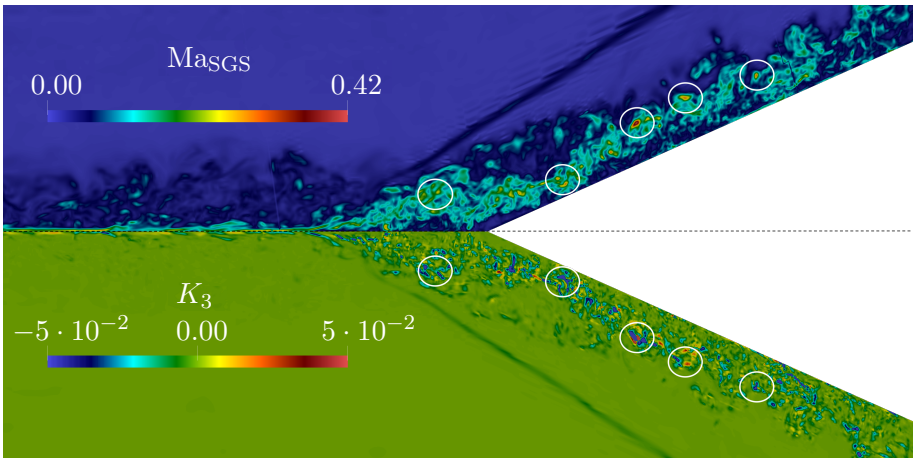

Figure 8.54: Visual comparison of SGS dissipation (bottom) and SGS Mach number (top) for a given instantaneous filtered field ($\Delta = 4h$). The two quantities are shown in a specular way to ease the comparison. Circles highlight strong energy transfer regions.

dissipation of the resolved scales.

Considering the filtered counterparts, a large amount of backscatter is present, even if the JPDF is still clearly asymmetric toward negative values of K_3. In a similar way with respect to the averaged terms, both forward and backscatter tend to increase for larger SGS Mach numbers. This can be clearly observed in figure 8.54 as well, where a direct comparison of the two quantities is shown for a given instantaneous filtered field.

Figure 8.53 links two quantities which are both unresolved, since the definition of SGS Mach number involves the turbulent kinetic energy. On the contrary, figure 8.51 relates an unclosed term, such as the dissipation of the resolved kinetic energy, with the large scale pressure-dilatation work, giving more useful informations in terms of turbulence modelling.

8.4.4 Eddy-viscosity hypothesis

In the previous discussions, the dissipation of the resolved kinetic energy has been used as the sole indicator of backscatter. Still, due to the intrinsic compressible character of the equations, it is reasonable to decompose the dissipation term in two separate contributions,

$$-\tau_{ij}\frac{\partial \widetilde{u}_i}{\partial x_j} = -\left(\tau^d_{ij} + \frac{1}{3}\tau_{kk}\delta_{ij}\right)\frac{\partial \widetilde{u}_i}{\partial x_j} = -\tau^d_{ij}\frac{\partial \widetilde{u}_i}{\partial x_j} - \frac{1}{3}\tau_{kk}\frac{\partial \widetilde{u}_i}{\partial x_i}\,, \tag{8.22}$$

where $\tau^d_{ij} = \tau_{ij} - \frac{1}{3}\tau_{kk}\delta_{ij}$ is the deviatoric part of the SGS tensor. Under incompressible conditions, such decomposition is redundant from an energetic point of view, due to the solenoidal nature of the velocity field. In

other words, the influence of the trace of the SGS tensor on the large-scale kinetic energy is directly proportional to the level of compressibility of the flow, quantified by the velocity field dilatation. To recover a traceless tensor, in compressible LES, only the deviatoric part of the SGS tensor is commonly modelled using an eddy-viscosity hypothesis (see equation 8.14). The influence of this hypothesis on the total resolved kinetic energy is then expressed as:

$$-\tau_{ij}\frac{\partial\widetilde{u}_i}{\partial x_j}+\frac{1}{3}\tau_{kk}\frac{\partial\widetilde{u}_l}{\partial x_l}=-2\overline{\rho}\nu_t\widetilde{S}^d_{ij}\frac{\partial\widetilde{u}_i}{\partial x_j}\,, \tag{8.23}$$

(see [289]) which leads to the following expression of eddy-viscosity:

$$\nu_t=\frac{K_3+\Lambda}{-2\overline{\rho}\widetilde{S}^d_{ij}(\partial\widetilde{u}_i/\partial x_j)}\,, \tag{8.24}$$

where $\Lambda=-(2/3)\overline{\rho}k(\partial\widetilde{u}_l/\partial x_l)$. Such formulation can be interpreted in both filtered and averaged sense.

The term Λ represents the turbulent kinetic energy transfer due to the spherical part of the SGS tensor. It is usually modelled following the [25] approach, also with a dynamic formulation [26]. This term, involving the turbulent kinetic energy, vanishes in the incompressible case and the presence of negative/positive eddy-viscosities is entirely caused by the sign of the dissipation term (*i.e.*, backscatter implies negative eddy-viscosities and, vice-versa, forward kinetic energy transfer causes positive eddy-viscosities). Consequently, the unresolved part of the turbulent kinetic energy does not play a role in terms of dissipation of the resolved part of the kinetic energy in incompressible conditions. For non-spectral filters, as observed by Vreman et al. [290], the turbulent kinetic energy always takes positive values. Consequently, in the compressible case, the term Λ is negative in expansion regions and positive in compression regions, thus following an opposite trend with respect to K_3.

In figure 8.55 the joint probability density function of these two terms has been plotted for both averaging and explicit filtering. The solid black line denotes the line $\nu_t=0$ (*i.e.*, $K_3=-\Lambda$). Below such line, the eddy-viscosity assumes positive values, whereas, above of it, the eddy-viscosity is negative. Regarding the JPDF within the RANS context, a clear prevalence of forward kinetic energy cascade can be observed. The term K_3 assumes mostly negative values and it is particularly clustered around the vertical line $\Lambda=0$. This property indicates that most of the energy transfers are located in regions of negligible dilatation (at least in mean). Furthermore, a distinct bandwidth of non-null values of the JPDF is almost perfectly aligned with the $\nu_t=0$ line. This narrow stripe is located slightly below the $\nu_t=0$ line, as it extends for relatively large values of Λ. Finally, the JPDF is almost entirely confined below the $\nu_t=0$ line, indicating that, in statistical mean, the assumption of positive eddy-viscosity can be fairly accurate, even

in presence of backscatter. The term Λ, in fact, compensates the backscatter phenomenon, preventing the occurrence of negative eddy-viscosities. With the space filtered fields, the same tendencies are present but in a less evident form. Even if a forward kinetic energy cascade is generally more likely to occur than backscatter, a large amount of the flow field is characterised by negative values of the eddy-viscosity.

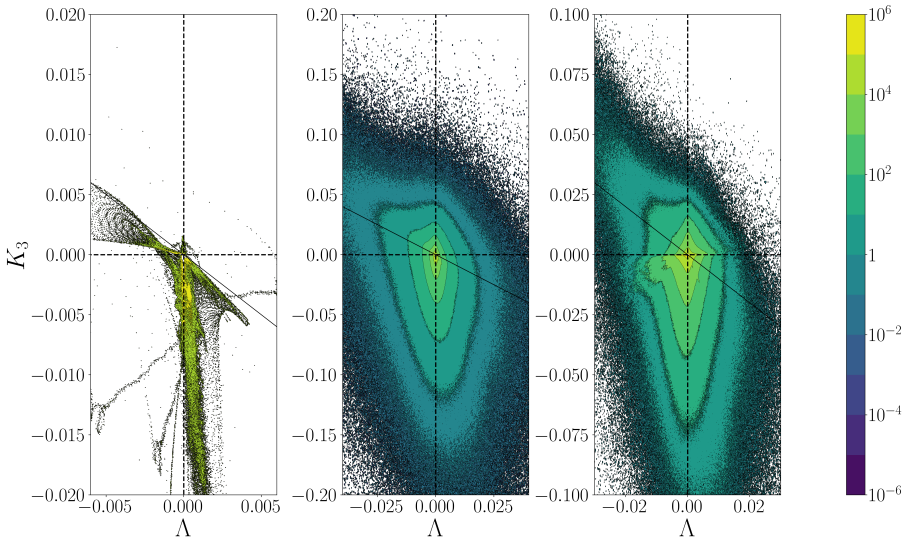

Figure 8.55: JPDF of SGS dissipation and Λ. The solid black line denotes the line $\nu_t = 0$. Left plot, averaged data; middle plot, filtered data with $\Delta = 4h$; right plot, filtered data with $\Delta = 8h$. Both K_3 and Λ are normalised by $\rho_\infty u_\infty^3/\delta$.

To highlight the difference between K_3 and the sum $K_3 + \Lambda$, their averaged values are shown in figure 8.56. Following the classical definition of kinetic energy transfer based on K_3, the expansion region experiences strong backscatter (left figure), but, if the compressible contribution Λ is accounted for, only negative values are observed in the whole domain. It is then reasonable to conclude, that the deviatoric part of the SGS tensor, in average, has an essentially dissipative role, whereas the trace is directly responsible for the backscatter observed in proximity of the expansion corner.

To evaluate the contribution of the spherical part on the total SGS kinetic energy dissipation, the joint probability function of the deviatoric contribution $K_3 + \Lambda$ with respect to the large scale pressure-dilatation work K_1 has been computed and shown in figure 8.57. Starting from the JPDF of the averaged field, in agreement with figure 8.56, the deviatoric contribution of the SGS kinetic energy dissipation takes negative values only. The backscatter region observed in the left side of figure 8.51 completely disappears when the spherical part is subtracted. In the filtered case, instead, a mild correla-

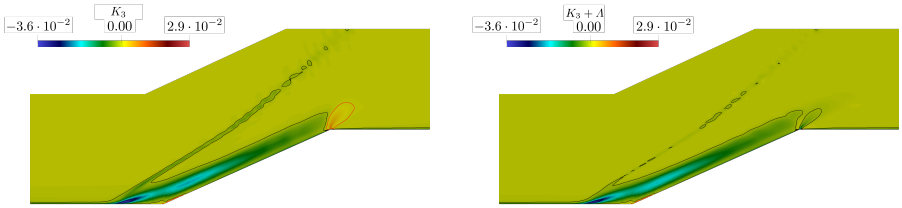

(a) K_3. (b) $K_3 + \Lambda$.

Figure 8.56: Comparison between averaged terms K_3 and $K_3 + \Lambda$. Both terms are normalised by $\rho_\infty u_\infty^3/\delta$.

tion between the two terms can still be observed even though considerably weaker, in particular for small filter widths. These observations highlight a clearly different behaviour between averaged and filtered approaches. On the one hand, the correlation, once observed, completely vanishes in mean when the spherical part is subtracted. On the other, the same correlation persists when evaluated on filtered fields.

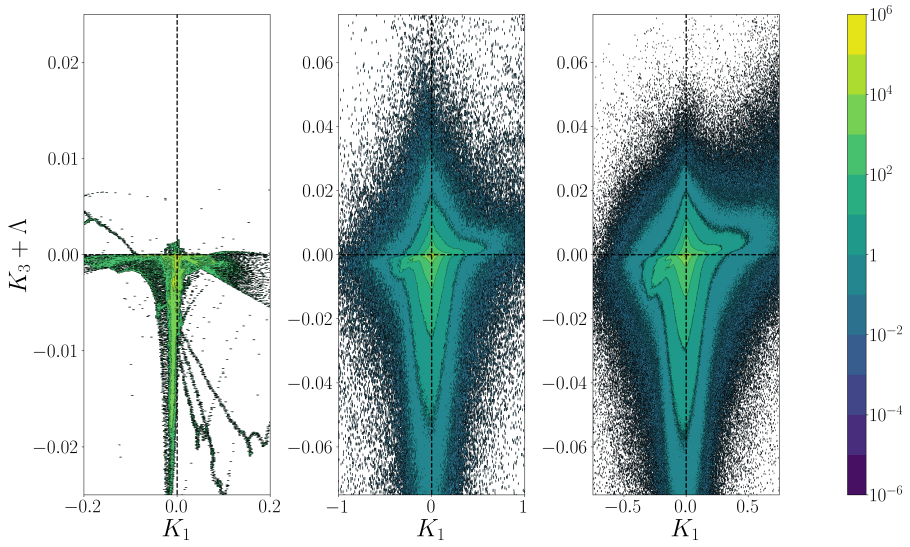

Figure 8.57: JPDF of deviatoric SGS dissipation and large scale pressure-dilatation work. Left plot, averaged data; middle plot, filtered data with $\Delta = 4h$; right plot, filtered data with $\Delta = 8h$.

To facilitate the comparison, figure 8.58 shows the JPDFs of the averaged field accounting, respectively, for both deviatoric and spherical contributions or for deviatoric contributions only. A spherical bulk term, as the one introduced by the artificial viscosity scheme, can be interestingly interpreted as

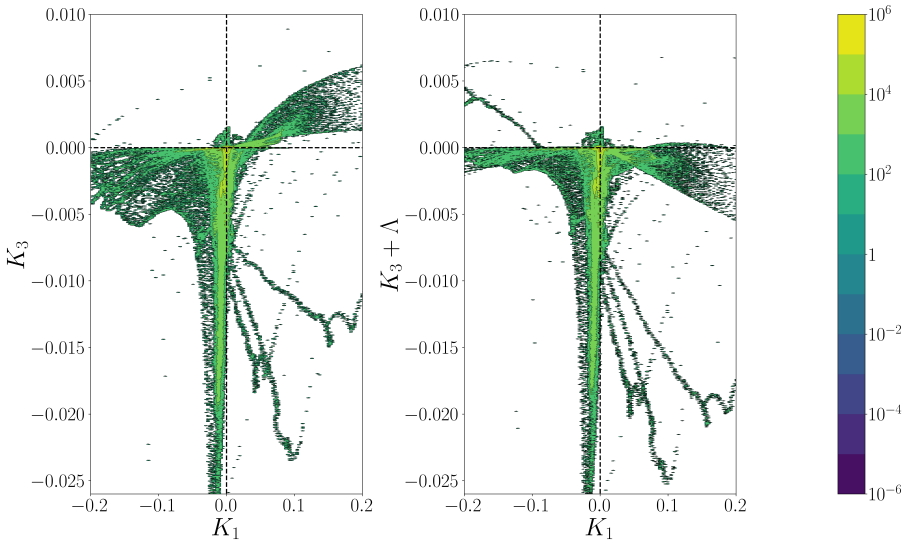

Figure 8.58: Averaged JPDF of standard and deviatoric SGS dissipation and large scale pressure-dilatation work. Left, K_3; right, $K_3 + \Lambda$.

some kind of approximation of the turbulent kinetic energy itself. In fact, close to the shock wave, the flow field divergence is negative and the term

$$\beta \frac{\partial \widetilde{u}_k}{\partial x_k}$$

is consistently negative too, where β is a bulk viscosity. From a direct comparison of such term with the spherical part of the SGS tensor the following heuristic expression can be easily obtained:

$$\frac{2}{3}\overline{\rho}k \sim -\beta \frac{\partial \widetilde{u}_k}{\partial x_k}. \tag{8.25}$$

Away from the shock, such similarity is less evident. Nevertheless, the parallelism between compression regions and positive turbulent kinetic energy can be conveniently used for modelling purposes. In fact, it can be easily proved that a bulk viscosity term in the momentum equation causes large scale kinetic energy dissipation. Therefore, the additional bulk term would ideally reproduce only the dissipative character of the turbulent kinetic energy on the large scales, in a fashion which resembles eddy-viscosity models, where only the direct kinetic energy transfers are modelled. In a similar way, [246, 279] proposed a simplified relation between SGS dissipation and dilatation, reporting a scaling close to $(\partial \widetilde{u}_k/\partial x_k)^2$ in compression regions, which is the same form of a bulk viscosity term. In their work, the total SGS dissipation was analysed, including both deviatoric and spherical contributions. The bulk viscosity, furthermore, has a well-knows dissipative

character on the dilatation field, reinforcing the idea of SGS modelling as essentially a regularisation technique.

In the incompressible case, vorticity is smoothed thorough explicit filtering of DNS data and an analogous mechanism needs to be present in under-resolved *a-priori* simulations, for example, through an augmented shear viscosity. In the same way, a similar tendency is expected for the dilatation as well. The filtered dilatation will result less singular and irregular. Thus, a regularisation of it would be successfully produced by an artificial bulk term in the resolution of the filtered momentum equation. The natural decoupling between dilatational and solenoidal contributions in compressible turbulence (see [229]) clearly indicates a convenient dichotomy based on Helmholtz decomposition. The contraposition between solenoidal and dilatational field (and consequently vorticity and divergence) could possibly suggest a parallelism in the SGS modelling as well, based on the difference between deviatoric and spherical components of the SGS tensor, that could be possibly modelled using their respective natural choices of shear and bulk viscosities. A methodical development of such a model is far beyond the scope of the present work. Nevertheless, the preliminary results herein presented can be interpreted as very first step in this direction and future research will be focused on this matter.

8.4.5 Conclusions

A Direct Numerical Simulation of a 24° compression/expansion ramp has been performed using a high-order spectral difference code. The presented setup has been chosen as a popular example of shock wave-turbulence interaction. Despite its relatively simple geometry, the interaction between a supersonic boundary layer and compression/expansion ramps is representative of many different complex features of compressible turbulent flows.

After a thorough validation, considering mean profiles and wall coefficients, a series of a-priori analyses have been considered. The present work has been developed using both averaging and explicit filtering, providing a clear dualism between RANS and LES approaches, respectively. Most of the attention has been focused on specific terms which appear in the resolved kinetic energy balance in both filtered and averaged sense. In particular, the well-known dissipation term has been analysed in detail. It has been shown that, in the present setup, following both the averaging and filtering formalisms, the presence of both direct and reverse kinetic energy cascade was observed. In agreement with previous observations [246, 245], compression regions are mostly characterised by forward kinetic energy transfers whereas an inverse cascade is promoted by expansion motions.

Subsequently, the dissipation term has been decomposed in deviatoric and spherical contributions. Such procedure has been used to evaluate the suitability of eddy-viscosity models for the deviatoric part of the SGS ten-

sor in compressible flows. Averaged results have shown that the expression of equivalent eddy-viscosity rarely assumes negative values throughout the whole domain. It is then evident that the correlation, already observed, between large scale dilatation and SGS dissipation is, in large part, caused by the spherical part of the SGS tensor. Its corresponding term in the total kinetic energy balance is, in fact, directly proportional to the divergence of the velocity field. The importance of proper modelling of the spherical part of the SGS tensor is then highlighted.

For sufficiently high turbulent Mach numbers, the influence of expansion/compression motions and, consequently, of the spherical part of the SGS tensor, increases, revealing a clear mechanism of backscatter based on the local levels of compressibility. It has been observed that, inspired by classical eddy-viscosity models for the deviatoric part, a bulk viscosity could be used as an SGS model for the turbulent kinetic energy. Further analyses will be focused on a better understanding of solenoidal and dilatational contributions on kinetic energy transfers. The ultimate goal of such analyses is identified in the development of SGS models (in particular for the turbulent kinetic energy) more suitable to high-order simulations of compressible flows.

Chapter 9

Conclusions and perspectives

High-order methods represent an expanding field in the CFD community. Their use is becoming more and more widespread both in academia and industry. Still, aspects such as numerical stability, turbulence modelling and shock-capturing, represent the real bottle-neck for their definitive blossoming in the industry. Along these lines, the present work was structured touching all these fundamental topics of high-order methods. In the first chapter 2 was focused on the fundamental equations considered in this work, such as Euler and Navier-Stokes equations. Later, the problem of turbulence modelling, within the framework of Large-Eddy Simulations, was first introduced in chapter 3. Finally, the specific numerical scheme herein studied (*i.e.*, the Spectral Difference scheme) was presented in chapter 4. All the relevant details on its implementation, from the interpolation and differentiation operators to inviscid and viscous fluxes, have been thoroughly discussed. These three first chapters aim at providing a sufficiently extensive background knowledge on high-order simulations of turbulent flows.

Continuing with the reading, more and more complex systems have been considered. In chapter 5, a series of spectral analyses have been applied, not only to the Spectral Difference scheme but also on two different variations of the Flux-Reconstruction scheme. Such analyses aim at providing a better understanding on the general behaviour of high-order schemes in the simulation of under-resolved flows. The current state-of-the-art of spectral analyses for high-order methods is mainly composed by temporal eigen-analysis, spatial eigen-analysis and non-model analysis. These three techniques are all based on the numerical discretisation of the one-dimensional linear advection equation using Bloch wave-like functions. Nonetheless, high-order methods, employed in three-dimensional, strongly non-linear problems can behave very differently. In the present work, a generalisation of the up-cited techniques for non-constant advection velocity was proposed as a first step toward more complex systems. A deep theoretical study, considering different schemes and different classes of numerical fluxes has been used to gain useful insights

about the spatial discretisation and its dependency on non-linear fluxes. A series of relevant numerical experiments have been considered, confirming the theoretical findings. The Spectral Difference scheme has shown to be more dissipative for spatially evolving turbulence with respect to the nodal Discontinuous Galerkin recovering Flux Reconstruction scheme. The dynamics of numerical dissipation for increasing levels of inhomogeneity in the advection velocities was considered responsible of such behaviour.

In chapter 6, once known the concept of numerical dissipation and the most commonly used techniques to quantified it, the informations gathered in the previous chapter have been used in connection with Sub-Grid Scales modelling. The Spectral Element Dynamic Model (SEDM) has been now properly introduced with all the implementational details and its intrinsic connection with numerical dissipation has been thoroughly discussed. The aim of the SEDM is to develop an SGS model, within the high-order SD discretisation, which is aware of the local levels of numerical dissipation. The SEDM can be, in fact, interpreted as a linking point between Implicit LES and Explicit LES. For sufficiently low orders of approximation numerical dissipation is used to mimic the dissipative influence of the smallest scales on the resolved field. On the other hand, increasing the order, and consequently decreasing numerical diffusion, explicit SGS dissipation is injected in the system to keep the simulation accurate and stable. In chapter 6, two numerical simulations of transitional flows have been considered to highlight the capabilities of the SEDM. Namely, the bypass transition on a zero-pressure-gradient flat plate simulation and the flow transitional flow over an SD7003 airfoil. Both computations where considered in almost incompressible conditions. The aim of such computations was highlighting the behaviour of the SEDM for complex flows where different levels of resolution coexisted within the domain. The SEDM, in fact, has shown a significant improvement with respect to standard SGS models in transitional flow was observed. Its ability to automatically distinguish between laminar and turbulent flows has shown to be a crucial point in simulating transition. Furthermore, in particular for the SD7003 simulation, the drawbacks of Implicit LES have been highlighted: the SEDM has shown to keep the simulation stable also for relatively high-order of approximation ($N = 6$ and $N = 8$).

The last two chapters were dedicated to the generalisation of the previously presented concepts to compressible flows. The first obstacle in simulating compressible turbulence flows is certainly represented by the natural development of shock-waves in the flow field. The numerical discretisation of discontinuities such as shock waves can be particularly complex in the framework of high-order numerical scheme. Consequently, in chapter 7, the notion of shock-capturing techniques was introduced. More specifically, a bulk-based, low dissipative, artificial viscosity (AV) approach was proposed and compared with a more classical laplacian regularisation model. It was shown that the bulk-based artificial viscosity was able to present the non-

monotonic behaviour of the entropy field across the shock-wave and to drastically reduce the levels of dissipation for under-resolved turbulent flows. It was, in fact, shown that the laplacian approach caused a significantly strong dissipation of vorticity modes, leading to an extremely fast decay of kinetic energy. Instead, the bulk viscosity has shown to leave almost untouched the vorticity field. On the other hand, the bulk artificial viscosity caused a non-negligible deterioration of temperature and dilatation fluctuations, although smaller than the one provoked by the laplacian model.

Consequently, chapter 8 starts with the introduction of a Ducros-based correction on the proposed AV technique. The improved model was then applied to a turbulent transonic airfoil simulation in combination with the SEDM. In such scenario, it was shown the correct activation of both artificial viscosity and SGS model within the domain. The bulk viscosity field was observed to take high values only in proximity of the shock-wave developing on the upper side of the airfoil. The SGS model, in a similar way, was active only in the narrow detached region of the flow field. The transonic airfoil simulation was used a first, simplified example of shock-turbulence interaction.

In the second part of chapter 8 the interaction between a fully-developed turbulent boundary layer and a compression ramp was presented.

Firstly, in order to develop more generalised versions of the SEDM for compressible flows, a Direct Numerical Simulation study has been performed on a compression/expansion ramp. In particular, the transfer of kinetic energy has been evaluated using explicit filtering and Reynolds averaging. Such analyses have been performed with the goal of a better understanding on the general form of turbulence SGS models in the presence of non-negligible compressibility effects. Most of the attention has been focused on specific terms which appear in the resolved kinetic energy balance in both filtered and averaged sense. In particular, the well-known dissipation term has been analysed in detail. It has been shown that, in the present setup, following both the averaging and filtering formalisms, the presence of both direct and reverse kinetic energy cascade was observed. In agreement with previous observations [246, 245], compression regions are mostly characterised by forward kinetic energy transfers whereas an inverse cascade is promoted by expansion motions.

Subsequently, the dissipation term has been decomposed in deviatoric and spherical contributions. Such procedure has been used to evaluate the suitability of eddy-viscosity models for the deviatoric part of the SGS tensor in compressible flows. Averaged results have shown that the expression of equivalent eddy-viscosity rarely assumes negative values throughout the whole domain. It is then evident that the correlation, already observed, between large scale dilatation and SGS dissipation is, in large part, caused by the spherical part of the SGS tensor. Its corresponding term in the total kinetic energy balance is, in fact, directly proportional to the divergence of

the velocity field. The importance of proper modelling of the spherical part of the SGS tensor is then highlighted.

Finally, an LES computation was performed to evaluate, once again, the coexistence between the shock-capturing and SGS model. The combination of SGS and AV is well balanced thanks to the addition of Ducros sensor [22] to the standard modal sensor by Peraire and Persson [7] within the shock-capturing procedure. The activation of the AV is mainly limited to the outer layer, where the shock is laminar and unaffected by turbulence. The SGS model, in the same way, thanks to its dynamical natural is mainly active in the turbulent boundary layer. An extensive validation of the present test case has been performed, including temporal/spatial kinetic energy spectra, wall-normal profiles and Reynolds Stress Anisotropy Invariant Maps flow representation.

The present work, as mentioned at the beginning of this section, was structured in order to touch the three main aspects of high-order simulations of compressible turbulent flows: numerical dissipation/dispersion (chapter 5), Sub-Grid Scales modelling (chapter 6), compressibility effects (chapters 7 and 8). As a whole, the work presented in each of these chapters continues and expands the field of high-order methods for compressible turbulence. Each of the sub-topics therein presented can evolve in several different ways, exploring a large variety of new techniques and applications. More and more complex spectral analyses techniques are likely to appear in the field, considering more complex sets of equations and mathematical tools to study them. In addition, for example, a fully-discrete version of the present techniques focused on the interaction between spatial and temporal errors in currently in development by the author.

Different improvements of the bulk artificial viscosity model can be explored. In particular, possible future work could be focused on the identification of optimal sets of variables to better detect shock wave and reduce the artificial dissipation as much as possible. Finally, the DNS database generated with the compression/expansion ramp can be extremely useful in the development of more sophisticated SGS models for compressible flows. The highly resolved flow field can provide useful informations on the local structure of wall-bounded, compressible turbulence. In similarity with respect to the shock-capturing technique, also the SEDM could be easily modified in a more generalised form, detecting turbulence under-resolution using not only the velocity field but also thermodynamic variables. The global knowledge on numerical dissipation/dispersion, shock-capturing and compressibility effects could lead to a unified SGS model able to detect under-resolution associated to shock waves and turbulence using different sets of variables and treat them using models specifically design to interact with each other.

Archival Publications

N. Tonicello, G. Lodato, L. Vervisch, *Entropy preserving low dissipative shock capturing with wave characteristic based sensor for high- order methods*, Computers & Fluids 197 (2020) 104357.
https://doi.org/10.1016/j.compfluid.2019.104357.

N. Tonicello, G. Lodato, L. Vervisch, *A comparative study from spectral analyses of high-order methods with non-constant advection velocities*, Journal of Scientific Computing 87 (3) (2021) 1-38.
https://doi.org/10.1007/s10915-021-01484-1.

N. Tonicello, G. Lodato, L. Vervisch, *Analysis of high-order explicit LES dynamic modeling applied to airfoil flows*, Flow, Turbulence and Combustion (2021) 1–28.
https://doi.org/10.1007/s10494-021-00273-y.

G. Lodato, N. Tonicello, B. Pinto, *Large-eddy simulation of bypass transition on a zero-pressure-gradient flat plate using the spectral-element dynamic model*, Flow Turbul. Combust. (2021).
https://doi.org/10.1007/s10494-021-00262-1 .

Bibliography

[1] J.-B. Chapelier, G. Lodato, A spectral-element dynamic model for the large-eddy simulation of turbulent flows, Journal of Computational Physics 321 (2016) 279–302.

[2] R. Jacobs, P. Durbin, Simulations of bypass transition, Journal of Fluid Mechanics 428 (2001) 185–212.

[3] B. Pinto, G. Lodato, Synthetic freestream disturbance for the numerical reproduction of experimental zero-pressure-gradient bypass transition test cases, Flow, Turbulence and Combustion 103 (1) (2019) 25–54.

[4] V. M. Calo, Residual-based multiscale turbulence modeling: finite volume simulations of bypass transition, Ph.D. thesis, Stanford University USA (2004).

[5] D. J. Garmann, M. R. Visbal, P. D. Orkwis, Comparative study of implicit and subgrid-scale model large-eddy simulation techniques for low-reynolds number airfoil applications, International Journal for Numerical Methods in Fluids 71 (12) (2013) 1546–1565.

[6] D. J. Garmann, M. R. Visbal, C3. 3: Implicit large eddy-simulations of transitional flow over the sd7003 airfoil using compact finite-differencing and filtering, in: 2nd International workshop on high-order CFD methods, Cologne, Germany, 2013.

[7] P.-O. Persson, J. Peraire, Sub-cell shock capturing for discontinuous Galerkin methods, AIAA Paper 2006-112 (2006) 1–13, 44th AIAA Aerospace Sciences Meeting and Exhibit, Reno, NV, Jan. 9–12, 2006.

[8] P.-O. Persson, Shock capturing for high-order discontinuous Galerkin simulation of transient flow problems, AIAA Paper 2013-3061 (2013) 1–9, 21st AIAA Computational Fluid Dynamics Conference, San Diego, CA, Jun. 24–27, 2013.

[9] S. Hoyas, J. Jiménez, Scaling of the velocity fluctuations in turbulent channels up to re τ= 2003, Physics of fluids 18 (1) (2006) 011702.

[10] J. H. Bell, R. D. Mehta, Development of a two-stream mixing layer from tripped and untripped boundary layers, AIAA journal 28 (12) (1990) 2034–2042.

[11] X. Zhu, C. Yu, F. Tong, X. Li, Numerical study on wall temperature effects on shock wave/turbulent boundary-layer interaction, AIAA Journal 55 (1) (2017) 131–140.

[12] S. Priebe, M. P. Martín, Low-frequency unsteadiness in shock wave–turbulent boundary layer interaction, Journal of Fluid Mechanics 699 (2012) 1–49.

[13] M. Ringuette, P. Bookey, C. Wyckham, A. Smits, Experimental study of a mach 3 compression ramp interaction at re {theta}= 2400, AIAA journal 47 (2) (2009) 373–385.

[14] M. Wu, M. P. Martin, Direct numerical simulation of supersonic turbulent boundary layer over a compression ramp, AIAA journal 45 (4) (2007) 879–889.

[15] N. Tonicello, G. Lodato, L. Vervisch, A comparative study from spectral analyses of high-order methods with non-constant advection velocities, Journal of Scientific Computing 87 (3) (2021) 1–38.

[16] G. Lodato, N. Tonicello, B. Pinto, Large-eddy simulation of bypass transition on a zero-pressure-gradient flat plate using the spectral-element dynamic model, Flow Turbul. Combust. (2021). doi:10.1007/s10494-021-00262-1.

[17] N. Tonicello, G. Lodato, L. Vervisch, Analysis of high-order explicit les dynamic modeling applied to airfoil flows, Flow, Turbulence and Combustion (2021) 1–28.

[18] N. Tonicello, G. Lodato, L. Vervisch, Entropy preserving low dissipative shock capturing with wave characteristic based sensor for high-order methods, Computers & Fluids 197 (2020) 104357.

[19] L. F. Richardson, Weather prediction, Numerical Process (1922).

[20] A. N. Kolmogorov, The local structure of turbulence in incompressible viscous fluid for very large reynolds numbers, Cr Acad. Sci. URSS 30 (1941) 301–305.

[21] S. Ghosal, An analysis of numerical errors in large-eddy simulations of turbulence, Journal of Computational Physics 125 (1) (1996) 187–206.

[22] F. Ducros, P. Comte, M. Lesieur, Large-eddy simulation of a spatially growing boundary layer over an adiabatic flat plate at low mach number, International journal of heat and fluid flow 16 (5) (1995) 341–348.

[23] M. Lesieur, O. Métais, P. Comte, Large-eddy simulations of turbulence, Cambridge university press, 2005.

[24] B. Vreman, B. Geurts, H. Kuerten, A priori tests of large eddy simulation of the compressible plane mixing layer, Journal of engineering mathematics 29 (4) (1995) 299–327.

[25] A. Yoshizawa, Statistical theory for compressible turbulent shear flows, with the application to subgrid modeling, Phys. Fluids 29 (7) (1986) 2152–2164.

[26] P. Moin, K. Squires, W. Cabot, S. Lee, A dynamic subgrid-scale model for compressible turbulence and scalar transport, Phys. Fluids 11 (3) (1991) 2746–2757.

[27] L. F. Richardson, Weather prediction by numerical process, Cambridge university press, 1922.

[28] T. M. Eidson, Numerical simulation of the turbulent rayleigh–bénard problem using subgrid modelling, Journal of Fluid Mechanics 158 (1985) 245–268.

[29] G. Erlebacher, M. Y. Hussaini, C. G. Speziale, T. A. Zang, Toward the large-eddy simulation of compressible turbulent flows, Journal of fluid mechanics 238 (1992) 155–185.

[30] U. Piomelli, P. Moin, J. H. Ferziger, Model consistency in large eddy simulation of turbulent channel flows, The Physics of fluids 31 (7) (1988) 1884–1891.

[31] C. Meneveau, Statistics of turbulence subgrid-scale stresses: Necessary conditions and experimental tests, Physics of Fluids 6 (2) (1994) 815–833.

[32] W. C. Reynolds, The potential and limitations of direct and large eddy simulations, in: Whither turbulence? Turbulence at the crossroads, Springer, 1990, pp. 313–343.

[33] S. Liu, C. Meneveau, J. Katz, On the properties of similarity subgrid-scale models as deduced from measurements in a turbulent jet, Journal of Fluid Mechanics 275 (1994) 83–119.

[34] R. C. J. Ferziger, W. Reynolds, Evaluation of subgrid-scale models using an accurately simulated turbulent ow, J. Fluid Mech 91 (1979) 1–16.

[35] J. Bardina, J. Ferziger, W. Reynolds, Improved subgrid-scale models for large-eddy simulation, in: 13th fluid and plasmadynamics conference, 1980, p. 1357.

[36] O. V. Vasilyev, T. S. Lund, P. Moin, A general class of commutative filters for les in complex geometries, Journal of computational physics 146 (1) (1998) 82–104.

[37] T. Lund, On the use of discrete filters for large eddy simulation, Annual Research Briefs (1997) 83–95.

[38] J. Smagorinsky, General circulation experiments with the primitive equations: I. the basic experiment, Monthly weather review 91 (3) (1963) 99–164.

[39] F. Nicoud, F. Ducros, Subgrid-scale stress modelling based on the square of the velocity gradient tensor, Flow, Turbulence and Combustion 62 (3) (1999) 183–200.

[40] F. Ducros, F. Nicoud, T. Poinsot, Wall-adapting local eddy-viscosity models for simulations in complex geometries (1998).

[41] F. Nicoud, H. B. Toda, O. Cabrit, S. Bose, J. Lee, Using singular values to build a subgrid-scale model for large eddy simulations, Physics of Fluids 23 (8) (2011) 085106.

[42] J. Slotnick, A. Khodadoust, J. Alonso, D. Darmofal, W. Gropp, E. Lurie, D. Mavriplis, CFD vision 2030 study: A path to revolutionary computational aerosciences, Tech. rep., NASA Langley Research Center, Hampton, Virginia 23681-2199, NASA Contractor Report 218178 (Mar. 2014).

[43] P. E. Vincent, A. Jameson, Facilitating the adoption of unstructured high-order methods amongst a wider community of fluid dynamicists, Mathematical Modelling of Natural Phenomena 6 (3) (2011) 97–140.

[44] D. A. Kopriva, J. H. Kolias, A conservative staggered-grid chebyshev multidomain method for compressible flows, Journal of computational physics 125 (1) (1996) 244–261.

[45] Y. Liu, M. Vinokur, Z. Wang, Spectral difference method for unstructured grids I: basic formulation, J. Comput. Phys. 216 (2) (2006) 780–801.

[46] Z. Wang, Y. Liu, G. May, A. Jameson, Spectral difference method for unstructured grids II: Extension to the Euler equations, J. Sci. Comput. 32 (1) (2007) 45–71.

[47] A. Jameson, P. Vincent, P. Castonguay, On the non-linear stability of flux reconstruction schemes, J. Sci. Comput. 50 (2) (2012) 434–445.

[48] A. Jameson, A proof of the stability of the spectral difference method for all orders of accuracy, J. Sci. Comput. 45 (1) (2010) 348–358.

[49] J.-B. Chapelier, G. Lodato, Optimal high-order Spectral Difference schemes for the computation of aeroacoustics and turbulence, AIAA Paper 2017-1228 (2017) 1–17, 55th AIAA Aerospace Sciences Meeting, Grapevine, TX, Jan. 9–13, 2017. doi:10.2514/6.2017-1228.

[50] E. F. Toro, Riemann solvers and numerical methods for fluid dynamics: a practical introduction, Springer Science & Business Media, 2013.

[51] B. Cockburn, C.-W. Shu, The local discontinuous galerkin method for time-dependent convection-diffusion systems, SIAM Journal on Numerical Analysis 35 (6) (1998) 2440–2463.

[52] J. S. Hesthaven, T. Warburton, Nodal Discontinuous Galerkin Methods: Algorithms, Analysis, and Applications, Springer Science+Business Media, LLC, 2008.

[53] F. Bassi, S. Rebay, A high-order accurate discontinuous finite element method for the numerical solution of the compressible navier–stokes equations, Journal of computational physics 131 (2) (1997) 267–279.

[54] J. Manzanero, E. Ferrer, G. Rubio, E. Valero, On the role of numerical dissipation in stabilising under-resolved turbulent simulations using discontinuous Galerkin methods (2018).

[55] T. Colonius, S. K. Lele, P. Moin, Boundary conditions for direct computation of aerodynamic sound generation, AIAA journal 31 (9) (1993) 1574–1582.

[56] C. S. Yoo, H. G. Im, Characteristic boundary conditions for simulations of compressible reacting flows with multi-dimensional, viscous and reaction effects, Combustion Theory and Modelling 11 (2) (2007) 259–286.

[57] M. Baum, T. Poinsot, D. Thevenin, Accurate boundary conditions for multicomponent reactive flows, Journal of computational physics 116 (2) (1995) 247–261.

[58] G. Lodato, H. Pitsch, Characteristic boundary conditions with transverse effects: a comparative study, in: APS Division of Fluid Dynamics Meeting Abstracts, Vol. 63, 2010, pp. CD–003.

[59] S. Godunov, A. Zabrodin, G. Prokopov, A computational scheme for two-dimensional non stationary problems of gas dynamics and calculation of the flow from a shock wave approaching a stationary state, USSR Computational Mathematics and Mathematical Physics 1 (4) (1962) 1187–1219.

[60] Y. Sun, Z. J. Wang, Y. Liu, High-order multidomain spectral difference method for the navier-stokes equations, in: 44th AIAA Aerospace Sciences Meeting and Exhibit, 2006, p. 301.

[61] G. Mengaldo, D. De Grazia, F. Witherden, A. Farrington, P. Vincent, S. Sherwin, J. Peiro, A guide to the implementation of boundary conditions in compact high-order methods for compressible aerodynamics, in: 7th AIAA Theoretical Fluid Mechanics Conference, 2014, p. 2923.

[62] P. Fernandez, N.-C. Nguyen, J. Peraire, On the ability of discontinuous Galerkin methods to simulate under-resolved turbulent flows, arXiv preprint arXiv:1810.09435 (2018).

[63] P. Fernandez, N. Nguyen, J. Peraire, The hybridized discontinuous Galerkin method for implicit large-eddy simulation of transitional turbulent flows, Journal of Computational Physics 336 (2017) 308 – 329. doi:10.1016/j.jcp.2017.02.015.

[64] P. Fernandez, N.-C. Nguyen, J. Peraire, Entropy-stable hybridized discontinuous Galerkin methods for the compressible Euler and Navier-Stokes equations, arXiv preprint arXiv:1808.05066 (2018).

[65] A. D. Beck, T. Bolemann, D. Flad, H. Frank, G. J. Gassner, F. Hindenlang, C.-D. Munz, High-order discontinuous Galerkin spectral element methods for transitional and turbulent flow simulations, International Journal for Numerical Methods in Fluids 76 (8) (2014) 522–548. doi:10.1002/fld.3943.

[66] D. Flad, G. Gassner, On the use of kinetic energy preserving dg-schemes for large eddy simulation, Journal of Computational Physics 350 (2017) 782 – 795. doi:10.1016/j.jcp.2017.09.004.

[67] G. Karniadakis, S. Sherwin, Spectral/hp element methods for computational fluid dynamics, Oxford University Press, 2013.

[68] S. K. Lele, Compact finite difference schemes with spectral-like resolution, Journal of computational physics 103 (1) (1992) 16–42.

[69] C. Bogey, C. Bailly, A family of low dispersive and low dissipative explicit schemes for flow and noise computations, Journal of Computational physics 194 (1) (2004) 194–214.

[70] K. Van den Abeele, C. Lacor, Z. J. Wang, On the stability and accuracy of the spectral difference method, Journal of Scientific Computing 37 (2) (2008) 162–188.

[71] P. E. Vincent, P. Castonguay, A. Jameson, Insights from von neumann analysis of high-order flux reconstruction schemes, Journal of Computational Physics 230 (22) (2011) 8134–8154.

[72] R. C. Moura, S. J. Sherwin, J. Peiró, Linear dispersion–diffusion analysis and its application to under-resolved turbulence simulations using discontinuous Galerkin spectral/hp methods, Journal of Computational Physics 298 (2015) 695–710.

[73] J. Vanharen, G. Puigt, X. Vasseur, J.-F. Boussuge, P. Sagaut, Revisiting the spectral analysis for high-order spectral discontinuous methods, Journal of Computational Physics 337 (2017) 379–402.

[74] J. S. Hesthaven, T. Warburton, Nodal discontinuous Galerkin methods: algorithms, analysis, and applications, Springer Science & Business Media, 2007.

[75] B. Cockburn, C. Shu, The local discontinuous Galerkin finite element method for convection-diffusion systems, SIAM J. Numer. Anal. 35 (1998) 2440–2463.

[76] B. Cockburn, C. Shu, The Runge-Kutta discontinuous Galerkin finite element method for conservation laws V: Multidimensional systems, J. Comput. Phys. 141 (1998) 199–224.

[77] H. T. Huynh, A flux reconstruction approach to high-order schemes including discontinuous Galerkin methods, in: 18th AIAA Computational Fluid Dynamics Conference, 2007, p. 4079.

[78] P. Vincent, P. Castonguay, A. Jameson, A new class of high-order energy stable flux reconstruction schemes, J. Sci. Comput. 47 (1) (2010) 1–23.

[79] F. Q. Hu, H. L. Atkins, Eigensolution analysis of the discontinuous Galerkin method with nonuniform grids: I. one space dimension, Journal of Computational Physics 182 (2) (2002) 516–545.

[80] G. Mengaldo, R. Moura, B. Giralda, J. Peiró, S. Sherwin, Spatial eigensolution analysis of discontinuous Galerkin schemes with practical insights for under-resolved computations and implicit LES, Computers & Fluids 169 (2018) 349–364.

[81] G. Mengaldo, D. De Grazia, R. C. Moura, S. J. Sherwin, Spatial eigensolution analysis of energy-stable flux reconstruction schemes and influence of the numerical flux on accuracy and robustness, Journal of Computational Physics 358 (2018) 1–20.

[82] R. Moura, M. Aman, J. Peiró, S. Sherwin, Spatial eigenanalysis of spectral/hp continuous Galerkin schemes and their stabilisation via dg-mimicking spectral vanishing viscosity: Application to high reynolds number flows, Journal of Computational Physics (2019) 109112.

[83] P. J. Schmid, Nonmodal stability theory, Annu. Rev. Fluid Mech. 39 (2007) 129–162.

[84] L. N. Trefethen, A. E. Trefethen, S. C. Reddy, T. A. Driscoll, Hydrodynamic stability without eigenvalues, Science 261 (5121) (1993) 578–584.

[85] L. N. Trefethen, Pseudospectra of linear operators, SIAM review 39 (3) (1997) 383–406.

[86] J. Manzanero, G. Rubio, E. Ferrer, E. Valero, Dispersion-dissipation analysis for advection problems with nonconstant coefficients: Applications to discontinuous Galerkin formulations, SIAM Journal on Scientific Computing 40 (2) (2018) A747–A768.

[87] J. Manzanero, G. Rubio, E. Ferrer, E. Valero, D. A. Kopriva, Insights on aliasing driven instabilities for advection equations with application to gauss-lobatto discontinuous Galerkin methods (2017).

[88] P. Fernandez, R. C. Moura, G. Mengaldo, J. Peraire, Non-modal analysis of spectral element methods: Towards accurate and robust large-eddy simulations, Computer Methods in Applied Mechanics and Engineering 346 (2019) 43–62. doi:10.1016/j.cma.2018.11.027.

[89] P. E. Vincent, P. Castonguay, A. Jameson, A new class of high-order energy stable flux reconstruction schemes, Journal of Scientific Computing 47 (1) (2011) 50–72.

[90] K. Asthana, A. Jameson, High-order flux reconstruction schemes with minimal dispersion and dissipation, Journal of Scientific Computing 62 (3) (2015) 913–944.

[91] C. Liang, S. Premasuthan, A. Jameson, High-order accurate simulation of low-mach laminar flow past two side-by-side cylinders using spectral difference method, Computers & structures 87 (11-12) (2009) 812–827.

[92] C. Liang, A. Jameson, Z. J. Wang, Spectral difference method for compressible flow on unstructured grids with mixed elements, Journal of Computational Physics 228 (8) (2009) 2847–2858.

[93] G. I. Taylor, A. E. Green, Mechanism of the production of small eddies from large ones, Proc. R. Soc. Lond. A 158 (895) (1937) 499–521.

[94] J.-B. Chapelier, G. Lodato, A. Jameson, A study on the numerical dissipation of the spectral difference method for freely decaying and wall-bounded turbulence, Comput. Fluids 139 (2016) 261–280. doi:10.1016/j.compfluid.2016.03.006.

[95] R. C. Moura, G. Mengaldo, J. Peiró, S. J. Sherwin, On the eddy-resolving capability of high-order discontinuous Galerkin approaches to implicit LES/under-resolved DNS of Euler turbulence, Journal of Computational Physics 330 (2017) 615–623.

[96] C. Cantwell, D. Moxey, A. Comerford, A. Bolis, G. Rocco, G. Mengaldo, D. D. Grazia, S. Yakovlev, J.-E. Lombard, D. Ekelschot, B. Jordi, H. Xu, Y. Mohamied, C. Eskilsson, B. Nelson, P. Vos, C. Biotto, R. Kirby, S. Sherwin, Nektar++: An open-source spectral/hp element framework, Computer Physics Communications 192 (2015) 205 – 219. doi:10.1016/j.cpc.2015.02.008.

[97] F. F. Grinstein, L. G. Margolin, W. J. Rider, Implicit large eddy simulation, Vol. 10, Cambridge university press Cambridge, 2007.

[98] E. Garnier, M. Mossi, P. Sagaut, P. Comte, M. Deville, On the use of shock-capturing schemes for large-eddy simulation, Journal of computational Physics 153 (2) (1999) 273–311.

[99] A. Kravchenko, P. Moin, On the effect of numerical errors in large eddy simulations of turbulent flows, Journal of computational physics 131 (2) (1997) 310–322.

[100] B. Vreman, B. Geurts, H. Kuerten, Discretization error dominance over subgrid terms in large eddy simulation of compressible shear layers in 2D, Communications in numerical methods in engineering 10 (10) (1994) 785–790.

[101] J.-B. Chapelier, G. Lodato, A. Jameson, A study on the numerical dissipation of the spectral difference method for freely decaying and wall-bounded turbulence, Comput. Fluids 139 (2016) 261–280. doi:10.1016/j.compfluid.2016.03.006.

[102] J.-B. Chapelier, G. Lodato, Study of the Spectral Difference numerical dissipation for turbulent flows using unstructured grids, Flow Turbul. Combust. 99 (3) (2017) 643–664. doi:10.1007/s10494-017-9847-5.

[103] G. Lodato, J.-B. Chapelier, Evaluation of the Spectral Element Dynamic Model for large-eddy simulation on unstructured, deformed meshes, Flow Turbul. Combust. 101 (2) (2018) 271–294. doi:10.1007/s10494-018-9935-1.

[104] G. B. Schubauer, H. K. Skramstad, Laminar-boundary-layer oscillations and transition on a flat plate, Tech. rep., NATIONAL AERONAUTICS AND SPACE ADMINISTRATION WASHINGTON DC (1948).

[105] M. V. Morkovin, Bypass transition to turbulence and research desiderata, Transition in Turbines 2386 (1985) 161–204.

[106] P. R. Voke, Z. Yang, Numerical study of bypass transition, Physics of Fluids 7 (9) (1995) 2256–2264.

[107] X. Huai, R. D. Joslin, U. Piomelli, Large-eddy simulation of transition to turbulence in boundary layers, Theoretical and computational fluid dynamics 9 (2) (1997) 149–163.

[108] F. Ducros, P. Comte, M. Lesieur, Large-eddy simulation of transition to turbulence in a boundary layer developing spatially over a flat plate, Journal of Fluid Mechanics 326 (1996) 1–36.

[109] O. Métais, M. Lesieur, Spectral large-eddy simulation of isotropic and stably stratified turbulence, Journal of Fluid Mechanics 239 (1992) 157–194.

[110] T. Sayadi, P. Moin, Large eddy simulation of controlled transition to turbulence, Physics of Fluids 24 (11) (2012) 114103.

[111] S. Lardeau, M. Leschziner, T. Zaki, Large eddy simulation of transitional separated flow over a flat plate and a compressor blade, Flow, turbulence and combustion 88 (1-2) (2012) 19–44.

[112] P. Jonáš, O. Mazur, V. Uruba, On the receptivity of the by-pass transition to the length scale of the outer stream turbulence, European Journal of Mechanics-B/Fluids 19 (5) (2000) 707–722.

[113] M. Matsubara, P. H. Alfredsson, Disturbance growth in boundary layers subjected to free-stream turbulence, Journal of fluid mechanics 430 (2001) 149–168.

[114] J. H. Fransson, M. Matsubara, P. H. Alfredsson, Transition induced by free-stream turbulence, Journal of Fluid Mechanics 527 (2005) 1–25.

[115] S. Nagarajan, S. Lele, J. Ferziger, Leading-edge effects in bypass transition, Journal of Fluid Mechanics 572 (2007) 471–504.

[116] V. Ovchinnikov, M. M. Choudhari, U. Piomelli, Numerical simulations of boundary-layer bypass transition due to high-amplitude free-stream turbulence, Journal of Fluid Mechanics 613 (2008) 135–169.

[117] Y. Liu, M. Vinokur, Z. Wang, Spectral difference method for unstructured grids i: basic formulation, Journal of Computational Physics 216 (2) (2006) 780–801.

[118] J.-B. Chapelier, G. Lodato, A. Jameson, A study on the numerical dissipation of the spectral difference method for freely decaying and wall-bounded turbulence, Computers & Fluids 139 (2016) 261–280.

[119] M. Klein, A. Sadiki, J. Janicka, A digital filter based generation of inflow data for spatially developing direct numerical or large eddy simulations, Journal of computational Physics 186 (2) (2003) 652–665.

[120] C. D. Tomkins, R. J. Adrian, Spanwise structure and scale growth in turbulent boundary layers, Journal of Fluid Mechanics 490 (2003) 37–74.

[121] T. S. Lund, X. Wu, K. D. Squires, Generation of turbulent inflow data for spatially-developing boundary layer simulations, Journal of computational physics 140 (2) (1998) 233–258.

[122] D. R. Chapman, G. D. Kuhn, The limiting behaviour of turbulence near a wall, Journal of Fluid Mechanics 170 (1986) 265–292.

[123] M. Galbraith, M. Visbal, Implicit large eddy simulation of low reynolds number flow past the sd7003 airfoil, in: 46th AIAA Aerospace Sciences Meeting and Exhibit, 2008, p. 225.

[124] L. Nguyen, V. V. Golubev, M. R. Visbal, Numerical study of transitional SD7003 airfoil interacting with canonical upstream flow disturbances, AIAA Journal (2018) 158–181.

[125] D. Olson, A. Katz, A. Naguib, M. Koochesfahani, D. Rizzetta, M. Visbal, An investigation of the effect of freestream turbulence on the laminar separation bubble on an SD7003 airfoil, in: 49th AIAA Aerospace Sciences Meeting including the New Horizons Forum and Aerospace Exposition, 2011, p. 395.

[126] S. L. Herbst, C. J. Kähler, R. Hain, Influence of large-scale free-stream turbulence on an SD7003 airfoil at low reynolds numbers., in: 2018 Applied Aerodynamics Conference, 2018, p. 3490.

[127] Y. Zhou, Z. J. Wang, Implicit large eddy simulation of low Reynolds number transitional flow over a wing using high-order spectral difference method, in: 40th fluid dynamics conference and exhibit, 2010, p. 4442.

[128] A. Uranga, P.-O. Persson, M. Drela, J. Peraire, Implicit large eddy simulation of transitional flows over airfoils and wings, in: 19th AIAA Computational Fluid Dynamics, 2009, p. 4131.

[129] P. Castonguay, C. Liang, A. Jameson, Simulation of transitional flow over airfoils using the spectral difference method, in: 40th Fluid Dynamics Conference and Exhibit, 2010, p. 4626.

[130] V. Skarolek, K. Miyaji, Transitional flow over a SD7003 wing using flux reconstruction scheme, in: 52nd Aerospace Sciences Meeting, 2014, p. 0250.

[131] B. C. Vermeire, S. Nadarajah, P. G. Tucker, Implicit large eddy simulation using the high-order correction procedure via reconstruction scheme, International Journal for Numerical Methods in Fluids 82 (5) (2016) 231–260.

[132] R. Radespiel, J. Windte, U. Scholz, Numerical and experimental flow analysis of moving airfoils with laminar separation bubbles, AIAA journal 45 (6) (2007) 1346–1356.

[133] Y. Lian, W. Shyy, Laminar-turbulent transition of a low Reynolds number rigid or flexible airfoil, AIAA journal 45 (7) (2007) 1501–1513.

[134] J. N. Counsil, K. Goni Boulama, Low-Reynolds-number aerodynamic performances of the NACA 0012 and Selig-Donovan 7003 airfoils, Journal of aircraft 50 (1) (2013) 204–216.

[135] B. Shome, M. Radle, Assessment of transitional model for prediction of aerodynamic performance of airfoils at low Reynolds number flow regime, Tech. rep., SAE Technical Paper (2013).

[136] G. Lodato, J.-B. Chapelier, Evaluation of the spectral element dynamic model for large-eddy simulation on unstructured, deformed meshes, Flow, Turbulence and Combustion 101 (2018) 271–294.

[137] A. D. Beck, T. Bolemann, D. Flad, H. Frank, G. J. Gassner, F. Hindenlang, C.-D. Munz, High-order discontinuous Galerkin spectral element methods for transitional and turbulent flow simulations, International Journal for Numerical Methods in Fluids 76 (8) (2014) 522–548.

[138] P. Catalano, R. Tognaccini, Large eddy simulations of the flow around the sd7003 airfoil, in: AIMETA Conference, 2011, pp. 1–10.

[139] P. Boom, D. Zingg, Time-accurate flow simulations using an efficient newton-krylov-schur approach with high-order temporal and spatial discretization, in: 51st AIAA Aerospace Sciences Meeting including the New Horizons Forum and Aerospace Exposition, 2013, p. 383.

[140] M. S. Selig, Summary of low-speed airfoil data (1995).

[141] G. I. Taylor, The spectrum of turbulence, Proceedings of the Royal Society of London. Series A-Mathematical and Physical Sciences 164 (919) (1938) 476–490.

[142] T. J. Hughes, L. Mazzei, A. A. Oberai, A. A. Wray, The multiscale formulation of large eddy simulation: Decay of homogeneous isotropic turbulence, Physics of fluids 13 (2) (2001) 505–512.

[143] M. Inagaki, T. Kondoh, Y. Nagano, A mixed-time-scale sgs model with fixed model-parameters for practical les, Journal of fluids engineering 127 (1) (2005) 1–13.

[144] P. Clavin, G. Searby, Combustion Waves and Fronts in Flows, Cambridge University Press, Cambridge, 2016.

[145] X. Zhang, C.-W. Shu, On maximum-principle-satisfying high order schemes for scalar conservation laws, Journal of Computational Physics 229 (9) (2010) 3091–3120.

[146] R. Lamouroux, J. Gressier, G. Grondin, A high-order compact limiter based on spatially weighted projections for the spectral volume and the spectral differences method, Journal of Scientific Computing 67 (1) (2016) 375–403.

[147] L. Krivodonova, Limiters for high-order discontinuous Galerkin methods, Journal of Computational Physics 226 (1) (2007) 879–896.

[148] A. Burbeau, P. Sagaut, C.-H. Bruneau, A problem-independent limiter for high-order Runge–Kutta discontinuous Galerkin methods, Journal of Computational Physics 169 (1) (2001) 111–150.

[149] J. Qiu, C.-W. Shu, Runge–Kutta discontinuous Galerkin method using WENO limiters, SIAM Journal on Scientific Computing 26 (3) (2005) 907–929.

[150] J. Qiu, C.-W. Shu, Hermite WENO schemes and their application as limiters for Runge–Kutta discontinuous Galerkin method II: Two dimensional case, Computers & Fluids 34 (6) (2005) 642–663.

[151] H. Luo, J. D. Baum, R. Löhner, A Hermite WENO-based limiter for discontinuous Galerkin method on unstructured grids, Journal of Computational Physics 225 (1) (2007) 686–713.

[152] J. Zhu, J. Qiu, C.-W. Shu, M. Dumbser, Runge–Kutta discontinuous Galerkin method using WENO limiters II: unstructured meshes, Journal of Computational Physics 227 (9) (2008) 4330–4353.

[153] C. Liang, F. Ham, E. Johnsen, Discontinuous Galerkin method with WENO limiter for flows with discontinuity, in: Annual Research Briefs, Center for Turbulence Research, Stanford University, 2009, pp. 335–343.

[154] J. VonNeumann, R. D. Richtmyer, A method for the numerical calculation of hydrodynamic shocks, Journal of Applied Physics 21 (1950) 232 – 237. doi:10.1063/1.1699639.

[155] A. W. Cook, W. H. Cabot, A high-wavenumber viscosity for high-resolution numerical methods, Journal of Computational Physics 195 (2) (2004) 594–601.

[156] A. Klöckner, T. Warburton, J. S. Hesthaven, Viscous shock capturing in a time-explicit discontinuous Galerkin method, Mathematical Modelling of Natural Phenomena 6 (3) (2011) 57–83.

[157] X. Zhang, C.-W. Shu, Positivity-preserving high order discontinuous Galerkin schemes for compressible Euler equations with source terms, J. Comput. Physics 230 (2011) 1238–1248.

[158] F. Ducros, V. Ferrand, F. Nicoud, C. Weber, D. Darracq, C. Gacherieu, T. Poinsot, Large-eddy simulation of the shock/turbulence interaction, Journal of Computational Physics 152 (2) (1999) 517–549.

[159] G. Lodato, Characteristic modal shock detection for discontinuous finite element methods, Computers & Fluids 179 (2019) 309–333.

[160] W. Kollmann, Fluid Mechanics in Spatial and Material Description, University Readers, San-Diego, USA, 2011.

[161] D. Kopriva, J. Kolias, A conservative staggered-grid Chebyshev multidomain method for compressible flows, J. Comput. Phys. 125 (1) (1996) 244–261.

[162] Y. Sun, Z. Wang, Y. Liu, High-order multidomain spectral difference method for the Navier-Stokes equations on unstructured hexahedral grids, Commun. Comput. Phys. 2 (2) (2007) 310–333.

[163] A. Jameson, G. Lodato, A note on the numerical dissipation from high-order discontinuous finite element schemes, Comput. Fluids 98 (2014) 186–195, 12th USNCCM mini-symposium of High-Order Methods for Computational Fluid Dynamics – A special issue dedicated to the 80th birthday of Professor Antony Jameson. doi:10.1016/j.compfluid.2014.01.016.

[164] G. Lodato, L. Vervisch, P. Clavin, Direct numerical simulation of shock wavy-wall interaction: analysis of cellular shock structures and flow patterns, Journal of Fluid Mechanics 789 (2016) 221–258. doi:10.1017/jfm.2015.731.

[165] D. Moro, N. C. Nguyen, J. Peraire, Dilation-based shock capturing for high-order methods, International Journal for Numerical Methods in Fluids 82 (7) (2016) 398–416.

[166] M. Yu, F. X. Giraldo, M. Peng, Z. J. Wang, Localized artificial viscosity stabilization of discontinuous Galerkin methods for nonhydrostatic mesoscale atmospheric modeling, Monthly Weather Review 143 (12) (2015) 4823–4845.

[167] B. Denet, L. Biamino, G. Lodato, L. Vervisch, P. Clavin, Model equation for the dynamics of wrinkled shock waves. comparison with DNS and experiments, Combustion Science and Technology 187 (2015) 296–323. doi:10.1080/00102202.2014.973494.

[168] G. Lodato, L. Vervisch, P. Clavin, Numerical study of smoothly perturbed shocks in the Newtonian limit, Flow, Turbulence and Combustion 99 (3) (2017) 887–908. doi:10.1007/s10494-017-9830-1.

[169] P. Fernandez, N. Nguyen, J. Peraire, A physics-based shock capturing method for unsteady laminar and turbulent flows, AIAA Paper 2018-0062 (2018) 1–13, 2018 AIAA Aerospace Sciences Meeting Kissimmee, Florida.

[170] P. Fernandez, N.-C. Nguyen, J. Peraire, A physics-based shock capturing method for large-eddy simulation, arXiv preprint arXiv:1806.06449 (2018).

[171] A. Mani, J. Larsson, P. Moin, Suitability of artificial bulk viscosity for large-eddy simulation of turbulent flows with shocks, Journal of Computational Physics 228 (19) (2009) 7368–7374.

[172] S. Kawai, S. K. Shankar, S. K. Lele, Assessment of localized artificial diffusivity scheme for large-eddy simulation of compressible turbulent flows, Journal of Computational Physics 229 (5) (2010) 1739–1762.

[173] M. Morduchow, P. Libby, On a complete solution of the one-dimensional flow equations of a viscous, heat-conducting, compressible gas, Journal of the Aeronautical Sciences 16 (11) (1949) 674–684.

[174] J. Smoller, Shock waves and reaction—diffusion equations, Vol. 258, Springer Science & Business Media, 2012.

[175] M. D. Salas, A. Iollo, Entropy jump across an inviscid shock wave, Theoretical and computational fluid dynamics 8 (5) (1996) 365–375.

[176] J.-F. Colombeau, Multiplication of distributions, Bulletin of the american mathematical society 23 (2) (1990) 251–268.

[177] J. Colombeau, A. Le Roux, Multiplications of distributions in elasticity and hydrodynamics, Journal of Mathematical Physics 29 (2) (1988) 315–319.

[178] H. Hugoniot, Sur la propagation du mouvement dans les corps et spécialement dans les gaz parfaits, Journal de l'école polytechnique 58 (1889).

[179] J. L. Ellzey, M. R. Henneke, J. M. Picone, E. S. Oran, The interaction of a shock with a vortex: shock distortion and the production of acoustic waves, Physics of Fluids 7 (1) (1995) 172–184.

[180] L. Guichard, L. Vervisch, P. Domingo, Two-dimensional weak-shock vortex interaction in a mixing zone, AIAA Journal 33 (10) (1995) 2539–2544.

[181] A. Rault, G. Chiavassa, R. Donat, Shock-vortex interactions at high mach numbers, Journal of Scientific Computing 19 (1-3) (2003) 347–371.

[182] G. Lodato, P. Domingo, L. Vervisch, Three-dimensional boundary conditions for direct and large-eddy simulation of compressible viscous flows, Journal of Computational Physics 227 (10) (2008) 5105–5143.

[183] G. Lodato, F. Ham, H. Pitsch, Optimal inclusion of transverse effects in the nonreflecting outflow boundary condition, AIAA journal 50 (6) (2012) 1291–1306.

[184] E. Johnsen, J. Larsson, A. V. Bhagatwala, W. H. Cabot, P. Moin, B. J. Olson, P. S. Rawat, S. K. Shankar, B. Sjögreen, H. C. Yee, et al., Assessment of high-resolution methods for numerical simulations of compressible turbulence with shock waves, Journal of Computational Physics 229 (4) (2010) 1213–1237.

[185] D. Kotov, H. C. Yee, A. A. Wray, B. Sjögreen, A. G. Kritsuk, Numerical dissipation control in high order shock-capturing schemes for LES of low speed flows, Journal of Computational Physics 307 (2016) 189–202.

[186] K. Hillewaert, J. Cagnone, S. Murman, A. Garai, Y. Lv, M. Ihme, Assessment of high-order DG methods for LES of compressible flows, in: Proceedings of the Summer Program, Center for Turbulence Research. Stanford University, 2016, pp. 363–72.

[187] B. Denet, L. Biamino, G. Lodato, L. Vervisch, P. Clavin, Model equation for the dynamics of wrinkled shockwaves: comparison with dns and experiments, Combustion Science and Technology 187 (1-2) (2015) 296–323.

[188] G. Lodato, L. Vervisch, P. Clavin, Direct numerical simulation of shock wavy-wall interaction: analysis of cellular shock structures and flow patterns, Journal of Fluid Mechanics 789 (2016) 221–258.

[189] Y. Stiriba, R. Donat, A numerical study of postshock oscillations in slowly moving shock waves, Computers & Mathematics with Applications 46 (5-6) (2003) 719–739.

[190] M.-S. Liou, Unresolved problems by shock capturing: Taming the overheating problem, NASA Report E-18552, ICCFD7-2012-2203, NASA Glenn Research Center, 7th International Conference on Computational Fluid Dynamics (ICCFD7), Big Island, HI, Jul. 9–13, 2012 (2012).

[191] M.-S. Liou, Open problems in numerical fluxes: proposed resolutions, AIAA paper 3055 (2011) 2011.

[192] W. J. Rider, Revisiting wall heating, Journal of Computational Physics 162 (2) (2000) 395–410.

[193] M.-S. Liou, Why is the overheating problem difficult: The role of entropy, in: 21st AIAA Computational Fluid Dynamics Conference, 2013, p. 2697.

[194] R. Donat, A. Marquina, Capturing shock reflections: an improved ux formula, J. Comput. Phys 125 (1) (1996) 42.

[195] O. Zeman, Dilatation dissipation: The concept and application in modeling compressible mixing layers, Phys. Fluids A 2 (2) (1990).

[196] D. A. Kopriva, E. Jimenez, An assessment of the efficiency of nodal discontinuous galerkin spectral element methods, in: Recent Developments in the Numerics of Nonlinear Hyperbolic Conservation Laws, Springer, 2013, pp. 223–235.

[197] S. Pirozzoli, Numerical methods for high-speed flows, Annual Review of Fluid Mechanics 43 (1) (2011) 163–194. doi:10.1146/annurev-fluid-122109-160718.

[198] W. W. Liou, G. Huang, T.-H. Shih, Turbulence model assessment for shock wave/turbulent boundary-layer interaction in transonic and supersonic flows, Computers & fluids 29 (3) (2000) 275–299.

[199] K. Sinha, K. Mahesh, G. V. Candler, Modeling the effect of shock unsteadiness in shock/turbulent boundary-layer interactions, AIAA journal 43 (3) (2005) 586–594.

[200] T. Coakley, P. Huang, Turbulence modeling for high speed flows, in: 30th Aerospace Sciences Meeting and Exhibit, 1992, p. 436.

[201] D. D. Knight, G. Degrez, Shock wave boundary layer interactions in high Mach number flows a critical survey of current numerical prediction capabilities, AGARD ADVISORY REPORT AGARD AR 2 (1998) 1–1.

[202] J. Li, N. Grube, S. Priebe, P. Martin, LES study of shock wave and turbulent boundary layer interaction, in: 51st AIAA Aerospace Sciences Meeting including the New Horizons Forum and Aerospace Exposition, 2013, p. 984.

[203] C. M. Helm, M. P. Martin, New LES of a hypersonic shock/turbulent boundary layer interaction, in: 54th AIAA Aerospace Sciences Meeting, 2016, p. 0346.

[204] J. Li, N. E. Grube, S. Priebe, P. Martin, Analysis of the large eddy simulation of a shock wave and turbulent boundary layer interaction, in: 43rd AIAA Fluid Dynamics Conference, 2013, p. 2734.

[205] S. Priebe, J. H. Tu, C. W. Rowley, M. P. Martín, Low-frequency dynamics in a shock-induced separated flow, Journal of Fluid Mechanics 807 (2016) 441–477.

[206] M. R. Rahman, M. I. Labib, A. T. Hasan, M. Ali, Y. Mitsutake, T. Setoguchi, Effect of cavity on shock oscillation in transonic flow over RAE2822 supercritical airfoil, in: AIP conference proceedings, Vol. 1754, AIP Publishing LLC, 2016, p. 040025.

[207] B. Lee, Self-sustained shock oscillations on airfoils at transonic speeds, Progress in Aerospace Sciences 37 (2) (2001) 147–196.

[208] P. Cook, M. McDonald, M. Firmin, Aerofoil rae 2822: Pressure distribution and boundary layer and wake measurements. agard ar 138, Research and Technology Organisation, Neuilly-sur-Seine (1979).

[209] D. J. Mavriplis, L. Martinelli, Multigrid solution of compressible turbulent flow on unstructured meshes using a two-equation model, International Journal for Numerical Methods in Fluids 18 (10) (1994) 887–914. doi:10.1002/fld.1650181002.

[210] A. Antoniadis, P. Tsoutsanis, D. Drikakis, Assessment of high-order finite volume methods on unstructured meshes for RANS solutions of aeronautical configurations, Computers and Fluids 146 (2017) 86–104. doi:10.1016/j.compfluid.2017.01.002.

[211] G. Cao, H. Su, J. Xu, K. Xu, Implicit high-order gas kinetic scheme for turbulence simulation, Aerospace Science and Technology 92 (2019) 958 – 971. doi:10.1016/j.ast.2019.07.020.

[212] O. O. Kalkan, Implementation of k-epsilon turbulence models in a two dimensional parallel Navier-Stokes solver on hybrid grids, Middle East Technical University, Ankara, Turkey (2014).

[213] W. Zhang, L. Zhu, Y. Liu, J. Kou, Machine learning methods for turbulence modeling in subsonic flows over airfoils, arXiv preprint arXiv:1806.05904 (2018).

[214] H. Luo, J. D. Baum, R. Lohner, Extension of Harten-Lax-van Leer scheme for flows at all speeds., AIAA journal 43 (6) (2005) 1160–1166.

[215] T. Yun, G. Shiqi, L. Peiqing, W. Jinjun, Transonic buffet control research with two types of shock control bump based on RAE2822 airfoil, Chinese Journal of Aeronautics 30 (5) (2017) 1681–1696.

[216] D. Dawson, S. Kawai, S. Lele, Large-eddy simulation of a mach 2.9 turbulent boundary layer over a 24 compression ramp, in: 41st AIAA Fluid Dynamics Conference and Exhibit, 2011, p. 3431.

[217] S. Priebe, M. P. Martin, Low-frequency unsteadiness in the dns of a compression ramp shockwave and turbulent boundary layer interaction, in: 48th AIAA Aerospace Sciences Meeting Including the New Horizons Forum and Aerospace Exposition, 2010, p. 108.

[218] P. Bookey, C. Wyckham, A. Smits, M. Martín, New experimental data of stbli at dns/les accessible reynolds numbers, in: 43rd AIAA Aerospace Sciences Meeting and Exhibit, 2005, p. 309.

[219] M. P. Martín, E. M. Taylor, M. Wu, V. G. Weirs, A bandwidth-optimized weno scheme for the effective direct numerical simulation of compressible turbulence, Journal of Computational Physics 220 (1) (2006) 270–289.

[220] M. P. Martín, Direct numerical simulation of hypersonic turbulent boundary layers. part 1. initialization and comparison with experiments, Journal of Fluid Mechanics 570 (2007) 347–364.

[221] S. Xu, M. P. Martín, Assessment of inflow boundary conditions for compressible turbulent boundary layers, Physics of Fluids 16 (7) (2004) 2623–2639.

[222] X. Wu, Inflow turbulence generation methods, Annual Review of Fluid Mechanics 49 (2017) 23–49.

[223] B. Pinto, G. Lodato, Synthetic freestream disturbance for the numerical reproduction of experimental zero-pressure-gradient bypass transition test cases, Flow Turbul. Combust. 103 (1) (2019) 25–54. doi:10.1007/s10494-018-0004-6.

[224] E. Touber, Unsteadiness in shock-wave/boundary layer interactions, Ph.D. thesis, University of Southampton (2010).

[225] S. Pirozzoli, M. Bernardini, Turbulence in supersonic boundary layers at moderate reynolds number, Journal of Fluid Mechanics 688 (2011) 120–168.

[226] D. M. Dawson, S. K. Lele, J. Bodart, Assessment of wall-modeled large eddy simulation for supersonic compression ramp flows, in: 49th AIAA/ASME/SAE/ASEE Joint PropulsionConference, 2013, p. 3638.

[227] X. Zhang, C. Shu, On positivity-preserving high order discontinuous galerkin schemes for compressible euler equations on rectangular meshes, Journal of Computational Physics 229 (23) (2010) 8918–8934.

[228] L. Chen, Z. Xiao, Y. Shi, S. Chen, Constrained large-eddy simulation of supersonic turbulent boundary layer over a compression ramp, Journal of Turbulence 18 (8) (2017) 781–808.

[229] S. Pan, E. Johnsen, The role of bulk viscosity on the decay of compressible, homogeneous, isotropic turbulence, Journal of Fluid Mechanics 833 (2017) 717–744.

[230] U. Piomelli, W. H. Cabot, P. Moin, S. Lee, Subgrid-scale backscatter in turbulent and transitional flows, Physics of Fluids A: Fluid Dynamics 3 (7) (1991) 1766–1771.

[231] U. Piomelli, Y. Yu, R. J. Adrian, Subgrid-scale energy transfer and near-wall turbulence structure, Physics of Fluids 8 (1) (1996) 215–224.

[232] J. L. Lumley, G. R. Newman, The return to isotropy of homogeneous turbulence, Journal of Fluid Mechanics 82 (1) (1977) 161–178.

[233] S. B. Pope, Turbulent flows (2001).

[234] S. Pirozzoli, M. Bernardini, F. Grasso, Direct numerical simulation of transonic shock/boundary layer interaction under conditions of incipient separation, Journal of Fluid Mechanics 657 (2010) 361.

[235] F. Tong, C. Tang, Z.and Yu, X. Zhu, X. Li, Numerical analysis of shock wave and supersonic turbulent boundary interaction between adiabatic and cold walls, Journal of Turbulence 18 (6) (2017) 569–588.

[236] J. Fang, A. A. Zheltovodov, Y. Yao, C. Moulinec, D. R. Emerson, On the turbulence amplification in shock-wave/turbulent boundary layer interaction, Journal of Fluid Mechanics 897 (2020).

[237] J. Ackeret, F. Feldmann, N. Rott, Investigations of compression shocks and boundary layers in gases moving at high speed, NACA Technical Memorandum 1113, National Advisory Committee for Aeronautics (1947).

[238] H. W. Liepmann, The interaction between boundary layer and shock waves in transonic flow, Journal of the Aeronautical Sciences 13 (12) (1946) 623–637.

[239] D. S. Dolling, Fifty years of shock-wave/boundary-layer interaction research: what next?, AIAA journal 39 (8) (2001) 1517–1531.

[240] M. Wu, M. P. Martín, Analysis of shock motion in shockwave and turbulent boundary layer interaction using direct numerical simulation data, Journal of Fluid Mechanics 594 (2008) 71.

[241] B. Wang, N. D. Sandham, Z. Hu, W. Liu, Numerical study of oblique shock-wave/boundary-layer interaction considering sidewall effects, Journal of Fluid Mechanics 767 (2015) 526–561.

[242] N. A. Adams, Direct simulation of the turbulent boundary layer along a compression ramp at m= 3 and re θ= 1685, Journal of Fluid Mechanics 420 (2000) 47–83.

[243] J. A. Domaradzki, W. Liu, M. E. Brachet, An analysis of subgrid-scale interactions in numerically simulated isotropic turbulence, Physics of Fluids A: Fluid Dynamics 5 (7) (1993) 1747–1759.

[244] R. M. Kerr, J. A. Domaradzki, G. Barbier, Small-scale properties of nonlinear interactions and subgrid-scale energy transfer in isotropic turbulence, Physics of Fluids 8 (1) (1996) 197–208.

[245] J. O'Brien, J. Urzay, M. Ihme, P. Moin, A. Saghafian, Subgrid-scale backscatter in reacting and inert supersonic hydrogen–air turbulent mixing layers, Journal of fluid mechanics 743 (2014) 554–584.

[246] J. Wang, M. Wan, S. Chen, S. Chen, Kinetic energy transfer in compressible isotropic turbulence, Journal of Fluid Mechanics 841 (2018) 581–613.

[247] S. Khani, M. Waite, Backscatter in stratified turbulence, European Journal of Mechanics-B/Fluids 60 (2016) 1–12.

[248] D. Livescu, Z. Li, Subgrid-scale backscatter after the shock-turbulence interaction, in: AIP Conference Proceedings, Vol. 1793, AIP Publishing LLC, 2017, p. 150009.

[249] A. Moitro, A. S. Venkataraman, A. Poludnenko, Kinetic energy backscatter in high-speed, compressible reacting turbulence, in: APS Division of Fluid Dynamics Meeting Abstracts, 2019, pp. G05–007.

[250] W. Cabot, O. Schilling, Y. Zhou, Influence of subgrid scales on resolvable turbulence and mixing in rayleigh–taylor flow, Physics of fluids 16 (3) (2004) 495–508.

[251] D. Livescu, F. Jaberi, C. Madnia, The effects of heat release on the energy exchange in reacting turbulent shear flow, Journal of Fluid Mechanics 450 (2002) 35.

[252] H. Aluie, Scale decomposition in compressible turbulence, Physica D: Nonlinear Phenomena 247 (1) (2013) 54–65.

[253] D. Zhao, H. Aluie, Energy cascades in rayleigh-taylor turbulence, arXiv preprint arXiv:2006.04301 (2020).

[254] A. Lees, H. Aluie, Baropycnal work: A mechanism for energy transfer across scales, Fluids 4 (2) (2019) 92.

[255] Z. Zhao, N. Liu, X. Lu, Kinetic energy and enstrophy transfer in compressible rayleigh–taylor turbulence, Journal of Fluid Mechanics 904 (2020).

[256] H. Ribner, Convection of a pattern of vorticity through a shock wave. naca tech, Tech. rep., Note 2864 (1953).

[257] H. S. Ribner, Shock-turbulence interaction and the generation of noise, Vol. 1233, National Advisory Committee for Aeronautics, 1954.

[258] F. K. Moore, Unsteady oblique interaction of a shock wave with a plane disturbance, Vol. 1165, National Advisory Committee for Aeronautics, 1953.

[259] J. Kerrebrock, The interaction of flow discontinuities with small disturbances in a compressible fluid, Ph.D. thesis, California Institute of Technology (1956).

[260] L. S. Kovasznay, Turbulence in supersonic flow, Journal of the Aeronautical Sciences 20 (10) (1953) 657–674.

[261] S. Lee, S. K. LELE, P. Moin, Direct numerical simulation and analysis of shock turbulence interaction, in: 29th Aerospace Sciences Meeting, 1991, p. 523.

[262] S. Lee, S. K. Lele, P. Moin, Direct numerical simulation of isotropic turbulence interacting with a weak shock wave, Journal of Fluid Mechanics 251 (1993) 533–562.

[263] S. Lee, S. K. Lele, P. Moin, Interaction of isotropic turbulence with shock waves: effect of shock strength, Journal of Fluid Mechanics 340 (1997) 225–247.

[264] K. Mahesh, S. K. Lele, P. Moin, The influence of entropy fluctuations on the interaction of turbulence with a shock wave, Journal of Fluid Mechanics 334 (1997) 353–379.

[265] S. Jamme, J. Cazalbou, F. Torres, P. Chassaing, Direct numerical simulation of the interaction between a shock wave and various types of isotropic turbulence, Flow, Turbulence and Combustion 68 (3) (2002) 227–268.

[266] K. Mahesh, S. Lee, The interaction of an isotropic field of acoustic waves with a shock wave, J. Fluid Mech 300 (1995) 383–407.

[267] J. Qiu, C. Shu, Hermite weno schemes and their application as limiters for runge–kutta discontinuous galerkin method: one-dimensional case, Journal of Computational Physics 193 (1) (2004) 115–135.

[268] M. D. Salas, Shock fitting method for complicated two-dimensional supersonic flows, Aiaa Journal 14 (5) (1976) 583–588.

[269] P. Rawat, X. Zhong, On high-order shock-fitting and front-tracking schemes for numerical simulation of shock–disturbance interactions, Journal of Computational Physics 229 (19) (2010) 6744–6780.

[270] M. Zahr, P. Persson, An r-adaptive, high-order discontinuous galerkin method for flows with attached shocks, in: AIAA Scitech 2020 Forum, 2020, p. 0537.

[271] M. Zahr, A. Shi, P. Persson, Implicit shock tracking using an optimization-based, r-adaptive, high-order discontinuous galerkin method, arXiv preprint arXiv:1912.11207 (2019).

[272] J. VonNeumann, R. Richtmyer, A method for the numerical calculation of hydrodynamic shocks, Journal of applied physics 21 (3) (1950) 232–237.

[273] C. Jiang, G.and Shu, Efficient implementation of weighted eno schemes, Journal of computational physics 126 (1) (1996) 202–228.

[274] X. Li, D. Fu, Y. Ma, X. Liang, Direct numerical simulation of shock/turbulent boundary layer interaction in a supersonic compression ramp, Science China Physics, Mechanics and Astronomy 53 (9) (2010) 1651–1658.

[275] F. Tong, C. Yu, X. Tang, Z.and Li, Numerical studies of shock wave interactions with a supersonic turbulent boundary layer in compression corner: Turning angle effects, Computers & Fluids 149 (2017) 56–69.

[276] M. Adler, D. Gonzalez, C. Stack, D. Gaitonde, Synthetic generation of equilibrium boundary layer turbulence from modeled statistics, Computers & Fluids 165 (2018) 127–143.

[277] I. W. Kokkinakis, D. Drikakis, K. Ritos, S. M. Spottswood, Direct numerical simulation of supersonic flow and acoustics over a compression ramp, Physics of Fluids 32 (6) (2020) 066107.

[278] O. Zeman, Dilatation dissipation - The concept and application in modeling compressible mixing layers, Phys. Fluids A 2 (2) (1990) 178–188.

[279] X. Wang, S. Chen, J. Wang, H. Li, M. Wan, S. Chen, Effect of compressibility on the local flow topology in homogeneous shear turbulence, Physics of Fluids 32 (1) (2020) 015118.

[280] M. Germano, Differential filters of elliptic type, The Physics of fluids 29 (6) (1986) 1757–1758.

[281] S. Chen, J. Wang, H. Li, M. Wan, S. Chen, Effect of compressibility on small scale statistics in homogeneous shear turbulence, Physics of Fluids 31 (2) (2019) 025107.

[282] J. Wang, M. Wan, S. Chen, C. Xie, S. Chen, Effect of shock waves on the statistics and scaling in compressible isotropic turbulence, Physical Review E 97 (4) (2018) 043108.

[283] T. Wang, J.and Gotoh, T. Watanabe, Scaling and intermittency in compressible isotropic turbulence, Physical Review Fluids 2 (5) (2017) 053401.

[284] G. Sidharth, G. Candler, Subgrid-scale effects in compressible variable-density decaying turbulence, Journal of Fluid Mechanics 846 (2018) 428–459.

[285] G. Erlebacher, M. Y. Hussaini, C. G. Speziale, T. A. Zang, Toward the large-eddy simulation of compressible turbulent flows, Tech. rep., Institute for Computer Applications in Science and Engineering, Hampton VA (1990).

[286] T. Passot, A. Pouquet, Numerical simulation of compressible homogeneous flows in the turbulent regime, Journal of Fluid Mechanics 181 (1987) 441–466.

[287] S. Sarkar, G. Erlebacher, M. Y. Hussaini, Direct simulation of compressible turbulence in a shear flow, Theoretical and Computational Fluid Dynamics 2 (1991) 291–305.

[288] S. Sarkar, G. Erlebacher, M. Y. Hussaini, H. O. Kreiss, The analysis and modelling of dilatational terms in compressible turbulence, Journal of Fluid Mechanics 227 (1991) 473–493.

[289] R. S. Rogallo, P. Moin, Numerical simulation of turbulent flows, Annual Review of Fluid Mechanics 16 (1) (1984) 99–137.

[290] B. Vreman, B. Geurts, H. Kuerten, Realizability conditions for the turbulent stress tensor in large-eddy simulation, Journal of Fluid Mechanics 278 (1994) 351–362.

Appendices

Appendix A

Flux Reconstruction schemes

Collocation based nodal DG and SD have been widely used in the last few years due to their simplicity. The FR method [77, 78] provides a simple and general framework among which popular schemes like DG and SD can be recovered for linear advection problems.

The FR scheme, apart from being a robust and promising numerical scheme for aerodynamics simulations, is also a very useful tool to study a wide range of different high-order numerical schemes. Like nodal DG schemes, FR schemes exploit a high-order (nodal) polynomial basis to approximate the solution within each element of the computational domain, and like nodal DG schemes, inter-element continuity is not strongly enforced. However, unlike nodal DG schemes, FR methods are based solely on the governing system in a differential form. A description of the FR approach in one dimension is presented below.

For simplicity, let us consider a reference element $\Omega_n = \{\hat{x}| -1 \leq \hat{x} \leq 1\}$ in which the general one-dimensional conservation law is defined

$$\frac{\partial u}{\partial t} + \frac{\partial (f(u))}{\partial \hat{x}} = 0. \tag{A.1}$$

The FR approach to solve Eq. (A.1) within the standard element can be described in five stages. The first stage involves the representation of the approximated solution $\hat{u}$ in terms of a nodal basis function:

$$\hat{u}(\hat{x}) = \sum_{i=0}^{N} u_i l_i(\hat{x}), \tag{A.2}$$

where l_i are the Lagrange polynomials defined on a certain set of points $\hat{x}_i$ (with i=0 to N) called solution points. Notice that this implies a polynomial representation of $\hat{u}$ of degree k. The second stage consists in the construction of a degree N polynomial flux $\hat{f}^D = \hat{f}^D(\hat{x}, t)$ which is based on the same

collocation basis as $\hat{u}$:

$$\hat{f}^D(\hat{x}) = \sum_{i=0}^{N} f_i^D l_i(\hat{x}), \tag{A.3}$$

where flux nodal values can be easily evaluated directly from the approximated solution. The third stage involves the evaluation of the approximate solution at the end points of the standard element (namely, $\hat{u}(\pm 1)$). Subsequently, this information is used to compute the numerical flux at the left $\hat{f}_L^I$ and right $\hat{f}_R^I$ interfaces. The fourth stage involves the construction of the degree $N+1$ polynomial $\hat{f}$, by adding a correction flux $\hat{f}^C = \hat{f}^C(\hat{x}, t)$ of degree $N+1$ to $\hat{f}^D$, such that their sum recovers the numerical interface flux at $\hat{x} = \pm 1$, yet in some sense follows $\hat{f}^D$ within the interior of Ω_s. This is the key step of FR schemes since an higher order polynomial (degree $N+1$) is summed to the interpolated one, leading to a difference in approximation order that plays a fundamental role in the whole procedure.

In order to define $\hat{f}^C$ such that it satisfies the above requirements, consider first two degree $N+1$ correction functions $g_L = g_L(\hat{x})$ and $g_R = g_R(\hat{x})$ approximating zero (in some sense) within Ω_s and satisfying the following conditions:

$$g_L(-1) = 1, \quad g_L(1) = 0, \tag{A.4}$$

$$g_R(-1) = 0, \quad g_R(1) = 1, \tag{A.5}$$

and

$$g_L(\hat{x}) = g_R(-\hat{x}). \tag{A.6}$$

Then a suitable formulation for $\hat{f}^C$ can now be written as

$$\hat{f}^C = (\hat{f}_L^I - \hat{f}_L^D) g_L + (\hat{f}_R^I - \hat{f}_R^D) g_R, \tag{A.7}$$

where $\hat{f}_L^D = \hat{f}^D(-1, t)$ and $\hat{f}_R^D = \hat{f}^D(1, t)$. Using this expression, the degree $N+1$ approximate total flux $\hat{f}$ within Ω_s can be constructed from the discontinuous and correction fluxes as follows

$$\hat{f} = \hat{f}^D + \hat{f}^C = \hat{f}^D + (\hat{f}_L^I - \hat{f}_L^D) g_L + (\hat{f}_R^I - \hat{f}_R^D) g_R. \tag{A.8}$$

The fifth and final stage of the FR approach involves the evaluation of the flux divergence at each solution point $\hat{x}_i$ using the expression

$$\frac{\mathrm{d}\hat{f}}{\mathrm{d}\hat{x}}(\hat{x}_i) = \sum_{j=0}^{N} \hat{f}_j^D \frac{\mathrm{d}l_j}{\mathrm{d}\hat{x}}(\hat{x}_i) + (\hat{f}_L^I - \hat{f}_L^D) \frac{\mathrm{d}g_L}{\mathrm{d}\hat{x}}(\hat{x}_i) + (\hat{f}_R^I - \hat{f}_R^D) \frac{\mathrm{d}g_R}{\mathrm{d}\hat{x}}(\hat{x}_i). \tag{A.9}$$

These values can then be used to advance $\hat{u}$ in time via a suitable temporal discretisation of the following semi-discrete expression

$$\frac{\mathrm{d}\hat{u}_i}{\mathrm{dt}} = -\frac{\mathrm{d}\hat{f}}{\mathrm{d}\hat{x}}(\hat{x}_i). \tag{A.10}$$

The nature of a particular FR scheme depends solely on three factors:

1. the location of the solution points $\hat{x}_i$;
2. the methodology for calculating the interface fluxes $\hat{f}_L^I$ and $\hat{f}_R^I$;
3. the form of the flux correction functions g_L and g_R.

It has been shown by Huynh [77] that, for particular choices of the correction functions, it is possible to recover some well known collocation methods (among which, nodal DG and SD) for the linear advection equation. In particular, Vincent-Catonguay-Jameson-Huynh Flux Reconstruction schemes can be obtained with the following choice of correction functions:

$$\begin{aligned} g_L(x) &= \frac{(-1)^N}{2}\left[L_N(x) - \left(\frac{\eta_N L_{N-1}(x) + L_{N+1}(x)}{1+\eta_N}\right)\right], \\ g_R(x) &= \frac{1}{2}\left[L_N(x) + \left(\frac{\eta_N L_{N-1}(x) + L_{N+1}(x)}{1+\eta_N}\right)\right], \end{aligned} \tag{A.11}$$

where

$$\eta_N = \frac{c(2N+1)(a_N N!)^2}{2} \quad \text{and} \quad a_N = \frac{(2N)!}{2^N (N!)^2}. \tag{A.12}$$

In the above relations, L_N is a Legendre polynomial of degree N, and c is a free scalar parameter that must lie within the range

$$c_- < c < c_\infty, \quad \text{with} \quad c_- = \frac{-2}{(2N+1)(a_N N!)^2} \quad \text{and} \quad c_\infty = \infty.$$

For the particular choice of the parameter c nodal DG and SD schemes are recovered. In particular:

$$c_{DG} = 0 \quad \text{and} \quad c_{SD} = \frac{2(N+1)}{(2N+1)N(a_N N!)^2}.$$

In this way, the respective correction functions for DG and SD simplify in the following expressions:

$$\begin{aligned} g_L^{DG}(x) &= \frac{(-1)^N}{2}(L_N(x) - L_{N+1}(x)), \quad & g_R^{DG}(x) &= \frac{(-1)^N}{2}(L_N(x) + L_{N+1}(x)), \\ g_L^{SD}(x) &= \frac{(-1)^N}{2}(1-x)L_N(x), & g_R^{SD}(x) &= \frac{1}{2}(1+x)L_N(x). \end{aligned} \tag{A.13}$$

An example of correction functions recovering DG and SD schemes, namely, the DG-FR and SD-FR schemes, respectively, is shown in Fig. A.1.

In the particular case of the linear advection equation with unitary advection velocity, the FR scheme can be expressed in a matrix form as

$$\frac{\mathrm{d}\hat{\mathbf{u}}}{\mathrm{dt}} = -2\mathbf{D}\hat{\mathbf{u}} - (2\hat{f}_L^I - 2\mathbf{l}^T\hat{\mathbf{u}})\mathbf{g}^L - (2\hat{f}_R^I - 2\mathbf{r}^T\hat{\mathbf{u}})\mathbf{g}^R, \tag{A.14}$$

where $\hat{\mathbf{u}}_i = \hat{u}(\hat{x}_i)$, $\mathbf{D}_{ij} = \frac{\mathrm{d}l_j}{\mathrm{d}\hat{x}}(\hat{x}_i)$, $\mathbf{g}_i^{L/R} = \frac{\mathrm{d}g_{L/R}}{\mathrm{d}\hat{x}}(\hat{x}_i)$ and $\mathbf{r}_i = l_i(1)$, $\mathbf{l}_i = l_i(-1)$.

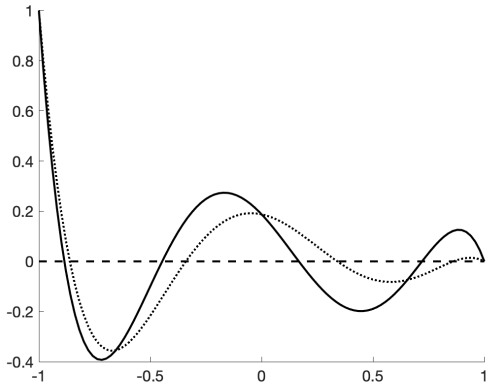

Figure A.1: FR correction functions (g_L) of degree $N = 5$ recovering DG and SD schemes: solid line, DG-FR; dotted line, SD-FR.

Appendix B

SD scheme versus SD-FR scheme

In order to highlight the connection between the SD method and the corresponding FR recovering scheme, it is interesting to rewrite Eq. (4.5) at the general location $\hat{x}$ as

$$\frac{\mathrm{d}\hat{f}}{\mathrm{d}\hat{x}}(\hat{x}) = \sum_{j=0}^{N+1} f_j \frac{\mathrm{d}l_j^f}{\mathrm{d}\hat{x}}(\hat{x}) + (\hat{f}_L^I - f_0)\frac{\mathrm{d}l_0^f}{\mathrm{d}\hat{x}}(\hat{x}) + (\hat{f}_R^I - f_{N+1})\frac{\mathrm{d}l_{N+1}^f}{\mathrm{d}\hat{x}}(\hat{x}), \quad \text{(B.1)}$$

where the contributions of the interpolated fluxes at $\hat{x} = \pm 1$ have been added and subtracted. Observing this formulation, it is clearly evident the analogy with Eq. (A.9). In particular, it is easy to show that the first summation of the two equations is exactly the same for a linear flux function. In fact, considering the linear advection equation with unitary advection velocity, namely $f(\hat{x}) \equiv u(\hat{x})$:

$$\begin{aligned}\sum_{j=0}^{N+1} f_j \frac{\mathrm{d}l_j^f}{\mathrm{d}\hat{x}}(\hat{x}) = \sum_{j=0}^{N+1}\left(\sum_{i=0}^{N} u_i l_i^s(\hat{x}_j^f)\right)\frac{\mathrm{d}l_j^f}{\mathrm{d}\hat{x}}(\hat{x}) = \sum_{i=0}^{N} u_i \sum_{j=0}^{N+1} l_i^s(\hat{x}_j^f)\frac{\mathrm{d}l_j^f}{\mathrm{d}\hat{x}}(\hat{x}) = \\ = \sum_{i=0}^{N} u_i \frac{\mathrm{d}}{\mathrm{d}\hat{x}}\left(\sum_{j=0}^{N+1} l_i^s(\hat{x}_j^f) l_j^f(\hat{x})\right) = \sum_{i=0}^{N} u_i \frac{\mathrm{d}l_i^s}{\mathrm{d}\hat{x}}(\hat{x}).\end{aligned} \quad \text{(B.2)}$$

The last equality has been obtained by noting that the Lagrange interpolation over $N+2$ points of the Lagrange polynomial of order $N+1$, namely $l_i^s(\hat{x})$, coincides with this last.

Notice that, if a non-constant advection velocity is considered and the

flux is defined as $\hat{f} = a(\hat{x})u(\hat{x})$, following the original SD case:

$$\sum_{j=0}^{N+1} f_j \frac{\mathrm{d}l_j^f}{\mathrm{d}\hat{x}}(\hat{x}) = \sum_{j=0}^{N+1} a(\hat{x}_j^f)\left(\sum_{i=0}^{N} u_i l_i^s(\hat{x}_j^f)\right)\frac{\mathrm{d}l_j^f}{\mathrm{d}\hat{x}}(\hat{x}) = \sum_{i=0}^{N} u_i \sum_{j=0}^{N+1} a(\hat{x}_j^f) l_i^s(\hat{x}_j^f)\frac{\mathrm{d}l_j^f}{\mathrm{d}\hat{x}}(\hat{x}) =$$
$$= \sum_{i=0}^{N} u_i \frac{\mathrm{d}}{\mathrm{d}\hat{x}}\Bigg(\underbrace{\sum_{j=0}^{N+1} a(\hat{x}_j^f) l_i^s(\hat{x}_j^f) l_j^f(\hat{x})}_{\mathcal{I}^f[a(\hat{x})l_i^s(\hat{x})]}\Bigg) = \sum_{i=0}^{N} u_i \frac{\mathrm{d}(\mathcal{I}_l[a(\hat{x})l_i^s(\hat{x})])}{\mathrm{d}\hat{x}}(\hat{x}), \tag{B.3}$$

where $\mathcal{I}^f[\cdot]$ denotes the Lagrange interpolation operation over the $N+2$ flux points. Eq. (B.3) evidently differs from what would be obtained from the FR procedure:

$$\sum_{i=0}^{N} f_i \frac{\mathrm{d}l_i^s}{\mathrm{d}\hat{x}}(\hat{x}) = \sum_{i=0}^{N} a(\hat{x}_i^s) u_i \frac{\mathrm{d}l_i^s}{\mathrm{d}\hat{x}}(\hat{x}). \tag{B.4}$$

Clearly the two right-hand sides are equal only when the advection velocity is constant.

Considering now the second part of Eq. (B.1), it is evident that, in order for the FR method to recover the SD scheme, $g_L(\hat{x}) = l_0^f(\hat{x})$ and $g_R(\hat{x}) = l_{N+1}^f(\hat{x})$. So, just changing polynomial basis, the classical expressions for g_L and g_R are recovered:

$$g_L^{SD}(\hat{x}) = \frac{(-1)^N}{2}(1-\hat{x})L_N(\hat{x}) \quad \text{and} \quad g_R^{SD}(\hat{x}) = \frac{1}{2}(1+\hat{x})L_N(\hat{x}), \tag{B.5}$$

where L_N is the Legendre polynomial of degree N.

It is worthwhile stressing that the definition of flux points is a key ingredient in the SD method. In fact, considering the SD discretisation of the linear advection equation, according to the particular choice of flux nodes, a correction function in the FR framework is implicitly defined. This link will be of fundamental importance in the proof of equivalence between the two schemes under such conditions.

Appendix C

Original Roe's solver

The idea of Roe is the definition of a parameter vector $\mathbf{Q}$ such that both variables and fluxes can be defined through it:

$$\mathbf{U} = \mathbf{U}(\mathbf{Q}) \quad \mathbf{F} = \mathbf{F}(\mathbf{Q}) \tag{C.1}$$

then is useful to use two matrices which, depending on the choice of A and Q, are able to describe the jumps of primitive variables and fluxes linearly:

$$\Delta\mathbf{U} = \tilde{B}\Delta\mathbf{Q} \quad \Delta\mathbf{F} = \tilde{C}\Delta\mathbf{Q} \tag{C.2}$$

this implicitly defines $\tilde{A} = \tilde{C}\tilde{B}^{-1}$.

Let's consider the one-dimensional isothermal case as an example. Notice that in this case the speed of sound a is a constant value.

$$\mathbf{U}_t + \mathbf{F}(\mathbf{U})_x = 0 \tag{C.3}$$

with

$$\mathbf{U} = \begin{pmatrix} U_1 \\ U_2 \end{pmatrix} = \begin{pmatrix} \rho \\ \rho u_1 \end{pmatrix} \quad \mathbf{F} = \begin{pmatrix} f_1 \\ f_2 \end{pmatrix} = \begin{pmatrix} \rho u_1 \\ \rho u_1^2 + a^2\rho \end{pmatrix} \tag{C.4}$$

The exact jacobian can be easily computed as:

$$A(\mathbf{U}) = \begin{bmatrix} 0 & 1 \\ a^2 - u_1^2 & 2u_1 \end{bmatrix} \tag{C.5}$$

with eigenvalues $\lambda_1 = u_1 - a$ and $\lambda_2 = u_1 + a$, and eigenvectors:

$$L^{(1)} = \begin{pmatrix} 1 \\ u - c \end{pmatrix} \quad L^{(2)} = \begin{pmatrix} 1 \\ u + c \end{pmatrix} \tag{C.6}$$

We can now choose the parameter vector as:

$$\mathbf{Q} = \begin{pmatrix} q_1 \\ q_2 \end{pmatrix} = \frac{\mathbf{U}}{\sqrt{\rho}} \tag{C.7}$$

In this way we can define the jumps of variables and fluxes using the matrices $\tilde{B}$ and $\tilde{C}$:

$$\tilde{B} = \begin{bmatrix} 2\tilde{q}_1 & 0 \\ \tilde{q}_2 & \tilde{q}_1 \end{bmatrix}, \qquad \tilde{C} = \begin{bmatrix} \tilde{q}_2 & \tilde{q}_1 \\ 2a^2\tilde{q}_1 & 2\tilde{q}_2 \end{bmatrix}, \tag{C.8}$$

where $\tilde{\mathbf{Q}} = \frac{1}{2}(\mathbf{Q}_L + \mathbf{Q}_R)$. Now it's easy to derive that

$$A(\mathbf{U}) = \begin{bmatrix} 0 & 1 \\ a^2 - \tilde{u}^2 & 2\tilde{u} \end{bmatrix}, \tag{C.9}$$

with

$$\tilde{u}_1 = \frac{\sqrt{\rho_L}u_L + \sqrt{\rho_R}u_R}{\sqrt{\rho_L} + \sqrt{\rho_R}}. \tag{C.10}$$

So, known $\tilde{A}$, is possible to compute the correspondent eigenvalue and eigenvectors (exactly the same as before but using the averaged velocity $\tilde{u}$).

Once this is done, as we have seen we can find the coefficients α considering the jump between the primitive variables and finally compute the flux using (4.48).

Finally, all these results can be generalized to the x-split three dimensional time dependent Euler equations for real gases.

Appendix D

Split form of Roe's flux for Euler equations

The three dimensional Euler equations can be written as follows:

$$\frac{\partial \mathbf{U}}{\partial t} + A_1 \frac{\partial \mathbf{U}}{\partial x} + A_2 \frac{\partial \mathbf{U}}{\partial y} + A_3 \frac{\partial \mathbf{U}}{\partial z} = 0 \tag{D.1}$$

where $\mathbf{U} = (\rho, \rho u_1, \rho u_2, \rho u_3, \rho E)^T$ and

$$A_1 = \begin{bmatrix} 0 & 1 & 0 & 0 & 0 \\ (\gamma-1)H-u_1^2-a^2 & (3-\gamma)u_1 & -(\gamma-1)u_2 & -(\gamma-1)u_3 & \gamma-1 \\ -u_1u_2 & u_2 & u_1 & 0 & 0 \\ -u_1u_3 & u_3 & 0 & u_1 & 0 \\ u_1[(\gamma-1)H-a^2] & H-(\gamma-1)u_1^2 & -(\gamma-1)u_1u_2 & -(\gamma-1)u_1u_3 & -(\gamma-1)u \end{bmatrix} \tag{D.2}$$

$$A_2 = \begin{bmatrix} 0 & 0 & 1 & 0 & 0 \\ -u_1u_2 & u_2 & u_1 & 0 & 0 \\ (\gamma-1)H-u_2^2-a^2 & -(\gamma-1)u_1 & (3-\gamma)u_2 & -(\gamma-1)u_3 & \gamma-1 \\ -u_2u_3 & 0 & u_3 & u_2 & 0 \\ u_2[(\gamma-1)H-a^2] & -(\gamma-1)u_1u_2 & H-(\gamma-1)u_2^2 & -(\gamma-1)u_2u_3 & -(\gamma-1)u_2 \end{bmatrix} \tag{D.3}$$

$$A_3 = \begin{bmatrix} 0 & 0 & 0 & 1 & 0 \\ -u_1u_3 & u_3 & 0 & u_1 & 0 \\ -u_2u_3 & 0 & u_3 & u_2 & 0 \\ (\gamma-1)H-u_3^2-a^2 & -(\gamma-1)u_1 & -(\gamma-1)u_2 & (3-\gamma)u_3 & \gamma-1 \\ u_3[(\gamma-1)H-a^2] & -(\gamma-1)u_1u_3 & -(\gamma-1)u_2u_3 & H-(\gamma-1)u_3^2 & -(\gamma-1)u_3 \end{bmatrix} \tag{D.4}$$

It can be theoretically proved that there's no change of variables capable of diagonalising A_1,A_2, and A_3 simultaneously. Then, a different strategy is usually chosen in order to study the three-dimensional case where, as reference jacobian the following linear combination is used:

$$A_n = A_1 n_1 + A_2 n_2 + A_3 n_3. \tag{D.5}$$

In this way, whenever the one of the particular direction is considered a consistent one-dimensional formulation is easily recovered. The definition of

A_n given in Eqn. (D.5) admits the following eigenvector and eigenvalues:

$$L^{(1)} = \begin{pmatrix} 1 \\ u_1 - an_1 \\ u_2 - an_2 \\ u_3 - an_3 \\ H - au_n \end{pmatrix}, \quad L^{(2)} = \begin{pmatrix} n_1 \\ n_1 u_1 \\ n_1 u_2 + an_3 \\ n_1 u_3 - an_2 \\ n_1 q - aw_1 \end{pmatrix}, \quad L^{(3)} = \begin{pmatrix} n_2 \\ n_2 u_1 - an_3 \\ n_2 u_2 \\ n_2 u_3 + an_1 \\ n_2 q - aw_2 \end{pmatrix}, \tag{D.6}$$

$$L^{(4)} = \begin{pmatrix} n_3 \\ n_3 u_1 + an_2 \\ n_3 u_2 - an_1 \\ n_3 u_3 \\ n_3 q - aw_3 \end{pmatrix}, \quad L^{(5)} = \begin{pmatrix} 1 \\ u_1 + an_1 \\ u_2 + an_2 \\ u_3 + an_3 \\ H + au_n \end{pmatrix}, \tag{D.7}$$

$$\lambda_1 = u_n - a, \quad \lambda_2 = \lambda_3 = \lambda_4 = u_n, \quad \lambda_5 = u_n + a, \tag{D.8}$$

with $H = \frac{1}{\rho}(E + p)$ and $q = \frac{1}{2}(u_1^2 + u_2^2 + u_3^2)$, $u_n = \mathbf{u} \cdot \mathbf{n}$ and $\mathbf{w} = \mathbf{n} \times \mathbf{u}$.

For simplicity, the case $\mathbf{n} = (1, 0, 0)^T$ will be considered. In this way the parameter vector can be defined as:

$$\mathbf{Q} = \sqrt{\rho} \begin{pmatrix} 1 \\ u_1 \\ u_2 \\ u_3 \\ H \end{pmatrix}. \tag{D.9}$$

The jumps of conserved variables and fluxes can then be defined using the parameter vector as $\Delta\mathbf{U} = \tilde{B}\Delta\mathbf{Q}$ and $\Delta\mathbf{F} = \tilde{C}\Delta\mathbf{Q}$ where expressions for $\tilde{B}$ and $\tilde{C}$ can be easily calculated and used to obtain the Roe matrix $\tilde{A} = \tilde{B}\tilde{C}^{-1}$. Finally, $\tilde{(\cdot)}$ denotes quantities evaluated using the arithmetic mean components of the parameter vector. Namely, the relevant averages can be expressed as:

$$\tilde{u}_1 = \frac{\frac{1}{2}((q_2)_L + (q_2)_R)}{\frac{1}{2}((q_1)_L + (q_1)_R)} = \frac{(\sqrt{\rho}u_1)_L + (\sqrt{\rho}u_1)_R}{\sqrt{\rho_L} + \sqrt{\rho_R}} \tag{D.10}$$

$$\tilde{u}_2 = \frac{\frac{1}{2}((q_3)_L + (q_3)_R)}{\frac{1}{2}((q_1)_L + (q_1)_R)} = \frac{(\sqrt{\rho}u_2)_L + (\sqrt{\rho}u_2)_R}{\sqrt{\rho_L} + \sqrt{\rho_R}} \tag{D.11}$$

$$\tilde{u}_3 = \frac{\frac{1}{2}((q_4)_L + (q_4)_R)}{\frac{1}{2}((q_1)_L + (q_1)_R)} = \frac{(\sqrt{\rho}u_3)_L + (\sqrt{\rho}u_3)_R}{\sqrt{\rho_L} + \sqrt{\rho_R}} \tag{D.12}$$

$$\tilde{H} = \frac{\frac{1}{2}((q_5)_L + (q_5)_R)}{\frac{1}{2}((q_1)_L + (q_1)_R)} = \frac{\sqrt{\rho_L}H_L + \sqrt{\rho_R}H_R}{\sqrt{\rho_L} + \sqrt{\rho_R}} \tag{D.13}$$

$$\tilde{a} = \sqrt{(\gamma - 1)[\tilde{H} - \tilde{q}]} \tag{D.14}$$

So, matrix $\tilde{A}$ is exactly equal to (D.5) but evaluated using Roe averages. Consequently, the eigenvalues are the same as well.

In analogy with the classical approach in 1D, the conserved variables' jumps can be written using the eigenvalues $\tilde{L}$'s as :

$$\Delta \mathbf{U} = \sum_{i=1}^{5} \tilde{\gamma}_i \tilde{L}^{(i)}. \tag{D.15}$$

Storing the eigenvalues as columns of the matrix L an alternative expression reads:

$$\Delta \mathbf{U} = \tilde{\boldsymbol{\gamma}} L \qquad \rightarrow \qquad \tilde{\boldsymbol{\gamma}} = L^{-1} \Delta \mathbf{U}. \tag{D.16}$$

Finally, the expression of the numerical flux at the interface can be evaluated as:

$$\mathbf{F}_{i+\frac{1}{2}} = \frac{1}{2}(\mathbf{F}_L + \mathbf{F}_R) - \frac{1}{2} \sum_{i=1}^{5} \tilde{\gamma}_i |\tilde{\lambda}_i| \tilde{L}^{(i)} \tag{D.17}$$

and so:

$$\mathbf{F}_{i+\frac{1}{2}} = \frac{1}{2}(\mathbf{F}_L + \mathbf{F}_R) - \frac{1}{2} L |\Lambda| L^{-1} \Delta \mathbf{U} \tag{D.18}$$

where $\Lambda = \mathrm{diag}(\tilde{\lambda}_i)$. Such formulation is particularly important since it can be clearly subdivided in a part that will be shown to be essentially the approximation of the flux at interface whereas the second part represents a dissipative term as it will be seen in more detail in the following subsection.

As already mentioned, the present approach has been explicitly followed for the case of $\mathbf{n} = (1, 0, 0)^T$. Nevertheless, in the three-dimensional case, the element in the physical space can be always easily transformed back in a reference frame where the element edges are aligned with the (x, y, z) axis. Then, the simple example herein shown is the only relevant one for practical implementations following the tensor product approach already introduced in the previous section about the Spectral Difference scheme.

High-order spectral element methods for the simulation of compressible turbulent flows

Keywords: CFD, high-order methods, turbulence, numerical dissipation/dispersion

Abstract

This thesis is focused on the application of high-order methods to compressible turbulent flows. Aspects such as numerical dissipation/dispersion, dynamic Sub-Grid Scale modelling, shock-capturing techniques and compressibility effects on turbulence modelling are thoroughly discussed. The thesis manuscript is organised for increasing levels of complexity, leading ultimately to the simulation of fully compressible turbulent flows where all the up-mentioned difficulties are simultaneously involved. The results presented in this work fit into development of reliable and robust high-order solvers for computational fluid dynamics applications.

An innovative generalisation of standard spectral analyses techniques applied to high-order methods is first presented. Special attention is dedicated to the Spectral Difference scheme used for the numerical simulations performed for this thesis. Spectral analyses of high-order methods are normally based on the numerical discretisation of the one-dimensional linear advection equation. In the present work, such approach has been generalised for non-constant advection velocities to gain more meaningful insights about high-order numerical discretisations of non-linear equations, such as Navier-Stokes or Euler equations. The Spectral Difference method has shown some significant differences with respect to the correspondent Flux Reconstruction recovering scheme when non-constant advection velocities are considered. The general behaviour of dissipative curves has shown remarkable deviations between SD, FR-SD and the Flux Reconstruction Discontinuous Galerkin recovering scheme. Numerical experiments have been conducted to highlight the role played by numerical fluxes and order of approximation for Spectral Difference and FR-DG methods.

The informations gathered from spectral analyses are then used to present the Spectral Element Dynamic Model. The SEDM has been developed by Chapelier & Lodato [1] to link numerical dissipation, which represents a typical build-in feature of spectral element methods, and classical explicit SGS dissipation within the framework of Large-Eddy Simulations of turbulent flows. A series of relevant transitional turbulent flows are then considered to better evaluate the performance of the SEDM in more complex conditions. Namely, a zero-pressure-gradient flow over a flat plate and a low-Reynolds SD7003 airfoil simulation. Both computations are meant to study in deep

the dynamic nature of the SEDM for complex geometries and transitional flows.

Within the framework of compressible flows, an innovative low dissipative bulk-based artificial viscosity shock-capturing technique is presented and analysed in detail. Numerical simulations in one to three dimensions, inviscid and viscous, laminar and turbulent flows are considered to provide a sufficiently wide range of flow configurations where the proposed model performs well. In particular, in comparison with another widely diffused artificial viscosity model based on a laplacian regularisation. The bulk-based artificial viscosity provides, in fact, considerably reduced levels of artificial dissipation of vortical structures, keeping, at the same time, the simulation stable.

Finally, in the last part of the manuscript, the coexistence of all the up-mentioned investigations and models presented throughout the thesis is studied for more complex compressible turbulent flows. Among these, the transonic flow around an RAE2822 airfoil and the interaction between a turbulent boundary layer with a 24° compression ramp have been simulated using an LES approach, where the SEDM has been coupled with the proposed bulk-based AV technique. Both simulations provided results in good agreement with other simulations and experiments, certifying the robustness and reliability of the combined effect of the two models.

In the end, in order to generalise even more the SEDM to more compressible applications, a Direct Numerical Simulation study for a compression/expansion ramp configuration has been performed. The highly-resolved data have been used to reveal insightful informations regarding the SGS kinetic energy dissipation expected to take place in the presence of non-negligible compressibility effects for wall bounded flows. The impact of the spherical part of the SGS tensor (*i.e.*, the turbulent kinetic energy), often not explicitly modelled for weakly compressible flows, appeared to have a relevant role in kinetic energy transfer. The SGS dissipation term has shown to be directly connected to the local levels of compressibility, identified by the velocity dilatation field. Compressions motions are more likely to experience classical direct kinetic energy cascade, whereas expansions promote back-scatter phenomena. Such informations can be particularly useful in the development of more compressible formulations of classical LES models, including, for example, a model for the spherical part of the SGS tensor.

All the contributions, ideas and investigations presented in this thesis represent the first step toward a unified LES model able to handle, at the same time, both turbulence under-resolution and shock-waves with techniques and strategies specifically tailored for high-order numerical schemes.

Resumé

Cette thèse se concentre sur l'application des méthodes d'ordre élevé aux écoulements turbulents compressibles. Des aspects tels que la dissipation/dispersion numérique, la modélisation dynamique à l'échelle de sous-maille (SGS), les techniques de capture des chocs et les effets de la compressibilité sur la modélisation de la turbulence sont discutés. Le manuscrit de thèse est organisé selon des niveaux de complexité croissants, menant à la simulation d'écoulements turbulents entièrement compressibles où toutes les difficultés mentionnées ci-dessus sont simultanément impliquées. Les résultats présentés dans ce travail s'inscrivent dans le développement de solveurs d'ordre élevé fiables et robustes pour les applications de mécanique des fluides numérique.

Une généralisation innovante des techniques d'analyses spectrales standard appliquées aux méthodes d'ordre élevé est d'abord présentée. Une attention particulière est consacrée au schéma de différence spectrale utilisé pour les simulations numériques réalisées dans le cadre de cette thèse. Les analyses spectrales des méthodes d'ordre élevé sont généralement basées sur la discrétisation numérique de l'équation d'advection linéaire unidimensionnelle. Dans ce travail de thèse, cette approche a été généralisée pour des vitesses d'advection non constantes afin d'obtenir des informations plus significatives sur les discrétisations numériques d'ordre élevé des équations non linéaires, telles que les équations de Navier-Stokes ou d'Euler. La méthode de différence spectrale a montré quelques différences significatives par rapport au schéma correspondant de récupération par reconstruction de flux lorsque des vitesses d'advection non constantes sont considérées. Le comportement général des courbes dissipatives a montré des écarts remarquables entre la méthode SD, la méthode FR-SD et le schéma de récupération par reconstruction de flux de Galerkin discontinu. Des expériences numériques ont été menées pour mettre en évidence le rôle joué par les flux numériques et l'ordre d'approximation pour les méthodes SD et FR-DG.

Les informations recueillies à partir des analyses spectrales sont ensuite utilisées pour présenter le modèle dynamique des éléments spectraux. Le modèle SEDM a été développé par Chapelier & Lodato [1] pour relier la dissipation numérique, qui représente une caractéristique intégrale typique des méthodes par éléments spectraux, et la dissipation de sous-maille ex-

plicite classique dans le cadre des simulations à grande échelle d'écoulements turbulents. Une série d'écoulements turbulents transitoires pertinents sont ensuite considérés pour mieux évaluer la performance du modèle SEDM dans des conditions plus complexes. Il s'agit d'un écoulement à gradient de pression nul sur une plaque plane et d'une simulation d'un profil aérodynamique SD7003 à faible nombre de Reynolds. Les deux calculs sont destinés à étudier en profondeur la nature dynamique du modèle SEDM pour des géométries complexes et des écoulements transitoires.

Dans le cadre des écoulements compressibles, une technique innovante de capture des chocs par viscosité artificielle à faible dissipation est présentée et analysée en détail. Des simulations numériques unidimensionnel et tridimensionnel, inviscides et visqueuses, laminaires et turbulentes, sont considérées comme fournissant une gamme suffisamment large de configurations d'écoulement où le modèle proposé donne de bons résultats. En particulier, en comparaison avec un autre modèle de viscosité artificielle largement répandu basé sur une régularisation laplacienne. La viscosité artificielle basée sur le volume fournit des niveaux considérablement réduits de dissipation artificielle des structures tourbillonnaires, en gardant, en même temps, la simulation stable.

Enfin, dans la dernière partie du manuscrit, la coexistence de toutes les recherches et modèles présentés tout au long de la thèse est étudiée pour des écoulements turbulents compressibles plus complexes. Parmi ceux-ci, l'écoulement transsonique autour d'un profilé RAE2822 et l'interaction entre une couche limite turbulente et une rampe de compression de 24° ont été simulés à l'aide d'une approche LES, où le modèle SEDM a été couplé avec la technique AV basée sur le volume proposée. Les deux simulations ont fourni des résultats en accord avec d'autres simulations et expériences, certifiant la robustesse et la fiabilité de l'effet combiné des deux modèles.

Enfin, afin de généraliser encore plus le modèle SEDM à des applications plus compressibles, une étude en simulation numérique directe pour une configuration de rampe de compression/détente a été réalisée. Les données hautement résolues ont été utilisées pour révéler des informations instructives sur la dissipation de l'énergie cinétique de sous-maille qui devrait avoir lieu en présence d'effets de compressibilité non négligeables pour des écoulements limités par des parois. L'impact de la partie sphérique du tenseur SGS (*i.e.*, l'énergie cinétique turbulente), souvent non modélisée explicitement pour les écoulements faiblement compressibles, est apparu comme ayant un rôle pertinent dans le transfert d'énergie cinétique. Le terme de dissipation SGS s'est avéré être directement lié aux niveaux locaux de compressibilité, identifiés par le champ de dilatation de la vitesse. Les mouvements de compression sont plus susceptibles de connaître une cascade d'énergie cinétique directe classique, tandis que les expansions favorisent les phénomènes de rétrodiffusion. Ces informations peuvent être particulièrement utiles dans le développement de formulations plus compressibles des modèles LES classiques, y compris,

par exemple, un modèle pour la partie sphérique du tenseur SGS.

Toutes les contributions, idées et recherches présentées dans cette thèse représentent le premier pas vers un modèle LES unifié capable de traiter, en même temps, la sous-résolution de la turbulence et les ondes de choc avec des techniques et stratégies spécifiquement adaptées aux schémas numériques d'ordre élevé.